

RÉPUBLIQUE DU CAMEROUN  
Paix - Travail - Patrie

UNIVERSITÉ DE YAOUNDÉ I

CENTRE DE RECHERCHE ET DE FORMATION  
DOCTORALE EN SCIENCES, TECHNOLOGIES  
ET GEOSCIENCES

Unité de recherche et de formation  
Doctorale en physiques et applications

B.P 812 Yaoundé  
Email: crfd\_stg@uy1.uninet.cm



REPUBLIC OF CAMEROON  
Peace - Work - Fatherland

UNIVERSITY OF YAOUNDE I

POSTGRADUATE SCHOOL OF SCIENCES,  
TECHNOLOGY AND GEOSCIENCES

Research and postgraduate training  
unit for physics and Applications

P.O. Box 812 Yaounde  
Email: crfd\_stg@uy1.uninet.cm

DÉPARTEMENT DE PHYSIQUE  
DEPARTMENT OF PHYSICS

LABORATOIRE DE MÉCANIQUE, MATÉRIAUX ET STRUCTURES  
LABORATORY OF MECHANICS, MATERIALS AND STRUCTURES

***PT/APT*-symmetric electronic systems in wave  
transport phenomena: the cases of Anderson  
Localization and Electromagnetically Induced  
Transparency**

*Thesis submitted and defended in partial fulfillment of the requirements for the awards  
of a Doctor of Philosophy (Ph.D) degree in Physics*

**Specialty: Mechanics, Materials and Structures  
Option: Fundamental Mechanics and Complex Systems**

By

**TAGOUEGNI Senghor**

*Registration number: 09W1324  
Master in Physics*

Under the supervision of:

**FOTSA NGAFFO Fernande**  
*Associate Professor  
University of Yaounde I*

**KENFACK JIOTSA Aurélien**  
*Professor  
University of Yaounde I*



© Year: 2022

RÉPUBLIQUE DU CAMEROUN

Paix - Travail - Patrie

UNIVERSITÉ DE YAOUNDÉ I

CENTRE DE RECHERCHE ET DE FORMATION  
DOCTORALE EN SCIENCES, TECHNOLOGIES  
ET GEOSCIENCES

Unité de recherche et de formation  
doctorale en physiques et applications

B.P 812 Yaoundé  
Email: crfd\_stg@uy1.uninet.cm



REPUBLIC OF CAMEROON

Peace - Work - Fatherland

UNIVERSITY OF YAOUNDE I

POSTGRADUATE SCHOOL OF SCIENCES,  
TECHNOLOGY AND GEOSCIENCES

Research and postgraduate training  
unit for physics and applications

P.O. Box 812 Yaounde  
Email: crfd\_stg@uy1.uninet.cm

DÉPARTEMENT DE PHYSIQUE  
DEPARTMENT OF PHYSICS

LABORATOIRE DE MÉCANIQUE, MATÉRIAUX ET STRUCTURES  
LABORATORY OF MECHANICS, MATERIALS AND STRUCTURES

***PT/APT-symmetric electronic systems in wave  
transport phenomena: the cases of Anderson  
Localization and Electromagnetically Induced  
Transparency***

*Thesis submitted and defended in partial fulfillment of the requirements for the awards  
of a Doctor of Philosophy (Ph.D) degree in Physics*

**Specialty: Mechanics, Materials and Structures**  
**Option: Fundamental Mechanics and Complex Systems**

By

**TAGOUEGNI Senghor**  
Registration number: 09W1324  
Master in Physics

**Jury:**

<b><u>President:</u></b>	<b>WOAFO Paul</b>	<i>Professor, University of Yaounde I</i>
<b><u>Supervisors:</u></b>	<b>KENFACK JIOTSA Aurélien</b> <b>FOTSA NGAFFO Fernande</b>	<i>Professor, University of Yaounde I</i> <i>Associate Professor, University of Yaounde I</i>
<b><u>Examiners :</u></b>	<b>NANA ENGO Serge Guy</b> <b>NDJAKA Jean-Marie Bienvenue</b> <b>NANA Bonaventure</b>	<i>Professor, University of Yaounde I</i> <i>Professor, University of Yaounde I</i> <i>Associate Professor, University of Bamenda</i>

**UNIVERSITÉ DE YAOUNDÉ**  
THE UNIVERSITY OF YAOUNDE I



**FACULTÉ DES SCIENCES**  
FACULTY OF SCIENCES

**DÉPARTEMENT DE PHYSIQUE**  
DEPARTMENT OF PHYSICS

## **ATTESTATION DE CORRECTION DE LA THÈSE DE DOCTORAT/Ph.D**

Nous, Professeur **NANA ENGO Serge Guy** et Professeur **WOAFO Paul**, respectivement Examineur et Président du jury de la Thèse de Doctorat/Ph.D. de Monsieur **TAGOUEGNI Senghor**, Matricule **09W1324**, préparée sous la direction des Professeurs **KENFACK JIOTSA Aurélien** (Université de Yaoundé I) et **FOTSA NGAFFO Fernande** (Université de Yaoundé I), intitulée : « **PT/APT SYMMETRIC ELECTRONIC SYSTEMS IN WAVE TRANSPORT PHENOMENA: THE CASES OF ANDERSON LOCALIZATION AND ELECTROMAGNETICALLY INDUCED TRANSPARENCY** », soutenue le lundi, **19 décembre 2022**, en vue de l'obtention du grade de Docteur/Ph.D. en Physique, Spécialité **Mécanique, Matériaux et Structures**, option **Mécanique Fondamentale et Systèmes Complexes**, attestons que toutes les corrections demandées par le jury de soutenance ont été effectuées.

En foi de quoi, la présente attestation lui est délivrée pour servir et valoir ce que de droit.

Fait à Yaoundé, le **10 FEV 2023**

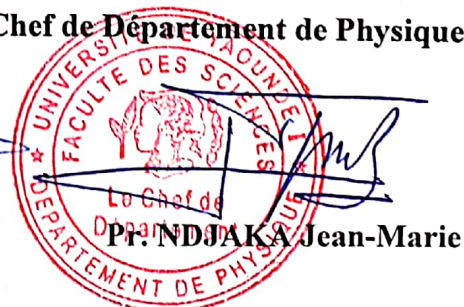
**Examineur**

**Pr. NANA ENGO Serge Guy**

**Le Président du jury**

**Pr. WOAFO Paul**

**Le Chef de Département de Physique**



**Pr. NDJAKA Jean-Marie**

*PT/APT*-symmetric electronic systems in wave transport phenomena: the cases of Anderson Localization and Electromagnetically Induced Transparency

THESIS

Thesis submitted to the Department of Physics  
in partial fulfillment of the requirements for the degree of Doctor  
of Philosophy in the field of Fundamental Mechanics and Complex Systems

By

**TAGOUEGNI Senghor**

*Master in Physics*

*Ph.D. candidate*

Specialty: Mechanics, Materials and Structures

Option : Fundamental Mechanics and Complex Systems

Co-Directors:

FOTSA NGAFFO Fernande  
Associate Professor  
University of Yaounde I

KENFACK JIOTSA Aurélien  
Professor  
University of Yaounde I

University of Yaounde I  
Centre de Recherche et de Formation Doctorale en Sciences, Technologie et Geosciences  
B.P. Box 812 Yaoundé, Cameroon

©2022

---

---

# Citation

---

*“If we knew what it was we were doing,  
it would not be called research, would it ?”*

*Albert Einstein*

---

---

# Dedications

---

♡ *To my late beloved father,  
peace to his soul **TCHOFFO Michel,**  
**1961-2017***

♡ *To my mother  
**TCHOFFO** born **MANTO Louise***

---

# Declaration

---

This is to certify that the research work presented in this thesis, entitled “*PT/APT-symmetric electronic systems in wave transport phenomena: the cases of Anderson Localization and Electromagnetically Induced Transparency*” was done by me under the guidance of Pr. Fernande FOTSA NGAFFO and Pr. Aurélien KENFACK JIOTSA. No part of this work has been included anywhere else for any other degree. This is submitted to the Department of Physics of the University of Yaounde I, in partial fulfillment of the requirements for the degree of Doctor of Philosophy in the Field of Fundamental Mechanics and Complex Systems.

Authors :

**TAGOUEGNI Senghor**

*Ph.D. candidate*

University of Yaounde 1

**NGAFFO FOTSA Fernande**  
**Associate Professor**  
University of Yaounde 1

**KENFACK JIOTSA Aurélien**  
**Professor**  
University of Yaounde 1

---

# Acknowledgments

---

This thesis would have been impossible without the help and support from several people. Here, I would like to express my sincere gratitude to them.

First of all, I would like to thank **God, the Almighty** for giving me the patience, the strength and the mercy to accomplish this modest work, despite the difficulties encountered.

I would like to express my thankfulness to my advisor, **Pr. Fernande FOTSA NGAFFO**. It has not always been easy to integrate and accept your rigor in the research. That's the reason I went to your school. I learned a lot with you, patience, a job well done, discipline, thanks to your research experience, especially in the field of non-Hermitian systems. There is no doubt that I am in this area of research today thanks to you. Our many long hours of discussions have greatly influenced the way I think about research problems in general and of this thesis in particular. Thank you also, for all the advice and support you have given me over the years. As a mother, you taught me to get up in the face of difficulties, a behavior I remain proud of.

Next, I am also express my deepest gratitude and my unwavering attachment to my thesis supervisor, **Pr. Aurélien KENFACK JIOTSA**, who accepted me in his Laboratory since the Master's degree until this Ph.D thesis, where I was able to combine, throughout these years of fruitful and stimulating collaboration, the pleasures of research and intellectual complicity. I hope I have been worthy of the trust you have placed in me. I have no other ambition than to include my future works in this continuity. The clarity of this manuscript owes much to its many and necessary corrections. His sympathetic attitude and encouragements have enabled me to broaden my knowledge and improve my research skill and capability.

I would like to thank each member of jury who has accepted to evaluate the present work.

I would also like to thank all those who dedicated their time to teach me a part



of what they knew, from primary school to University, with a particular emphasis on the teaching staff of the Departments of Physics of the University of Yaounde I and the Higher Teachers' Training College; I am particularly grateful to **Pr. Luc Calvin Owono Owono, Pr. Jean-Marie Bienvenu NDJAKA, Pr. Timoléon Crépin KOFANE, Pr. Paul Wofo, Pr. Clement Tchawoua, Pr. Bernard Essimbi Zobo, Pr. Serge ZEKENG, Pr. Blaise Romeo NANA NBENDJO, Pr. Bonaventure NANA, Pr. Bruno LENTA and Dr. Edmond Gnokam.**

Many thanks to **Dr. Emmanuel FENDZI DONFACK**, for all our many fruitful exchanges on different aspects of physics. Without forgetting his availability and unconditional help.

I express my gratitude to **Dr. Eric TALA TEBUE, Dr. Zacharie DJOUFACK, Dr. Deschances TSOBGNI, Dr. Bertin DJOB, Dr. Hervé KAMDOUM, Dr. Anne Justine ETINDELE, Dr. Jean Calvin SEUTCHE, Dr. Boris BEKONO and Mr. Jean Paul DJIOKO** for their support in job search.

Special thanks go to my collaborator and wonderful friend **Stéphane Boris TABEU** for his fruitful and stimulating discussions during this work and concerning research questions in general.

My gratitude also goes to all my lab mates from the ANALOGICAL SIMULATION LAB under the supervision of **Pr. Aurélien KENFACK JIOTSA, Idriss NJIKE NJIKE, Ibrahim AZEGHAP SIMO, Arnaud TIKENG, Marcial BADUIDANA, Landry SILATCHOM, Junior MBAH NDEDA, Daniel MBANG, Stephane NOUPEYI, Jean Paul TEGUIA, Rommuald TATSITSA, Cedric NGONGANG, Steve SAHLEUHEU and Vianick LECPA**, for the sincere collaboration, solidarity, spirit of group and the uplifting debates that elucidated me.

I am grateful to my colleagues of **G.B.H.S. AKONO** for their multiple encouragements during the development of this work.

My deepest gratitude goes to my family for their support throughout my life. I want to thank my siblings: **Romeo KAMTA, Jorelle MASSAH, Desmon FOKOU, Lérick MENO, Anéda MAFOKOU and Léovic NGOUAGNA**, who have always appreciated me; I remember their encouragement whenever I broach the research questions. To my loving wife **Chimène Rosy NGAFFO**: Thank you for being the most loving, caring, and comprehensive companion I could ever dream of. Thank you for making my happiness grow, and my disappointments fade. To my children **Ostwald Nathan, Erwan and Joanna TAGOUEGNI**: Thank you for making sense of my life. I would

like to thank my late father **Michel TCHOFFO**, and my mom **Louise MANTO** for sacrificing her life for me. Thank you for the education you installed in me, for the affection, the tenderness, the support, the advice and above all for the immeasurable Love that you have always shown towards me. You always remind me that “ *success comes at the end of the effort*”. Find here the fruit of all these works Mom! My gratitude also goes to my sister-in-law **Eugenie CHUELE FOKOU** for its encouragements.

I must remember the blessings of the members of the great families **TALACDJO-NZEUPI** in general and in particular of Yaoundé, not forgetting the extended family **TAGNIBA**, for their continuous love and support throughout my life. I feel blessed to be your son, and none of this would have been possible had it not been because of your unbending belief in me.

My profound gratitude goes to my whole family-in-law, especially to my mother-in-law **Colette NGAFFO** for the encouragements and the support to my modest person.

I can't forget both the families **Bertin LONTOUO** and **Appaulinaire KOTSAF** for their multiple encouragements during the development of this work.

I would like to pay particularly my gratefulness to the family **Celestin SIMO GUELA**. Its support and assistance can never be overestimated. I would like to express my gratitude to it.

I especially acknowledge my friends **Mr. Aimé Severin TSAFACK**, **Mr. Ghislain Brice TEMGOUA MOMO**, **Mr. Apolinaire FOKOU**, **Mr. Roger FOMEKONG**, **Mr. Mitterand MOUKAM** and **Dr. william HYOUMBI** who have always kept a place for me in their prayers and have supported me throughout this work as well as during difficult times.

My sincere thanks also go to all my neighbours for their encouragement.

To all members of the **High Tech and Slow Technology Club (HITASTEC)**, I am grateful for their instructive exchanges on the experimental level.

To all those who have contributed directly or indirectly to this work, and whose names do not appear on this page, do not feel forgotten, we are together!

*To all of you, thank you.*  
*Senghor.*

---

# Abstract

---

This thesis is devoted to the study through electronic systems of quantum interference phenomena related to wave transport. In particular, our interest is focused on Electromagnetically Induced Transparency (EIT), which has its basis in atomic physics and Anderson Localization (AL), a key concept in condensed matter physics. Several models are proposed to reproduce them and to facilitate their interpretation. Emphasis is placed on the non-Hermiticity aspect when modelling, and correspondances are made with the real physical systems. The circuits are based on usual L, R and C components and/or imaginary resistance Z, all linear. Starting from Kirchhoff's laws, the equations and the Hamiltonian describing each system are derived. Analytical, numerical, and analogical simulation methods are described. Firstly, the study is focused on EIT and the related phenomena. It appears by modulating the non-Hermitian parameter of the MLC/ZRC circuit that, EIT, Electromagnetically Induced Amplification (EIA) and Autler-Townes Splitting (ATS) windows can be reproduced in the weak and strong coupling regimes, respectively. At the zero effective coupling point, all the phenomena disappear. This suggests a possible way of controlling EIT experiments. The theoretical results are well confirmed by the LTspice simulations. The ZRC multi dimer permits the replication of EIT windows and/or related phenomena, simultaneously, according to a number of dimers considered. Secondly, we focus on the AL phenomenon.  $\mathcal{PT}$  dimer MLC is first inserted as a default in a Hermitian LC conservative transmission line (TL). When propagating the real wavenumbers  $k$ , the scattering properties reveal exceptional points (EPs), where unidirectional invisibility occurs. Between the EPs, the transmission is superunitary, and the modes propagation are extended. Outside the EPs, transmission is subunitary, suggesting modes propagation localized. Lasing modes appear for imaginary wavenumber values, corresponding to real or purely imaginary values of the non-Hermitian parameter, demonstrating the ability to control forbidden waves in a linear regime.  $\mathcal{APT}$  scattering system exhibits a non-reciprocity propagation for real wave numbers. For the non-Hermitian ZRC TL in the  $\mathcal{PT}/\mathcal{APT}$  exact phase, the current distribution is always extended and symmetric. This symmetry disappears when the TL enters the complex phase, and the localized modes emerge with the localization length proportional to the cells number in the TL. This reveals embryonic applications in cryptography, switching and system control.

**Keywords:** *Non-Hermitian, imaginary resistance, quantum interference, EIT/ATS, Anderson localization.*

---

# Résumé

---

Cette thèse est consacrée à l'étude, au moyen des systèmes électroniques, des phénomènes d'interférence quantique liés au transport d'ondes. En particulier, notre intérêt est porté sur la Transparence Electromagnétique Induite (EIT), qui prend son fondement en physique atomique et la Localisation d'Anderson (AL), un concept clé de la physique de la matière condensée. Plusieurs modèles sont proposés pour les reproduire et pour faciliter leur interprétation. L'accent est mis sur l'aspect non-Hermiticité lors de la modélisation, et des correspondances sont établies avec les systèmes physiques réels. Les circuits sont basés sur les composants L, R et C usuels et/ ou la résistance imaginaire Z, tous linéaires. En partant des lois de Kirchhoff, les équations et l'Hamiltonien décrivant chaque système sont obtenus. Des méthodes analytiques, numériques et de simulation analogiques sont décrites. Premièrement, l'étude est portée sur l'EIT et les phénomènes y relatifs. Il apparaît en modulant le paramètre de non-Hermiticité du circuit dimère MLC/ZRC que, les fenêtres d'EIT/d'Amplification Induite Electromagnétiquement (EIA) et d'Autler-Townes (AT) peuvent être reproduites dans les régimes de couplage faible et fort, respectivement. Au point de couplage effectif nul, tous ces phénomènes disparaissent, suggérant un moyen possible pour contrôler les expériences d'EIT. Les résultats théoriques sont confirmés par les simulations LTspice. Le multi dimère ZRC permet de reproduire plusieurs fenêtres simultanées d'EIT et/ou de phénomènes analogues, proportionnellement au nombre de dimères considérés. Secondairement, nous nous focalisons sur l'étude du phénomène de localisation d'Anderson. Le dimère MLC  $\mathcal{PT}$  est d'abord inséré comme défaut dans une ligne de transmission (TL) Hermitienne LC conservatrice. Lors de la propagation des nombres d'onde réels ( $k$ ), les propriétés de diffusion révèlent des points exceptionnels (EPs), où l'invisibilité unidirectionnelle se produit. Entre ces EPs, la transmission est superunitaire, et la propagation des modes est étendue. A l'extérieur des EPs, la transmission est subunitaire, suggérant les modes de propagation localisés. Les modes d'émission laser apparaissent pour des valeurs imaginaires de  $k$ , correspondant à des valeurs réelles ou purement imaginaires du paramètre non-Hermitien, ce qui démontre la possibilité de contrôler les ondes interdites dans un régime linéaire. Les propriétés de diffusion du dimère MLC  $\mathcal{APT}$  révèlent un caractère de non-réciprocité. Pour la ligne ZRC non-Hermitienne dans la phase  $\mathcal{PT}/\mathcal{APT}$  exacte, la distribution du courant est étendue et toujours symétrique. Cette symétrie disparaît dans la phase complexe, et les modes localisés émergent avec la longueur de localisation proportionnelle au nombre de cellules. Cela révèle des applications embryonnaires en cryptographie, en commutation et en contrôle de systèmes.

**Mots clés :** *Non-Hermitien, résistance imaginaire, interférence quantique, EIT/ATS, localisation d'Anderson.*

---

---

# Contents

---

Citation	i
Dedication	ii
Declaration	iii
Acknowledgments	iv
Abstract	vii
Résumé	viii
Contents	ix
List of Tables	xii
List of Figures	xiii
List of Abbreviations	xxix
General Introduction	xxx
<b>1 Literature Review</b>	<b>1</b>
1.1 Quantum Hermitian and non-Hermitian theories . . . . .	1
1.1.1 Quantum Hermitian theory . . . . .	1
1.1.2 Quantum non-Hermitian theory . . . . .	2
1.1.2.1 Background . . . . .	2
1.1.2.2 $\mathcal{PT}$ -symmetry . . . . .	4
1.1.2.3 $\mathcal{PT}$ symmetry in electronics . . . . .	7
1.1.2.4 Experimental Observation of $\mathcal{PTS}$ scattering . . . . .	10
1.1.2.5 Non-Hermitian $\mathcal{APT}$ symmetric systems . . . . .	14
1.2 Imaginary resistance . . . . .	19
1.2.1 What is the imaginary resistance ? . . . . .	19
1.2.2 Imaginary resistance build from a gyrator . . . . .	20
1.2.3 Imaginary resistance based on ideal transformers . . . . .	22

1.2.4	Imaginary resistance based $\mathcal{PT}$ symmetry electronics dimers . . . . .	22
1.3	Generalities on wave transport phenomena . . . . .	24
1.3.1	Generalities on EIT and related phenomena . . . . .	24
1.3.1.1	Basic formalism . . . . .	25
1.3.1.2	Classical analogs of Electromagnetically Induced Transparency . . . . .	29
1.3.1.3	Classical analog of double EIT . . . . .	32
1.3.1.4	Electromagnetically Induced Absorption (EIA) . . . . .	34
1.3.2	Generalities on Anderson Localization . . . . .	35
1.3.2.1	Theoretical background . . . . .	35
1.3.2.2	Anderson Localization in non-periodic electrical transmission lines . . . . .	37
1.3.2.3	Anderson Localization in a $\mathcal{PT}$ transmission line . . . . .	46
<b>2</b>	<b>Models and methods</b> . . . . .	<b>50</b>
2.1	Fundamentals . . . . .	50
2.2	Description, modeling of non-Hermitian systems . . . . .	52
2.2.1	Atomic system using electronic circuits . . . . .	52
2.2.1.1	Three level atomic system using coupled oscillators LRC . . . . .	52
2.2.1.2	Three level atomic system using coupled oscillators ZRC . . . . .	54
2.2.1.3	Multi level atom using coupled oscillators ZRC . . . . .	56
2.2.2	Description, modeling $\mathcal{PT}/\mathcal{APT}$ electronic dimers . . . . .	57
2.2.3	Description and modeling of the electrical transmission lines (ETLs) . . . . .	59
2.2.3.1	Hermitian ZC ETL . . . . .	59
2.2.3.2	Non-Hermitian ZRC ETL . . . . .	59
2.3	Analytical methods . . . . .	60
2.3.1	Analytical methods for the analog models . . . . .	60
2.3.1.1	Dimer MLC series . . . . .	61
2.3.1.2	ZRC dimer . . . . .	63
2.3.1.3	ZRC multi dimer . . . . .	66
2.3.2	Scattering formalism . . . . .	67
2.3.3	Analytical methods for the non-Hermitian ZRC ETLs . . . . .	71
2.3.3.1	Schrödinger equation . . . . .	71
2.3.3.2	Eigenvalues for a non-Hermitian ZRC ETL . . . . .	72
2.3.3.3	Electric current function in a non-Hermitian ZRC ETL . . . . .	73
2.3.3.4	Diagnostic tools to study the localization behavior . . . . .	74
2.4	Numerical methods . . . . .	75
2.5	Simulations with LTSpice . . . . .	75

<b>3</b>	<b>Results and Discussions</b>	<b>77</b>
3.1	Analysis close to the resonance of the effect of non-Hermiticity on dispersive properties in coupled LRC/ZRC oscillators driven by a harmonic voltage: EIT and multiple EIT behavior and related phenomena . . . . .	77
3.1.1	Eigenmodes analysis . . . . .	78
3.1.1.1	Eigenmodes of the dimer MLC series . . . . .	78
3.1.1.2	Eigenmodes of the ZRC dimer . . . . .	82
3.1.1.3	Eigenmodes of the ZRC multi dimer . . . . .	86
3.1.2	Steady state dynamic and dispersive properties . . . . .	88
3.1.2.1	Dispersive properties of a dimer MLC . . . . .	88
3.1.2.2	Dispersive properties in a single ZRC oscillator . . . . .	95
3.1.2.3	Dispersive properties in a ZRC dimer . . . . .	97
3.1.2.4	Dispersive properties in a ZRC multi dimer . . . . .	102
3.1.3	Concluding remarks on the analysis close to the resonance of coupled LRC/ZRC oscillators driven by a harmonic voltage . . . . .	106
3.2	Scattering properties of non-Hermitian electronic dimers . . . . .	107
3.2.1	Scattering properties of the $\mathcal{PT}$ symmetric dimer MLC . . . . .	107
3.2.2	Scattering properties of the $\mathcal{APT}$ symmetric dimer MLC . . . . .	113
3.2.3	Concluding remarks on scattering properties of a $\mathcal{PT}/\mathcal{APT}$ dimer MLC . . . . .	115
3.3	Energy transport and Anderson-like localization in non-Hermitian electrical transmission lines . . . . .	115
3.3.1	Modes dynamic . . . . .	117
3.3.1.1	$\mathcal{PTS}$ configuration . . . . .	117
3.3.1.2	$\mathcal{APTS}$ configuration . . . . .	119
3.3.2	Transport properties . . . . .	122
3.3.2.1	Transport in $\mathcal{PT}$ configuration . . . . .	122
3.3.2.2	Transport in $\mathcal{APT}$ configuration . . . . .	124
3.3.3	Anderson-like localization . . . . .	125
3.3.3.1	$\mathcal{PT}$ configuration . . . . .	126
3.3.3.2	$\mathcal{APT}$ configuration . . . . .	127
3.3.4	Concluding remarks on the analysis of a dimer ZRC based non-Hermitian electrical transmission line . . . . .	128
	<b>General Conclusion</b>	<b>129</b>
	<b>Bibliography</b>	<b>133</b>
	<b>List of Publications</b>	<b>144</b>

---

---

# List of Tables

---

2.1	Combination of circuit elements for either positive or negative charges. . .	56
3.1	Electronic components used in LTspice experimental simulations with the CP dimer L in the weak driving regime. . . . .	91
3.2	Electronic components used in LTspice experimental simulations with the CP dimer L in the strong driving regime. . . . .	94
3.3	RH ETL characteristics . . . . .	116
3.4	LH ETL characteristics . . . . .	116



---

# List of Figures

---

1.1	Energy eigenvalues for the Hamiltonian $\mathcal{H} = \hat{p}^2 + \hat{x}^2(i\hat{x})^\varepsilon$ for varying $\varepsilon$ , taken from [1]. . . . .	5
1.2	(a) $\mathcal{PT}$ -symmetric with balanced gain and loss (upper panel) and its equivalent circuit with $L' = L + M$ and $M' = (L^2 - M^2)/M$ (lower panel). Here, gain is achieved by an effective negative resistance. (b) A floating negative resistance. Figure is taken from ref. [28] . . . . .	8
1.3	The physical symmetry of the system corresponds to its symmetric equations of motion. The figure is adapted from [124]. . . . .	9
1.4	(Left) Real (upper panel) and imaginary (lower panel) parts of the eigenfrequencies $\omega$ as a function of the normalized gain and loss parameter $\gamma/\gamma_{PT}$ . The solid curves (dots) show the theoretical (experimental) results. Experimentally measured temporal dynamics of the capacitance energy $E_C^{tot}(\tau)$ of the total system for various $\gamma$ -values. As $\gamma \rightarrow \gamma_{PT}$ , the $\tau^2$ behavior, a signature of the spontaneous $\mathcal{PT}$ -symmetry breaking, is observed. The figures are adapted from ref. [28]. . . . .	9
1.5	Experimental reflectances for a single TL attached to the lossy ( $R_R$ ) or the gain ( $R_L$ ) side of the dimer (see lower insets) for $\mu = 0.29$ ; $\gamma = 0.188875$ ; $\eta = 0.0305$ . The black line corresponds to $R_L^{-1}$ and confirms the non-reciprocal nature $R_L R_R = 1$ of the $\mathcal{PT}$ -scattering. The upper inset shows the measurements for the left (right) reflection phases $\phi_L$ ( $\phi_R$ ). The blue lines are the theoretical results. The figure is adapted from ref. [80]. . . . .	10
1.6	The $\omega - \gamma$ phase diagram for $\mu = 0.57$ , indicating the existence of a subunitary ( $\log_{10}(R_R) < 0$ ) and a complimentary super-unitary ( $\log_{10}(R_R) > 0$ ) domain for the set-up shown at the lower left inset of Fig. 1.5. The figure is adapted from ref. [80]. . . . .	11

- 1.7 The spatial potential distribution inside the dimer versus the frequency  $\omega$ . The TL is coupled to the lossy side. The parameters used are the those used in Fig. 1.5. The blue dashed lines indicate the boundaries between sub-unitary to super-unitary scattering. The figure is adapted from ref. [80]. 12
- 1.8 Measurements (symbols) and numerics (lines of corresponding color) of  $T$ ,  $R_{L/R}$  for the two-port scattering set-up. The vertical black dashed lines indicate the frequencies where unidirectional transparency occurs. The conservation relation is also evaluated using the experimental data. The horizontal dashed blue line is drawn for the eye and indicates the value 1. The parameters used are the those used in Fig. 1.5. The figure is adapted from ref. [80]. . . . . 13
- 1.9 (a) The overall output coefficient  $\Theta(\omega)$  versus frequency  $\omega$  near the amplification/attenuation frequency  $\omega_J$  (vertical dashed line). The  $\mathcal{PTS}$  electronic circuit is coupled to two ports and has  $\eta = 0.110$ ;  $\gamma = 0.186$ ;  $c = 0.161$ . At  $\omega = \omega_J$  the system acts as a perfect absorber when the input signal satisfies the coherent attenuation relation  $V_R^- = \mathcal{M}_{21}(\omega) V_L^+$ . For any other incident signal (e.g. see the blue line corresponding to  $V_R^- = V_L^+$ ) the system acts as an amplifier. The dots are experimental values while the lines are numerical results. (b) Plots of experimental  $\Theta(\omega_J)$  versus the relative phase  $\phi$  of the signal entering the structure from the lossy node. Various curves correspond to different excitation amplitudes. Note the extremely sharp dependence at the Janus condition. Figures are adapted from ref. [87]. . . . . 14
- 1.10 Schematic diagrams of  $\mathcal{PT}$  and anti- $\mathcal{PT}$  symmetric binary systems. a)  $\mathcal{PT}$ -symmetric coupled oscillators implied by the  $\mathcal{PTS}$  Hamiltonian  $\mathcal{H}^{(\mathcal{PT})}$ . b)  $\mathcal{APT}$ -symmetric binary system derived from the relation  $\mathcal{H}^{(\mathcal{APT})} = \pm j\mathcal{H}^{(\mathcal{PT})}$ . In the two diagrams,  $\kappa$  denotes inter-resonator coupling constant and vertical arrows indicate directions of energy exchange between the coupled-resonator system and environment. Figures are adapted from ref. [50]. . . . . 15
- 1.11  $\mathcal{APT}$ -symmetric model circuit and its spectral property. Circuit diagram of  $\mathcal{APT}$ -symmetric LRC resonators. The circuit consists of two resistively coupled amplifying LRC resonators with negative resistance units. A variable inductor is used for  $L_2$  to precisely control the energy-detuning parameter  $\varepsilon$ . The figure is taken from ref. [50]. . . . . 16

1.12 $\varepsilon$ -dependent resonance-excitation spectrum $W_1(f)$ . The Figure is adapted from ref. [50]. . . . .	17
1.13 Eigensystem structure of an $\mathcal{APT}$ -symmetric circuit. Real (a) and imaginary (b) eigenvalues inferred from the resonance-excitation spectra in Fig. 1.12 in comparison with theory. The theoretical curves are obtained by a binary Hamiltonian model derived from Kirchhoff's circuit laws. The shaded area for $\varepsilon/\kappa$ indicates the parametric region of the broken $\mathcal{PTS}$ phase. Figures are adapted from ref. [50]. . . . .	17
1.14 Energy-difference conserving dynamics in time domain. a) Measured time evolution of the total energy $T_n$ , electric energy $E_n$ , and magnetic energy $M_n$ for an initial state $ v(0)\rangle = (0\ 1)^T$ . $\varepsilon = 1.48\kappa$ in this measurement. b) Measured voltage-product energy rate $V_1V_2/R$ . c) Integrated voltage-product energy rate $\sum (V_1V_2/R)\Delta t$ showing an exact correlation with the beating patterns in $T_n$ . Here, the sampling time interval $\Delta t = 4\ \mu s$ . Figures are taken from ref. [50]. . . . .	18
1.15 Imaginary resistance. Figure is taken from ref. [133]. . . . .	19
1.16 Gyration. Figure is taken from ref. [133]. . . . .	20
1.17 Imaginary resistance realized by using gyration and resistors for arbitrary phase-difference $\theta$ . Figure is taken from ref. [133]. . . . .	21
1.18 Imaginary resistance realized by using ideal transformer. Figure is taken from ref. [136]. . . . .	22
1.19 a) The ZRC dimer setup in which the gain and the loss cells are coupled by an imaginary resistance and a capacitor. b) Normal modes dynamics. Subset (i): in the breakable region, $c = -0.1$ . In dash $c = 2$ . Subset (ii) in the unbreakable region for $c = -2$ ( $\nu = 0.75$ ). Figures are adapted from ref. [62] with the permission. . . . .	23

1.20	Simple EIT Plot. Here we are plotting the real and imaginary components of the complex linear susceptibility. The imaginary component corresponds to absorption - on the left we see a typical Lorentzian absorption peak while the control laser is inactive. When the control laser is applied, the absorption peak splits revealing a transparency at what was the maximal absorption. The real components appear in the dispersion relation, relating wave speed to frequency. . . . .	25
1.21	All three level structures capable of demonstrating EIT, namely, $\Lambda$ -type (left), V-type (middle), and ladder type (right). . . . .	25
1.22	$\Lambda$ three level-atomic system with all the atoms in the ground state $ 1\rangle$ . The system has two possible transitions, denoted as $\omega_a$ or the <i>probe</i> and $\omega_b$ or the <i>control</i> frequency. . . . .	26
1.23	An example of a dark state that is a superposition of $ 1\rangle$ and $ 2\rangle$ . The probe and control frequency excitation interfere destructively at level $ 3\rangle$ , thereby inhibiting absorption of radiation. The system continues to be in the superposition state, hence being transparent to both the probe and control frequencies. . . . .	27
1.24	Classical analogs of EIT. a) The mechanical model. b) The electrical circuit model. Figures are adapted from ref. [59]. . . . .	30
1.25	The power transferred to the circuit $R_2L_2C_{e2}$ as a function of the frequency $\omega_S$ for different values of the coupling capacitor $C$ . The values of $C$ are $C = 0.196 \mu F$ , with resonance frequency $f_{res} = \omega_2/2\pi = 20 kHz$ , (b) $C = 0.150 \mu F$ , $f_{res} = 19.5 kHz$ , (c) $C = 0.096 \mu F$ , $f_{res} = 19.5 kHz$ , (d) $C = 0.050 \mu F$ , $f_{res} = 26.5 kHz$ . The open squares correspond to measurements made with the switch SW open, which is equivalent to turning the pump off. The open circles correspond to measurements made with the switch closed. The evolution from EIT to the Autler–Townes regime is clearly observed. Figures are taken from [59]. . . . .	31
1.26	Classical analog of DEIT. a) The mechanical model. b) The electrical circuit model. Figures are adapted from ref. [164]. . . . .	33

- 1.27 Power transferred to the  $R_1L_1C_{e1}$  circuit as a function of the detuning  $\delta = \omega - \omega_R$ . This detuning was defined as the difference between the driving field frequency  $\omega$  and the resonance frequency of the circuit  $\omega_R$ . The parameters used were  $R_2 = R_3 = 5.0\Omega$ ,  $R_1 = 50\Omega$ ,  $C_1 = C_2 = C_3 = 0.1\mu F$ ,  $C = 0.2\mu F$  and  $L_1 = 0.0010H$ . For plots (a)  $L_2 = L_3 = 0.0010H$ ; (b)  $L_2 = 0.0010H$  and  $L_3 = 0.0015H$ ; (c)  $L_2 = 0.0020H$  and  $L_3 = 0.0003H$ ; (d)  $L_2 = 0.0005H$  and  $L_3 = 0.0003H$ . The solid line represents  $P_R$ , whereas the dashed line represents  $P_X$ .  $P$  is given in arbitrary units. Figures are adapted from ref. [164]. . . . . 34
- 1.28 Probe absorption in an N-system with (left) and without (right) transfert of coherence for various coupling laser intensities. The dotted lines correspond to the one-photon lorentzian probe absorption in the absorption of coupling laser. the coupling intensity increases from top bottom (as reported in [181]). 35
- 1.29 A partial view of an ideal transmission line.  $Z_n$  ( $\gamma_n$ ) represent horizontal (vertical) impedances, respectively. For direct TL,  $Z_n$  is associated with inductances and  $\gamma_n$  with capacitances. Conversely, for dual TL,  $Z_n$  is associated with capacitances and  $\gamma_n$  with inductances. The arrows indicate the direction of the electric current in each cell. We arbitrarily consider the initial flow from the left, because we are using open boundary conditions. Figure is taken from ref. [212]. . . . . 37
- 1.30 A segment of a mixed transmission line formed by  $p = 2$  direct cells and  $q = 3$  dual cells. The full system is formed by the repetition of the basic unit formed by  $d = (p + q)$  cells. Inductances are represented by rectangles and capacitances by circles. In addition, dual cells are marked with orange color-filled symbols. The arrows indicate the direction of the electric current in each cell. Figure is taken from ref. [212]. . . . . 39
- 1.31 (a) Global sub-band structure of the Shannon entropy  $S(\omega) = R_1(\omega)$  versus  $\omega$  for the Fibonacci quasi-periodic distribution of inductances  $L_n$  discussed in ref. [201]. (b)Self-replication structure of the sub-band indicated by the vertical arrow in (a). Figure is taken from Ref. [212]. . . . . 41

- 1.32  $\xi(\omega)$  versus  $\omega$  for the  $m$ -tupling distribution of inductances  $L_n$  in the direct TL, for three values of  $m$ , namely  $m = \{2, 3, 13\}$  (a-c). (d)  $\Lambda(\omega)$  versus  $\omega$ . A short vertical bar indicates the existence of an extended state ( $\Lambda(\omega) \geq 1$ ). The number of extended states for  $m = 3$  is very small compared to the case  $m = 2$ . Conversely, for  $m \gg 3$  ( $m = 8$  and  $m = 13$ ), the number of extended states increases and becomes comparable to the  $m = 2$  case. Figure is taken from ref. [212]. . . . . 42
- 1.33 Map  $(b, \omega)$  for the Aubry–André distribution of inductances with  $L_0 = 4.0$ . Each point of the map indicates an extended state, because  $\Lambda \geq 1.0$ . For increasing values of the amplitude  $b$ , the number of sub-bands of extended states diminishes, and for  $b$  close to  $b = L_0$ , there is only a small sub-band where almost all states are extended states, namely  $0 \leq \omega \leq 0.45$ . Figure is taken from ref. [212]. . . . . 44
- 1.34 Transmission coefficient  $T(\omega)$  versus  $\omega$ , for mixed transmission line with  $p = 2, q = 1$ , for (a)  $b = 0.3$ , (b)  $b = 0.7$ , (c)  $b = 1.1$  and (d)  $b = 1.5$ . For (a)  $b = 0.3$  we find  $d = (p + q) = 3$  bands containing extended states, localized states and gaps. For increasing values of  $b$ , the number of extended states within each band decreases. Therefore, for (c)  $b = 1.1$ , the leftmost band has already disappeared, and for (d)  $b = 1.5$ , the rightmost band is about to disappear. Figure is taken from ref. [212]. . . . . 44
- 1.35 (a) Phase diagram separating non-conducting from conducting states in the thermodynamics limit in terms of the symmetric map parameter  $b_c(\infty)$  as a function of the correlation exponent  $\alpha$ . The plotted points correspond to values of the correlation exponent  $\alpha \geq 0.55$ , i.e., the disordered system always presents long-range correlation. (b) Normalized localization length  $\Lambda(\omega)$  as a function of the frequency  $\omega$  for the asymmetric ternary map when  $b_1 = -0.9$ ;  $b_2 = 1.7$  for different correlation exponents  $\alpha = \{1.7, 1.8, 2.0, 2.6\}$ . Figures are adapted from ref. [199] . . . . . 45
- 1.36 Phase diagram  $(\gamma, b_c)$  separating localized states from extended states in the thermodynamic limit in terms of the map parameter  $b_c(\infty)$  as a function of the parameter  $\gamma$ . (a) Case  $C = 0.3$ . The inset shows the normalized localization length  $\Lambda(b)$  as a function of the map parameter  $b$  for  $C = 0.3$  and  $\gamma$  going from  $\gamma = 0.001$  to  $\gamma = 4.0$ . (b)  $C = (\varepsilon\gamma)^2$  and  $\varepsilon = 1$  (limit case). The inset shows  $\Lambda(b)$  as a function of  $b$  for  $\gamma$  going from  $\gamma = 1$  to  $\gamma = 10^4$  for the same limit case. For all inset plots,  $\omega = 3.5$ ,  $N = 40\,000$ . Figures are adapted from ref. [200] . . . . . 46

1.37	A $\mathcal{PTS}$ resistance configuration in a direct ETL. Figure is taken from ref. [60].	47
1.38	Modulus of the electric current function $ I_n $ as a function of $n$ for both frequencies $\omega_{1,2}(R, k_d)$ . (a) Symmetric and extended state for $R = 0.23(\Omega) < R_c$ with frequencies $\omega_1 = 1.43 \times 10^7$ (rad/s) and $\omega_2 = 1.40 \times 10^7$ (rad/s). (b) Asymmetrical and dissipative state for $R = 31(\Omega) > R_I$ with eigenvalues $\omega_1 = j9.15 \times 10^6$ (rad/s) and $\omega_2 = j2.18 \times 10^7$ (rad/s). Figures are adapted from ref. [60].	48
1.39	(a): Normalized localization length $\Lambda(R, \omega_1)$ and $\Lambda(R, \omega_2)$ vs $R$ for fixed $N = 30$ and $k_{d=N}$ . For both frequencies $\omega_1$ and $\omega_2$ , $\Lambda(R, \omega)$ determines three regions with different localization behaviors, which are delimited by critical points $R_c = 0.3642(\Omega)$ and $R_I = 28.28(\Omega)$ (see insets). For $R \leq R_c$ , insets (a) $\omega_1$ and (b) $\omega_2$ show a zoom of the unbroken $\mathcal{PTS}$ phase which corresponds to extended electric current functions $\Lambda(R, \omega_{1,2}) \geq 1$ . For $R > R_c$ we can only find a dissipative behavior which corresponds to the broken $\mathcal{PTS}$ phase [ $\Lambda(R, \omega_{1,2}) < 1$ ]. Inset (c) shows $\Lambda(R, \omega_{1,2})$ in the neighborhood of $R_I = 28.28(\Omega)$ . Figure is taken from ref. [60].	48
2.1	(a) Coupled LRC circuits used to reproduce EIT and related phenomena. The couplings operate when the switch SW is closed. (b) Energy diagram of a three level-atom in lambda ( $\Lambda$ ) configuration interacting with two lasers beams coupling ground states $ 1\rangle$ and $ 2\rangle$ to a common excited state $ 3\rangle$ .	53
2.2	The oscillator ZRC series.	54
2.3	A dimer ZRC series used as a $\Lambda$ -three level atomic system.	55
2.4	(a): ZRC Multi dimer circuit used for a single and multiple EIT, ATS and EIA windows. (b): Energy diagram of a $(N+2)$ level atomic system in a multipod type configuration consisting of $(N+1)$ lower levels $ i\rangle$ ( $i = 0..N$ ) of which $N$ pumping lasers couple near resonantly each state to the upper state $ e\rangle$ , while a probe laser couples level $ 0\rangle$ to $ e\rangle$ .	56
2.5	Electronic model of a general dimer MLC: The models take into account mutual inductive coupling ( $M$ ), inductive coupling ( $L_0$ ) and capacitive coupling ( $C_0$ ).	58
2.6	Diagram of a Hermitian ZC ETL.	59

2.7	Segment of a non-Hermitian ZRC ETL. . . . .	60
2.8	Schematic of a generic one-dimensional scattering system. . . . .	67
2.9	Diagram of a Hermitian LC ETL. . . . .	68
3.1	Effective CP dimer L. (a, b): Variation of the real and imaginary parts of $\omega_{\pm}/\omega_0$ as function of $\nu_C/\nu_{C_{cr}}$ for different values of $\varepsilon$ . $\varepsilon = -1$ (red); $\varepsilon = -0.5$ (green); $\varepsilon = 0$ (black); $\varepsilon = 0.5$ (blue); $\varepsilon = 1$ (magenta). (c, d): The real and imaginary parts of the eigenfrequencies splitting. . . . .	79
3.2	Effective CP dimer MC (when $\mu = 0.50$ , $\kappa \neq \mu$ ). (a, b): Variation of the real and imaginary parts of $\omega_{\pm}/\omega_0$ as function of $\kappa/\kappa_{cr1}$ for different values of $\varepsilon$ . $\varepsilon = -1$ (red); $\varepsilon = -0.5$ (green); $\varepsilon = 0$ (black); $\varepsilon = 0.5$ (blue); $\varepsilon = 1$ (magenta). (c, d): The real and imaginary parts of the eigenfrequencies splitting and coupling threshold evolution. The coupling thresholds are indicated in green and white color as $\kappa_{cr1}$ and $\kappa_{cr2}$ with ( $\kappa_{cr1} < \kappa_{cr2}$ ) between which is located the weak coupling regime. Both critical values merge to only one point for $\varepsilon = 1$ when $\kappa = \mu$ . At this last point the weak regime vanishes. The color bar indicates the magnitude of the splitting. For all plots $\gamma_2 = 0.05$ . The first and second column represent the real and imaginary parts, respectively. Except for dimer ML, all plots obtained here qualitatively describe what is observed in other types of CP dimers of category 2. . . . .	80
3.3	3D top view of the real (first column) and imaginary (second column) parts of the normalized eigenfrequencies $\omega_{\pm}/ \omega_0 $ of the ZRC dimer as function of the controlling coupling parameter $\beta_c$ and the gain/loss ratio $\varepsilon$ , in the case of dimer Z of which $c = \beta_c$ ((a), (b)) and of the dimer ZC when fixed $\kappa = 0.75$ ((c), (d)). The coupling threshold $\beta_{C_{th}}$ is indicated with the dashed magenta color. For all plots $\beta_0 = 0.5$ . . . . .	83
3.4	Cross section of the real (solid) and the imaginary (dashed) parts of the eigenfrequencies $\omega_{\pm}/ \omega_0 $ shown in Fig. 3.3 for different values of $\varepsilon$ : (e) the dimer Z and (f): dimer ZC ( $\kappa = 0.75$ ). The values of $\varepsilon$ are indicated on the plots. For all plots $\beta_0 = 0.5$ . . . . .	84



- 3.5 Eigenfrequencies of the dimer as function of the variation  $\Delta$ . (a) Uncoupled loops ( $c = 0$ , with  $\beta_C = \kappa = 0$ ). Dimer Z in weak (b) and strong (c) coupling regime. Dimer ZC in weak (d) and strong (e) coupling regime. (f) Dimer ZC at the couplingless point ( $c = 0$ , with  $\beta_C = \kappa = 0.75$ ). In all plots,  $\beta_0 = 0.5$ ,  $\omega_0 < 0$  and  $\varepsilon = 0$ . . . . . 85
- 3.6 The normalized roots of  $D(\omega)$  as function of the imaginary resistive coupling parameter  $\beta_C$  for the multi dimer ZC (when  $\kappa = 0.75$ ). First row: the bi dimer ZC (N=2). Second row: the tri dimer ZC (N=3) and in third row: the tetra dimer ZC (N=4). The first column shows the real parts of the roots ( $\text{Re}(\omega/|\omega_0|)$ ) and the second column shows their imaginary parts ( $\text{Im}(\omega/|\omega_0|)$ ). The other plot parameters are:  $\varepsilon = 0$ ,  $\beta_0 = 0.5$  and  $\omega_0 < 0$ . The inset in (a) corresponding to the case of the bi dimer Z ( $\kappa = 0$ ), allows to show the robustness of the multiple coupling. . . . . 87
- 3.7 The solid black (white) curve is the absorption spectrum of the mesh (2) as function of the normalized frequency detuning  $\delta/\omega_0$  (frequency  $\omega$ ) when SW is off. The dashed black (white) is the corresponding dispersion curve. The first and second column represent the theoretical and the experimental LTspice results, respectively. (a, b): the mesh (2) is passive ( $\gamma_2 = 0.05$ ). (c, d): the mesh (2) is active ( $\gamma_2 = -0.05$ ). The experimental parameters are  $R_2 = 50 \Omega$ ;  $L_2 = 5 \text{ mH}$ ;  $L_C = 0.272 \text{ mH}$ ;  $C_2 = 0.1 \mu\text{F}$ . . . . . 89
- 3.8 Absorption spectrum of the mesh (2) in Effective CP dimers as function of  $\delta/\omega_0$  for different values of  $\varepsilon$ . We assume coupling in the weak driving regime. For illustration, we have considered the case of CP dimer L where  $\nu_C/\nu_{Ccr} = 0.5$ . The solid blue, green and red curves are the real parts of the resonances  $P_{21}/p_0$ ,  $P_{22}/p_0$  and the total dissipated power  $P_2/p_0$ . From (a)-(d) and from (i)-(l) are theoretical results. From (e)-(h) and from (m)-(p) are experimental LTspice simulation results. The experimental parameters are indicated in Table 3.1. first column:  $\varepsilon = 0.1$ ; second column:  $\varepsilon = 0$ ; third column:  $\varepsilon = -0.05$ ; last column:  $\varepsilon = -0.1$ . In the first and second rows, the mesh (2) is passive ( $\gamma_2 = 0.05$ ), while in the third and last row it is active ( $\gamma_2 = -0.05$ ). . . . . 90

- 3.9 Absorption spectrum of the mesh (2) in Effective CP dimers as function of  $\delta/\omega_0$  for different values of  $\varepsilon$ . We assume coupling in the strong driving regime. For illustration, we have considered the case of CP dimer L where  $\nu_C/\nu_{Ccr} = 2$ . The solid blue, green and red curves are the resonances  $P_{21}/p_0$ ,  $P_{22}/p_0$  and the total dissipated power  $P_2/p_0$ . From (a)-(d) and from (i)-(l) are theoretical results. From (e)-(h) and from (m)-(p) are experimental LTspice simulation results. The experimental parameters are indicated in Table 3.2. First column:  $\varepsilon = 0.5$ ; second column:  $\varepsilon = 0$ ; third column:  $\varepsilon = -0.5$ ; last column:  $\varepsilon = -1.0$ . In the first and second rows, the mesh (2) is passive ( $\gamma_2 = 0.05$ ) while in the third and last row it is active ( $\gamma_2 = -0.05$ ). . . . . 93
- 3.10 (a) and (b) Absorption spectrum of the mesh (2) in Effective CP dimers of category 2 (dimer MC with  $\mu = 0.5$  for illustration), as function of  $\delta/\omega_0$  and the active coupling ( $\kappa$  for illustration). We assume  $\varepsilon = 0$  and the active coupling  $\kappa$  evolves in the weak driving regime. We note a particular behavior at the center of this regime corresponding to the disappearance of EIT and related phenomena. (c) and (d) are experimental LTspice simulation results at the CPLP when  $\varepsilon = 0$ ,  $\kappa = \mu = 0.5$ . The experimental values used for the simulations are:  $R_2 = 50 \Omega$ ;  $R_1 = 55 \Omega$ ;  $L_2 = 5 \text{ mH}$ ;  $L_C = 0.986 \text{ mH}$ ;  $C_2 = 0.1 \mu F$ . In first column: the mesh (2) is passive ( $\gamma_2 = 0.05$ ) while in the second column it is active ( $\gamma_2 = -0.05$ ). . . . . 95
- 3.11 Transient evolution of the normalized current into the loop in absence of the harmonic voltage for different values of the quality factor (a, d):  $\beta_0^{-1} = 10$ ; (b, e):  $\beta_0^{-1} \rightarrow \infty$ ; (c, f):  $\beta_0^{-1} = -10$ . From (a)-(c):  $\omega_0 > 0$ ; from (d)-(f):  $\omega_0 < 0$ . . . . . 96
- 3.12 The real (solid lines) and the imaginary (dashes/dots lines) parts of the steady state normalized power dissipated by the  $Z_0 R_0 C_0$  loop as a function of the normalized frequency  $\omega/\omega_0$  for different values of the non-Hermitian parameter  $\beta_0$ . The plot parameters are shown in the figure. In all plots, green and blue curves correspond to the loss loop ( $\beta_0 = 0.5$ ) whereas purple and red curves are associated to the gain loop ( $\beta_0 = -0.5$ ), respectively. . . 97

- 3.13 Time evolution of the energy in each cell of the dimer Z (first column) and the dimer ZC (second column). (a) and (b) correspond to dimer Z in presence of strong ( $\beta_C = 0.5$ ) and weak ( $\beta_C = 0.02$ ) coupling regimes, respectively. (c) and (d) represent the dimer ZC (when  $\kappa = 0.75$ ) in the strong ( $\beta_C = 0.2$ ) and the weak ( $\beta_C = 0.71$ ) couplings, respectively. (e) correspond to the dimer ZC at the CPLP ( $\beta_C = \kappa = 0.75$ ). For all plots  $\varepsilon = 0$  and  $\beta_0 = 0.1$  and  $\omega_0 = 1\text{rad.s}^{-1} > 0$ . The solid green and red dashes curves represent the energies  $|Q_0|^2$  and  $|Q_1|^2$ , respectively. . . . . 98
- 3.14 Time evolution of the energy in each cell of the dimer Z (first column) and the dimer ZC (second column). (f) and (g) correspond to dimer Z in presence of strong ( $\beta_C = 0.5$ ) and weak ( $\beta_C = 0.02$ ) coupling regimes, respectively. (h) and (i) represent the dimer ZC (when  $\kappa = 0.75$ ) in the strong ( $\beta_C = 0.2$ ) and the weak ( $\beta_C = 0.71$ ) couplings, respectively. (j) correspond to the dimer ZC at the CPLP ( $\beta_C = \kappa = 0.75$ ). For all plots  $\varepsilon = 0$  and  $\beta_0 = 0.1$  and  $\omega_0 = -1\text{rad.s}^{-1} < 0$ . The solid green and red dashes curves represent the energies  $|Q_0|^2$  and  $|Q_1|^2$ , respectively. . . . . 99
- 3.15 Absorbed power (dissipated) by the main loop of the dimer ZC (from (a) to (c)) when the natural frequencies of the loops are positive  $\omega_0 > 0$  and the one of the dimer Z (d) when natural frequencies are negative  $\omega_0 < 0$ . The solid blue and dashed red correspond to the real and imaginary parts of the absorbed power when the main loop is loss ( $\beta_0 = 0.1 > 0$ ). The insets in green show the real part of the power corresponding to the main loop gain ( $\beta_0 = -0.1 < 0$ ). The other parameters used to plot the graphs are the same as those used in Fig. 3.12. . . . . 100
- 3.16 The real and imaginary parts of the steady state normalized dissipated power  $P_0/p_0$  as a function of the normalized frequency  $\omega/|\omega_0|$  in the case of the bi dimer ZC (N=2) according to the coupling regime: (a) weak coupling, (b) strong coupling. In all plots, we set  $\omega_0 < 0$ ,  $\beta_0 = 0.5$  and  $\kappa = 0.75$ . The other parameters used to plot the graphs are inserted in text. 103
- 3.17 The real and imaginary parts of the steady state normalized dissipated power  $P_0/p_0$  as a function of the normalized frequency  $\omega/|\omega_0|$  in the case of the tri dimer ZC (N=3) according to the coupling regime: c) weak coupling, d) strong coupling. In all plots, we set  $\omega_0 < 0$ ,  $\beta_0 = 0.5$  and  $\kappa = 0.75$ . The other parameters used to plot the graphs are inserted in text. 105

- 3.18 The real and imaginary parts of the steady state normalized dissipated power  $P_0/p_0$  as a function of the normalized frequency  $\omega/|\omega_0|$  in the case of the tetra dimer ZC (N=4) according to the coupling regime: e) weak coupling, f) strong coupling. In all plots, we set  $\omega_0 < 0$ ,  $\beta_0 = 0.5$  and  $\kappa = 0.75$ . The other parameters used to plot the graphs are inserted in text. 106
- 3.19 Spectra of  $\gamma_r$  for which  $D = 0$ . The case TH dimer ML is depicted in (a) and (b), and the case THL dimer MLC is plotted in (c) and (d). The first column is the real part representation, while the imaginary part is depicted in the second column. F1 and F2 define the frontiers of regions I (real  $k$ ), II (complex  $k$ ), and III (purely imaginary  $k$ ). The TH dimer does not allow imaginary wave propagation;  $\gamma_r$  is either real or complex. The THL dimer allows control of real, complex, and imaginary propagation wavenumbers. The existence of region III-2 implies that lasing modes occur for imaginary  $\gamma_r$  and  $k_r$ . . . . . 108
- 3.20 Scattering normalized coefficient  $T$  and  $R$  of THL dimer MLC versus the gain/loss parameter in region I.  $\nu = 0.25$ ,  $c = 0.5$  and  $\vartheta = 0.1$ . (a)  $k$  and  $\gamma$  are real; EPs occur for the gain/loss incidence while in (b)  $\vartheta = 4$ , and the EP occurs only for the loss incidence at two different points.  $T > 1$  in between the EP in both cases. Lasing modes are observed inside the EPs, where the transmission is superunitary. (c) At  $\gamma_g$  and  $\gamma_l$ , the phase transmission corresponding to (a) does not change. In (d), the spectrum of  $\vartheta$  is plotted for  $c = 0.5$  and  $\mu = 0.5$ ; the green color indicates the region where the dimer is  $\mathcal{PTS}$  in two opposite directions (at  $\gamma_{g/l}$ ), while in the red region, the dimer is  $\mathcal{PTS}$  in one direction (two distinct values of  $\gamma_l$ ). . 111

- 3.21 Scattering normalized coefficient  $T$  and  $R$  of THL dimer MLC versus the gain/loss parameter  $\nu = 0.25$ ,  $c = 0.5$  and  $\vartheta = 0.1$ . (a) At the frontiers F1 ( $\mu = 0.447$ ,  $k = 0$ ) and F2 ( $\mu = 0.627$ ,  $k = \pi$ ), the transmission vanishes completely:  $T = 0$ ;  $R_g = R_l = 1$ . (b) In region II,  $\mu = 0.75$ ,  $k$  is complex and  $\gamma$  is real,  $\gamma_c$  occurs at  $R_g = T = 1$  below which  $T > 1$  and  $T < 1$  above. Lasing modes occur in the region of superunitary transmission. Far from  $\gamma_r$ ,  $R_l = 0$ . (c) Region III-1,  $k$  is imaginary but  $\gamma$  is real. Lasing mode occurs around  $\gamma_r = 0.062$ . The transmission vanishes completely, i.e.,  $T = 0$  and  $R_g = 1 (< R_l)$ . (d) Region III-2,  $\mu = 0.75$ ;  $k$  and  $\gamma$  are both imaginary.  $|\gamma|$  is the magnitude of the imaginary gain/loss parameter  $\gamma$ . Lasing mode is observed inside the region defined by  $\gamma_{c1}$  and  $\gamma_{c2}$  where  $R_g = R_l$ . Far from  $\gamma_c$ ,  $T = 0$  and  $R_l > R_g$ . The inset indicates that all real  $\gamma$  incidences are totally attenuated in transmission and perfectly reflected in the gain side ( $R_g = 1$ ), while the loss reflected wave is amplified ( $R_l > R_g$ ). 112
- 3.22 (a), (b): 3D (top view) representation of  $T = |T_{R/L}|^2 / |T_{R/L}|_{\max}^2$  and (c):  $R_{1/2} = |R_{L/R}|^2 / |R_{L/R}|_{\max}^2$  for the  $\mathcal{APT}$  dimer MLC ( $\nu = 1$ ,  $\mu = 0.5$ ,  $\vartheta = 0.5$  and  $c = 1$ ) in the domain (I). The lasing mode occurs at  $\gamma_r \approx -0.34$ , for  $k_r \approx 0.3\pi$ . we note a reciprocity in both reflection and transmission. (d): Scattering normalized coefficient for  $k = k_r$ . . . . . 113
- 3.23 (a), (b) and (c): 3D top view of  $T = |T_{R/L}|^2 / |T_{R/L}|_{\max}^2$  and  $R_{1/2} = |R_{L/R}|^2 / |R_{L/R}|_{\max}^2$  in the domain (II) for the  $\mathcal{APT}$  dimer MLC ( $\nu = 1$ ,  $\mu = 0.5$ ,  $\vartheta = 0.5$  and  $c = 0.1$ ). There is not reciprocity in reflections since the wave number is complex and the lasing mode does not occurs. (d): Scattering normalized coefficient for  $k = \pi - 1.76j$ . . . . . 114
- 3.24 3D top view ETLs normalized frequencies spectra  $\Omega_{\pm}^{RH}(\beta, k_p)$  as function of  $k_p$  and  $\beta$  in  $\mathcal{PTS}$  configuration. Column (a) for the real parts and column (b) for the imaginary parts.  $\beta_{cr1} < \beta_{cr} < \beta_{cr2}$  is the transition range values separating the real and the complex modes. Beyond this range the modes are thresholdless. The insets (i) and (ii) highlight the domain situated before  $\beta_{cr1}$ . . . . . 117
- 3.25 The real (black color) and the imaginary parts (red color) of the eigenvalues  $\Omega_{\pm}^{RH}$  as function of the wave number  $k_p$  for several values of the gain/loss  $\beta$  in  $\mathcal{PTS}$  configuration. The values of  $\beta$  used correspond to the domains illustrated in Fig. 3.24. (a)  $\beta = 0.01 < \beta_{cr1}^{RH}$ ; (b)  $\beta_{cr1}^{RH} < \beta = 1 < \beta_{cr2}^{RH}$ ; (c)  $\beta = 20 > \beta_{cr2}^{RH}$ . . . . . 118

- 3.26 3D top view ETLs normalized frequencies spectra  $\Omega_{\pm}^{LH}(\beta, k_p)$  as function of  $k_p$  and  $\beta$  in  $\mathcal{PTS}$  configuration. Column (a) for the real parts and column (b) for the imaginary parts.  $\beta_{cr1} < \beta_{cr} < \beta_{cr2}$  is the transition range values separating the real and the complex modes. Beyond this range the modes are thresholdless. . . . . 118
- 3.27 The real (green color) and the imaginary parts (purple color) of the eigenvalues  $\Omega_{\pm}^{LH}$  as function of the wave number  $k_p$  for several values of the gain/loss  $\beta$  in  $\mathcal{PTS}$  configuration. The values of  $\beta$  used correspond to the domains illustrated in Fig. 3.26. (a)  $\beta = 0.01 < \beta_{cr1}^{LH}$ ; (b)  $\beta_{cr1}^{LH} < \beta = 1 < \beta_{cr2}^{LH}$ ; (c)  $\beta = 3 > \beta_{cr2}^{LH}$ . . . . . 119
- 3.28 3D top view ETLs normalized frequencies spectra  $\Omega_{\pm}^{RH}(\beta, k_p)$  as function of  $k_p$  and  $\beta$  in  $\mathcal{APT}^{RH}$  configuration. Column (a) for the real parts and column (b) for the imaginary parts. The threshold  $\beta_{cr}$  separates the complex and the purely imaginary mode regions. The insets (i) and (ii) highlight the domain situated before  $\beta_{cr1}$ . . . . . 120
- 3.29 The real (blue color) and the imaginary parts (magenta color) of the eigenvalues  $\Omega_{\pm}^{RH}$  as function of the wave number  $k_p$  for several values of the gain/loss  $\beta$  in  $\mathcal{APT}^S$  configuration. The values of  $\beta$  used correspond to the domains illustrated in Fig. 3.28. (a)  $\beta = 0.01 < \beta_{cr1}^{RH}$ ; (b)  $\beta_{cr1}^{RH} < \beta = 1 < \beta_{cr2}^{RH}$ ; (c)  $\beta = 20 > \beta_{cr2}^{RH}$ . . . . . 120
- 3.30 3D top view ETLs normalized frequencies spectra  $\Omega_{\pm}^{LH}(\beta, k_p)$  as function of  $k_p$  and  $\beta$  in  $\mathcal{APT}^{LH}$  configuration, where the system is unbreakable. Column (a) for the real parts and column (b) for the imaginary parts. . . . 121
- 3.31 The real (cyan color) and the imaginary parts (orange color) of the eigenvalues  $\Omega_{\pm}^{LH}$  as function of the wave number  $k_p$  for the gain/loss  $\beta = 1$  in  $\mathcal{APT}^S$  configuration. the frequencies are complex . . . . . 121
- 3.32 The modulus square  $|I_n(\beta, \Omega)|^2$  of the electric current in the  $\mathcal{PT}^{RH}$  configuration. Columns (a) and (b): 3D top view for several values of  $p$  as a function of  $\beta$  and  $n$ . Columns (c)–(e): 2D plot as function of  $n$  for different values of  $p$ ,  $\beta = 0.01$  in the 1st row and  $\beta = 20$  in the 2nd row. We note a symmetric energy transport of the  $\mathcal{PT}^{RH}$  exact phase whereas energy transport is asymmetrical in the  $\mathcal{PT}^{RH}$  broken phase. . . . . 122

- 3.33 The modulus square  $|I_n(\beta, \Omega)|^2$  of the electric current in the  $\mathcal{PT}^{LH}$  configuration. Columns (a) and (b): 3D top view for several values of  $p$  as a function of  $\beta$  and  $n$ . Columns (c)–(e): 2D plot as function of  $n$  for different values of  $p$ ,  $\beta = 0.01$  in the 1st row and  $\beta = 2.5$  in the 2nd row. We note a symmetric energy transport of the  $\mathcal{PT}^{LH}$  exact phase whereas energy transport is asymmetrical in the  $\mathcal{PT}^{LH}$  broken phase. . . . . 123
- 3.34 The modulus square  $|I_n(\beta, \Omega)|^2$  of the electric current in the  $\mathcal{APT}^{RH}$  configuration. Columns (a) and (b): 3D top view for several values of  $p$  as a function of  $\beta$  and  $n$ . Columns (c)–(e): 2D plot as function of  $n$  for different values of  $p$ ,  $\beta = 0.01$  in the 1st row and  $\beta = 35$  in the 2nd row. We note a symmetric energy transport of the  $\mathcal{APT}^{RH}$  exact phase whereas energy transport is asymmetrical in the  $\mathcal{APT}^{RH}$  broken phase. . . . . 124
- 3.35 The modulus square  $|I_n(\beta, \Omega)|^2$  of the electric current in the  $\mathcal{APT}^{LH}$  configuration. In column (a):  $\Omega = \Omega_+^{LH}$  and in column (b):  $\Omega = \Omega_-^{LH}$ . In all plots, we are situated in the broken phase since the system is unbreakable and we note an asymmetry transport of energy for small values  $\beta$ , even if it becomes almost symmetry for higher values of  $\beta$  . . . . . 125
- 3.36 Normalized localization length  $\Lambda(\beta, \Omega_{\pm})$  in semi-log scale for the system in  $\mathcal{PTS}$  configuration as function of  $\beta$  for different values of  $p$  when  $N = 25$ . (a):  $\mathcal{PT}^{RH}$ , and (b):  $\mathcal{PT}^{LH}$ . For the values of  $p$  indicated in the plots, we observed extended modes (i.e  $\Lambda(\beta, \Omega_{\pm}) > 1$ ) in the  $\mathcal{PT}$  exact phase, while the localized modes (i.e  $\Lambda(\beta, \Omega_{\pm}) < 1$ ) occur in the  $\mathcal{PT}$  broken phase. Both localization behavior are separated by the gray curves which marks  $\Lambda(\beta, \Omega_{\pm}^{RH, LH}) = 1$ . In  $\mathcal{PT}^{RH}$ , the appearance of the localized modes in the broken phase required a minimum of cells ( $p = 15$ ) since below that value, all modes remain extended (i.e.  $\Lambda(\beta, \Omega_+^{RH}) > 1$ ). While,  $\mathcal{PT}^{LH}$  configuration, confined modes even for the smallest value  $p = 1$  (not shown). 126

- 3.37 Normalized localization length  $\Lambda(\beta, \Omega_{\pm})$  in semi-log scale for the system in  $\mathcal{APTS}$  configuration as function of  $\beta$  for different values of  $p$  when  $N = 25$ . (a):  $\mathcal{APT}^{RH}$ , and (b):  $\mathcal{APT}^{LH}$ . For the values of  $p$  indicated in the plots, we observe in  $\mathcal{APT}^{RH}$  extended modes (i.e  $\Lambda(\beta, \Omega_{\pm}^{RH}) > 1$ ) in the exact phase (pure imaginary frequencies), while the localized modes (i.e  $\Lambda(\beta, \Omega_{\pm}^{RH}) < 1$ ) occur in the  $\mathcal{APT}$  broken phase (complex frequencies). Both localization behaviors are separated by the gray curve corresponding to  $\Lambda(\beta, \Omega_{\pm}^{RH,LH}) = 1$ . Also remark that for the  $\mathcal{APT}^{RH}$ , the appearance of the localized modes in the broken phase required a minimum of cells ( $p = 15$ ) since below that value, all modes become extended (i.e  $\Lambda(\beta, \Omega_{+}^{RH}) > 1$ ) however in  $\mathcal{APT}^{LH}$  configuration, the modes are localized even for infinitesimal value  $p = 1$  (not shown). . . . . 127



---

# List of Abbreviations

---

$\mathcal{P}$  : Parity

$\mathcal{T}$  : Time

$\mathcal{APT}$  : Anti Parity Time

$\mathcal{APTS}$  : Anti Parity Time Symmetric

$\mathcal{PT}$  : Parity Time

$\mathcal{PTS}$  : Parity Time Symmetric

**AL**: Anderson Localization

**ATS**: Autler-Townes Splitting

**ATSA**: Autler-Townes Splitting with Amplification

**CP**: Coupling

**CPL**: Couplingless

**CPLP**: Couplingless Point

**EIA**: Electromagnetically Induced Absorption

**EIAA**: Electromagnetically Induced Absorption Amplified

**EIAT**: Electromagnetically Induced Amplified Transparency

**EITA**: Electromagnetically Induced Transparency with Amplification

**EIT**: Electromagnetically Induced Transparency

**EP**: Exceptional Point

**ETL**: Electrical Transmission Line

**LH**: Left Handed

**NHH**: Non-Hermitian Hamiltonian

**RWA**: Rotating Wave Approximation

**RH**: Right Handed

**TH**: Threshold

**THL**: Thresholdless

**THLP**: Thresholdless Point

**TL**: Transmission Line

---

# General Introduction

---

While it is widely recognized that no researcher doubts as to the usefulness of gain mechanisms in boosting signal and transmitting information, it is also widely believed that loss mechanisms are undesirable for the most part of time and unfortunately lead to signal attenuation and system energy losses despite the abundance of losses in nature. The original idea of making the gain and the loss coexist within the same system only dates back to 1998 with the introduction into quantum mechanics of the concept of parity time ( $\mathcal{PT}$ ) symmetry by Carl Bender and co-workers [1–3]. In a well-developed mathematical formalism, they proved that such systems are described by non-Hermitian Hamiltonians  $\mathcal{H}$  delicately combining the gain and the loss in the same quantities, which under the conditions of commutation with the  $\mathcal{PT}$  operator, i.e.,  $[\mathcal{H}, \mathcal{PT}] = 0$ , can admit real eigenvalues, in contradiction with the predictions of quantum mechanics, where the real spectrum is guaranteed by the condition of Hermiticity  $\mathcal{H} = \mathcal{H}^\dagger$ . Since then, the concept of  $\mathcal{PT}$  symmetry gradually open up to other fields and specialties of physics and, today non-Hermitian systems constitute a major field of investigations. It is shown that the reality of the real spectrum in quantum mechanics is relative to the complex potential which must satisfy the relation  $V(x) = V^*(-x)$  with an even real part and an odd imaginary part [1–6]. In optics, the refractive index of the medium must obey  $n(x) = n^*(-x)$  [7–13], while  $\varepsilon(x) = \varepsilon^*(-x)$  for the relative permittivity in metamaterials [14–17]. The notion of  $\mathcal{PT}$  symmetry has also been extended to the field of photonics [7–13], mechanics [18–20], optomechanics [20–23], acoustics [24–26], condensed matter [27] and electronics [28, 29], to name a few. In the later field, which serves as a framework of this thesis, the concept of  $\mathcal{PT}$  symmetry has been there introduced in 2011, thanks to the pioneering works carried out by Joseph Schindler and co-workers on an active pair of coupled LRC circuits, one of which with amplification and the other with an equivalent attenuation [28]. Later, investigations on wave transport through such parity time symmetric ( $\mathcal{PTS}$ ) dimer systems served to highlight a wide range of intriguing features as power oscillations, unidirectional invisibility [7, 13, 30–33], nonreciprocal Bloch oscillations [34], absorption enhanced transmission [35], simultaneous coherent-perfect absorber lasing [36], and localized termination modes [37].

At the same time as these works carried out with the aim of broadening the field of investigation of  $\mathcal{PT}$  symmetry systems, and the quest for new properties, a counterpart of  $\mathcal{PTS}$  systems was born: these are anti Parity Time ( $\mathcal{APT}$ ) symmetry systems, where the commutator  $[\mathcal{H}, \mathcal{PT}] = 0$  is replaced by the anticommutator, i.e.,  $\{\mathcal{H}, \mathcal{PT}\} = 0$  [38–45].

This new class of systems obeys the properties of anti-symmetry. Thus, the potential in quantum mechanics must satisfy to  $V(x) = -V^*(-x)$  whereas in the field of optics and metamaterials, the refractive index and the relative permittivity are respectively satisfying to  $n(x) = -n^*(-x)$  and  $\varepsilon(x) = -\varepsilon^*(-x)$ . It is also noted that, the real parts of the potential, the refractive index or of the permittivity are the odd functions, while their imaginary parts remain the even functions. This gives possibility of realizing  $\mathcal{APT}$  symmetry dimers by precisely coupling two gain-gain or loss-loss cells. The later configuration is of enormous interest given the ease of finding dissipative systems in nature.  $\mathcal{APT}$  was suggested in particular in optics [38, 44–46], in flying atom [39], atomic lattice [48], and more recently in electronics [49, 50]. The  $\mathcal{APT}$  systems have presented several applications including telemetry, asymmetric transport, generation of qubits for quantum computing, wireless power transfer, switching, single mode power lasers and many other utilities [9–12, 17, 40, 44, 51–56].

Like  $\mathcal{PT}/\mathcal{APT}$  symmetry, some concepts in quantum mechanics, although older, are still relevant to research today because of their potential applications. For example, the concepts of Electromagnetic Induced Transparency (EIT) in atomic physics, and Anderson Localization (AL) in condensed matter physics. While for the first concept, the basic idea is to modify the optical properties (absorption spectrum, dispersion) of an atomic medium resonated by an electromagnetic wave, for the second concept, the original idea is to control the conductivity in a metal when it is in the presence of impurities. These two notions can only be explained in general if they are treated in a purely quantum framework. It has been shown that the observed facts are the result of interference phenomena between the different possible transitions of the excited atom on the one hand, and between the possible paths of electron scattering in the metal on the other. However, the interpretation of quantum interference phenomena has often proved to be quite tedious, making their understanding difficult for the layman. How to explain for example that the superposition of two monochromatic lights gives interference fringes? that an atom absorbing a laser beam of a given frequency becomes transparent to this same beam in the presence of another laser? or, how to admit that conduction suddenly stops in a metal? Also, experimenting with quantum mechanics would mean building quantum systems. However, most of these systems are extremely fragile, and any perturbation or measurement process would destroy the quantum state of the system.

Among the various fields of study presented above, that of electronics appears as privileged, this because of its relative theoretical and experimental simplicity [57] in the sense that it offers a wide range of components for experimentation. In this logic, in recent years, several analogous models have been proposed with the aim to facilitate understanding of quantum mechanics, optics, atomics and condensed matter physics phenomena. For example, the investigations on quantum interference phenomena such as fano resonance [58], EIT [59], AL [60] to name a few, have recently been made possible in electronics. The electronic models are easily accessible, and could help researchers or the laymen to quickly

understand the theory. The other advantages in electronics are based on the flexibility and the simplicity of equations that describe the physical models. Moreover, the use of innovative circuits for both theoretical and experimental investigation is also emerging. For example, thanks to a little-known component such as the imaginary resistor [61], Stéphane B. TABEU and co-workers have recently presented how to achieve  $\mathcal{PT}$  and  $\mathcal{APT}$  symmetric dimers [62, 63].

Whether it is EIT or AL by restriction, these quantum interferences phenomena are related to the wave transport, storage, wireless transfer [64], or propagation. They can therefore be modelled by electrical circuits or transmissions lines (TLs). However in the case of EIT for instance, the existing models were based on circuits with L, R and C positive components, and did not emphasize negative resistances [28]. While, it has been shown that systems combining gain and loss are generally described by non-Hermitian Hamiltonians, whose the frequency spectrum (real or complex) depends on the degree of non-Hermiticity [65, 66] of the system. On the other hand, EIT is known as a resonant phenomenon resulting from the splitting of normal mode frequencies of the system. It would therefore be interesting to discuss the contribution of a negative resistance on the eigenmodes and the absorption profiles while reproducing EIT effects. In other words, what would be the influence of the non-Hermiticity on the eigenfrequencies and absorption profiles?

Recent studies of Anderson localization with electrical lines have gained much interests for the transport in disordered media. While most of these works have been focused on the type of disorder simulated in the TL, very little modelling have aimed on the use of a negative resistance and, as a result, the non-Hermitian ( $\mathcal{PT}/\mathcal{APT}$ ) nature of the line has not been sufficiently studied.

The imaginary resistance [50, 62, 63] has a frequency independent complex impedance  $Z$ . It has been shown that it can validly replace the inductance L in a conventional LRC circuit thus, given the circuit the ability to oscillate at desirable frequencies without worrying about its values. This flexibility also allows the imaginary resistance to be combined with negative circuitry components and favours the description of the circuits by first order differential equations (instead of second order). This offers the possibility of investigating at both positive and negative frequencies, and, enhances the description of systems by Hamiltonians at two energy levels, rather than four, bypassing the rotating frame often used in other fields to indirectly create such frequencies. In this respect, it would be of great interest to take into account the effect of the imaginary resistance on propagation when modelling the quantum phenomena mentioned above.

To overcome the aforementioned problems and, motivated by the previous works we propose in this thesis to use non-Hermitian electronic systems to investigate on wave transport phenomena, focussing in particular on EIT and AL phenomena. The idea is to facilitate the replication and the understanding of such wave interference phenomena via electronics. In addition to use L, R, C components, we also use circuits built with the

imaginary and negative resistances.

The main objective of this thesis is twofold:

- First, we want to extend the study made on the analog electronics models of the EIT/multiple EIT and related phenomena, by analyzing the effect of the non-Hermiticity on the dispersive properties in a dimer/multi dimer driven by a harmonic voltage source. The importance of multiple coupling between cells would also be highlighted.
- Second, to take more ownership of the AL phenomenon, we want to analyze on one hand, the scattering properties of a  $\mathcal{PT}$  or  $\mathcal{APT}$  dimer embedded as a defect into a Hermitian conservative ETL. On other hand, to investigate on energy transport and the localization behavior in the repetitive sequence of dimers so as to form a non-Hermitian  $\mathcal{PT}/\mathcal{APT}$  symmetric electric transmission line (ETL).

This thesis is organised into three chapters, followed by the list of references cited and articles published.

\* **Chapter 1** presents some generalities on Hermitian and non-Hermitian quantum theory, which allows us to review previous works on  $\mathcal{PT}$  and  $\mathcal{APT}$  systems in the context of electronics; in the same chapter, we present the imaginary resistance and some generalities on EIT, related phenomena and AL.

\* **Chapter 2** is devoted to the methodology. Emphasis is first placed on the description of the electronic systems proposed, in particular dimers and ETLs. Analogies are also made between each model and the real atomic/quantum systems. Thereafter, the standard techniques of analysis (analytical, numerical and experimental simulation methods) are applied to the different proposed models to describe them.

\* **Chapter 3** is devoted to the presentation and analysis of the results obtained. This chapter is structured as follows: in the first section, we analyze the effect of the non-Hermiticity on the dispersive properties in a coupled LRC and ZRC oscillators driven by a harmonic voltage. This allows us to simulate the EIT, multiple EIT effect and related phenomena. The second section presents the scattering properties of  $\mathcal{PTS}/\mathcal{APTS}$  dimer when inserting it as impurity in a Hermitian conservative ETL. The obtained results motivate to investigate in the last section on the energy transport and to test quantum effects of the Anderson localization in non-Hermitian ETLs formed by a cascade association of ZRC dimers.

This dissertation work ends with a general conclusion, where we summarize our main results which have been the subject of publications. However, after a deep analysis of the results presented, some perspectives are to be considered.

---

# Literature Review

---

## Introduction

This chapter presents the background and an overview of the fundamental concepts underlying non-Hermitian systems. These systems were first introduced as a curiosity in quantum mechanics. And subsequently, the highlighting in 1998 of the Parity Time ( $\mathcal{PT}$ )-symmetry concept [1, 2, 67] will open a fertile field for entirely new and unexpected features. This initiates an intense research effort for the exploration of non-Hermitian systems both theoretically and experimentally, in diverse areas of physics. The present chapter details the notion of  $\mathcal{PT}$ -symmetry and Anti Parity Time ( $\mathcal{APT}$ )-symmetry. We restrict ourselves to the field of electronics which is the framework of our study, where we present the pioneer works and pay a particular attention to a new component, weakly mentioned in the literature: the imaginary resistance. Thereafter, an overview is also made on quantum phenomena resulting from the wave transport, such as EIT or related phenomena and Anderson localization (AL) behavior.

## 1.1 Quantum Hermitian and non-Hermitian theories

### 1.1.1 Quantum Hermitian theory

Quantum physics describes the behavior of matter on the atomic scale [68]. The study of the microscopic behaviors of certain systems led Schrödinger, Heisenberg and Dirac to formulate quantum theory in the years 1925-1930. Due to numerous experimental verifications of its theoretical predictions, quantum physics is today an established discipline and an accepted component of modern science. The fundamental postulate of quantum physics is that every measurable dynamic quantity is represented by a Hermitian linear operator acting on the wave function. This postulate results from another postulate in quantum physics stating that: the quantities we observe are the eigenvalues of the operators which represent the measurable quantities [69]. Since measurable quantities such as the momentum of free particles or the energy of stable atoms and molecules are real quantities, the operators that represent them should be Hermitian. For example, the  $x$ -component of the momentum,  $\hat{p}_x$ , is represented by  $-i\hbar\partial/\partial x$ , the Hamiltonian is represented by  $\hat{\mathcal{H}}$ , etc. The fundamental equation of quantum mechanics is the time-dependant

Schrödinger equation which is written as:

$$i\hbar \frac{\partial \psi(t)}{\partial t} = \mathcal{H} \psi(t), \quad (1.1)$$

where  $\mathcal{H}$  is the Hamiltonian of the system. Its eigenvalues represent the energies. The state  $\psi(t)$  in Eq. (1.1) evolves over time through the time-evolution operator  $U(t)$ , as  $\psi(t) = U(t - t_0) \psi(t_0)$ , where  $\psi(t_0)$  is a time-independent Schrödinger solution. Assuming  $\mathcal{H}$  to be time-independent, it follows that  $\psi(t) = e^{-\frac{i}{\hbar} \mathcal{H} t} \psi(t_0)$  from which we can deduce the form of the time-evolution operator as  $U(t) = e^{-\frac{i}{\hbar} \mathcal{H} t}$ . If we normalize our state, we require that  $\langle \psi | \psi \rangle = 1$ , that is, the total probability of measuring the state to be in any eigenstate is equal to one. We can then state that the time evolution of our system must be unitary [70], that is,

$$U(t) U^\dagger(t) = U^\dagger(t) U(t) = \mathbf{1}, \quad (1.2)$$

where by  $\dagger$ , we mean the Dirac Hermitian adjoint symbol which represents combined operation of matrix transposition and complex conjugation [71] and  $\mathbf{1}$  is the identity matrix. If the operator  $U$  is unitary, then the absolute value of the state is preserved under time evolution, and so probability is conserved

$$\langle \psi(t) | \psi(t) \rangle = \langle \psi(t_0) | \psi(t_0) \rangle. \quad (1.3)$$

In conventional quantum mechanics, we stipulate that the Hamiltonian be Hermitian as an axiom of the theory. If we require this property of our theory, we can guarantee that we have unitary time evolution of the states of the system as well as an entirely real spectrum for the energy eigenstates. We can see that unitary time evolution follows as :

$$U^\dagger(t) U(t) = e^{\frac{i}{\hbar} \mathcal{H}^\dagger t} \cdot e^{-\frac{i}{\hbar} \mathcal{H} t} = e^{-\frac{i}{\hbar} (\mathcal{H}^\dagger - \mathcal{H}) t} = \mathbf{1}, \quad (1.4)$$

and since we have required that  $\mathcal{H} = \mathcal{H}^\dagger$  the product of  $U(t)$  and  $U^\dagger(t)$  is the identity. Finally, as the Hamiltonian operator defines the time evolution of the system any operation under which the system is invariant will commute with the Hamiltonian.

## 1.1.2 Quantum non-Hermitian theory

### 1.1.2.1 Background

Physical systems are generally dissipative, which is a major concern for physicists who look to neglect or to minimize losses by putting in place devices that can mitigate them, although it is still almost impossible to get rid of them entirely. From this perspective, it is therefore difficult to consider the advantages linked to losses in a system, while avoiding their intrinsically harmful nature. This is probably the reason why very little work has so far been devoted to exploring the potential applications of losses in the literature. On the other hand, no one doubts the importance of gain in a physical system because of its

multiple applications such as amplification, to name but a few. From the above, several questions arise: is it possible to tame the losses in order to increase the efficiency of the system? Can losses and gains coexist in a system in order to have potential useful applications? The answers to these questions are hidden in a new class of structured materials called  $\mathcal{PT}$  symmetric systems, which belong to the more general class of non-Hermitian systems. For a long time, it was known that non-Hermitian systems play a destructive role in wave control due to their nature to dissipate energy. However, this design will be revolutioned with the discovery of  $\mathcal{PT}$  symmetric systems.

It all started in 1998 when Carl Bender and Stefan Boettcher without violating any of the physical axioms of quantum physics, have developed an alternative formulation of quantum theory, in which the mathematical axiom of Hermiticity to have real eigenvalues, long considered to be absolute evidence, is replaced by the theory of  $\mathcal{PT}$  symmetry. In this new formulation, the necessary condition to obtain real eigenvalues is that the Hamiltonian must be invariant with respect to space-time reflection symmetry [1, 2]. They have thus demonstrated that a large class of non-Hermitian Hamiltonians can still provide real eigenvalues, and consequently describe physical systems when they obey the conditions of  $\mathcal{PT}$  symmetry. Interestingly, they have shown that  $\mathcal{PTS}$  Hamiltonians exhibit a phase transition from real eigenvalues to complex ones which can be attributed to the spontaneous breaking of the  $\mathcal{PT}$  symmetry of the eigenfunctions of the system. This revolutionary idea led to a review of the quantum theory of Hermiticity [72, 73]. Thus, a few years later, Ali Mostafazadeh introduced the notion of pseudo-Hermiticity [4, 74] with the aim of establishing a mathematical relationship with the notion of  $\mathcal{PT}$ -symmetry. He explored the basic structure responsible for the spectrum reality of non-Hermitian Hamiltonians and established that all  $\mathcal{PTS}$  Hamiltonians are pseudo-Hermitians. Therefore, a new mathematical framework for the description of non-Hermitian Hamiltonians emerged [38, 71, 75–78]. However, due to the lack of practical evidence, the concept of  $\mathcal{PT}$ -symmetry initially proposed in quantum mechanics theory remain purely speculative for many years. On the other hands, a mathematical equivalence between the one-body Schrödinger equation in quantum physics and a set of wave equations or linearized equations of motion in classical physics, has allowed to simulate non-Hermitian wave physics with classical systems. Such equivalences go back to the work of Schrödinger [81] who highlighted the analogy between the emerging classical motion of a point particle in quantum mechanics and the ray optics approximation of electromagnetic waves. However, we had to wait for the years 2007 and 2008 to have the first suggestions of the physical realization of the  $\mathcal{PT}$  systems in the field of optics [13, 82]; This has given rise to the first experimental observations of the spontaneous rupture of the  $\mathcal{PT}$ -symmetry in a system of passive waveguides [83] and later in coupled active optical waveguides with balanced gain and loss [7]. This is how the field of optics became a fertile ground for the realization of systems exhibiting  $\mathcal{PT}$ -symmetry. The field of non-Hermitian photonics rapidly developed



and then experience a fuliginous rise due to interesting light-matter interactions which have no analogy with conventional Hermitian structures [84]. In this way, several works have been carry out to understand the non-Hermitian dynamics of optical systems [9, 85] and the research field will gradually open up to a variety of fields of classical physics such as electronics [28, 86, 87], plasmonics [88], microwaves [89], mechanics [90, 91], acoustics [92], [93], Bose condensates [27], optomechanics [94, 95], metamaterials [15–17, 96] and biological transport [97]. Whether for linear or non-linear systems, the concept of  $\mathcal{PT}$ -symmetry has opened up new avenues for intriguing phenomena such as double refraction [13], optical solitons [30, 98], Bloch oscillations [25], spectral singularities [99, 100], non-linearity induced  $\mathcal{PT}$ -symmetry breaking [101, 102], power oscillations and phase singularities [103],  $\mathcal{PTS}$  wave chaos [104], perfect optical absorption [36], [105], unidirectional invisibility [106], Talbot effect [107], defect states [108], loss-induced suppression and revival of lasing [109], thresholdless  $\mathcal{PT}$ -symmetry breaking [65], resonant mode conversion [110], optical tunneling [111], asymmetric chirality [112], directional lasing [113], polarization mode conversion [114], etc. Due to the very wide field of applications of  $\mathcal{PTS}$  systems, in this thesis, we only focus ourselves on the field of  $\mathcal{PT}$ -symmetry in electronics.

### 1.1.2.2 $\mathcal{PT}$ -symmetry

#### a) Non-Hermitian Hamiltonians with real spectra

The Hamiltonian  $\mathcal{H}$  specifies the energy levels and time evolution of a quantum theory. The requirement that  $\mathcal{H}$  be Hermitian dates back to the early days of quantum theory because Hermiticity guarantees that the energy spectrum is real and that time evolution is unitary (probability-preserving). However, in 1998, Bender and Boettcher proposed Hamiltonians  $\mathcal{H}$  that were not Hermitian but whose spectrum could be real. The examples of non-Hermitian Hamiltonians they have proposed are:

$$\mathcal{H} = \hat{p}^2 + i\hat{x}^3, \quad (1.5)$$

and

$$\mathcal{H} = \hat{p}^2 - \hat{x}^4. \quad (1.6)$$

Bender and co-worker [1] showed amazingly that, the energy levels of the above strange-looking Hamiltonians are all real and positive even though be non-Hermitian, contrary to what one would naively expect. In addition, these Hamiltonians specify a unitary time evolution. It is straightforward to remark that the form of Hamiltonians given in Eqs. (1.5) and (1.6) are special cases of the general parametric family of  $\mathcal{PTS}$  one,

$$\mathcal{H} = \hat{p}^2 + \hat{x}^2(i\hat{x})^\varepsilon, \quad (\varepsilon \text{ real}) \quad (1.7)$$

As we would expect, the reason of which  $\mathcal{H}$  admits real eigenvalues (see Fig. (1.1)) is that, it satisfies the  $\mathcal{PT}$  symmetry condition, i.e.,

$$\mathcal{H} = \mathcal{H}^{\mathcal{PT}}. \quad (1.8)$$

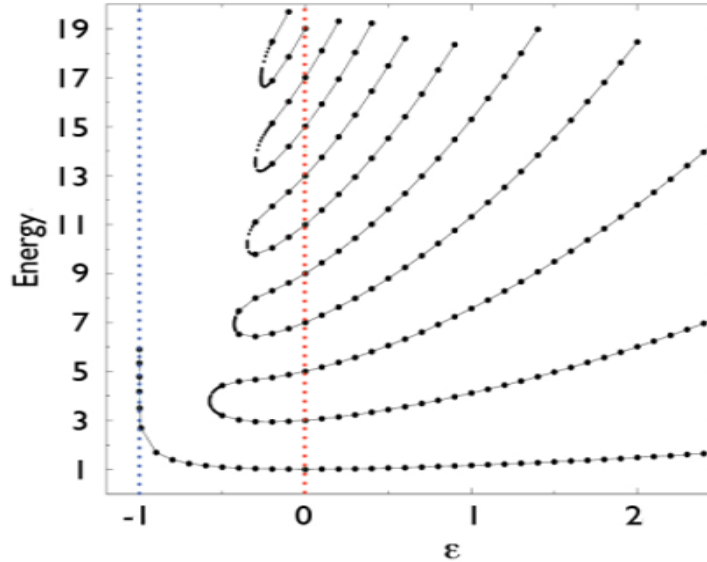


Figure 1.1: Energy eigenvalues for the Hamiltonian  $\mathcal{H} = \hat{p}^2 + \hat{x}^2(ix)^{\epsilon}$  for varying  $\epsilon$ , taken from [1].

Dorey, Dunning, and Tateo [115, 116] proved rigorously that for all  $\epsilon \geq 0$ , the  $\mathcal{PT}$  symmetry is unbroken, that is, the eigenstates of  $\mathcal{H}$  are also eigenstates of the  $\mathcal{PT}$  operator. As a consequence, the eigenvalues of  $\mathcal{H}$  are entirely real and positive. However, if  $\epsilon < 0$ , the  $\mathcal{PT}$  symmetry of  $\mathcal{H}$  is broken. In this case, the eigenvalues of  $\mathcal{H}$  are not those of the  $\mathcal{PT}$  operator; therefore eigenvalues of  $\mathcal{H}$  become complex. In short, authors in refs. [117, 118] proposed that the physical requirement of  $\mathcal{PT}$  symmetry (that is, space time reflection symmetry) could be used in place of the mathematical condition of Hermiticity. The Hamiltonians that previously would have been rejected as unphysical can now be considered as potentially valid descriptions of physical processes.

### b) The $\mathcal{P}$ and $\mathcal{T}$ operators

Parity  $\mathcal{P}$  and Time-reversal  $\mathcal{T}$  transformations are fundamental symmetry operations in physics. Mathematically, they are defined by their actions on physical variables such as position, momentum and time parameter  $t$ .  $\mathcal{P}$  is a linear operator defined by a spatial inversion of the system. In a one dimensional system, this corresponds to the reflection  $x \rightarrow -x$  across one spatial axis. Any physical quantity dependent on odd powers of  $x$  or its derivatives such as momentum  $p_x$  are inverted as well. In quantum theory,  $\mathcal{P}$  operates on the position operator  $\hat{x}$  and the momentum operator  $\hat{p}$  as follows [1]:

$$\mathcal{P} : (j, \hat{x}, \hat{p}) \rightarrow (j, -\hat{x}, -\hat{p}). \quad (1.9)$$

Therefore, the simplest representation of  $\mathcal{P}$  in two dimensions is given by

$$\mathcal{P} = \sigma_x = \begin{pmatrix} 0 & 1 \\ 1 & 0 \end{pmatrix}, \quad (1.10)$$

$\mathcal{T}$  on the other hand is an anti-linear operator (that is complex conjugation) which reverses the time  $t \rightarrow -t$ . Any physical quantity dependent on odd powers of  $t$  such as momentum is reversed. In the context of wave theories, the  $\mathcal{T}$  operator is equivalent to the transformation  $i \rightarrow -i$ . So,  $\mathcal{T}$  has the effect to change the sign of quantum mechanics operators as follows:

$$\mathcal{T} : (j, \hat{x}, \hat{p}) \rightarrow (-j, \hat{x}, -\hat{p}). \quad (1.11)$$

Hence, in two dimensions the  $\mathcal{T}$  operator is defined as

$$\mathcal{T} = \begin{pmatrix} 1 & 0 \\ 0 & 1 \end{pmatrix} \mathcal{K}, \quad (1.12)$$

where  $\mathcal{K}$  denotes the complex conjugate operation.

Another property is that the square of both  $\mathcal{P}$  and  $\mathcal{T}$  is the identity operator ( $\mathcal{P}^2 = \mathcal{T}^2 = \mathbf{1}$ ) and the two reflection operators commute with each other.

$$[\mathcal{P}, \mathcal{T}] = \mathcal{PT} - \mathcal{TP} = 0, \quad (1.13)$$

therefore, the  $\mathcal{PT}$  operator performs the following transformation :

$$\mathcal{PT} : (j, \hat{x}, \hat{p}) \rightarrow (-j, -\hat{x}, -\hat{p}). \quad (1.14)$$

### c) The $\mathcal{PT}$ operator

While systems invariant under parity  $\mathcal{P}$  or time-reversal  $\mathcal{T}$  transformations or both have been thoroughly studied, there has also been much interest in systems which do not obey  $\mathcal{P}$  or  $\mathcal{T}$  symmetries separately but which respect the combined  $\mathcal{PT}$  symmetry. A system is said to be  $\mathcal{PT}$  symmetric if the Hamiltonian  $\mathcal{H}$  which is described it, in addition to obeying Eq. (1.8) [117–119], commutes with a joint  $\mathcal{PT}$  operator, that is,

$$[\mathcal{H}, \mathcal{PT}] = \mathcal{HPT} - \mathcal{PTH} = 0 \quad (1.15)$$

To better understand, if we consider a simple Hamiltonian  $\mathcal{H}$  expressed in the form of position and momentum operator  $\mathcal{H} = p^2 + V(r)$  where  $V(r)$  represents a potential, for a real value of  $V(r)$ ,  $\mathcal{H}$  is Hermitian, (i.e.  $\mathcal{H} = \mathcal{H}^\dagger$ , where  $\dagger$  denotes the adjoint, conjugate transpose, operation) and holds entirely real eigenvalues. The  $\mathcal{PT}$ -symmetric condition on the Hamiltonian  $\mathcal{H}$  requires that the potential should satisfies the relation:  $V(r) = V^*(r)$  implying that the real and imaginary parts of the complex potential be even and odd

function of space, respectively:  $\Re(V(r)) = \Re(V(-r))$  and  $\Im(V(r)) = -\Im(V(-r))$ .

In general, non-Hermitian Hamiltonians are used to describe phenomenology of many physical dissipative systems. Then, a  $\mathcal{PTS}$  system can be constructed by adding parity-symmetric, balanced energy gain/loss elements to a conservative, symmetric system. Due to these elements the system is non-conservative, but the balanced gain and loss can result in net energy conservation of the solutions to the system. As the degree of the balanced gain/loss  $\gamma$  that controls the non-Hermiticity [4] is increased, the solutions can undergo a sudden transition from net conservation (the exact phase) to net non-conservation (the broken phase); this spontaneous  $\mathcal{PT}$  symmetry breaking is one of the fundamental properties of  $\mathcal{PT}$  symmetric systems. For low but non-zero  $\gamma$ , the spectrum can be entirely real with  $\mathcal{H}$  and  $\mathcal{PT}$  sharing the same eigenvectors, that is  $[\mathcal{H}, \mathcal{PT}] = 0$ ; the system is in the exact phase. However, as  $\gamma$  is increased, past a critical point  $\gamma_{PT}$ , the eigenvectors of  $\mathcal{H}$  cease to be eigenvectors of  $\mathcal{PT}$ , that is,  $[\mathcal{H}, \mathcal{PT}] \neq 0$ , and the spectrum becomes complex; the system is in the broken phase. The critical point is known in the litterarture as an Exceptional point (EP) [13] and its presence in  $\mathcal{PTS}$  systems have special significance for many technological applications ranging from non-reciprocal devices [120, 121] to ultra-sensitive measurement devices [122, 123].

### 1.1.2.3 $\mathcal{PT}$ symmetry in electronics

More recently ideas of  $\mathcal{PT}$  have been extended into the realm of electronic circuitry. The first work in the domain were conducted by Joseph Schindler and co-workers in ref. [28] where, it was demonstrated that a pair of coupled LRC circuits, one with amplification and the other with equivalent amount of attenuation, provide the simplest experimental realization of a  $\mathcal{PTS}$  system. The setup of the so-called  $\mathcal{PT}$ -dimer is depicted in Fig. 1.2(a). The loss is simply generated with a resistance  $R$  whereas gain is introduced via negative resistance  $-R$ . Figure 1.2(b) illustrates how an ideal linear amplifier can be configured to achieve negative resistance. Notice that, the  $\mathcal{PTS}$  dimer is defined by invariance under combined  $\mathcal{P}$  and  $\mathcal{T}$  operators where the operations are related to spatial and temporal symmetries in a natural system. However, in the field of electronics, spatial considerations disappear, and spatial symmetry is reduced to a matter of circuit topology. Therefore,  $\mathcal{P}$  is defined by the interchange of labels corresponding to left and right sides of a circuit configuration. It switches the places of the amplifier and the resistance. As one expects,  $\mathcal{T}$  on the other hand, changes the sign of the resistances, thus turning the positive resistance to a negative one and vice versa. The details of experimental implementation of  $\mathcal{PT}$  electronics is given in ref. [28] (see Fig. 1.2).

The dimensionless charges  $Q_i^C, i = 1, 2$  through the capacitors are describing by the

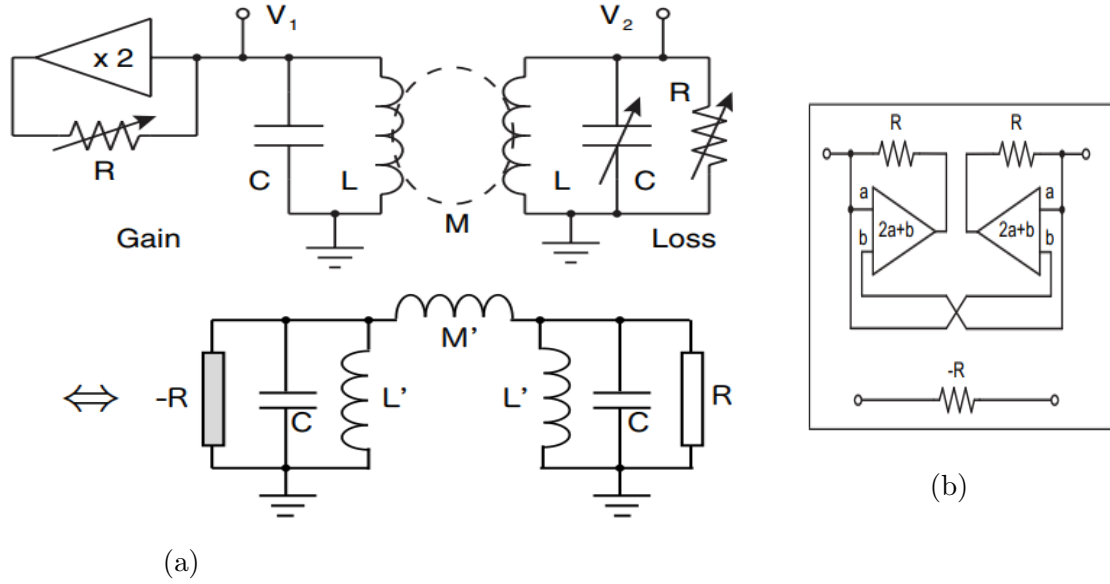


Figure 1.2: (a)  $\mathcal{PT}$ -symmetric with balanced gain and loss (upper panel) and its equivalent circuit with  $L' = L + M$  and  $M' = (L^2 - M^2)/M$  (lower panel). Here, gain is achieved by an effective negative resistance. (b) A floating negative resistance. Figure is taken from ref. [28]

following set of coupled second order differential equations:

$$\begin{cases} \frac{d^2 Q_1^C}{d\tau^2} = -\alpha Q_1^C + \mu\alpha Q_2^C + \gamma \frac{dQ_1^C}{d\tau} \\ \frac{d^2 Q_2^C}{d\tau^2} = \mu\alpha Q_1^C - \alpha Q_2^C - \gamma \frac{dQ_2^C}{d\tau} \end{cases} \quad (1.16)$$

where  $\tau = \omega_0 t$ ,  $\omega_0 = 1/\sqrt{LC}$ ;  $\gamma = \frac{1}{R} \sqrt{\frac{L}{C}}$ ;  $\mu = \frac{M}{L}$ ;  $\alpha = \frac{1}{1-\mu^2}$ .

$\gamma$  is the symmetric gain/loss strength parameter associated with the resistance.

The  $\mathcal{PT}$ -symmetry of the equations of motion is easily confirmed. In the framework of Eq. (1.16), the  $\mathcal{PT}$  operation swaps the indices 1 and 2, and reverses the sign of  $\tau$ . These operations in conjunction leave the equations unaltered. The symmetry of the equations of motion correspond to the physical symmetry of the system. Figure 1.3 illustrates the presence of physical symmetry. An alternate analysis of the dimer is necessary for a proper analytical consideration of the dynamics, and is accomplished by recasting time-domain Eq. (1.16) governing the system into a rate equation form by making use of a Liouvillian formalism [125],

$$\frac{d\psi}{dt} = \mathcal{L}\psi, \quad (1.17)$$

where  $\psi = (Q_1^C, Q_2^C, \dot{Q}_1^C, \dot{Q}_2^C)^T$ ,  $\mathcal{L} = \begin{pmatrix} \mathbf{0} & \mathbf{1} \\ \mathbf{D} & \gamma\sigma_Z \end{pmatrix}$ ,  $\mathbf{D} = \alpha(\mu\mathbf{1} - \mathbf{1})$  and  $\sigma_Z$  is the third Pauli matrix. This formulation opens new exciting directions for applications of generalized  $\mathcal{PT}$ -mechanics as it can be interpreted as a Schrödinger equation with non-Hermitian effective Hamiltonian  $\mathcal{H}_{eff} = j\mathcal{L}$ ,  $j^2 = -1$ . It can be easily verified that  $\mathcal{H}_{eff}$  is symmetric

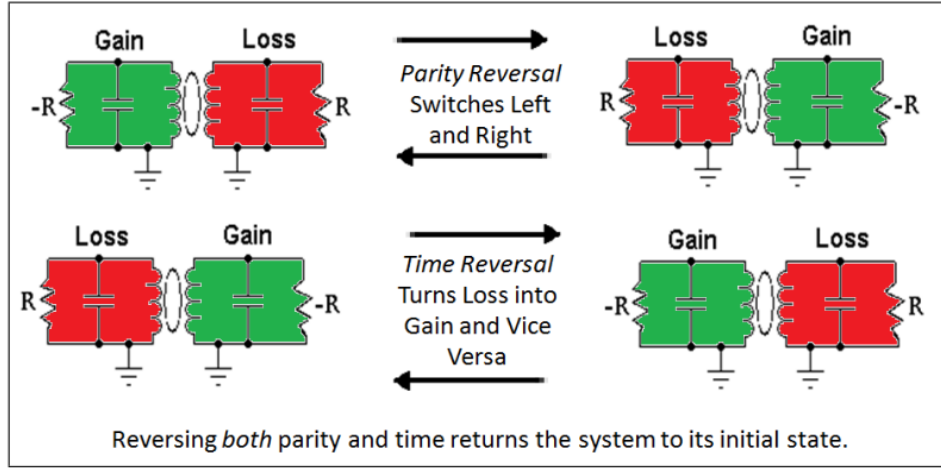


Figure 1.3: The physical symmetry of the system corresponds to its symmetric equations of motion. The figure is adapted from [124].

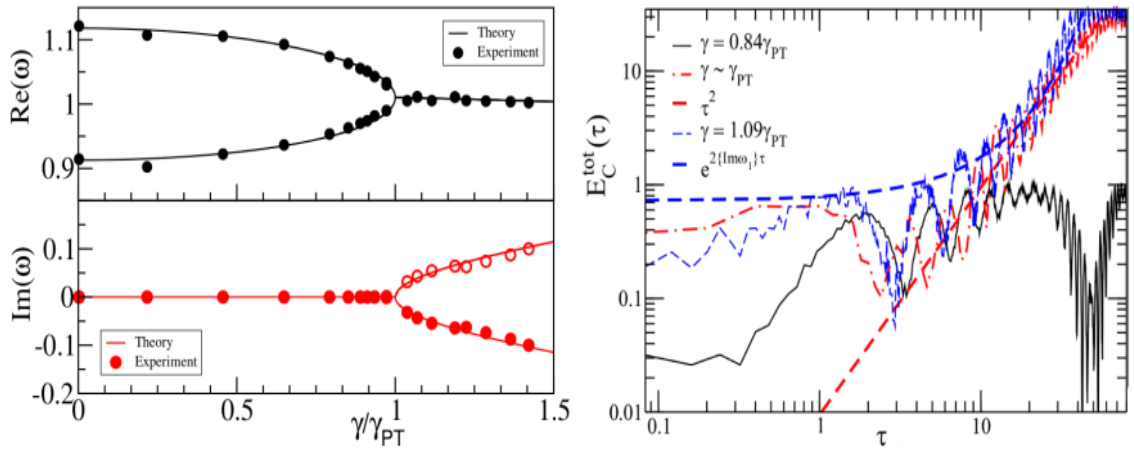


Figure 1.4: (Left) Real (upper panel) and imaginary (lower panel) parts of the eigenfrequencies  $\omega$  as a function of the normalized gain and loss parameter  $\gamma/\gamma_{PT}$ . The solid curves (dots) show the theoretical (experimental) results. Experimentally measured temporal dynamics of the capacitance energy  $E_C^{tot}(\tau)$  of the total system for various  $\gamma$ -values. As  $\gamma \rightarrow \gamma_{PT}$ , the  $\tau^2$  behavior, a signature of the spontaneous  $\mathcal{PT}$ -symmetry breaking, is observed. The figures are adapted from ref. [28].

with respect to generalized  $\mathcal{PT}$  transformations, i.e.  $[\mathcal{PT}, \mathcal{H}_{eff}] = 0$ , where

$$\mathcal{P} = \begin{pmatrix} \sigma_x & \mathbf{0} \\ \mathbf{0} & \sigma_x \end{pmatrix}, \mathcal{T} = \begin{pmatrix} \mathbf{1} & \mathbf{0} \\ \mathbf{0} & -\mathbf{1} \end{pmatrix} \mathcal{K}, \quad (1.18)$$

here,  $\sigma_x$  and  $\mathcal{K}$  are respectively the first Pauli matrix and the complex conjugation operation. The system admits four eigenfrequencies whose the positive ones are given as:

$$\omega_{1,2} = \omega_0 \sqrt{\frac{2 + \gamma^2 (\mu^2 - 1) \pm \sqrt{4 (\mu^2 - 1) + [2 + \gamma^2 (\mu^2 - 1)]^2}}{2 (1 - \mu^2)}} \quad (1.19)$$

These two eigenvalues coalesce at the exceptional point (EP) [13],

$$\gamma_{PT} = \frac{1}{\sqrt{1-\mu}} - \frac{1}{\sqrt{1+\mu}} \quad (1.20)$$

In Fig. 1.4 (left panel), the authors of ref. [28] have reported the measurements for the frequencies of the experimental circuitry in Fig. 1.2(a). A comparison with the theoretical results of Eq. (1.16) indeed shows an excellent agreement. They have also observed the spatio-temporal evolution of the total energy of the system (right panel), i.e.,  $E_{tot}^C = \frac{1}{2C} \left[ (Q_1^C(\tau))^2 + (Q_2^C(\tau))^2 \right]$  which reveals the occurrence of  $\mathcal{PT}$ -symmetry breaking. For  $\gamma < \gamma_{PT}$  where the eigenfrequencies are real, the circuit is characterized by bounded power oscillations, whereas when  $\gamma > \gamma_{PT}$ , the dynamics becomes unstable exhibiting exponential growth in stored energy. As  $\gamma \rightarrow \gamma_{PT}$ , the  $\tau^2$  behavior signaling the spontaneous  $\mathcal{PT}$ -symmetry breaking is observed.

#### 1.1.2.4 Experimental Observation of $\mathcal{PT}\mathcal{S}$ scattering

##### a) Single Port Scattering

The properties of the normal modes of the  $\mathcal{PT}\mathcal{S}$  dimer can be used to create novel scattering systems with useful engineering applications. For this, two cases are envisaged. In the first case, a transmission line (TL) is attached to the left (amplified) circuit of

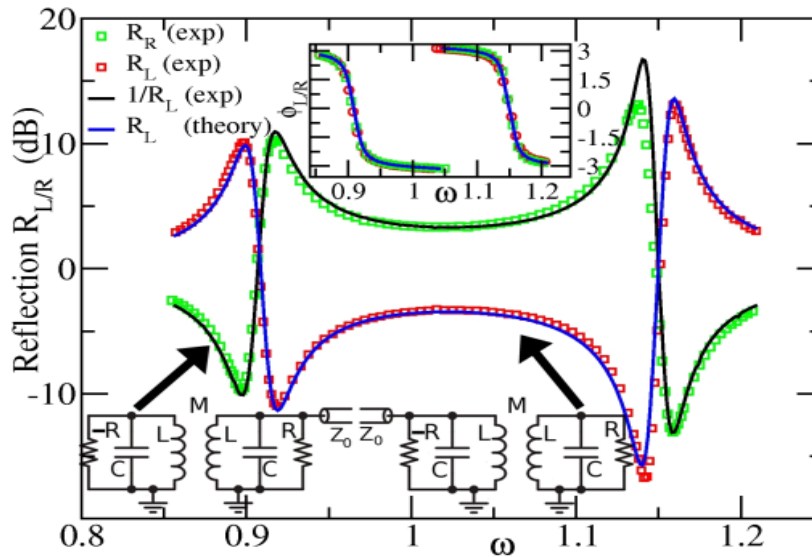


Figure 1.5: Experimental reflectances for a single TL attached to the lossy ( $R_R$ ) or the gain ( $R_L$ ) side of the dimer (see lower insets) for  $\mu = 0.29$  ;  $\gamma = 0.188875$  ;  $\eta = 0.0305$ . The black line corresponds to  $R_L^{-1}$  and confirms the non-reciprocal nature  $R_L R_R = 1$  of the  $\mathcal{PT}$ -scattering. The upper inset shows the measurements for the left (right) reflection phases  $\phi_L$  ( $\phi_R$ ). The blue lines are the theoretical results. The figure is adapted from ref. [80].

the dimer load while in the second case, the TL is connected to the right (lossy) circuit of the load (see lower right and left insets of Fig. 1.5 respectively) [125]. The authors

of ref. [125] were interested to the behavior of the reflectance and the spatial profile of the potential inside the scattering domain were analyzed as the gain/loss parameter  $\gamma$  and the frequency  $\omega$  changes. For  $\mathcal{PT}\mathcal{S}$  structures, the corresponding scattering signals satisfy generalized unitarity relations which reveal the symmetries of the scattering target. Specifically, in the single-port set up this information is encoded solely in the reflection. So observe that the lower left set-up of Fig. 1.5 is the  $\mathcal{PT}\mathcal{S}$  replica of the lower right one. Assuming therefore that a potential wave at the left lead (lower right inset) has the form  $V_L(x) = e^{jkx} + r_L e^{-jkx}$ , the form of the wave at the right lead associated with the lower left set-up is deduced as  $V_R(x) = e^{-jkx} + r_R e^{jkx} = V_L^*(x)$  where  $r_L$  and  $r_R$  are the reflection amplitudes for the left or right incident waves. For this specific case, the exact expressions for the complex reflection amplitudes were analytically obtained as:

$$\begin{aligned}
 r_L(\omega) &= -f(-\eta, -\gamma) / f(\eta, -\gamma) \\
 r_R(\omega) &= -f(-\eta, \gamma) / f(\eta, \gamma) \\
 f &= 1 - [2 - \gamma m (\gamma + \eta)] \omega^4 + m \omega^4 - j \eta \omega (1 - m \omega^2) \\
 m &= 1 / \sqrt{1 - \mu^2}
 \end{aligned} \tag{1.21}$$

In the main panel of Fig. 1.5, a representative measurement of the reflection signals for the two scattering configurations are plotted and the results indicate that, the measured reflectances  $R_L$  and  $R_R$  satisfy the generalized conservation relation  $R_L R_R = 1$  while for the reflection phases  $\phi_L = \phi_R$ . The experiment results also demonstrates that a

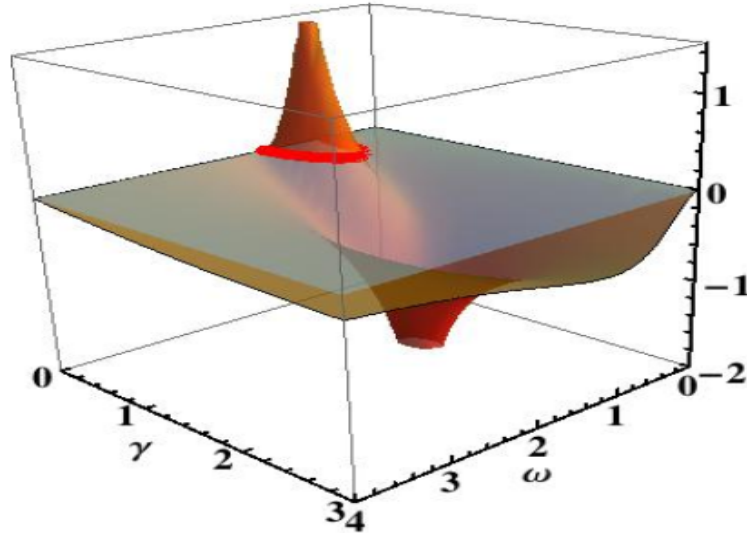


Figure 1.6: The  $\omega - \gamma$  phase diagram for  $\mu = 0.57$ , indicating the existence of a subunitary ( $\log_{10}(R_R) < 0$ ) and a complimentary super-unitary ( $\log_{10}(R_R) > 0$ ) domain for the set-up shown at the lower left inset of Fig. 1.5. The figure is adapted from ref. [80].

$\mathcal{PT}\mathcal{S}$  load is a simple electronic Janus device that for the same values of the parameters  $\mu$ ,  $\gamma$ ,  $\omega$  acts as an absorber as well as a signal amplifier, depending on the direction of incident signal. The  $(\omega, \gamma)$  parameter space can then be partitioned into a sub-unitary



domain for which  $R < 1$  (flux is diminished), and a super-unitary domain for which  $R > 1$  (flux is enhanced). At the transition between the two domains,  $R_L = R_R = 1$  in which case the scattering from both sides conserves flux. Such a reflectance degeneracy (RD) occurs along the continuous boundary between the two domains, defined by  $|r_R| = 1$ . A

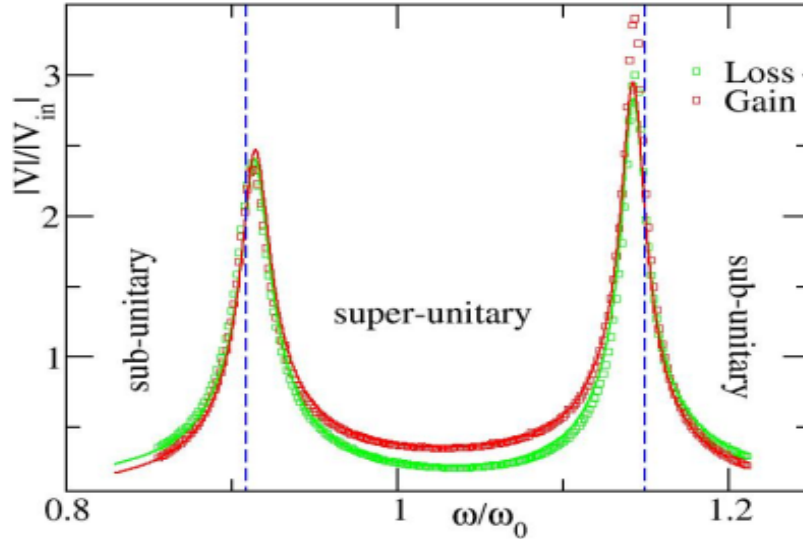


Figure 1.7: The spatial potential distribution inside the dimer versus the frequency  $\omega$ . The TL is coupled to the lossy side. The parameters used are the those used in Fig. 1.5. The blue dashed lines indicate the boundaries between sub-unitary to super-unitary scattering. The figure is adapted from ref. [80].

panorama of theoretical  $R_R(\omega, \gamma)$  are presented in Fig. 1.6, where we note in a domain, a singularity point for which  $R_R \rightarrow \infty$ , while a reciprocal point for which  $R_R = 0$  is found in the complementary domain. The sub-unitary to super-unitary  $\mathcal{PT}\mathcal{S}$  transition is also manifest in the spatial structure of the potential ( $V_L; V_R$ ) inside the dimer. It is observed from Fig. 1.7 when the transmission line attached to the loss side (see lower left inset of Fig. 1.5), that these potential are in general asymmetric. We note that in the super-unitary domain, the gain side is characterized by a larger potential amplitude  $|V_L| > |V_R|$  while in the sub-unitary domain the scenario is reversed and  $|V_L| < |V_R|$ . This ensures that more power is being consumed than compensated by the gain circuit, while the inverse argument applies for the former configuration. At frequencies where the reflection degeneracy occurs, the nodal voltages are spatially symmetric. This is consistent with the intuitive expectation that in order to conserve flux the excitation must on average spend equal amounts of time in the loss and gain circuits of the structure. Obviously, the reverse scenario occurs if we couple the transmission into the  $\mathcal{PT}$ -dimer from the gain side.

### b) Double port scattering

Here, the case of double port scattering is analysed (see Fig. 1.8), where the above active  $\mathcal{PT}$  LRC dimer was used for the first time to experimentally identify the occurrence

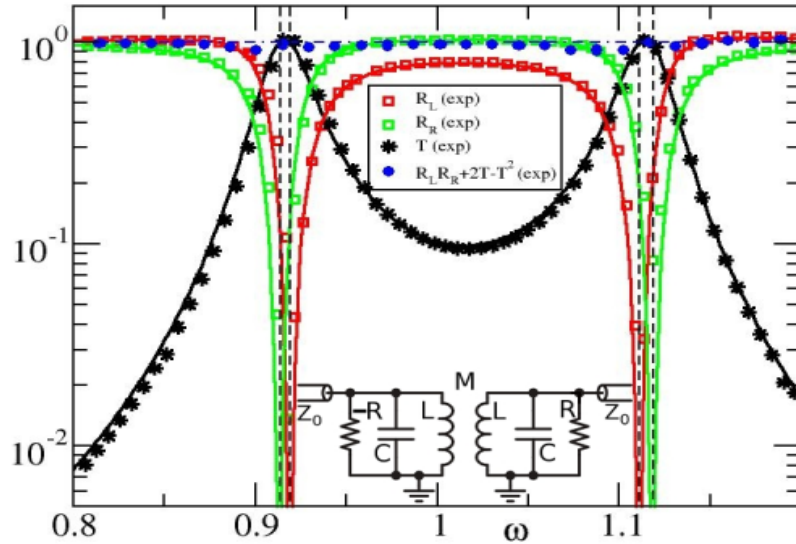


Figure 1.8: Measurements (symbols) and numerics (lines of corresponding color) of  $T$ ,  $R_{L/R}$  for the two-port scattering set-up. The vertical black dashed lines indicate the frequencies where unidirectional transparency occurs. The conservation relation is also evaluated using the experimental data. The horizontal dashed blue line is drawn for the eye and indicates the value 1. The parameters used are the those used in Fig. 1.5. The figure is adapted from ref. [80].

of the unidirectional transparency. It can be straightforwardly check that transmittance  $T$  and  $R$  reflectance satisfy the generalized conservation relation  $\sqrt{R_L R_R} = |T - 1|$ . The measurements for  $R_{L/R}$  and  $T$  are shown in Fig. 1.8, where the quantity  $R_L R_R + 2T - T^2$  (blue circles) was also evaluated from the experimental data and it is found to be 1 as it is expected from the conservation relation. An interesting result is that at specific  $\omega$ -values (marked with vertical dashed lines), the transmittance becomes  $T = 1$ , while at the same time one and only one of the reflectances vanishes. Hence, the scattering for this direction of incidence is flux conserving and the structure is unidirectionally transparent. It is interesting to note that a periodic repetition of such a  $\mathcal{PT}\mathcal{S}$  unit it will result in the creation of unidirectionally transparent frequency bands.

Figure 1.9 illustrates another interesting feature of two-port  $\mathcal{PT}\mathcal{S}$  scattering, a so-called simultaneous coherent perfect absorber-amplifier, or CPA laser [36]. This functionality was first implemented [87] in the capacitively coupled version of the electronic dimer scatterer shown in the inset of Fig. 1.9(a). It was shown that the twoport  $\mathcal{PT}\mathcal{S}$  dimer can behave simultaneously as a perfect absorber and as an amplifier, a property which can be explored using an overall output coefficient  $\Theta$  defined as

$$\Theta = \frac{|V_R^+|^2 + |V_L^-|^2}{|V_L^+|^2 + |V_R^-|^2}, \quad (1.22)$$

where  $V_{L,R}^+$  and  $V_{L,R}^-$  represent the forward and the backward wave amplitudes. The

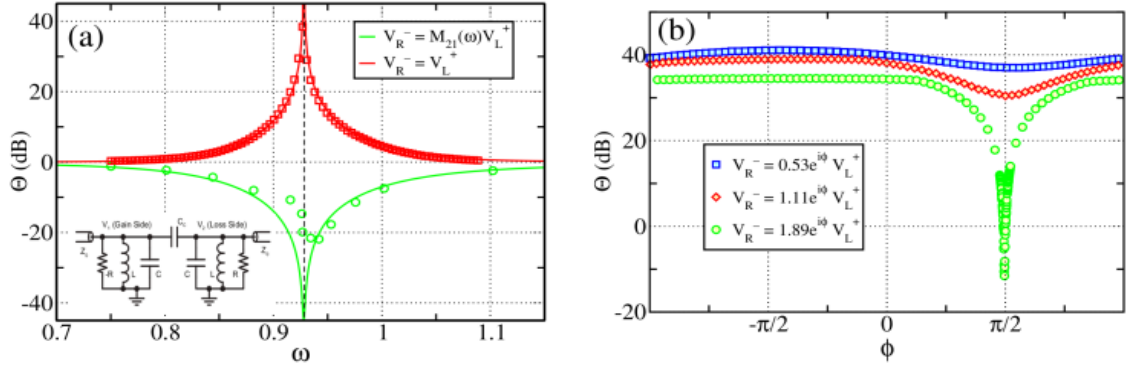


Figure 1.9: (a) The overall output coefficient  $\Theta(\omega)$  versus frequency  $\omega$  near the amplification/attenuation frequency  $\omega_J$  (vertical dashed line). The  $\mathcal{PTS}$  electronic circuit is coupled to two ports and has  $\eta = 0.110$ ;  $\gamma = 0.186$ ;  $c = 0.161$ . At  $\omega = \omega_J$  the system acts as a perfect absorber when the input signal satisfies the coherent attenuation relation  $V_R^- = \mathcal{M}_{21}(\omega)V_L^+$ . For any other incident signal (e.g. see the blue line corresponding to  $V_R^- = V_L^+$ ) the system acts as an amplifier. The dots are experimental values while the lines are numerical results. (b) Plots of experimental  $\Theta(\omega_J)$  versus the relative phase  $\phi$  of the signal entering the structure from the lossy node. Various curves correspond to different excitation amplitudes. Note the extremely sharp dependence at the Janus condition. Figures are adapted from ref. [87].

singular behavior of the theoretical  $\Theta$  in Fig. 1.9(a), solid curves, illustrate that at the Janus frequency  $\omega_J$  the injected signals can result in either amplification or complete attenuation, depending on the relative amplitude and phase of the injected signals. Fig. 1.9(b) shows extreme sensitivity of the injection parameters to the phase of the right input signal near  $\omega_J$  and illustrates practical limits to the achievement of the coherent perfect absorber-amplifier condition.

### 1.1.2.5 Non-Hermitian $\mathcal{APT}$ symmetric systems

As a supplementary probe to the  $\mathcal{PTS}$  developments, and, in the quest of novel artificial structures possessing a non-Hermitian Hamiltonian, the recent works in optics have suggested new ways of controlling light propagation and confinement involving spontaneous symmetry-breaking transition and non-Hermitian singularities. Nowadays, a new class of non-Hermitian systems called pseudo anti-Hermitian of which is belonging anti- $\mathcal{PT}$  symmetry is emerging, and has been treated in positive-negative index multilayers [126], optically dressed atom lattices [127] and rapid coherent photo-atomic transport experiments [39]. Anti- $\mathcal{PT}$  symmetry was also suggested in optics in a few theoretical works [7, 9, 13, 45, 45, 126–131] and demonstrated in a recent experiment based on flying atoms in a warm atomic vapor cell [39]. As a counterpart of standard  $\mathcal{PT}$  symmetry interestingly, an anti- $\mathcal{PTS}$  Hamiltonian satisfies the anti-commutation relation with the  $\mathcal{PT}$  operator,  $\{\mathcal{PT}, H\} = 0$ . In others words a Hamiltonian  $\mathcal{H}$  is said to be anti  $\mathcal{PTS}$  if,

$$(\mathcal{PT})\mathcal{H} = -\mathcal{H}(\mathcal{PT}). \quad (1.23)$$

mathematically, multiplying a conventional  $\mathcal{PTS}$  Hamiltonian  $\mathcal{H}$  by "j" would render it anti- $\mathcal{PT}$  symmetric, i.e.,  $\mathcal{H}^{\mathcal{AP}\mathcal{T}} = j\mathcal{H}^{\mathcal{PT}}$  [83] indicating that anti- $\mathcal{PT}$  systems exhibit properties completely conjugate to those of  $\mathcal{PT}$  systems. Consequently,  $\mathcal{PT}$ -symmetric like eigensystem structures involving exceptional points (EP), spontaneous symmetry-breaking transition, and self-intersecting energy-spectral topology appear and they result in  $\mathcal{PT}$ - $\mathcal{AP}\mathcal{T}$  conjugate phenomena such as refractionless propagation, flat total transmission bands, and continuous lasing spectra [13, 39, 126].

Within the context of non-conserving binary oscillator, a  $\mathcal{PTS}$  system has a characteristic Hamiltonian [50],

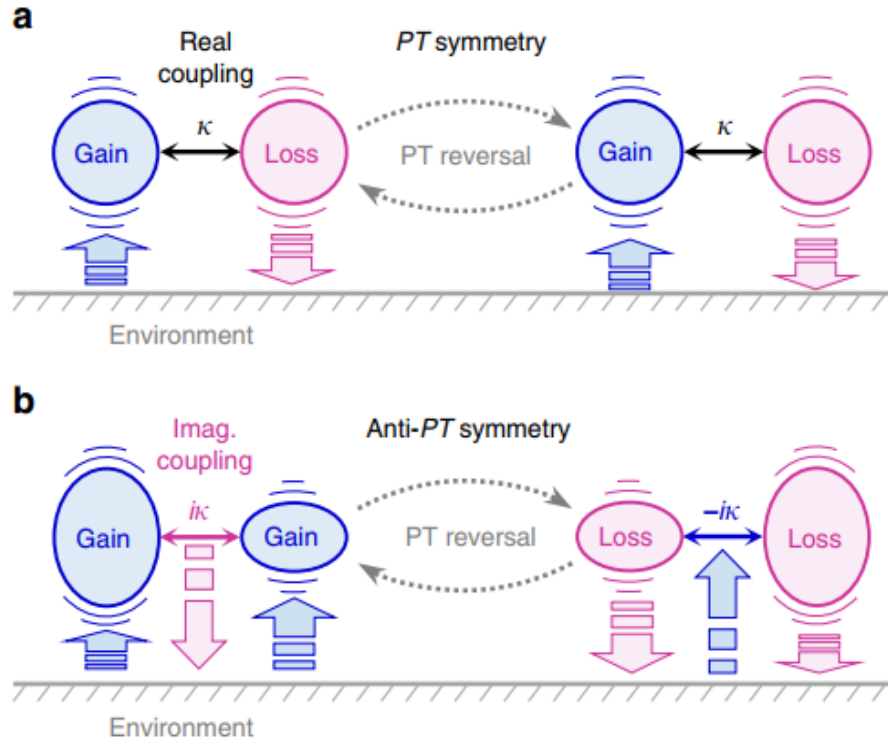


Figure 1.10: Schematic diagrams of  $\mathcal{PT}$  and anti- $\mathcal{PT}$  symmetric binary systems. a)  $\mathcal{PT}$ -symmetric coupled oscillators implied by the  $\mathcal{PTS}$  Hamiltonian  $\mathcal{H}^{(\mathcal{PT})}$ . b)  $\mathcal{AP}\mathcal{T}$ -symmetric binary system derived from the relation  $\mathcal{H}^{(\mathcal{AP}\mathcal{T})} = \pm j\mathcal{H}^{(\mathcal{PT})}$ . In the two diagrams,  $\kappa$  denotes inter-resonator coupling constant and vertical arrows indicate directions of energy exchange between the coupled-resonator system and environment. Figures are adapted from ref. [50].

$$\mathcal{H}^{(\mathcal{PT})} = \begin{pmatrix} \varepsilon + j\gamma & \kappa \\ \kappa & \varepsilon - j\gamma \end{pmatrix} \quad (1.24)$$

where  $\mathcal{H}^{(\mathcal{PT})}$  describes two equally tuned oscillators at energy level  $\varepsilon$  and with their attenuation or amplifying rates differing by  $2\gamma$  and  $\kappa$  the coupling, which is real. As it can be seen in Fig. 1.10(a), the system remains invariant under the simultaneous parity inversion ( $\mathcal{P}$ ) and gain-loss exchange ( $\mathcal{T}$ ) operations, thus reveals the  $\mathcal{PT}$  symmetry. The  $\mathcal{AP}\mathcal{T}$  symmetric counterpart is described by a Hamiltonian of the form,

$$\mathcal{H}^{(\mathcal{APT})} = \begin{pmatrix} -\varepsilon + j\gamma & j\kappa \\ j\kappa & \varepsilon + j\gamma \end{pmatrix} \quad (1.25)$$

which implies two equally amplifying oscillators at an amplification/attenuation rate  $\gamma$  and with their energy level differing by  $2\varepsilon$ , as illustrated in Fig. 1.10(b). It is important to notice that, no explicit physical symmetry is found for this generic  $\mathcal{APT}$ -symmetric system under the  $\mathcal{PT}$  operation. Moreover, the environmental energy-exchange scheme is completely different from the  $\mathcal{PTS}$  counterpart. This argument suggests that essential dynamics in  $\mathcal{APT}$ -symmetric systems might be remarkably different from the  $\mathcal{PT}$ -symmetric counterpart even though the relation  $\mathcal{H}^{(\mathcal{APT})} = \pm j\mathcal{H}^{(\mathcal{PT})}$  implies mathematically indistinguishable eigensystem structures for  $\mathcal{H}^{(\mathcal{PT})}$  and  $\mathcal{H}^{(\mathcal{APT})}$  in principle.

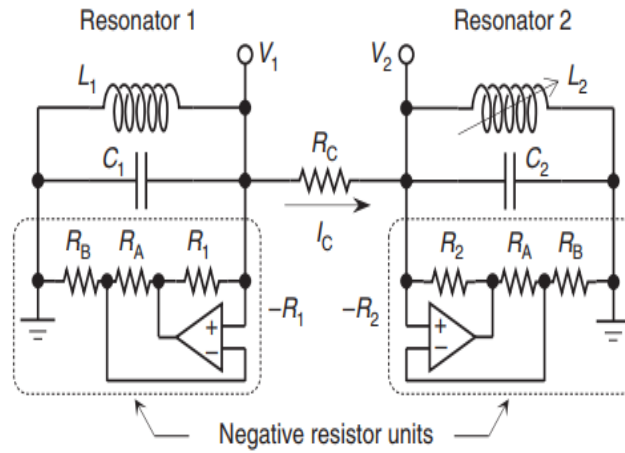


Figure 1.11:  $\mathcal{APT}$ -symmetric model circuit and its spectral property. Circuit diagram of  $\mathcal{APT}$ -symmetric LRC resonators. The circuit consists of two resistively coupled amplifying LRC resonators with negative resistance units. A variable inductor is used for  $L_2$  to precisely control the energy-detuning parameter  $\varepsilon$ . The figure is taken from ref. [50].

An experimentally electrical model circuit was proposed by Youngsun Choi and coworkers in ref. [50] where, the authors used two amplifying LRC resonators connected in parallel through a coupling resistance as shown in Fig. 1.11, to realize a generic  $\mathcal{APT}$ -symmetric system permitting precise parametric controls. The experimental setup simulates the  $\mathcal{APT}$ -symmetric environmental interaction scheme with negative resistance units ( $-R_1$  and  $-R_2$ ) providing a gain mechanism and with a coupling resistance ( $R_C$ ) as a loss mechanism. Setting  $R_A = R_B$ ,  $R_C = R_1 = R_2 = R$ ,  $C_1 = C_2 = C$  and using few steps of algebra, the authors demonstrated that essential dynamics of the system can be described by a Schrödinger type equation  $\frac{d}{dt} |v\rangle = -j\mathcal{H}^{(\mathcal{APT})} |v\rangle$ , where  $\mathcal{H}^{(\mathcal{APT})}$  is given by Eq. (1.25) and a state vector  $|v\rangle$  defined such that  $(V_1 \ V_2)^T \equiv \frac{1}{2} (e^{-j\omega_0 t} |v\rangle + e^{j\omega_0 t} |v\rangle^*)$ ,  $\omega_0 = \frac{1}{2} \left( \frac{1}{\sqrt{L_1 C}} + \frac{1}{\sqrt{L_2 C}} \right)$  being average uncoupled-resonance angular frequency. Therefore, Hamiltonian matrix elements are determined by  $\varepsilon = \frac{1}{2} \left( \frac{1}{\sqrt{L_2 C}} - \frac{1}{\sqrt{L_1 C}} \right)$ ,  $\gamma = 0$  and  $\kappa = \frac{1}{2RC}$ .

A characteristic resonance spectrum of the system is obtained by taking a Fourier-

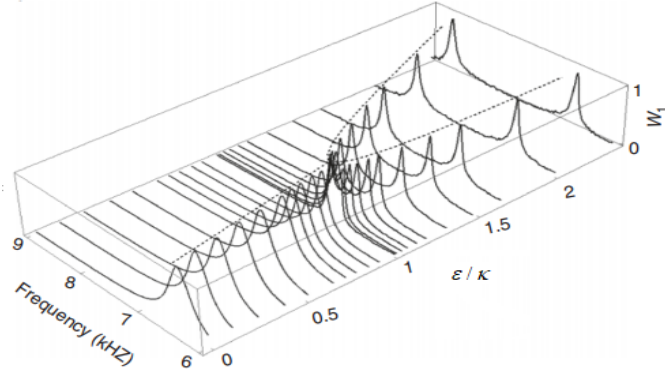


Figure 1.12:  $\varepsilon$ -dependent resonance-excitation spectrum  $W_1(f)$ . The Figure is adapted from ref. [50].

transformed intensity  $W_n(f) = |F[V_n(t)]|$  in the frequency ( $f$ ) domain. Hence, the measured  $W_1(f)$  spectrum as a function of the energy detuning parameter  $\varepsilon$  is shown in Fig. 1.12. It is obvious from the figure that a branch-point splitting of the resonance peak occurs at a threshold point (EP) of  $\varepsilon = \kappa$ . Loci and bandwidths of the resonance peaks in the measured spectral profiles correspond to the real and imaginary parts of the eigenvalue of  $\mathcal{H}^{(\mathcal{AP}\mathcal{T})}$  Hamiltonian describing the system given as:

$$\lambda = \pm\sqrt{\varepsilon^2 - \kappa^2} \quad (1.26)$$

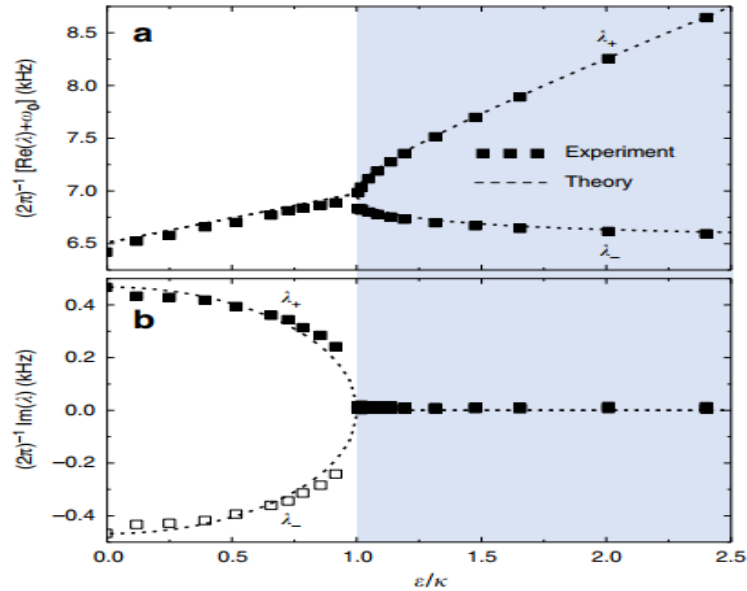


Figure 1.13: Eigensystem structure of an  $\mathcal{AP}\mathcal{T}$ -symmetric circuit. Real (a) and imaginary (b) eigenvalues inferred from the resonance-excitation spectra in Fig. 1.12 in comparison with theory. The theoretical curves are obtained by a binary Hamiltonian model derived from Kirchhoff's circuit laws. The shaded area for  $\varepsilon/\kappa$  indicates the parametric region of the broken  $\mathcal{P}\mathcal{T}\mathcal{S}$  phase. Figures are adapted from ref. [50].

The  $\text{Re}(\lambda_{\pm})$  and  $\text{Im}(\lambda_{\pm})$  in experiment can be inferred from the peak location and bandwidth, respectively, as shown in Fig. 1.13(a, b). Excellent agreement of the experimental values with the theory confirms that a generic  $\mathcal{AP}\mathcal{T}$  symmetric system is indeed realized in the model circuit with high degree of precision. In addition,  $\lambda_{\pm}$  shows a purely imaginary splitting for  $\varepsilon < \kappa$ , merging ( $\lambda_{+} = \lambda_{-}$ ) at  $\varepsilon = \kappa$  where eigenvectors simultaneously coalesce, and a purely real splitting for  $\varepsilon > \kappa$ . In this respect, the authors concluded that  $\mathcal{AP}\mathcal{T}$ -symmetric binary systems and associated phenomena can be treated in a manner similar to the  $\mathcal{PT}$  symmetry as far as their stationary responses are treated. Furthermore, the dynamic properties of a generic  $\mathcal{AP}\mathcal{T}$ -symmetric system in a

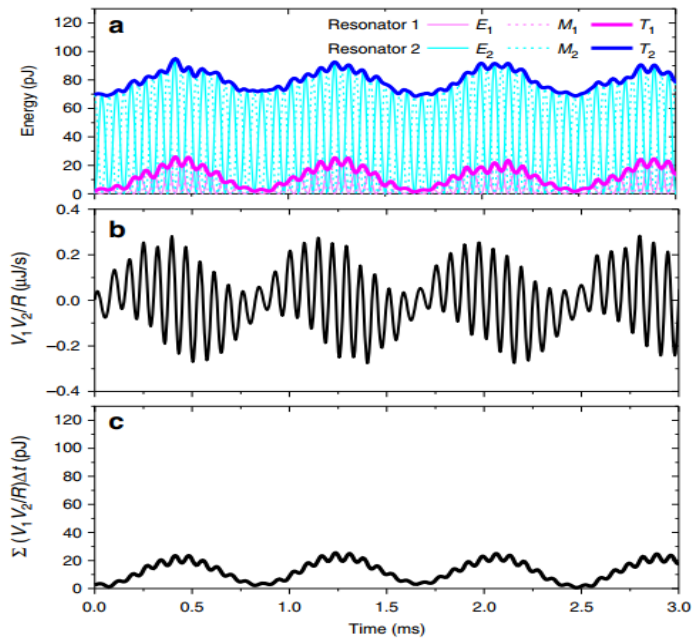


Figure 1.14: Energy-difference conserving dynamics in time domain. a) Measured time evolution of the total energy  $T_n$ , electric energy  $E_n$ , and magnetic energy  $M_n$  for an initial state  $|v(0)\rangle = (0 \ 1)^T$ .  $\varepsilon = 1.48\kappa$  in this measurement. b) Measured voltage-product energy rate  $V_1 V_2 / R$ . c) Integrated voltage-product energy rate  $\sum (V_1 V_2 / R) \Delta t$  showing an exact correlation with the beating patterns in  $T_n$ . Here, the sampling time interval  $\Delta t = 4 \mu s$ . Figures are taken from ref. [50].

resistively coupled LRC resonators were also investigated [50]. Measured electric energy  $E_n = \frac{1}{2} C_n V_n^2$  in capacitor  $C_n$ , magnetic energy  $M_n = \frac{1}{2} L_n I_n^2$  in inductor  $L_n$ , and total energy  $T_n = E_n + M_n$  for resonator  $n$  ( $n = 1, 2$ ) are plotted as functions of time. An unprecedented property revealed in the measured time-domain response is beating patterns that conserve the energy difference  $\Delta T = T_2 - T_1$ . This is in stark contrast to the standard Hermitian dynamics keeping the system's net energy  $T_1 + T_2$  constant and also to the  $\mathcal{PT}$ -symmetric dynamics conserving a cross-conjugate product  $v_1 v_2^* + v_1^* v_2$ . These results were summarized in Fig. 1.14 where the resonator's energy amplification or dissipation is determined by the sign of the voltage-product  $V_1 \cdot V_2$  where the specific beating patterns in Fig. 1.14(a) are understood by the periodic change of the  $V_1 \cdot V_2$ -product sign for the two resonators oscillating at slightly different frequencies. The Fig. 1.14(b)

indicated a measured voltage-product energy rate  $V_1 \cdot V_2/R$  whereas its integrated profile  $J(t_a) = \sum_b [V_1(t_a) V_2(t_b)/R] \Delta t$  is provided in Fig. 1.14(c). The beating pattern in  $J(t)$  in Fig. 1.14(c) shows a quantitative agreement with the  $T_n(t)$ ,  $n = 1, 2$  patterns in Fig. 1.14(a).

## 1.2 Imaginary resistance

### 1.2.1 What is the imaginary resistance ?

The imaginary resistance is a resistance whose element value is imaginary [132–135]. Its impedance  $Z_{jR}(j\omega)$  is defined by

$$Z_{jR}(j\omega) = jR, \quad (1.27)$$

where  $j$  is the imaginary unit and  $R$  is a real constant. Equation (1.27) shows that the imaginary resistance doesn't make power dissipation and it has the inductive property when  $R > 0$  and the capacitive property when  $R < 0$ . Thus, the imaginary resistance can be regarded as a kind of reactance element [132].

The case of exchanging an inductor  $L$  for the imaginary resistance  $jR_L$

$$jR_L = j\omega L, \quad (1.28)$$

the case of exchanging a capacitor  $C$  for the imaginary resistance  $jR_C$

$$jR_C = 1/j\omega C = -j/\omega C, \quad (1.29)$$

where  $\omega$  is a real constant.

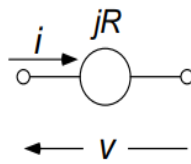


Figure 1.15: Imaginary resistance. Figure is taken from ref. [133].

The circuit equation of the imaginary resistance shown in Fig. 1.15 has the following form:

$$v = jR \cdot i \quad (1.30)$$

Recently, a possible way of directly or indirectly implementing the imaginary resistance were proposed in literature using an ideal transformer, the gyrators or op-amplifiers [132–137]. In the following, we review some of these realization methods.



## 1.2.2 Imaginary resistance build from a gyrator

The voltage  $v$  and the current  $i$  flowing through the imaginary resistance shown in Fig. 1.15, can be decomposed into their real and imaginary components as follows:

$$\begin{aligned} v &= v_r + jv_i, \\ i &= i_r + ji_i. \end{aligned} \quad (1.31)$$

where the subscripts  $r$  and  $i$  denote the real and imaginary signal paths, respectively. Substituting the above equation into Eq. (1.30) yields:

$$\begin{pmatrix} v_r \\ v_i \end{pmatrix} = \begin{pmatrix} 0 & -R \\ R & 0 \end{pmatrix} \begin{pmatrix} i_r \\ i_i \end{pmatrix}. \quad (1.32)$$

When this equation is regarded as a  $Z$ -matrix, which indicates the relationship between the ports  $r$  and  $i$ , its configuration reveals that the imaginary resistance can be equivalently realized by using a gyrator with a gyration resistance of  $R$  [136] as presented in Fig. 1.16. The signal path is decomposed into real and imaginary components. This means that the phase difference between them is  $\pi/2$  when an analytic signal is applied to the input terminals.

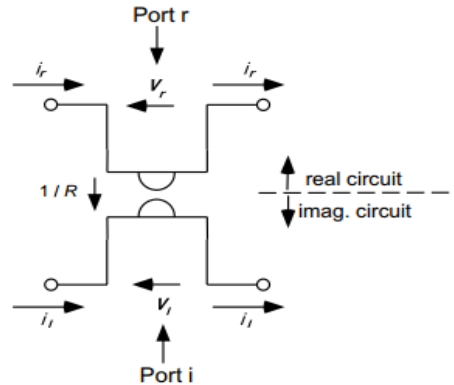


Figure 1.16: Gyrator. Figure is taken from ref. [133].

Let consider that the phase of the imaginary signal is lagged by  $\theta$ . In this case, the relationships among the resulting  $v_0$ ,  $v_1$ ,  $i_0$  and  $i_1$ , and the quadrature signal can be expressed as follows :

$$\begin{cases} v_r = v_0 \\ v_i = v_1 e^{j\theta} \\ i_r = i_0 \\ i_i = i_1 e^{j\theta} \end{cases} \quad (1.33)$$

Then, substituting the above equation into Eq. (1.30) yields :

$$v_0 + jv_1 e^{j\theta} = jR (i_0 + ji_1 e^{j\theta}) , \quad (1.34)$$

As  $e^{j\theta} = \cos \theta + j \sin \theta$ , we found

$$v_0 - v_1 \sin \theta + jv_1 \cos \theta = -Ri_1 \cos \theta + j (Ri_0 - Ri_1 \sin \theta) . \quad (1.35)$$

Rewriting the above equation in a Y-matrix form yields

$$\begin{pmatrix} i_0 \\ i_1 \end{pmatrix} = \begin{pmatrix} -\frac{1}{R} \tan \theta & \frac{1}{R} \frac{1}{\cos \theta} \\ -\frac{1}{R} \frac{1}{\cos \theta} & \frac{1}{R} \tan \theta \end{pmatrix} \begin{pmatrix} v_0 \\ v_1 \end{pmatrix} . \quad (1.36)$$

The above equation can be decomposed into the following form :

$$Y = \begin{pmatrix} -\frac{1}{R} \tan \theta & 0 \\ 0 & \frac{1}{R} \tan \theta \end{pmatrix} + \begin{pmatrix} 0 & \frac{1}{R} \frac{1}{\cos \theta} \\ -\frac{1}{R} \frac{1}{\cos \theta} & 0 \end{pmatrix} . \quad (1.37)$$

This means that the imaginary resistance  $jR$  can be equivalently realized by using the circuit shown in Fig. 1.17. When  $\theta$  is set to 0, this circuit becomes equivalent to the circuit shown in Fig. 1.15. The element values included in the circuit shown in Fig. 1.17 become :

$$\begin{aligned} g_m &= \frac{1}{R} \frac{1}{\cos \theta} , \\ R_p &= R \cot \theta . \end{aligned} \quad (1.38)$$

In the three-phase complex filter for example,  $\theta = -\pi/6$  [rad].

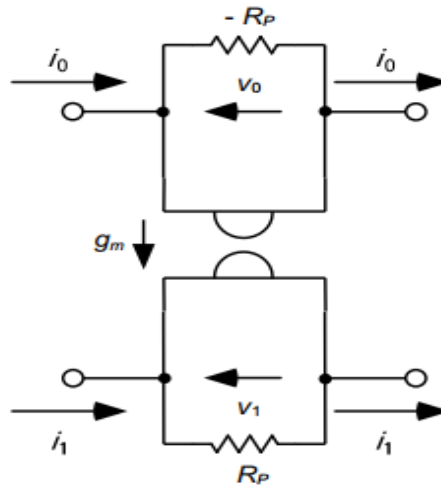


Figure 1.17: Imaginary resistance realized by using gyrator and resistors for arbitrary phase-difference  $\theta$ . Figure is taken from ref. [133].

### 1.2.3 Imaginary resistance based on ideal transformers

Reconsider again the matrix form given by the Eq. (1.33) and let's introduce new variables  $v_i'$  and  $i_i'$  defined as follows,

$$\begin{cases} v_i' = R_0 i_i, \\ i_i' = (1/R_0) v_i, \end{cases} \quad (1.39)$$

where  $R_0$  is a positive constant. Equation (1.39) implies that the current and voltage are interchanged in the imaginary circuit. Therefore, the imaginary circuit must represent a dual of the real circuit. Substituting Eq. (1.39) into Eq. (1.32) yields :

$$\begin{pmatrix} v_r \\ i_i' \end{pmatrix} = \begin{pmatrix} 0 & -R/R_0 \\ R/R_0 & 0 \end{pmatrix} \begin{pmatrix} i_r \\ v_i' \end{pmatrix}. \quad (1.40)$$

Re-written the above equation, it comes out that:

$$\begin{pmatrix} v_r \\ i_r \end{pmatrix} = \begin{pmatrix} -R/R_0 & 0 \\ 0 & -R_0/R \end{pmatrix} \begin{pmatrix} v_i' \\ -i_i' \end{pmatrix}. \quad (1.41)$$

Equation (1.41) expresses a two-port circuit written in an  $F$  matrix form. It represents an ideal transformer embedded between the real and imaginary circuits. Therefore, the imaginary resistance shown Fig. 1.15 can be equivalently realized by using the ideal transformer whose turn ratio is  $-R : R_0$  as shown in Fig. 1.18 [136].

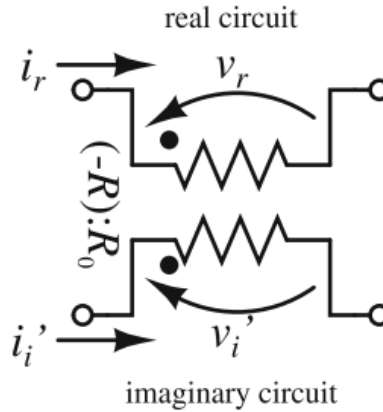


Figure 1.18: Imaginary resistance realized by using ideal transformer. Figure is taken from ref. [136].

### 1.2.4 Imaginary resistance based $\mathcal{PT}$ symmetry electronics dimers

Recently, Stephane B. Tabeu and co-workers [62] have proposed a first approach of fabricating a  $\mathcal{PT}$  symmetry electronic dimers circuits using an imaginary resistance  $Z$ , whose impedance is frequency independent. Their experimental setup as shown in Fig.

1.19(a) consists of one gain and one loss oscillators, all made of an imaginary resistance ( $Z = jr$ ), a real resistance  $R$  and a capacitor  $C$  (ZRC) coupled in parallel. Particularly, the authors showed that the imaginary resistance based electronic dimer breaks the dynamics of the conventional LRC oscillator, as the so-called ZRC dimer is described by a first order ordinary differential equation which induces single spontaneous breaking point from real to complex solutions. The expressions of the eigenfrequencies were found to be:

$$\Omega_{1,2} = \frac{(1 + \nu + c) \pm \sqrt{(1 + 2c)(\gamma_{PT}^2 - \gamma^2)}}{1 + 2c}, \quad (1.42)$$

where  $c$  and  $\nu$  are the capacitive and the imaginary resistive coupling, respectively whereas  $\gamma$  is the ratio of both the imaginary resistance and the real resistance value.  $\gamma_{PT} = \frac{c-\nu}{\sqrt{1+2c}}$  is the  $\mathcal{PT}$  threshold transition. The well plotting of eigenvalues exhibits the square root singularity  $\sqrt{\gamma_{PT}^2 - \gamma^2}$ , a generic feature of the  $\mathcal{PT}$  symmetry threshold breaking (EP). As it can be confirmed in Fig. 1.19(b)(inset (i)), before the breaking point, all frequencies are real, while they become complex after the transition point. However, at the EP, these eigenvalues coalesce. Remarkably, the authors characterized an unbreakable region for the negative capacitive coupling parameter i.e.,  $c < -0.5$ , where the EP cannot occurs, as the resistive coupling parameter  $\nu$  is set active (see Fig. 1.19(b)(inset (ii))).

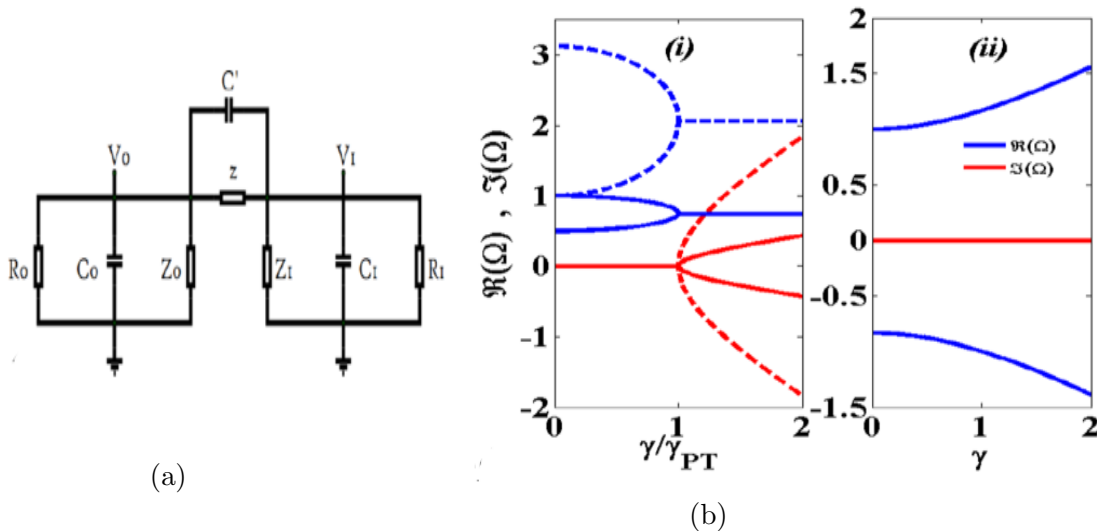


Figure 1.19: a) The ZRC dimer setup in which the gain and the loss cells are coupled by an imaginary resistance and a capacitor. b) Normal modes dynamics. Subset (i): in the breakable region,  $c = -0.1$ . In dash  $c = 2$ . Subset (ii) in the unbreakable region for  $c = -2$  ( $\nu = 0.75$ ). Figures are adapted from ref. [62] with the permission.

The combination of both a capacitor and an imaginary resistance coupling, then opens up to the various applications of the negative capacitor and resistors, in the characterization of the normal modes dynamical systems as well as in the steady and the transient states dynamic of the ZRC dimers. In addition, the dynamics [62] indicate that a system exhibits high frequencies propagation when operation is done before the thresholdless point (for which  $\gamma_{PT} = 0$ ) is reached and the transitionless regime indicates an

equilibrium point in the coupling for which the system turns to be conservative regardless the gain/loss values, and beyond which the gain/loss remarkably decays/amplifies wave. Finally, according to the authors, these results open avenues for innovative electronics architecture from integrated circuits to antenna arrays, thus allowing cutting edges to technological drawback.

## 1.3 Generalities on wave transport phenomena

### 1.3.1 Generalities on EIT and related phenomena

In recent years, advances in the theoretical understanding of quantum optics have led to the prospect of using quantum properties of light for the construction of quantum computers [138], the encryption of sensitive information [139], and ultra-sensitive measurements of fundamental parameters [140]. As consequence, the use of quantum physics for communication systems should require a use of quantum systems for building them. But as we know, quantum systems are extremely fragile, in that any disturbance or measurement process destroys the quantum state of the system. It then arise many questions: How can we use fragile quantum systems like photons for efficient quantum information processing? How do we process, store, and manipulate photons without disturbing them? In the quest for building a robust quantum optical system, a dramatic breakthrough in optical science in the past decade is the discovery of Electromagnetically Induced Transparency (EIT) [141–144]. EIT is a technique capable of drastically modifying a medium’s optical properties near an atomic resonance when an electromagnetic field is applied. As the name indicates, these properties include a transparency window at a normally highly absorbing resonance, but in addition to this, the dispersion properties of the medium are greatly enhanced. The observed effect is shown in Fig. 1.20. Since its discovery in 1989 by Harris et al., EIT has opened up for recent developments in “slowing” and “stopping” light [145–151]. It has been envisioned that slow and stopped light could be extremely important for optical communications, and particularly for quantum information processing [149, 152, 153]. As this progress has continued in classical and quantum optical technology, several proposals have sought to further exploit the EIT effect to control the relative properties of separate light pulses using multiple EIT systems [154, 155]. In particular, double EIT (DEIT), has been proposed to realize large optical nonlinearities between single photons [143], all optical light buffering [156], and quantum logic gates for use in a quantum computer. Let us understand the physics behind electromagnetically induced transparency. In the following, we discuss the importance of the quantum dark states and their consequences on slow and stopped light phenomena in atom clouds. This would provide a good framework for us to develop the idea of EIT in classical analog systems as electronic circuits.

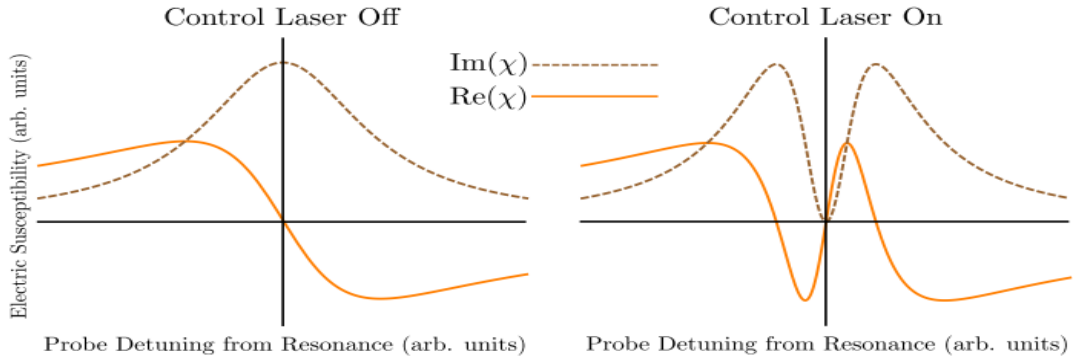


Figure 1.20: Simple EIT Plot. Here we are plotting the real and imaginary components of the complex linear susceptibility. The imaginary component corresponds to absorption - on the left we see a typical Lorentzian absorption peak while the control laser is inactive. When the control laser is applied, the absorption peak splits revealing a transparency at what was the maximal absorption. The real components appear in the dispersion relation, relating wave speed to frequency.

### 1.3.1.1 Basic formalism

Consider an atom interacting with two laser fields that are resonant to the transition between two separate states,  $|1\rangle$  and  $|2\rangle$ , to a common third state  $|3\rangle$ . Such a system is referred to as a three level atom. There are three possible types of three level atom that can demonstrate EIT as shown in Fig.1.21: the lambda ( $\Lambda$ )-type (left), the V-type (middle) and the ladder-type (right) system. In particular, for the  $\Lambda$  configuration, the state  $|3\rangle$  has the highest energy.

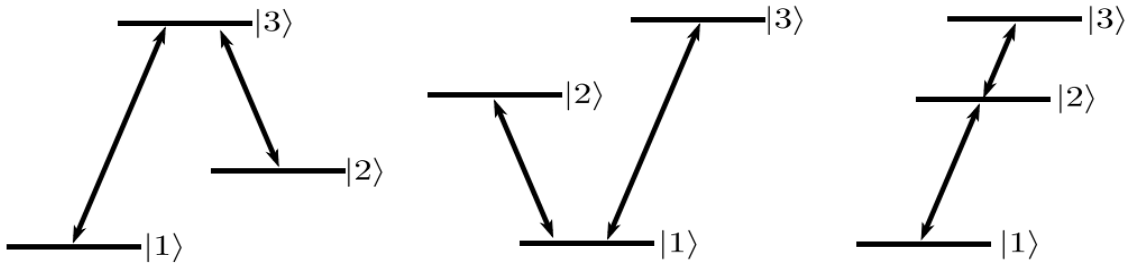


Figure 1.21: All three level structures capable of demonstrating EIT, namely,  $\Lambda$ -type (left), V-type (middle), and ladder type (right).

For a theoretical description of EIT, we refer ourselves to [157].

Let us start with a three level  $\Lambda$ -atomic system with all the atoms in the ground state  $|1\rangle$ , as shown in Fig. 1.22. The typical  $\Lambda$  system has two lower states,  $|1\rangle$  and  $|2\rangle$ . Each of the two meta-stable states  $|1\rangle$  and  $|2\rangle$  can be resonantly excited to the excited  $|3\rangle$  level at the *probe* and *control* frequency. Hence, depending on the initial state of the atom system, the atoms can absorb the *probe* and *control* frequencies coherently that give rise to Rabi oscillations [158] in  $(|1\rangle, |3\rangle)$  and  $(|2\rangle, |3\rangle)$  subspace. An interesting question that arises, in this system, is if the absorption of light can be inhibited? This is a non-trivial question,

and a solution to the question requires examination of quantum mechanical interference phenomena that can be better understood through dark states.

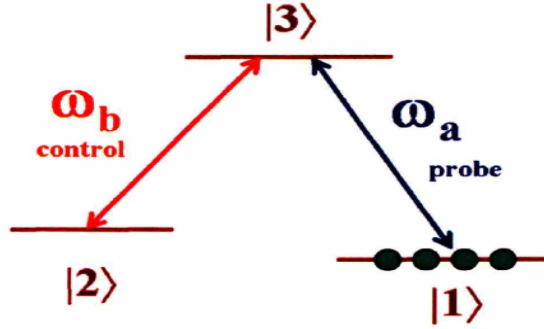


Figure 1.22: A three level-atomic system with all the atoms in the ground state  $|1\rangle$ . The system has two possible transitions, denoted as  $\omega_a$  or the *probe* and  $\omega_b$  or the *control* frequency.

### a) Dark State Phenomena

It is obvious to see that a three level EIT system can be transparent to the control frequency by having all the atoms in the  $|1\rangle$  state. As shown in Fig. 1.22, all the atoms are in state  $|1\rangle$ . This system is transparent to the control frequency as there are no atoms in state  $|2\rangle$  to absorb the control frequency. The state  $|1\rangle$  is known as the dark state of the system,  $|\Psi_{dark}\rangle = |1\rangle$  and is transparent to  $\omega_b$ . Similarly transferring all the atoms to the state  $|2\rangle$  makes the system transparent to the probe frequency, hence the dark state of the system is  $|\Psi_{dark}\rangle = |2\rangle$ . **How can this system be made transparent to both the control and probe frequencies at the same time?** A solution to this is the heart of quantum interference phenomena.

### b) Quantum Interference Pathways

The equations in this section are referenced from [157]. As it is well known in quantum mechanics, the phase of any quantum system plays a crucial role in many interesting effects like Ramsey interferometry [159], Aharonov Bohm [160] and interference based phenomena [161]. EIT is another interference phenomena, like these effects, where the relative phase of different levels of the quantum system can cause interference in such a manner leading to complete transparency to both the probe and control frequencies. Let us understand this effect mathematically and also intuitively.

Consider the state which is a superposition of  $|1\rangle$  and  $|2\rangle$ , known as a dark EIT state, that is transparent to both the probe and control frequencies, as shown Fig. 1.23. The dark EIT state can be written as,

$$|\Psi_{dark}\rangle = \frac{\Omega_{23}|1\rangle - \Omega_{13}|2\rangle}{\sqrt{\Omega_{13}^2 + \Omega_{23}^2}}, \quad (1.43)$$

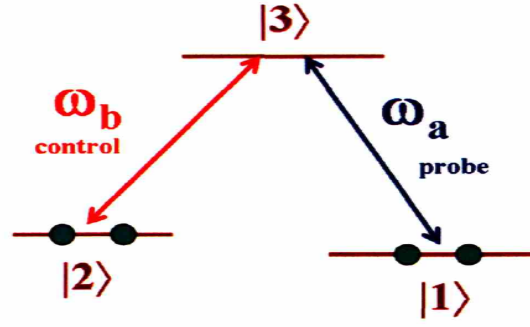


Figure 1.23: A example of a dark state that is a superposition of  $|1\rangle$  and  $|2\rangle$ . The probe and control frequency excitation interfere destructively at level  $|3\rangle$ , thereby inhibiting absorption of radiation. The system continues to be in the superposition state, hence being transparent to both the probe and control frequencies.

where,  $\Omega_{pq}$  are the Rabi frequencies for a given  $|p\rangle \rightarrow |q\rangle$  transition. To understand why this state is transparent to the probe and control frequencies, let us look at the system light interaction. The crucial point for EIT is that the presence of the probe and control frequencies changes the total Hamiltonian, such that an interaction Hamiltonian  $\mathcal{H}_{int}$  describing the interaction between the atom and the incoming light has to be added to the mere atomic Hamiltonian  $\mathcal{H}_{syst}$ :

$$\mathcal{H} = \mathcal{H}_{syst} + \mathcal{H}_{int}. \quad (1.44)$$

The system Hamiltonian can be written in the  $(|1\rangle, |2\rangle, |3\rangle)$  basis,

$$\mathcal{H}_{syst} = \hbar \begin{pmatrix} \omega_1 & 0 & 0 \\ 0 & \omega_2 & 0 \\ 0 & 0 & \omega_3 \end{pmatrix}, \quad (1.45)$$

where,  $\hbar\omega_p$  is the energy of the  $|p\rangle$  state.

The interaction Hamiltonian of the light can be written as:

$$\mathcal{H}_{int} = \begin{pmatrix} 0 & 0 & \Omega_{13}^* \cos \omega_{13}t \\ 0 & 0 & \Omega_{23}^* \cos \omega_{23}t \\ \Omega_{13} \cos \omega_{13}t & \Omega_{23} \cos \omega_{23}t & 0 \end{pmatrix}. \quad (1.46)$$

Here,  $\Omega_{pq} \cos \omega_{pq}t$  represents the excitation  $|p\rangle \rightarrow |q\rangle$  transition, with amplitude  $\Omega_{pq}$  and frequency given by  $\omega_{pq} = \omega_p - \omega_q$ . It is useful at this point to go into an interaction frame, with respect to the natural Hamiltonian  $\mathcal{H}_{syst}$ . The system-light interaction in the interaction frame is given by,



$$\begin{aligned}\mathcal{H}_{\text{int}} &= e^{\frac{i}{\hbar}\mathcal{H}_{\text{sys}}t}\mathcal{H}_{\text{pert}}e^{-\frac{i}{\hbar}\mathcal{H}_{\text{sys}}t} \\ &= \frac{\hbar}{2} \begin{pmatrix} 0 & 0 & \Omega_{13}^*(1 + e^{-2j\omega_{13}t}) \\ 0 & 0 & \Omega_{23}^*(1 + e^{-2j\omega_{23}t}) \\ \Omega_{13}(1 + e^{-2j\omega_{13}t}) & \Omega_{23}(1 + e^{-2j\omega_{23}t}) & 0 \end{pmatrix}\end{aligned}\quad (1.47)$$

In a rotating wave approximation (RWA), we can throw away the terms containing frequencies that are twice  $\omega_{13}$  and  $\omega_{23}$  respectively. This is valid as these fast oscillations average out to zero. Re-written the interaction Hamiltonian in the the rotating wave approximation (RWA) [158] leads:

$$\mathcal{H}_{\text{int}}^{(RWA)} = \frac{\hbar}{2} \begin{pmatrix} 0 & 0 & \Omega_{13}^* \\ 0 & 0 & \Omega_{23}^* \\ \Omega_{13} & \Omega_{23} & 0 \end{pmatrix}, \quad (1.48)$$

Diagonalizing this Hamiltonian gives us an eigenstate  $\alpha|1\rangle - \beta|2\rangle$ , where  $\alpha = \frac{\Omega_{23}}{\sqrt{\Omega_{13}^2 + \Omega_{23}^2}}$ ,  $\beta = \frac{\Omega_{13}}{\sqrt{\Omega_{13}^2 + \Omega_{23}^2}}$ , with eigenvalue equal to zero. A zero eigenvalue state means that the action of the Hamiltonian on the dark state,  $|\Psi_{\text{dark}}\rangle$ , leaves the quantum state undisturbed, hence transparency to both the probe and control frequencies. One can also understand this phenomenon intuitively as follows - the phase arriving at  $|3\rangle$  due to both the probe and control frequency excitation are opposite in sign. This causes the relative phase between  $|1\rangle$  and  $|2\rangle$  to be opposite in sign. Hence, resulting to destructive interference at level  $|3\rangle$ . This leaves the system unchanged, thus inhibiting any excitation to  $|3\rangle$  or equivalently transparency to both the probe and control frequencies is achieved at the same time. The two electromagnetic fields (probe and control) then propagate through the atom cloud without absorption. This is the heart of slow and stopped light, where ultra-slow light propagation due to EIT-based refractive-index modifications in atomic clouds has been observed [145–147].

### c) Slow and Stopped Light

The equations in this section are referenced from [157]. The concept of slow and stopped light arises due to EIT-based modification of the refractive index of atom clouds. It is often mistaken for what is being slowed in context of "slow" light. There are two different propagation speeds of light, one is the phase velocity and the other group velocity. The phase velocity is the speed at which each frequency component of a light pulse travels. This is typically close to the value,  $c = 3 \times 10^8 \text{m/s}$ , while the group velocity is the speed with which the maximum of a many frequency component envelope of a light pulse moves. The phase velocity is related to the refractive index as,

$$v_{ph} = \frac{c}{n}, \quad (1.49)$$

where  $n$  is the refractive index of the medium of propagation. The group velocity is associated with the dispersion of the refractive index, that is the variation of  $n(\omega)$  as a function of frequency  $\omega$  as,

$$v_g = \frac{c}{n + \omega_p \frac{dn}{d\omega_p}}, \quad (1.50)$$

where  $p$  is the probe. It is clear from this equation that when  $\frac{dn}{d\omega_p}$  becomes large,  $d\omega_p \ll 1$ . The group velocity tends to zero,  $v_g \rightarrow 0$ . In the atomic EIT, it turns out that EIT occurs in a narrow transparency window which also creates a steep variation of  $n(\omega)$  with frequency [142, 145, 146, 162]. Hence, the group velocity of light is reduced dramatically. During this process, a fraction of the photons corresponding to the probe signal are converted into a spin-wave via a two-photon (probe and control) process that maps the probe into a superposition of  $|1\rangle$  and  $|2\rangle$  or the dark EIT state. One can dramatically reduce the group velocity to zero, thereby "stopping" light, by turning off the control beam once the pulse with the probe frequency enters the EIT medium. When this happens, the probe is completely mapped onto the long lived states,  $|1\rangle$  and  $|2\rangle$ . This stopped light is then stored as long as the decoherence time of the ground states, or until the control beam is turned back on [149, 162]. These remarkable results can have enormous implications for quantum information processing [145, 146].

### 1.3.1.2 Classical analogs of Electromagnetically Induced Transparency

Recently, much attention has been paid to the study of the classical analogs of three-level atomic EIT in various systems, such as coupled resonators [58, 163], mechanical systems and electric circuits [59, 164, 165], optomechanic [166, 167], photonics crystals [168], plasmonic structures [169–172], metamaterial [173–175] and so on. Particularly, the electric analog of EIT [59] has attracted growing interest as, this analog helps to understand some elementary aspects of the underlying physics. Furthermore, such a model can be used as an introductory one when introducing coherent systems to beginners and laymen. In the scope of this thesis, we review in the following some of these electrical analog models.

The equations in this section are referenced from [59] where, the classical analog of EIT has been proposed in recent year by C. L. Garrido Alzar and co-workers. Even though EIT is inherently a quantum mechanical effect, the authors modelled it by a classical system formed of just two coupled harmonic oscillators subject to a harmonic driving force as presented in Fig.1.24(a). Interestingly, by using a well-known correspondence between a driven damped harmonic oscillator and an electrical circuit, they have successfully modelled a three level atom with a simple experiment system of two linearly coupled RLC circuits. This latter is much easier to realize since its offers the possibility to quickly interchange components to test various experimental configurations. Such a model is presented in Fig. 1.24(b). The circuit mesh consisting of the inductor  $L_1$  and

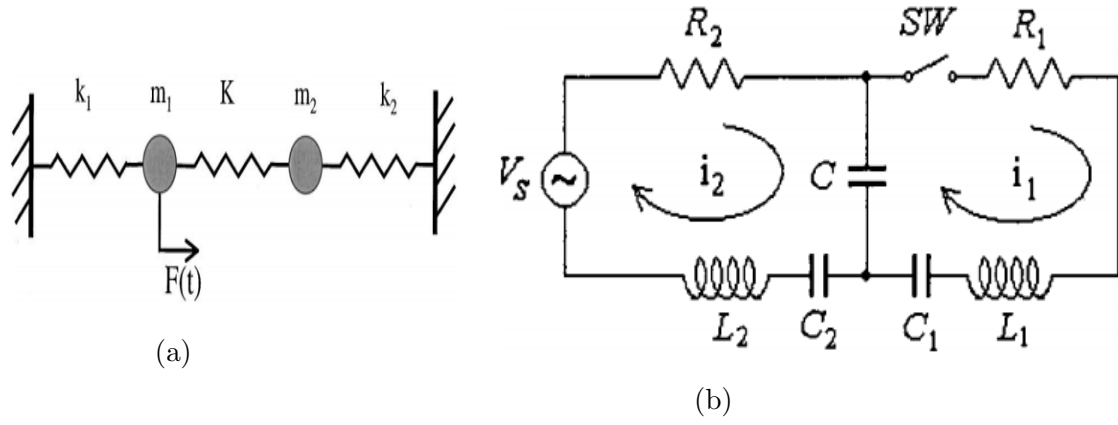


Figure 1.24: Classical analogs of EIT. a) The mechanical model. b) The electrical circuit model. Figures are adapted from ref. [59].

the capacitors  $C_1$  and  $C$  simulates the pumping oscillator, and the resistor  $R_1$  determines the losses associated with that oscillator. The atom is modeled using the resonant circuit formed by the inductor  $L_2$  and the capacitors  $C_2$  and  $C$ ; the resistor  $R_2$  represents the spontaneous radiative decay from the excited level. The capacitor  $C$ , belonging to both circuit meshes, models the coupling between the atom and the pumping field, and determines the Rabi frequency associated with the pumping transition. In this case, the probe field is simulated by the frequency-tunable voltage source  $V_S$ . The circuit mesh used to model the atom has only one resonance frequency representing the energy of the atomic excited level. That is, the probability of excitation of this circuit will be maximal when the applied harmonic force is on resonance. Because in this case there are two possible paths to accomplish this excitation, we are dealing with the analog of a three-level atom in the  $\Lambda$  configuration. Namely, the oscillator corresponding to the atom analog can be excited directly by the applied voltage  $V_S$  or by the coupling to the pumping oscillator. Hence, the induced transparency is investigated by analyzing the frequency dependence of the power  $P_2(V_S)$  transferred from the voltage source  $V_S$  to the resonant circuit  $R_2L_2C_{e2}$ ,  $P_2(\omega_S) = \Re(v_S I_2^*)$ , where  $v_S$  and  $I_2$  are, respectively, the complex representations of  $V_S$  and  $i_2(t)$ .

Setting the inductors constants ( $L_i = L$ ), the motion of the charges through a circuit can be described by Eq. 1.51:

$$\begin{cases} \ddot{q}_1(t) + \gamma_1 \dot{q}_1(t) + \omega_1^2 q_1(t) - \Omega_r^2 q_2(t) = 0, \\ \ddot{q}_2(t) + \gamma_2 \dot{q}_2(t) + \omega_2^2 q_2(t) - \Omega_r^2 q_1(t) = \frac{V_S}{L_2}. \end{cases} \quad (1.51)$$

Here  $\gamma_i = \frac{R_i}{L_i}$  ( $i = 1, 2$ );  $\omega_i^2 = 1/(L_i C_{ei})$ ;  $C_{ei} = C_i C / (C_i + C)$ ;  $\Omega_r^2 = 1/(L_2 C)$ .

Once the current  $i_2(t) = \dot{q}_2(t)$  is known, the power  $P_2(\omega_S)$  as a function of the frequency  $\omega_S$  of the applied voltage, when the switch SW in Fig. 1.24(b) is closed, is given by,

$$P_2(\omega_S) = \frac{P_{11}(\omega_S)}{P_{11}^2(\omega_S) + P_{12}^2(\omega_S)} |A_S|^2, \quad (1.52)$$

where

$$P_{11}(\omega_S) = R_2 + \frac{R_1/(\omega_S C)^2}{R_1^2 + (\omega_S L_1 - 1/(\omega_S C_{e1}))^2}, \quad (1.53)$$

$$P_{12}(\omega_S) = (\omega_S L_2 - 1/(\omega_S C_{e2})) - \frac{(1/(\omega_S C)^2)(\omega_S L_1 - 1/(\omega_S C_{e1}))}{R_1^2 + (\omega_S L_1 - 1/(\omega_S C_{e1}))^2}, \quad (1.54)$$

and  $A_S$  is the amplitude of the applied voltage. On the other hand, when the switch is opened, we have

$$P_2(\omega_S) = \frac{R_2}{R_2^2 + (\omega_S L_2 - 1/(\omega_S C_{e2}))^2} |A_S|^2. \quad (1.55)$$

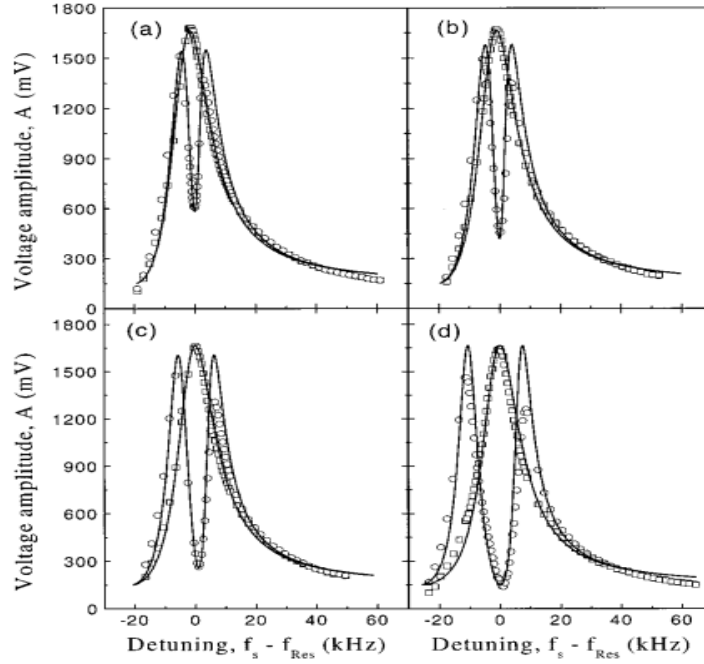


Figure 1.25: The power transferred to the circuit  $R_2 L_2 C_{e2}$  as a function of the frequency  $\omega_S$  for different values of the coupling capacitor  $C$ . The values of  $C$  are  $C = 0.196 \mu F$ , with resonance frequency  $f_{res} = \omega_2/2\pi = 20 kHz$ , (b)  $C = 0.150 \mu F$ ,  $f_{res} = 19.5 kHz$ , (c)  $C = 0.096 \mu F$ ,  $f_{res} = 19.5 kHz$ , (d)  $C = 0.050 \mu F$ ,  $f_{res} = 26.5 kHz$ . The open squares correspond to measurements made with the switch SW open, which is equivalent to turning the pump off. The open circles correspond to measurements made with the switch closed. The evolution from EIT to the Autler–Townes regime is clearly observed. Figures are taken from [59].

From Eq. 1.52, the real part of  $P_2(\omega_S)$  is plotted against the detuned frequency, corresponding to four values of the coupling capacitor  $C$ , as illustrated in Fig. 1.25. Clearly from the graphs, in the open switch configuration (no pumping), a maximum coupling of electrical power from the voltage source  $V_S$  to the resonant circuit  $R_2 L_2 C_{e2}$  at the resonant frequency (zero detuning). However, when the switch is closed, that is, when the pumping circuit (pumping force) is acting on the resonant circuit  $R_2 L_2 C_{e2}$ , the absorption of the electrical power of the voltage source at zero detuning is depressed. This fact corresponds to the transparent condition and is more pronounced when the value of

the coupling capacitor is reduced, corresponding to an increment of the Rabi frequency of the pumping field in EIT in atomic systems. Here, the observed transparency can be interpreted as a destructive interference between the power given by the voltage source to the resonant circuit  $R_2L_2C_{e2}$ , and the power transferred to the same circuit from the other oscillator representing the pumping force. For the minimum value of  $C$  used in the experiment (see Fig. 1.25(d)), we observe two absorption peaks, which are the classical analog of the Autler–Townes effect and correspond to the splitting of the normal modes.

### 1.3.1.3 Classical analog of double EIT

Besides the single EIT phenomenon in three-level atomic systems, double electromagnetic induced transparency (DEIT) may occur when a four-level atomic system with a tripod-type configuration is exposed to three laser fields that drive three different transitions with one common excited level [176–180]. In such settings, a single control laser field can modify the absorption and dispersion properties of the other two probe laser fields and produce large Kerr effects, especially cross phase modulations. Such system has also been used to engineer coherent superposition of two ground states, etc., very promising for applications in quantum information processing and quantum computing. In fact, systems displaying multiple EIT could be useful in the bifurcation of quantum information in multiple channels temporarily, which can then be used in multiplexing required in certain quantum information protocols. The release of stored information from multiple channels could be separately controlled by manipulating the group velocity of individual channels (via their control fields) in such systems.

Inspired by the recent works on classical analogs of EIT [59], more recently DEIT has been demonstrated in four-level systems, using two classical analogies : mass-spring systems (Fig. 1.25(a)) and RLC circuits (Fig. 1.25(b)) [164].

The electric circuit showing double EIT behaviour as illustrated in Fig. 1.25(b), is made up of three loops of LRC circuits. The resistance, inductance and capacitance of the loops were represented by  $R_i$ ,  $L_i$  and  $C_i$ , respectively ( $i = 1, 2, 3$ ). The first loop with resistance  $R_1$ , inductance  $L_1$ , and capacitances  $C_1$  and  $C/2$  represents the atom. Hence, by applying Kirchhoff’s second law and using a few step of algebra, the electric power dissipated by the resistive ( $P_R$ ) and the energy stored by the reactance ( $P_X$ ) parts of the circuit are giving by the following expressions:

$$P_R = \frac{A|V_S|^2}{A^2 + B^2} \text{ and } P_X = \frac{B|V_S|^2}{A^2 + B^2}, \quad (1.56)$$

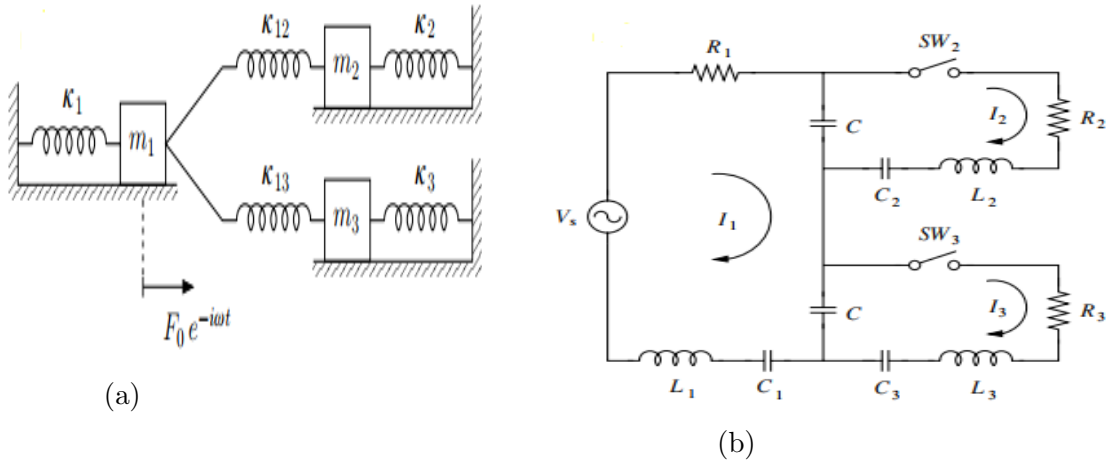


Figure 1.26: Classical analog of DEIT. a) The mechanical model. b) The electrical circuit model. Figures are adapted from ref. [164].

where  $A$  and  $B$  are given by:

$$\begin{aligned}
 A &\equiv R_1 + \frac{R_2 X_C^2}{R_2^2 + [X_{L_2} - (X_C + X_{C_2})]^2} + \frac{R_3 X_C^2}{R_3^2 + [X_{L_3} - (X_C + X_{C_3})]^2} \\
 B &\equiv X_{L_1} - (2X_C + X_{C_1}) - \frac{X_C^2 [X_{L_2} - (X_C + X_{C_2})]}{R_2^2 + [X_{L_2} - (X_C + X_{C_2})]^2} - \frac{X_C^2 [X_{L_3} - (X_C + X_{C_3})]}{R_3^2 + [X_{L_3} - (X_C + X_{C_3})]^2} .
 \end{aligned}
 \tag{1.57}$$

with  $X_C = 1/(\omega C)$ ,  $X_{C_i} = 1/(\omega C_i)$  and  $X_{L_i} = \omega L_i$ ,  $i = 1, 2, 3$ . In Fig. 1.27,  $P_R$  and  $P_X$  are plotted as a function of the frequency detuning  $\delta = \omega - \omega_R$  for different initial conditions of the parameters  $R$ ,  $L$  and  $C$ , where the effects of the coupling and pumping frequency detunings, in the double EIT scenario, are shown when parameters  $L_2$  and  $L_3$  took on different values. Fig. 1.27(a) shows that, at exact resonance conditions for both the coupling and pumping fields with the probe field ( $\Delta_c = \Delta_r = 0$ ), there was only a single dip in the curve (like single EIT) which are separated to form two EIT dips in the absorption line occurred when  $L_3$  was increased Fig. 1.27(b). The separation of the two EIT dips is shown more clearly in Fig. 1.27(c) for a different set of parameters  $L_2$  and  $L_3$ . Figure 1.27(d) shows that the dips shifted to the right for yet another different set of parameters  $L_2$  and  $L_3$ . All results were also reproduced experimentally. According to the authors [164], the interest on these experiments and the final purpose of the work is to help undergraduate students to develop a better understanding of single and double EIT, as well as to improve their experimental skills. These experiments are easy to adopt in any undergraduate physics laboratory and can be used to approach other compelling topics such as quantum coherence and quantum interference, which occur in atomic systems,

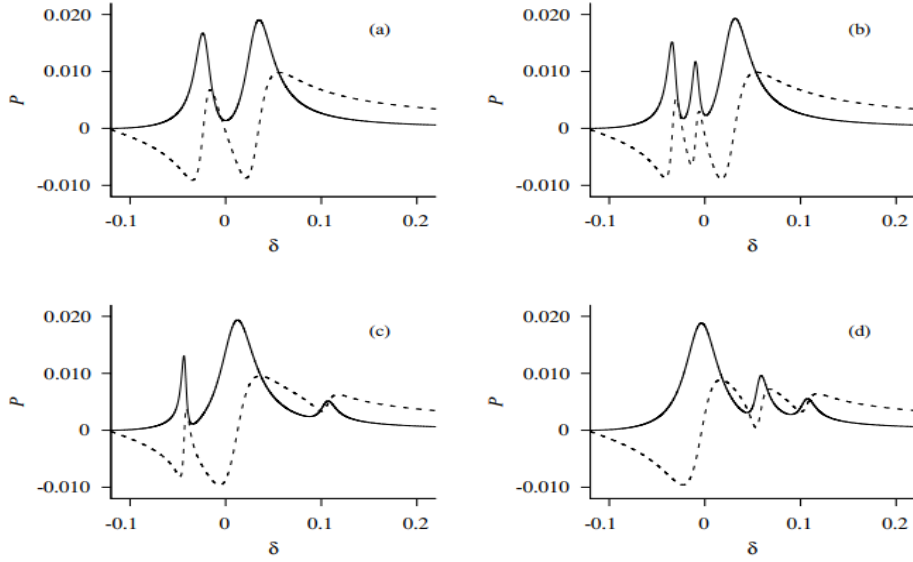


Figure 1.27: Power transferred to the  $R_1L_1C_{e1}$  circuit as a function of the detuning  $\delta = \omega - \omega_R$ . This detuning was defined as the difference between the driving field frequency  $\omega$  and the resonance frequency of the circuit  $\omega_R$ . The parameters used were  $R_2 = R_3 = 5.0 \Omega$ ,  $R_1 = 50 \Omega$ ,  $C_1 = C_2 = C_3 = 0.1 \mu F$ ,  $C = 0.2 \mu F$  and  $L_1 = 0.0010 H$ . For plots (a)  $L_2 = L_3 = 0.0010 H$ ; (b)  $L_2 = 0.0010 H$  and  $L_3 = 0.0015 H$ ; (c)  $L_2 = 0.0020 H$  and  $L_3 = 0.0003 H$ ; (d)  $L_2 = 0.0005 H$  and  $L_3 = 0.0003 H$ . The solid line represents  $P_R$ , whereas the dashed line represents  $P_X$ .  $P$  is given in arbitrary units. Figures are adapted from ref. [164].

and are particularly important in observing phenomena such as group velocity reduction of light, superconductivity and superfluidity, and quantum information processing.

### 1.3.1.4 Electromagnetically Induced Absorption (EIA)

As we seen, one fascinating aspect of the coherent interaction between electromagnetic field and atom is quantum interference of probability amplitudes between transition channels within an atomic system that modifies optical response of the atomic medium. The interference leads to either an enhancement (constructive interference) or a complete cancellation (destructive interference) of the total transition probability. The cancellation of total transition probability leads to an elimination of resonant absorption which is called the EIT, whereas the remaining case leads to an enhancement of absorption. This latter considered as the experimental counterpart of the electromagnetically induced transparency is called as electromagnetically induced absorption (EIA) [182]. Similarly to the EIT case, one can say that the system has entered into a bright state which is related to a constructive interference between different quantum paths for the probe laser light interacting with the atom [182]. EIA was firstly observed in a closed transition within the  $D_2$  line of Rubidium [183]. Shortly after its discovery, an interpretation of EIA was developed for a four level scheme [184]. This interpretation explained EIA as an effect generated through spontaneous transfer of coherence. Figure 1.28 gives the evolution of

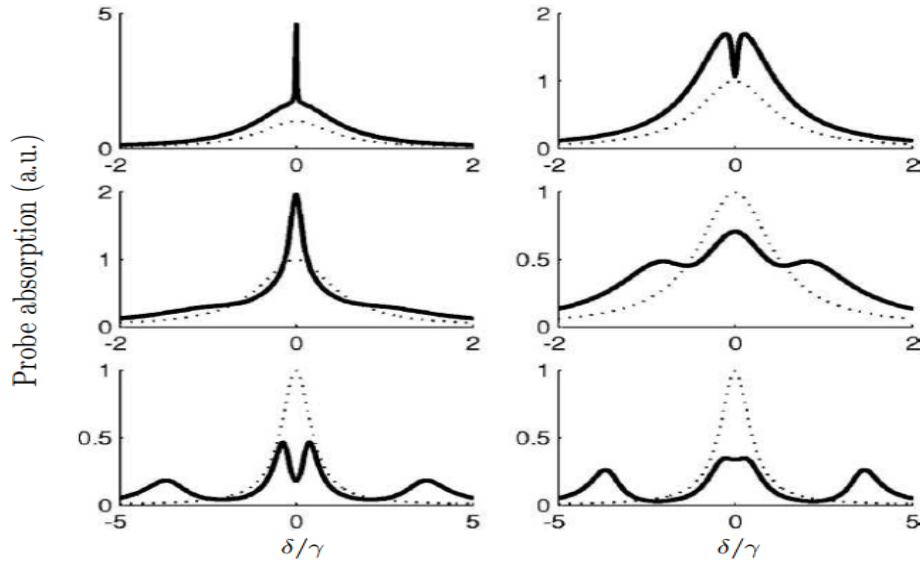


Figure 1.28: Probe absorption in an N-system with (left) and without (right) transfert of coherence for various coupling laser intensities. The dotted lines correspond to the one-photon lorentzian probe absorption in the absorption of coupling laser. the coupling intensity increases from top bottom (as reported in [181]).

the absorption spectra of the probe laser in an N-system configuration. The right column represents the absorption in the absence of transfer of coherence. It appears that in the absence of transfert of coherence, at least for low coupling intensities, the probe laser would experience a reduced absorption at the two-photon resonance. When the transfert of coherence is introduced, the spectrum of the probe laser at the two-photon resonance condition shows an enhanced absorption. For increasing coupling coupling laser intensity, the EIA spectra change and, quite interestingly, the probe laser switches from enhanced absorption to enhanced transparency.

## 1.3.2 Generalities on Anderson Localization

### 1.3.2.1 Theoretical background

The wave propagation in periodic and disordered crystal networks is at the foundation of modern condensed-matter physics. Thus, the problem of multiple scattering and localization of waves has been among the most difficult and fascinating topics in the study of wave propagation in disordered systems. An ubiquitous feature of wave propagation in such systems is the spatial confinement of waves called Anderson localization (AL) named so, after Phillip W. Anderson who first theoretically predicted the absence of diffusion in certain random electronic lattices [185]. In his seminal paper, published in 1958, Anderson conjectured that beyond a certain level of disorder, localized electronic states are formed, diffusion process stops, and a rapid phase transition from metals to insulators occurs. He had been confronted with peculiar experimental results indicating anomalously long spin relaxation times in heavily doped semiconductors at Bell Laboratories [186]. This



observation could be explained by assuming localized electrons but this revolutionary picture was in contradiction to the commonly accepted diffusive model of the electrons in the disordered lattices at the time. The study of the conductance of electrons is a very old problem in condensed matter physics. In particular, according to the classical Drude description of conductance in a metal, one imagines that electrons (or more generally the charge carriers) collide with the positive ions in the metal, thus following a diffusive motion. This theory is at the origin of the well known Ohm's law, where clearly the conductivity becomes proportional to the mean free path of the electron inside the metal. However, experimental observations made clear that the mean free path inside a metal is a couple of order of magnitude bigger than the lattice spacing and only with the development of the quantum theory it was possible to provide an explanation to this fact: in a regular lattice, electrons behave as waves and coherently diffract on the ions. The resistivity is therefore appearing only because of the impurities in the lattice. In this way the Drude theory becomes again reliable, but the electron is envisaged as zigzagging between impurities. It follows that the more are the impurities, the shorter will be the mean free path and the conductivity. With this picture in mind, Anderson tried to answer the question: **what happens if the density of impurity is increased?** Consistently with the known experimental results, he was able to provide convincing arguments, showing that the increasing of lattice disorder would not only keep decreasing the mean free path and the conductance, but beyond a critical amount of impurity scattering the diffusive, zigzag motion of the electron is not just reduced, but can come to a complete halt. The electron becomes trapped and the conductivity vanishes. Later in 1977, Philip Anderson, John van Vleck (his thesis advisor) and Nevil Mott shared the Nobel Prize in physics "for their fundamental theoretical investigations of the electronic structure of magnetic and disordered systems".

Even though Anderson proposed his idea for electronic lattices, the nature of the localization is the interference wave. Therefore it is not specific to a particular wave. In this sense, AL can be qualified as a universal phenomenon. As a matter of fact, in recent years a very large number of works concerned localization of both classical and quantum waves. In the literature, quantum waves usually refer to electrons, phonons or cold atoms (matter waves), whereas classical waves refer to light, sound, microwaves or elastic waves. With quantum waves, the wave nature is of quantum origin and propagation is based on the Schrödinger equation, whereas with classical waves, laws of classical wave physics govern wave propagation. The first experimental achievements related to Anderson localization date back to 1987, with, notably, the measurements of the conductivity at low temperatures demonstrating the Mott formula [187]. Since then, Anderson localisation is experimentally observed in microwaves [188], ultrasound [189, 190], light waves [191–194], quantum waves [195–197], cold atoms [198], and more recently in the field of electronics [60, 199–213].

### 1.3.2.2 Anderson Localization in non-periodic electrical transmission lines

In the last decades, the concept of AL has been extended in the framework of electronics, where the localization properties of the electric current function  $I(\omega)$  in non-periodic dual, direct and mixed ETLs, have been intensively studied by Edmundo Lazo and co-workers [199–211]. In order to simulate disorder in such systems, the electric components have been distributed in a variety of forms including aperiodic, incommensurate, and long-range correlated sequences. The localization properties of the TLs were measured using typical diagnostic tools of quantum mechanics like normalized localization length, transmission coefficient, average overlap amplitude, etc. As a result, it has been demonstrated that the localization properties of the classic ETLs are similar to the one-dimensional tight-binding quantum model, but also features some differences. In the following, we present some of important results of these works which have been summarized in the review paper by the author [212]. We describe dual, direct and mixed classic ETLs and equations governing them, followed by the description of a method to obtain the electric current and diagnostic tools used to study localization behavior in literature with some of the results. Then, we end the sub-section by presenting the state of art of AL in the context of non-Hermitian electric systems [60, 213].

#### a) Dual and Direct Electric Transmission Lines

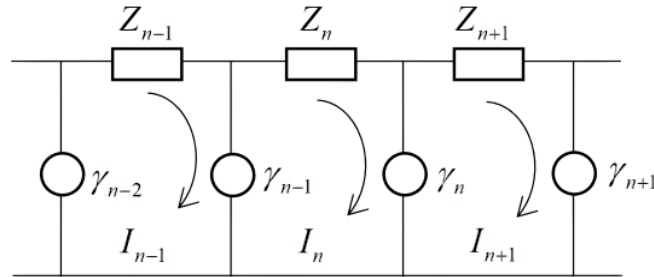


Figure 1.29: A partial view of an ideal transmission line.  $Z_n$  ( $\gamma_n$ ) represent horizontal (vertical) impedances, respectively. For direct TL,  $Z_n$  is associated with inductances and  $\gamma_n$  with capacitances. Conversely, for dual TL,  $Z_n$  is associated with capacitances and  $\gamma_n$  with inductances. The arrows indicate the direction of the electric current in each cell. We arbitrarily consider the initial flow from the left, because we are using open boundary conditions. Figure is taken from ref. [212].

Figure 1.29 shows a segment of a transmission line (dual or direct), with horizontal impedances denoted by  $Z_n$  and vertical impedances labeled  $\gamma_n$ . For direct TL the impedances are  $Z_n = (j\omega L_n)$  and  $\gamma_n = (j\omega C_n)^{-1}$ , but for dual TL we have  $Z_n = (j\omega C_n)^{-1}$  and  $\gamma_n = (j\omega L_n)$ . Here,  $C_n$  and  $L_n$  denote the capacitance and inductance values in cell  $n$ , respectively. To study the localization properties of the ETLs, capacitances  $C_n$ , inductances  $L_n$ , or both are distributed using aperiodic sequences. Using Kirchoff's laws, the electric currents circulating in the  $(n - 1)$ th,  $n$ th and  $(n + 1)$  th cells of the TL can be

described by a following generic linear relationship.

$$D_n I_n - B_{n-1} I_{n-1} - B_n I_{n+1} = 0, \quad (1.58)$$

where  $D_n = (B_{n-1} + B_n - A_n)$ ;  $A_n = \omega^2 L_n$  and  $B_n = C_n^{-1}$  for direct TL, but for dual TL we have  $A_n = (\omega^2 C_n)^{-1}$  and  $B_n = L_n$ .

Writting Eq. (1.58) in the form  $I_{n+1} = (\frac{D_n}{B_n})I_n - (\frac{B_{n-1}}{B_n})I_{n-1}$  and considering the trivial equation  $I_n = I_n$ , we obtain a map in the plane  $(I_n, I_{n+1})$

$$\begin{pmatrix} I_{n+1} \\ I_n \end{pmatrix} = M_n \begin{pmatrix} I_n \\ I_{n-1} \end{pmatrix}, \quad (1.59)$$

where matrix  $M_n$  is given by  $M_n = \begin{pmatrix} \frac{D_n}{B_n} & -\frac{B_{n-1}}{B_n} \\ 1 & 0 \end{pmatrix}$ .

Hence, the eigenvalues  $\lambda_n$  of the  $M_n$  matrix can be written in the following

$$\lambda_n = \frac{D_n}{2B_n} \pm \sqrt{\frac{B_{n-1}}{B_n} - \left(\frac{D_n}{2B_n}\right)^2}. \quad (1.60)$$

For a given frequency  $\omega$ , the map Eq. (1.59) is stable if the eigenvalues  $\lambda_n$  of the matrix  $M_n$  are complex numbers, which also implies that the trajectories of the map are bounded, which in turn means that the electric current  $I_n(\omega)$  is an extended function. Otherwise, the the trajectories of the map are unbounded and  $I_n(\omega)$  is a localized function. Consequently, the spectrum of allowed frequencies for direct and dual TL is given by general condition

$$\left[ \sqrt{L_n C_n} + \sqrt{L_{n-1} C_n} \right]^{-1} < \omega < \left[ \sqrt{L_n C_n} - \sqrt{L_{n-1} C_n} \right]^{-1}. \quad (1.61)$$

For pure direct TL with  $L_n = L_0$ ,  $C_n = C_0, \forall n$ , we find a band of frequencies, i.e.,  $0 < \omega < \frac{2}{\sqrt{L_0 C_0}}$ . Conversely, for pure dual TL with  $L_n = L_0$ ,  $C_n = C_0, \forall n$ , the typical band of frequencies is also found as  $\frac{1}{2\sqrt{L_0 C_0}} < \omega < \infty$ .

The mixed ETLs are formed by a basic unit of  $d = (p + q)$  cells consisting of a set of  $p$  successive direct cells followed by  $q$  successive dual cells. The  $N$  total number of cells in the mixed TL is given by  $N = dN_s$ , where  $N_s$  is the number of times the basic unit is repeated. Figure 1.30 shows a segment of a mixed TL with  $p = 2$ ,  $q = 3$  and  $d = 5$ . By applying Kirchoff's loop rules, equations describing mixed TLs can also be written in the same form as the generic Eq.(1.58) but now both coefficients  $D_n$  and  $B_n$  usually depend on the frequency  $\omega$ , the parameters  $p$ ,  $q$  and capacitances  $C_{n,x}$ ,  $C_{n,y}$ , and inductances  $L_{n,x}$ ,  $L_{n,y}$ , corresponding to direct and dual cells, respectively. As a consequence, mixed TL contain a richer parameter space to study the localization properties of the electric current function.

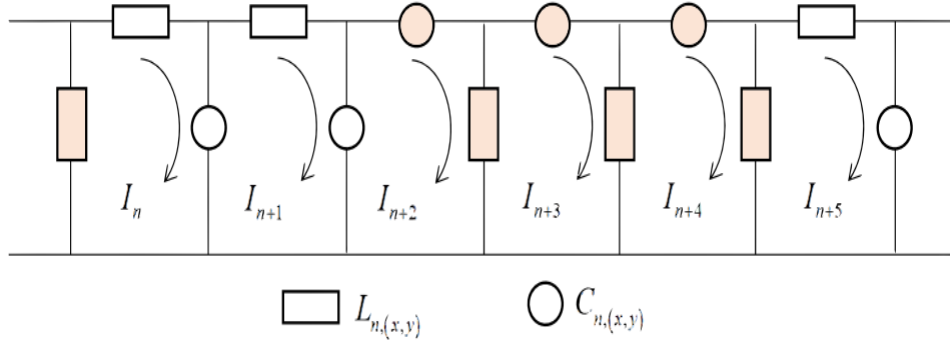


Figure 1.30: A segment of a mixed transmission line formed by  $p = 2$  direct cells and  $q = 3$  dual cells. The full system is formed by the repetition of the basic unit formed by  $d = (p + q)$  cells. Inductances are represented by rectangles and capacitances by circles. In addition, dual cells are marked with orange color-filled symbols. The arrows indicate the direction of the electric current in each cell. Figure is taken from ref. [212].

### b) Relation with the Tight-Binding Model

The generic Eq. (1.58) describing the relationship between three consecutive electric current amplitudes  $I_{n-1}(\omega)$ ,  $I_n(\omega)$  and  $I_{n+1}(\omega)$  in the classical ETL, has the same form that an equation describing a relationship between three consecutive amplitudes  $\phi_{n-1}(E)$ ,  $\phi_n(E)$  and  $\phi_{n+1}(E)$  of the wave function of the  $1\mathcal{D}$  dimensional tight-binding quantum model. This correspondence has allowed to test the effects of the disorder in  $1\mathcal{D}$  quantum systems using classical electrical circuits with random distribution of capacitances and inductances. Consequently, Eq. (1.58) can be mapped to the quantum  $1\mathcal{D}$  dimensional tight-binding model

$$(E - \varepsilon_n) \phi_n - V_{n-1} \phi_{n-1} - V_n \phi_{n+1} = 0, \quad (1.62)$$

where  $\varepsilon_n$  is the site energy,  $V_n$  the hopping between neighboring sites,  $E$  the eigenenergy, and  $\phi_n$  is the eigenfunction. Nonetheless, a correspondence between the tight-binding Eq. (1.62) and Eq. (1.58) exists. Applying the following transformation in the tight-binding Eq. (1.62) for example, we obtain the direct TL,

$$\begin{aligned} E &= -\omega^2, \quad \varepsilon_n = -L_n^{-1} (C_{n-1}^{-1} + C_n^{-1}), \quad \phi_n = I_n (L_n)^{-1/2} \\ V_{n-1} &= C_{n-1}^{-1} (L_{n-1} L_n)^{-1/2}, \quad V_n = C_n^{-1} (L_n L_{n+1})^{-1/2} \end{aligned} \quad (1.63)$$

### c) Methods to Obtain the Electric Current Function $I_n(\omega)$

The amplitudes  $I_n(\omega)$  of the electric current function, are obtained solving the generic Eq.(1.58). Two methods, the recurrence method and the Hamiltonian map method were presented in the review [212] to solve this equation.

- With the recurrence method, the electric current is calculated using an iterative process,

$$I_{n+1} = \left( \frac{\gamma_n}{B_n} \right) I_n, \quad \gamma_n = D_n - \frac{1}{\gamma_{n-1}} (B_{n-1})^2, \quad (1.64)$$

where  $2 \leq n \leq N$ . Iteration process start with  $\gamma_1 = D_1 = B_1 - A_1$  and the full set of  $\gamma_n$  values is obtained.

- The Hamiltonian map consists to write the amplitudes  $I_n$  as function of  $\Gamma_n$  and  $\theta_n$  in the following recurrence relation:

$$I_{n+1} = \Gamma_n \left( \frac{\sin \theta_{n+1}}{\sin \theta_n} \right) I_n, \quad (1.65)$$

where

$$\begin{cases} \tan \theta_{n+1} = \frac{\beta_n + \alpha_n \tan \theta_n}{1 - A_n \tan \theta_n}, \\ \Gamma_n^2 = (\alpha_n^2 + A_n^2) \sin^2 \theta_n + (\beta_n^2 + 1) \cos^2 \theta_n + (\alpha_n \beta_n - A_n) \sin 2\theta_n \end{cases}, \quad (1.66)$$

with  $\beta_n = \frac{1}{B_n}$  and  $\alpha_n = (1 - A_n \beta_n)$ .

#### d) Usual Diagnostic Tools

To study the localization of the disordered electric TL as a function of the frequency  $\omega$  and as a function of the kind and degree of disorder, the same tools used in the study of the localization behavior of quantum systems can be deployed: the Lyapunov exponent  $\lambda(\omega)$ , the normalized localization length  $\Lambda(\omega)$ , the participation number  $D(\omega)$ , the inverse participation ratio  $IPR(\omega)$ , the global density of states  $DOS(\omega)$  and the transmission coefficient  $T(\omega)$ , the Rényi entropies  $R_q(\omega)$  [214] and the moments  $\mu_q(\omega)$ . All localization tools are defined as a function of the normalized electric current amplitude  $I_n(\omega)$ , namely  $\sum_{n=1}^N |I_n(\omega)|^2 = 1$  as in the quantum case where the localization properties are measured using the amplitude of the normalized quantum wave function  $\phi_n(E)$ .

#### e) Disordered Electrical Transmission Lines

Here we present the results localization behavior of the electric current  $I(\omega)$  when the components are distributed following the **(1) aperiodic and incommensurate sequences**, and **(2) long-range correlated sequences**. The general results indicate that the band structure of non-periodic systems is determined by the type of TL (dual, direct or mixed) in which the disorder is introduced, and that the existence of discrete sets or extended state bands in the thermodynamic limit, it depends on the type of aperiodic disorder used to distribute the electrical components.

#### (1) Aperiodic Transmission Lines

##### ⇒ Generalized Fibonacci Sequence

A Fibonacci quasi-periodic sequence is given by substitution rule  $A \rightarrow A^m B^n$ ,  $B \rightarrow A$ , where  $m$  and  $n$  indicate the number of times a given letter,  $A$  or  $B$ , appears in the substitution rule, without considering the order in which these letters occur. For example,

for  $m = 1$  and  $n = 1$ , the corresponding Fibonacci sequence is the following

$$A \rightarrow AB \rightarrow ABA \rightarrow ABAAB \rightarrow ABAABABA \rightarrow \dots,$$

with the golden mean  $\sigma_{1,1} = \frac{1}{2}(1 + \sqrt{5})$  (see ref. [215] for more details). In ref. [201,210], dual and mixed transmission lines have been studied using a Fibonacci distribution of two different values of inductances  $L_A$  and  $L_B$ , namely  $L_A L_B L_A L_A L_B L_A L_B L_A L_A L_B L_A L_A L_B \dots$ . In dual TL when keeping constant the capacitances  $C_n = C_0, \forall n$ , the localization behavior of the Fibonacci quasi-periodic distribution of inductances  $L_n$  has been studied [201], analyzing the spectrum of the generalized Rényi entropies  $R_q(\omega)$  versus  $\omega$  and the spectrum of the inverse participation ratio  $N \times IPR(\omega)$  versus  $\omega$ .

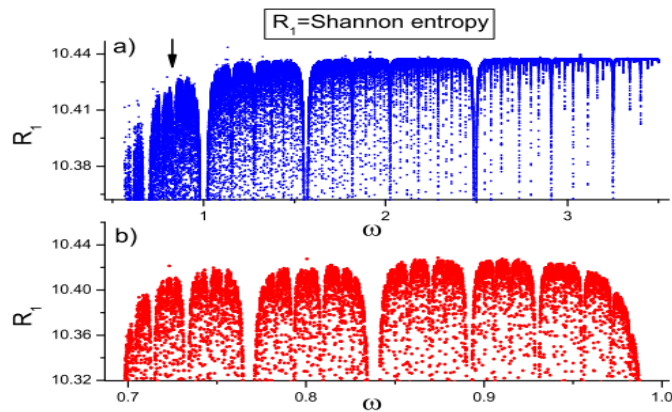


Figure 1.31: (a) Global sub-band structure of the Shannon entropy  $S(\omega) = R_1(\omega)$  versus  $\omega$  for the Fibonacci quasi-periodic distribution of inductances  $L_n$  discussed in ref. [201]. (b) Self-replication structure of the sub-band indicated by the vertical arrow in (a). Figure is taken from Ref. [212].

For each  $q$  value,  $R_q(\omega)$  and  $N \times IPR(\omega)$  show more than four global sub-bands. The spectrum shows the self-replication behavior, where each sub-band is divided into three sub-band until it is resolvable [201]. Inside each sub-band we find extended and localized states and gaps. As the system size  $N$  is growing, the number of gaps and localized states increases in such a way that the integrated density of states behaves in a fractal way. As a consequence, the total bandwidth goes to zero in the thermodynamic limit  $N \rightarrow \infty$ . The Shannon entropy  $S(\omega)$  corresponding to the Rényi entropy  $R_1(\omega)$  discussed in ref. [201] is presented in Fig. 1.31(a). The three sub-bands existing in the global sub-band indicated by the vertical arrow in Fig. 1.31(a) are also shown in Fig. 1.31(b). It is also noticed that the number of global sub-bands of the dual TL changes when the Fibonacci disorder is introduced in the  $q$  inductances of the dual cells of the mixed TL, while keeping constant the values of the other capacitances and inductances [210]. Thus, Lazo has concluded that for arbitrary values of  $p$  and  $q$  forming the mixed TL, the set of  $d = (p + q)$  bands accommodates the full spectrum generated by the Fibonacci distribution of inductances  $L_n$ . Inside each of the  $d$  band, the number of global sub-bands is always greater than or equal

to four, and the self replication process, new localized states and gaps appear repeatedly. Consequently, the integrated density of states has a fractal behavior and  $IDOS(\omega) \rightarrow 0$  in the thermodynamic limit [212].

### ⇒ Generalized Thue–Morse Sequence

The generalized Thue–Morse (TM) aperiodic sequence can be generated by means of the substitution rule  $A \rightarrow A^m B^n$ ,  $B \rightarrow B^n A^m$ . For the case  $m = 1$  and  $n = 1$ , we obtain the usual Thue–Morse sequence:  $A \rightarrow AB, B \rightarrow BA$ , namely

$$A \rightarrow AB \rightarrow ABBA \rightarrow ABBABAAB \rightarrow \dots,$$

The Thue–Morse and the  $m$ -tupling distribution of capacitances and inductances have been studied by [206–208]. For direct TL, two values of inductances  $L_A$  and  $L_B$  where distributed according to the  $m$ -tupling substitution rule  $L_A \rightarrow L_A L_B^{m-1}$ ,  $L_B \rightarrow L_B L_A^{m-1}$ ,  $m \geq 2$  keeping constant the capacitances [207, 208]. For  $m = 2$ , we obtain the usual Thue–Morse substitution rule  $L_A \rightarrow L_A L_B$ ,  $L_B \rightarrow L_B L_A$ .

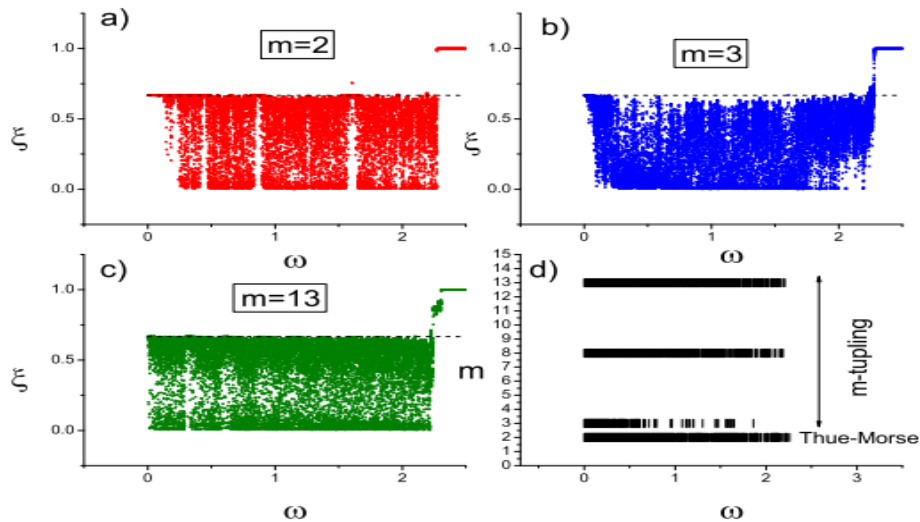


Figure 1.32:  $\xi(\omega)$  versus  $\omega$  for the  $m$ -tupling distribution of inductances  $L_n$  in the direct TL, for three values of  $m$ , namely  $m = \{2, 3, 13\}$  (a–c). (d)  $\Lambda(\omega)$  versus  $\omega$ . A short vertical bar indicates the existence of an extended state ( $\Lambda(\omega) \geq 1$ ). The number of extended states for  $m = 3$  is very small compared to the case  $m = 2$ . Conversely, for  $m \gg 3$  ( $m = 8$  and  $m = 13$ ), the number of extended states increases and becomes comparable to the  $m = 2$  case. Figure is taken from ref. [212].

It was shown that inside the  $m$ -tupling family, starting with  $m = 3$ , the number of extended states increases as the value of  $m$  increases, so that for  $m \gg 3$ , the allowed spectrum is similar to the spectrum of the case  $m = 2$  (Thue–Morse). In Fig. 1.32, the normalized participation number  $\xi(\omega)$  for three values of  $m$ , namely  $m = \{2, 3, 13\}$  (a) to (c). In Fig. 1.32(d), the spectrum of the extended states, namely the frequencies for which the normalized localization length  $\Lambda(\omega)$  meets the condition  $\Lambda(\omega) \geq 1$  is indicated with a short vertical bar. It is seen there that, the number of extended states for  $m = 3$

is small compared to the case  $m = 2$ . However, for the case  $m \gg 3$ , namely  $m = 8$  and  $m = 13$ , the number of extended states becomes comparable with case  $m = 2$ .

### ⇒ Incommensurate Sequences

The Aubry–André model has been used to distribute the inductances  $L_n$  in two different cases: **(i)** direct TL with constant capacitances  $C_n = C_0, \forall n$  [209] and **(ii)** mixed TLs with disorder only in the  $q$  inductances of the dual cells, keeping constant the value of all the other electrical components of the direct and dual cells [210].

In **case (i)**, the inductances  $L_n$  of the direct TL are distributed according to the Aubry–André sequence:

$$L_n = L_0 + b \cos(2\pi\beta n), \quad (1.67)$$

where  $L_0 = \text{const.}$  and  $b < L_0$ .

Fig. 1.33 shows the localization behavior of this classic electric model where the map  $(b, \omega)$  is shown for  $L_0 = 4.0$  and  $N = 7 \times 10^5$ . Each dot on the map indicates the existence of an extended state, because the normalized localization length fulfills condition  $\Lambda \geq 1$ . The spectrum exhibits four behaviors:

- For  $b \rightarrow 0$ , it is noted a single band of extended states that corresponds to the periodic case.
- For increasing values of  $b$ , i.e., for  $b \leq 1.9$ , we note three global sub-bands of extended states (with localized states and gaps) separated by two large gaps.
- For  $b > 1.9$  only two global sub-bands of extended states survive, which also contain localized states and gaps.
- Finally, for  $b$  close to  $b = L_0 = 4.0$ , there is only a small sub-band where almost all states are extended states, namely  $0 \leq \omega \leq 0.45$ .

In **case (ii)** for mixed TL, the inductances  $L_n$  of the  $q$  dual cells were distributed according to the Aubry–André sequence  $L_{n,y} = L_{0,y} + b \cos(2\pi\beta n)$ ,  $b < L_{0,y}$ , the influence of the  $b$  amplitude in the localization behavior is analyzed using the transmission coefficient  $T(\omega)$  for four values of  $b$ , namely  $b = \{0.3, 0.7, 1.1, 1.5\}$  for the case  $p = 2, q = 1$ . The plot is shown in Fig. 1.34 for  $L_{0,y} = 1.6$ . For example for  $b = 0.3$ , we find  $d = 3$  bands containing extended states, localized states and gaps. for increasing values of  $b$ , the number of extended states within each band decreases, and as a consequence both lateral bands begin to disappear.

## (2) Long-Range Correlated Disorder

The introduction of correlation in the disorder can trigger the appearance of a discrete set of extended states (short-range correlation) or bands of extended states (long-range correlation). The correlated disorder has been introduced in classic ETLs [199, 200, 202, 203, 211] and include continuous and discrete sequences. Indeed, in ref. [199], E. Lazo and E. Diez studied the behavior of the allowed and forbidden frequencies in disordered



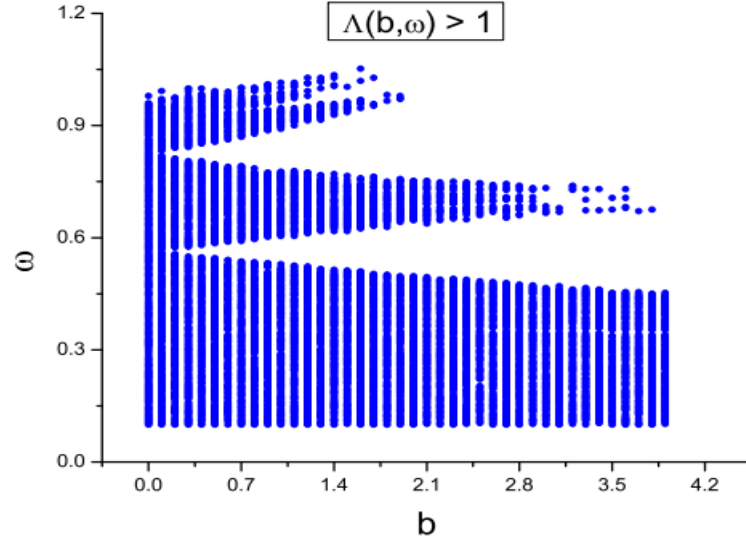


Figure 1.33: Map  $(b, \omega)$  for the Aubry–André distribution of inductances with  $L_0 = 4.0$ . Each point of the map indicates an extended state, because  $\Lambda \geq 1.0$ . For increasing values of the amplitude  $b$ , the number of sub-bands of extended states diminishes, and for  $b$  close to  $b = L_0$ , there is only a small sub-band where almost all states are extended states, namely  $0 \leq \omega \leq 0.45$ . Figure is taken from ref. [212].

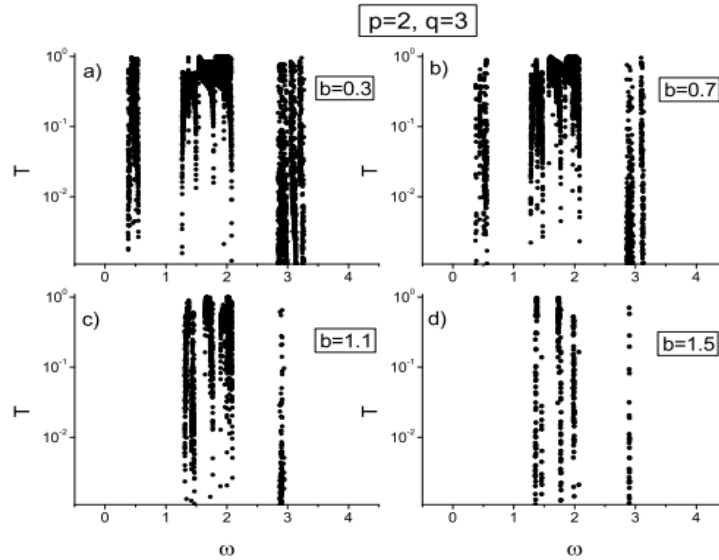


Figure 1.34: Transmission coefficient  $T(\omega)$  versus  $\omega$ , for mixed transmission line with  $p = 2$ ,  $q = 1$ , for (a)  $b = 0.3$ , (b)  $b = 0.7$ , (c)  $b = 1.1$  and (d)  $b = 1.5$ . For (a)  $b = 0.3$  we find  $d = (p + q) = 3$  bands containing extended states, localized states and gaps. For increasing values of  $b$ , the number of extended states within each band decreases. Therefore, for (c)  $b = 1.1$ , the leftmost band has already disappeared, and for (d)  $b = 1.5$ , the rightmost band is about to disappear. Figure is taken from ref. [212].

classical dual TL when the values of capacitances  $\{C_j\}$  are distributed according to a ternary model with long-range correlated disorder. They introduced the disorder from a random sequence with a power spectrum  $S(k) \propto k^{-(2\alpha-1)}$ , where  $\alpha \geq 0.5$  is the correlation

exponent. The asymmetric ternary map is generated using two map parameters  $b_1$  and  $b_2$ , which adjust the occupancy probability of each possible value of the capacitances  $C_j = \{C_A, C_B, C_C\}$ .

$$C_j = \begin{cases} C_A & \text{if } v_j < b_1 \\ C_C & \text{if } b_1 \leq v_j \leq b_2, \\ C_B & \text{if } v_j > b_2 \end{cases} \quad (1.68)$$

where, the sequence of  $\{v_k\}$  can be generated using  $v_k = u_k k^{-(2\alpha-1)/2}$ , a set of numbers  $\{u_k\}$  being uncorrelated random numbers with a Gaussian distribution (see ref. [199] for more details). For the white noise,  $\alpha = 0.5$ . The TL is in the non-conducting state for every frequency  $\omega$ . When the long-range correlation is introduced (for example  $\alpha = 0.55$ ), the ETLs can change their conducting properties and one can find a transition from the non-conducting to conducting state for a fixed system size, which implies the existence of critical values of the map parameters for each correlation exponent  $\alpha$ . Therefore, authors presented a phase diagram (see Fig. 1.35(a)) for the symmetric ternary model, separating the non-conducting state from the conducting one for the system presenting always a long-range correlation ( $\alpha \geq 0.55$ ). In addition, introducing one or more impurities in random places of the long-range correlated distribution of capacitances (see Fig. 1.35(b)), a dramatic change was observed in the conducting properties of the TL, leading the system to jump from conducting to non-conducting states, a behavior which can be considered as a possible mechanism to secure communication.

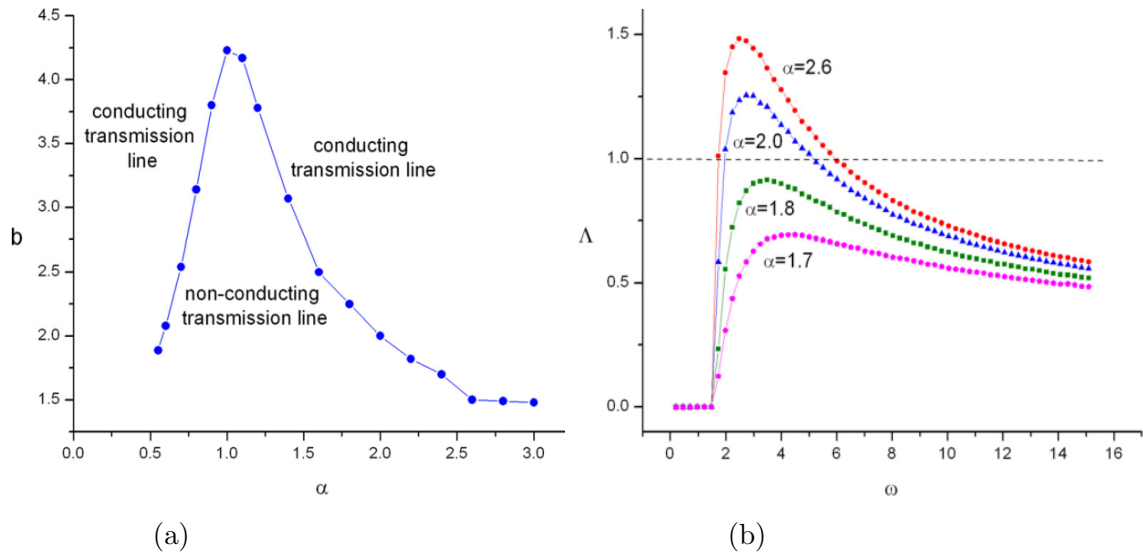


Figure 1.35: (a) Phase diagram separating non-conducting from conducting states in the thermodynamics limit in terms of the symmetric map parameter  $b_c(\infty)$  as a function of the correlation exponent  $\alpha$ . The plotted points correspond to values of the correlation exponent  $\alpha \geq 0.55$ , i.e., the disordered system always presents long-range correlation. (b) Normalized localization length  $\Lambda(\omega)$  as a function of the frequency  $\omega$  for the asymmetric ternary map when  $b_1 = -0.9$ ;  $b_2 = 1.7$  for different correlation exponents  $\alpha = \{1.7, 1.8, 2.0, 2.6\}$ . Figures are adapted from ref. [199]

In ref. [200] The localization effects of a TL with long-range correlated disorder in the

distribution of capacitances  $\{C_j\}$  in the form  $C_j = C_0\alpha_j$ , were also studied, using a ternary map and the Ornstein–Uhlenbeck (OU) process to generate the correlated sequence.

$$\alpha_j = \begin{cases} \alpha_A & \text{if } x_j < -b \\ \alpha_C & \text{if } -b \leq x_j \leq b, \quad b > 0, \\ \alpha_B & \text{if } x_j > b \end{cases} \quad (1.69)$$

where  $b$  is the map parameter and the sequence  $x_j$  is defined from the OU process, by the following differential equation:

$$\frac{dx}{dt} = -\gamma x(t) + \sqrt{C}\eta(t), \quad (1.70)$$

where  $\gamma$  is the viscosity coefficient and  $C$  is the diffusion coefficient.  $\eta(t)$  is a Gaussian white noise generated by the Box–Muller process (see ref. [200] for more details).

In the same logic as in the previous work [200], the authors have performed finite-size scaling and obtain the asymptotic value of the map parameter  $b$ , i.e.  $b_c$  in the thermodynamic limit in a selected range of values of the parameters  $\gamma$  and  $C$  of the OU and obtained the phase diagrams separating the localized states from the extended states of a dual TL (see Fig. 1.36(a, b)).

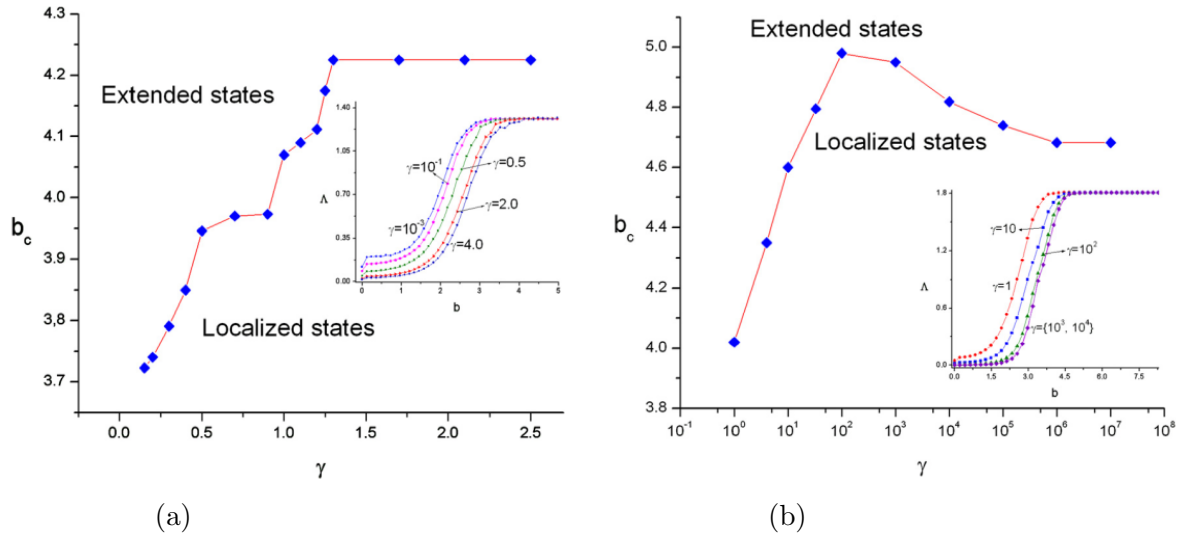


Figure 1.36: Phase diagram  $(\gamma, b_c)$  separating localized states from extended states in the thermodynamic limit in terms of the map parameter  $b_c(\infty)$  as a function of the parameter  $\gamma$ . (a) Case  $C = 0.3$ . The inset shows the normalized localization length  $\Lambda(b)$  as a function of the map parameter  $b$  for  $C = 0.3$  and  $\gamma$  going from  $\gamma = 0.001$  to  $\gamma = 4.0$ . (b)  $C = (\varepsilon\gamma)^2$  and  $\varepsilon = 1$  (limit case). The inset shows  $\Lambda(b)$  as a function of  $b$  for  $\gamma$  going from  $\gamma = 1$  to  $\gamma = 10^4$  for the same limit case. For all inset plots,  $\omega = 3.5$ ,  $N = 40\,000$ . Figures are adapted from ref. [200]

### 1.3.2.3 Anderson Localization in a $\mathcal{PT}$ transmission line

The study of localization properties has been extended in the framework of non-Hermitian systems. In this line,  $\mathcal{PTS}$  ETL models have been proposed in magnetic metamateri-

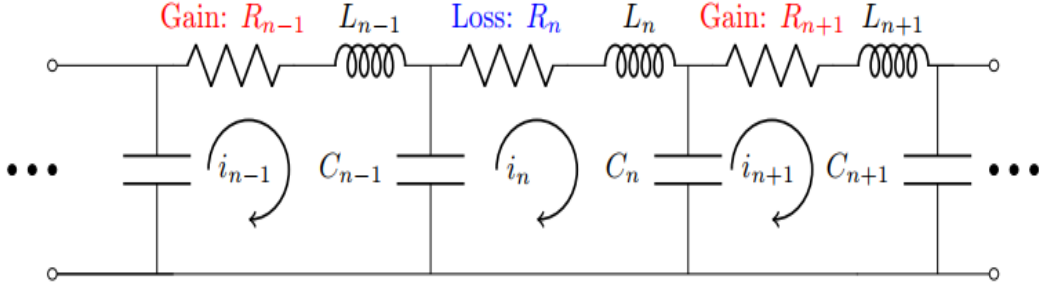


Figure 1.37: A  $\mathcal{PTS}$  resistance configuration in a direct ETL. Figure is taken from ref. [60].

als [216] and in noninvasive techniques to detect glucose changes [217]. More recently, Fernando R. Humire and Edmundo Lazo [60] studied a finite direct ETL as shown in Fig. 1.37, when they distributed resistors  $R_n$  according to a  $\mathcal{PT}$  distribution composed of a gain ( $-R$ ) and loss ( $+R$ ) sequence:

$$R_n = \begin{cases} +R, & n \text{ even} \\ -R, & n \text{ odd} \end{cases} \quad (1.71)$$

where  $n = 1, \dots, 2N$ . In addition, the zero boundaries conditions are considered at sites  $n = 0$  and  $n = (2N + 1)$ . The capacitances and inductances in each cell are considered constants, i.e.,  $L_n = L$  and  $C_n = C$ ,  $\forall n$ . Applying the Kirchoff's laws and using the Fourier transform, this  $\mathcal{PTS}$  direct TL model is described by

$$\left[ 2 - \left( \frac{\omega}{\omega_0} \right)^2 + j\beta_n \frac{\omega}{\omega_0^2} \right] I_n - I_{n-1} - I_{n+1} = 0, \quad (1.72)$$

where  $I_n(\omega)$  is the complex amplitude of the electric current intensity at site  $n$ ,  $\beta_n = \frac{R_n}{L}$  is the damping coefficient or the gain/loss parameter and  $\omega_0 = 1/\sqrt{LC}$ . Based in classical and quantum solutions used in  $\mathcal{PTS}$  problems [218, 219] for  $I_n$ , the eigenvalues of the system obtained for this dissipative system as:

$$\omega^2(R, k_d) = 2\omega_0^2 \left[ -M \pm \sqrt{M^2 - \sin^2(k_d)} \right], \quad (1.73)$$

where  $M = \left( \frac{\beta}{2\omega_0} \right)^2 - 1$  and  $k_d$ , the discrete values for the wave number. The analysis of the spectrum reveals a critical resistance value  $R_c$ , such that for  $R < R_c$ , the frequency spectrum is completely real, but for  $R > R_c$ , the frequency spectrum contains real and complex frequencies. The analysis of the transport properties of the electric current reveals that in the unbroken  $\mathcal{PT}$  phase (see Fig. 1.38(a)), the electric current  $|I_n|$  is always a symmetrical function. This symmetrical behavior disappears when the system goes to the broken  $\mathcal{PT}$  phase (see Fig. 1.38(b)). In addition, the localization properties of a TL were numerically studied through the normalized localization length  $\Lambda(R, k_d)$ , and the results demonstrated that in the unbroken  $\mathcal{PTS}$  phase, the electric current function  $I_n(\omega)$  is an

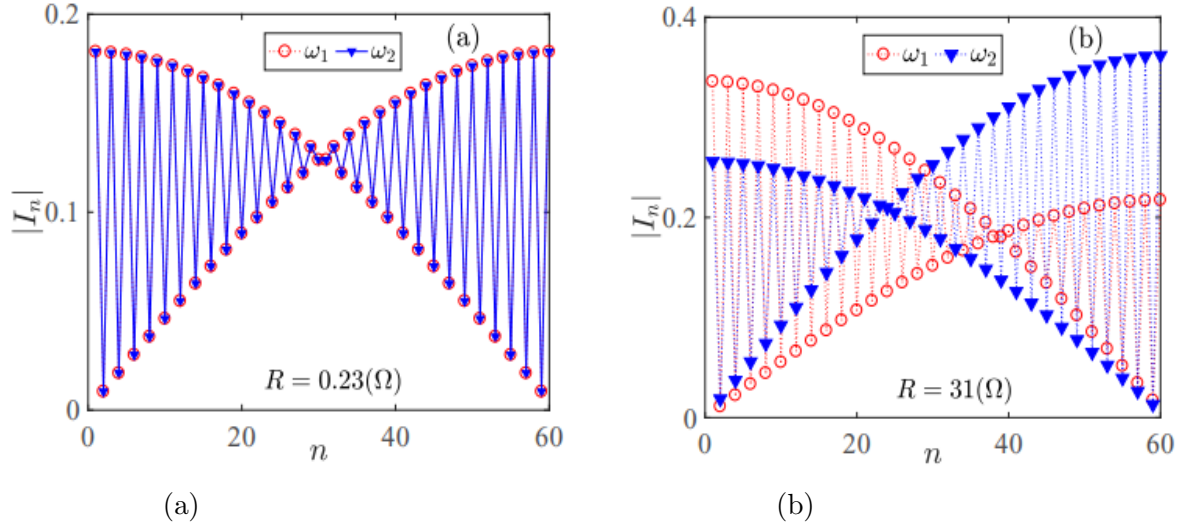


Figure 1.38: Modulus of the electric current function  $|I_n|$  as a function of  $n$  for both frequencies  $\omega_{1,2}(R, k_d)$ . (a) Symmetric and extended state for  $R = 0.23(\Omega) < R_c$  with frequencies  $\omega_1 = 1.43 \times 10^7$  (rad/s) and  $\omega_2 = 1.40 \times 10^7$  (rad/s). (b) Asymmetrical and dissipative state for  $R = 31(\Omega) > R_I$  with eigenvalues  $\omega_1 = j9.15 \times 10^6$  (rad/s) and  $\omega_2 = j2.18 \times 10^7$  (rad/s). Figures are adapted from ref. [60]

extended function. Conversely, in the broken phase,  $I_n(\omega)$  is a localized function (see Fig. 1.39).

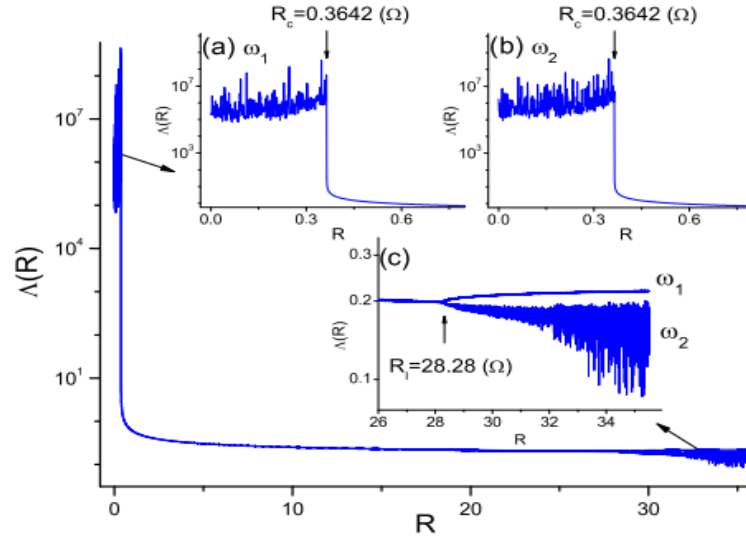


Figure 1.39: (a): Normalized localization length  $\Lambda(R, \omega_1)$  and  $\Lambda(R, \omega_2)$  vs  $R$  for fixed  $N = 30$  and  $k_{d=N}$ . For both frequencies  $\omega_1$  and  $\omega_2$ ,  $\Lambda(R, \omega)$  determines three regions with different localization behaviors, which are delimited by critical points  $R_c = 0.3642(\Omega)$  and  $R_I = 28.28(\Omega)$  (see insets). For  $R \leq R_c$ , insets (a)  $\omega_1$  and (b)  $\omega_2$  show a zoom of the unbroken  $\mathcal{PT}_S$  phase which corresponds to extended electric current functions  $\Lambda(R, \omega_{1,2}) \geq 1$ . For  $R > R_c$  we can only find a dissipative behavior which corresponds to the broken  $\mathcal{PT}_S$  phase [ $\Lambda(R, \omega_{1,2}) < 1$ ]. Inset (c) shows  $\Lambda(R, \omega_{1,2})$  in the neighborhood of  $R_I = 28.28(\Omega)$ . Figure is taken from ref. [60].

## Conclusion

In this chapter, we have presented some generalities on quantum Hermitian and non-Hermitian theories, the imaginary resistance and wave transport phenomena. After giving the background on quantum non-Hermitian formalism, a particular attention was paid on  $\mathcal{PT}$  and  $\mathcal{APT}$  symmetry in electronics. Then, we have presented some pioneer works and the applications. Concerning quantum phenomena, a particular attention was first devoted to electric analogs of EIT and related phenomena. Thereafter, we have presented the Anderson localization phenomenon by revisiting some essential works carried out in the context of electronics. In the next chapter, we will present the mathematical modelling, the analytical, numerical and experimental way used to obtain our results.

---

## Models and methods

---

### Introduction

In the previous chapter, we have discussed in a general way some quantum interference phenomena and wave scattering problems in Hermitian and non-Hermitian media but, without bringing out the theoretical or experimental details necessary to study their dynamical behavior. This chapter presents the methodology used to solve the problems in this thesis. We start by recalling some fundamentals. Then, we describe and mathematically model the proposed systems. To better understand the phenomena studied, we present the analytical and numerical methods used for each model. Finally, we describe the analogical simulation methods used to consolidate some analytical results.

### 2.1 Fundamentals

From Ohm's and Kirchhoff's laws, the use of which is undeniable and no longer needs to be demonstrated, it is easy to describe electronic circuits by differential equations which generally link the electric voltage, the electric current and the circuit parameters. However, solve these equations can sometimes prove difficult, due to the non-linearity associated with the components used, the order or the degree of the differential equations, etc. Then, certain equations must be approximated even before their resolution, thus making dependent the interpretation of the solutions and the methods used. The systems studied in this thesis are made only of electronic lumped elements as inductor  $L$ , capacitor  $C$ , real resistor  $R$  and an additive new component: the imaginary resistance  $Z = jr$ , which are all linear. Equations governing systems presented in this thesis will be derived using basic laws of electronics such as Ohm's law and Kirchhoff's voltage or current laws. First of all, let's remember these basics.

- **Complex impedance**

Consider a dipole of an electrical circuit in sinusoidal regime where the voltage and the current are noted:

$$u(t) = U_{\max} \cos(\omega t + \phi) , \quad (2.1)$$

and

$$i(t) = I_{\max} \cos(\omega t + \varphi), \quad (2.2)$$

where  $U_{\max}$ ,  $I_{\max}$ , represent the maximal amplitude of the voltage and the current, respectively, and  $\omega$  is the angular frequency. In complex notation, they can be represented by:

$$u(t) = \Re(U_{\max} e^{j\phi} e^{j\omega t}) = \Re(\underline{U} e^{j\omega t}), \quad (2.3)$$

and

$$i(t) = \Re(I_{\max} e^{j\varphi} e^{j\omega t}) = \Re(\underline{I} e^{j\omega t}), \quad (2.4)$$

where  $\underline{U} = U_{\max} e^{j\phi}$  and  $\underline{I} = I_{\max} e^{j\varphi}$ .

The complex impedance  $\underline{Z}$  is defined as the ratio of the complex amplitude of the voltage  $\underline{U}$  to the complex amplitude of the current  $\underline{I}$ :

$$\underline{Z} = \frac{\underline{U}}{\underline{I}} = \frac{U_{\max}}{I_{\max}} e^{j\theta}, \quad (2.5)$$

where  $\theta = \phi - \varphi$ .

- **Voltage-current relationship or Ohm's law of some dipoles**

Contrary to the static regime, the capacitors and the inductors behave in sinusoidal regime like impedances, the values of which vary according to the frequency. Hence, we recall the voltage-current for some dipoles used in this work as well as their characteristic impedance  $Z$  obtained from equations Eqs. (2.3), (2.4) and (2.5):

- **A real resistance  $R$ ,**

$$u(t) = R i(t) \quad ; \quad \underline{Z}_R = R. \quad (2.6)$$

- **A linear inductance  $L$ ,**

$$u(t) = L \frac{di}{dt} \quad ; \quad \underline{Z}_L = jL\omega. \quad (2.7)$$

- **A linear capacitance  $C$ ,**

$$i(t) = C \frac{du}{dt} \quad ; \quad \underline{Z}_C = \frac{1}{jC\omega}. \quad (2.8)$$

- **An imaginary resistance  $jr$ ,**

$$u(t) = jr i(t) \quad ; \quad \underline{Z} = jr. \quad (2.9)$$

- **Association of elements**

Complex impedances combine like resistances. The following relations give the equivalent impedance  $Z_{eq}$  for each type of association of dipoles:



**In series:**

$$Z_{eq} = Z_1 + Z_2 + \dots + Z_n. \quad (2.10)$$

**In parallel:**

$$(Z_{eq})^{-1} = (Z_1)^{-1} + (Z_2)^{-1} + \dots + (Z_n)^{-1}. \quad (2.11)$$

- **Kirchhoff Current Law**

“The algebraic sum of the intensities of the currents  $I_k$  arriving at a node is zero.”

$$\sum_{k=1}^n I_k = 0. \quad (2.12)$$

- **Kirchhoff Voltage Law**

“The algebraic sum of the potential differences (or voltage)  $\Delta U_k$  along a cell counted in a given direction is zero.”

$$\sum_{k=1}^n \Delta U_k = 0, \quad (2.13)$$

where  $\Delta U_k$  is an algebraic quantity.

- **Power in sinusoidal regime**

The instantaneous power consumed by a dipole is defined as the product of the voltage  $u(t)$  which appears at the terminals of the dipole and the intensity of the current  $i(t)$  flowing through it.

$$p(t) = u(t) i(t). \quad (2.14)$$

The instantaneous power being variable over time, it is often more interesting to know the average power  $p(t)$  over a period  $T = 2\pi/\omega$  from the instant  $t_0$  which reads as:

$$P(\omega) = \frac{1}{T} \int_{t_0}^{t_0+T} p(t) dt = \frac{1}{T} \int_{t_0}^{t_0+T} u(t) \cdot i(t) dt \quad (2.15)$$

## 2.2 Description, modeling of non-Hermitian systems

### 2.2.1 Atomic system using electronic circuits

#### 2.2.1.1 Three level atomic system using coupled oscillators LRC

- **Oscillator LRC series**

The conventional oscillator LRC series consists of an inductor  $L$ , a real resistor  $R$  and a capacitor  $C$ . The complex impedance  $Z_L$  of the inductor is linked to the frequency  $\omega$  by the relation  $Z_L = j\omega L$ , where  $j^2 = -1$ . The charge capacitor  $q(t)$  and the voltage

$V(t)$  across the inductor are linked by a second order differential equation  $V(t) = L \frac{d^2 q(t)}{dt^2}$ . Hence, the LRC circuit is governed by the following second order differential equation:

$$\frac{d^2 q(t)}{dt^2} + \frac{\omega_0}{\gamma} \frac{dq(t)}{dt} + \omega_0^2 q(t) = 0, \quad (2.16)$$

where  $\gamma = \frac{1}{R} \sqrt{\frac{L}{C}}$  and  $\omega_0 = \frac{1}{\sqrt{LC}}$  is the natural frequency;  $\omega_0$  value's remains positive if  $LC > 0$  and pure imaginary if  $LC < 0$ . The quality factor  $Q_f$  of the circuit is defined as:

$$Q_f = \frac{\gamma}{\omega_0}. \quad (2.17)$$

The sign of  $Q_f$  depends to that of  $\gamma$ . In particular, one can observe the attenuation/amplification behavior of the oscillations for positive/negative value of the quality factor.

- **Dimer MLC series**

Coupled LRC circuits have been used in ref. [59], to model a three level atom in lambda ( $\Lambda$ ) configuration. Inspired by that, we propose the model described by Fig. 2.1(a). Such electronic dimer consists of two active or passive LRC meshes ( $k$ ) ( $k = 1, 2$ ) coupled through an inductor ( $L_C$ ), a capacitor ( $C_C$ ) and mutually ( $M$ ). Each mesh ( $k$ ) is made of a real resistor  $R_k$ , two inductors ( $L_k$  and  $L_C$ ) in series and two capacitors ( $C_k$  and  $C_C$ ) also in series which respectively compose to an effective inductance  $l_k = L_k + L_C$  and capacitance  $C_{ek} = (C_k C_C) / (C_k + C_C)$ . The mesh (2) is directly driven by an external

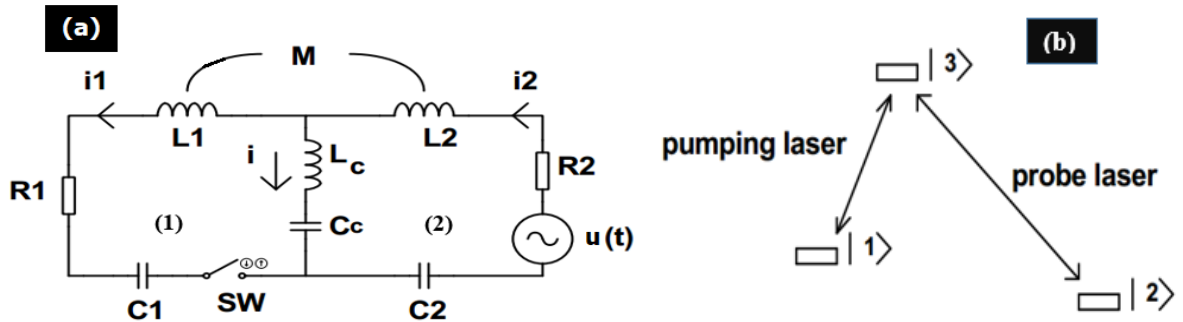


Figure 2.1: (a) Coupled LRC circuits used to reproduce EIT and related phenomena. The couplings operate when the switch SW is closed. (b) Energy diagram of a three level-atom in lambda ( $\Lambda$ ) configuration interacting with two lasers beams coupling ground states  $|1\rangle$  and  $|2\rangle$  to a common excited state  $|3\rangle$ .

harmonic voltage source  $u(t) = v_0 e^{j\omega t} + c.c$ , where c.c is the complex conjugate. When the switch SW is On, a single or a multiple coupling is established between the meshes, resulting in many possible configurations of dimers. Remarkably, the resistance value  $R_k$  in the meshes ( $k$ ) can be positive or negative and is responsible to the attenuation (loss) or to the amplification (gain). The experimental realization of the negative resistor can be found in refs. [28, 29]. The electrical model is analog to the three-level atom in lambda

( $\Lambda$ ) configuration of which the energy diagram is shown in Fig. 2.1(b). Both systems typically describe the same physics [59]. Therefore, the following correspondences can be established: the mesh (2) driven by the voltage source, models the probed atomic transition between the excited level  $|3\rangle$  and the ground level  $|2\rangle$ . The mesh (1) whose connection with the mesh (2) depends on the position of the switch SW, thus simulates the pump laser operating at the atomic transition  $|3\rangle$  to  $|1\rangle$ , whereas coupling between meshes determines the Rabi frequency associated to the pumping laser. The switch being closed, we consider that the capacitances and the inductances in each cell are constants, i.e.  $C_k = C$  and  $L_k = L$ . Then, the dynamic of the circuit is described as:

$$\begin{cases} \ddot{q}_1 + \Gamma_1 \dot{q}_1 + \omega_0^2 q_1 - \Omega^2 q_2 - d\ddot{q}_2 = 0 \\ \ddot{q}_2 + \Gamma_2 \dot{q}_2 + \omega_0^2 q_2 - \Omega^2 q_1 - d\ddot{q}_1 = u/l \end{cases}, \quad (2.18)$$

where  $\omega_0 = 1/\sqrt{lC_e}$ ;  $\Omega = 1/\sqrt{lC_c}$ ;  $\frac{1}{C_e} = \frac{1}{C} + \frac{1}{C_c}$ ;  $\Gamma_k = \frac{R_k}{l}$ , ( $k = 1, 2$ );  $d = \frac{\mu + \nu_C}{1 + \nu_C}$ ;  $\mu = \frac{M}{L}$ ;  $\nu_C = \frac{L_C}{L}$ ;  $\kappa = \frac{C_e}{C_c}$ ;  $l = l_k = L + L_C$  with  $\mu, \kappa \in [0; 1[$ ;  $\nu_C \in [0; \infty[$ .

### 2.2.1.2 Three level atomic system using coupled oscillators ZRC

- **Oscillator ZRC series**

The oscillator ZRC series cell as shown in Fig. 2.2 is obtained by merely replacing the inductance  $L$  in a LRC series oscillator by the imaginary resistance whose impedance  $Z = jr$  compared to that of the inductor, is frequency independent. The electric current

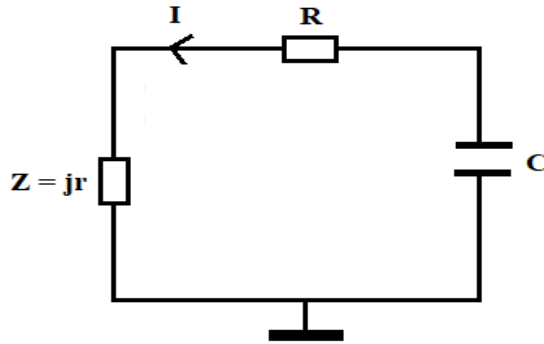


Figure 2.2: The oscillator ZRC series.

$I(t)$  or the circuit's charge  $q(t)$  and the electric voltage across the imaginary resistance are rather linked by the linear equations,  $V(t) = jrI(t)$  or  $V(t) = jr \frac{dq(t)}{dt}$ , respectively. Therefore, the ZRC circuit oscillates according to the first order differential equation:

$$(\beta + j) \frac{dq(t)}{dt} + \omega_0 q(t) = 0, \quad (2.19)$$

where  $\beta = \frac{R}{r}$  is the non-Hermitian parameter, responsible to the attenuation or the amplification into the oscillator.  $\omega_0 = \frac{1}{rC}$  is the natural frequency of the circuit, and the

circuit's quality factor is defined as:

$$Q_f = \frac{\omega_0}{\beta}. \quad (2.20)$$

These relations show that the signs of both  $Q_f$  and  $\omega_0$  can be positive/negative according to those of the circuitry elements. The reduction of the differential equation order from 2 in the LRC to 1 in the oscillator ZRC suggests the imaginary resistance, as tool to fabricate a new generation of oscillators.

- **ZRC Dimer**

The ZRC dimer as shown in Fig. 2.3 is obtained by coupling two oscillators ZRC (Fig. 2.2). Each  $Z_i R_i C_i$  ( $i = 0, 1$ ) circuit consists of a linear capacitor  $C_i$ , a real resistor  $R_i$  and an imaginary resistance of impedance  $Z_i$ , where  $Z_i = jr_i$  ( $j^2 = -1$ ), all arranged in series. In addition, a harmonic voltage source  $u(t)$  is added in series with the resistor  $R_0$ . The coupling between loops is realized thanks to the capacitor  $C_c$  and another imaginary resistance  $Z_c$  ( $Z_c = jr_c$ ), also arranged in series and belonging to the set of circuit meshes. This coupling operates when the switch SW is closed. Interestingly, the active controlling coupling can be used to refer the ZRC dimer. For convenience, for the dimer Z, only the imaginary resistive coupling ( $Z_c$ ) is active while in the case of the dimer ZC, the series combination  $Z_c - C_c$  is active.

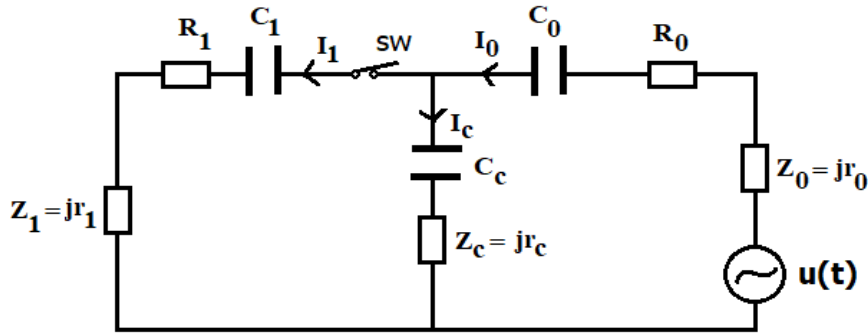


Figure 2.3: A dimer ZRC series used as a  $\Lambda$ -three level atomic system.

The experimental setup so-described can be used as an analog model of a three level atomic system in the  $\Lambda$  configuration. Our objective is to demonstrate later that, with such a circuit, EIT and the related quantum phenomena can be investigated. If SW is closed, the Kirchhoff's laws leads to the following coupled equation:

$$\begin{cases} (\beta_0 + j) \frac{dq_0(t)}{dt} - j\beta_{c0} \frac{dq_1(t)}{dt} + \omega_0 q_0(t) - \Omega_0 q_1(t) = \frac{u}{r_{e0}} \\ (\beta_1 + j) \frac{dq_1(t)}{dt} - j\beta_{c1} \frac{dq_0(t)}{dt} + \omega_1 q_1(t) - \Omega_1 q_0(t) = 0 \end{cases} \quad (2.21)$$

where  $\beta_i = \frac{R_i}{r_{ei}}$ ;  $r_{ei} = r_i + r_c$ ;  $\beta_{ci} = \frac{r_c}{r_{ei}}$ ;  $\omega_i = \frac{1}{r_{ei}C_{ei}}$ ;  $\Omega_i = \frac{1}{r_{ei}C_c}$ ;  $\frac{1}{C_{ei}} = \frac{1}{C_i} + \frac{1}{C_c}$ .  $q_i$  and  $dq_i/dt$  represent the charge and the current into each loop, respectively. The dimer

system leads to first order coupled ordinary differential equations, which can be easily analyzed. Moreover, the system can support negative frequencies, without altering its operating mode. Table 2.1 summarizes the different possible combinations of the circuit elements to have positive or negative charges in the loop.

	$r_C$		$C_C$		$C_{ei}$		$R_i$	
	$r_C > 0$	$r_C < 0$	$C_C > 0$	$C_C < 0$	$C_{ei} > 0$	$C_{ei} < 0$	$R_i > 0$	$R_i < 0$
$r_{ei} > 0$	$\beta_{Ci} > 0$	$\beta_{Ci} < 0$	$\Omega_i > 0$	$\Omega_i < 0$	$\omega_i > 0$	$\omega_i < 0$	$\beta_i > 0$	$\beta_i < 0$
$r_{ei} < 0$	$\beta_{Ci} < 0$	$\beta_{Ci} > 0$	$\Omega_i < 0$	$\Omega_i > 0$	$\omega_i < 0$	$\omega_i > 0$	$\beta_i < 0$	$\beta_i > 0$

Table 2.1: Combination of circuit elements for either positive or negative charges.

One of the key parameters of the system is the gain/loss parameter  $\beta_i = R_i/r_{ei}$ . This parameter defines the energy state of the system which can be Hermitian or non-Hermitian depending on the nature of  $\beta_i$ . The system is Hermitian when  $\beta_i = 0$ . As soon as  $\beta_i \neq 0$ , the system becomes non-Hermitian.  $\beta_i$  is thus called the non-Hermitian parameter responsible for the amplification or the damping in the loop. When  $r_{ei}$  and  $R_i$  have the same signs (i.e.,  $\beta_i > 0$ ), the loop is said “loss”, otherwise, it is said “gain”. When  $\beta_i$  exceeds a threshold value, the system is marked by a degeneracy and the threshold is called the exceptional point (EP) [13].

### 2.2.1.3 Multi level atom using coupled oscillators ZRC

The multi dimer circuit as shown in Fig. 2.4(a), is obtained by coupling  $(N+1)$  oscillators ZRC via a series branch  $Z_C - C_C$ , where  $Z_C$  and  $C_C$  are the imaginary resistance and the capacitance, respectively. The ZRC multi dimers are modeled so that the multipod

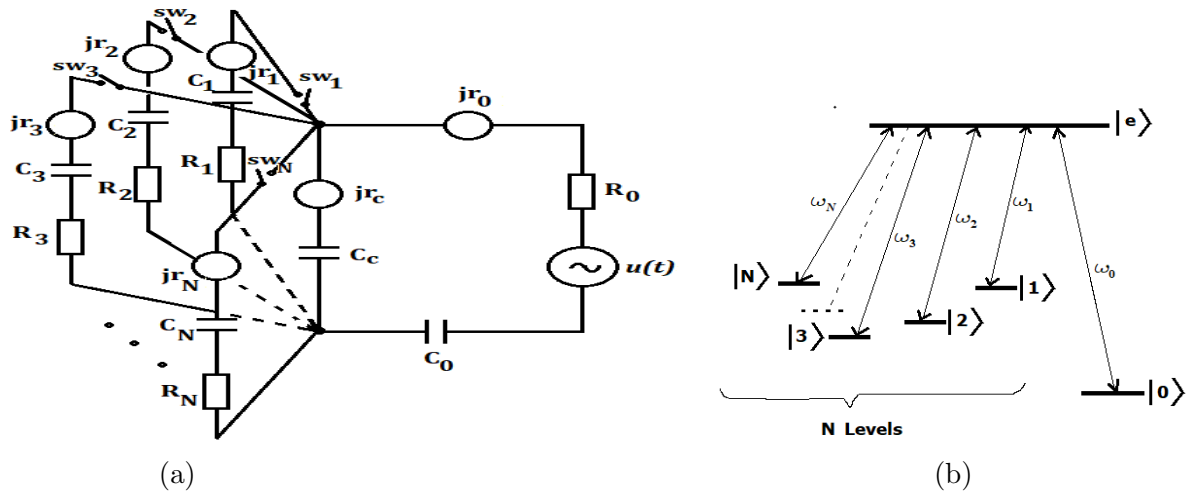


Figure 2.4: (a): ZRC Multi dimer circuit used for a single and multiple EIT, ATS and EIA windows. (b): Energy diagram of a  $(N+2)$  level atomic system in a multipod type configuration consisting of  $(N+1)$  lower levels  $|i\rangle$  ( $i = 0..N$ ) of which  $N$  pumping lasers couple near resonantly each state to the upper state  $|e\rangle$ , while a probe laser couples level  $|0\rangle$  to  $|e\rangle$ .

loops are connected to the central one ( $Z_0 R_0 C_0$ ). For example, in the cases of the bi and

the tri dimer,  $N=2$  and  $N=3$  loops are respectively connected to the central loop. The trivial case  $N=1$  corresponds to the single dimer. On the other hand, Fig. 2.4(b) illustrates a  $(N+2)$  level atomic system in a multipod type configuration, where the  $(N+1)$  lower states  $|i\rangle$  which can be degenerated or not, are coupled to a single excited upper level state  $|e\rangle$ . The atomic system is initially prepared in a particular state  $|0\rangle$  and interacts with a probe laser that couples the lower state  $|0\rangle$  to an excited state  $|e\rangle$ . Adding a total number of  $N$  light sources (each being in a state  $|i\rangle$ ) induces an atomic transition of frequency  $\omega_i$  from  $|e\rangle$  to  $|i\rangle$ . The absorption spectrum of the probe laser is modified once the  $N$  control fields simultaneously interact with the medium, which results in the interferences between the different transitions pathways of the atom. In this thesis, we demonstrate that the ZRC multi dimer circuit (Fig. 2.4(a)) is analog to the  $(N+2)$  level atomic system in a multipod type configuration. In this analogy, the loop  $Z_0R_0C_0$  of frequency  $\omega_0$  models the atom. This represents the central loop where the other loops are connected to. The harmonic voltage  $u(t)$  is the probe laser field. Once the switch  $SW_i$  is closed, each loop of frequency  $\omega_i$  acts as a control field to the central loop. If the switches  $SW_i$ ,  $i = (0\dots N)$  are closed, the Kirchhoff's laws leads to the following coupled equations:

$$\left\{ \begin{array}{l} (\beta_0 + j) \frac{dq_0}{dt} - j\beta_{c0} \sum_{n=1}^N \frac{dq_n}{dt} + \omega_0 q_0 - \Omega_0 \sum_{n=1}^N q_n = u/r_{e0} , \quad i = 0 \\ (\beta_i + j) \frac{dq_i}{dt} - j\beta_{ci} \left( \frac{dq_0}{dt} - \sum_{n=1, n \neq i}^N \frac{dq_n}{dt} \right) + \omega_i q_i - \Omega_i \left( q_0 - \sum_{n=1, n \neq i}^N q_n \right) = 0 , \quad i \neq 0 \end{array} \right. , \quad (2.22)$$

where  $\beta_i = \frac{R_i}{r_{ei}}$  ;  $r_{ei} = r_i + r_c$  ;  $\beta_{ci} = \frac{r_c}{r_{ei}}$  ;  $\omega_i = \frac{1}{r_{ei}C_{ei}}$  ;  $\Omega_i = \frac{1}{r_{ei}C_c}$  ;  $\frac{1}{C_{ei}} = \frac{1}{C_i} + \frac{1}{C_c}$  .

## 2.2.2 Description, modeling $\mathcal{PT}/\mathcal{APT}$ electronic dimers

The experimental setup of the  $\mathcal{PTS}$  dimer as shown in Fig. 2.5, consists of two oscillators made of inductor  $L$ , resistor  $R$ , and capacitor  $C$  (oscillator LRC), one with amplification (gain cell) generated by a negative resistance  $-R$  and the other with an equivalent amount of attenuation (loss cell) introduced by a positive resistance  $R$ , so that the gain and the loss are balanced. On the contrary, in the  $\mathcal{APTS}$  configuration, the gain does not necessarily compensates the loss. Thus, the dimer results from a coupling between identical cells of either gain-gain or loss-loss. The negative resistance circuit has been proposed using op-amplifiers [28, 29]. Whatever the model considered, both oscillators are linked by a mutual inductive  $M$ , inductive  $L_0$ , and capacitive  $C_0$  couplings. The possibility of several couplings allows to our model to be illustrated as a general model of dimers such that, only the active coupling is used in the following to refer to them. For

example, dimer L is the one of which, only the inductance coupling  $L_0$  is active. In the dimer LC both the inductance  $L_0$  and the capacitance  $C_0$  couplings are active while in the dimer MLC, all couplings are active.

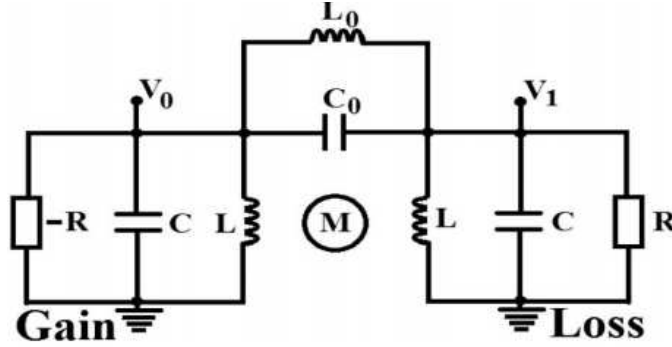


Figure 2.5: Electronic model of a general dimer MLC: The models take into account mutual inductive coupling ( $M$ ), inductive coupling ( $L_0$ ) and capacitive coupling ( $C_0$ ).

Assuming positive currents running down the page and applying standard circuit's laws to the  $\mathcal{PTS}$  dimer, we can write:

$$\begin{cases} I_R^0 + I_C^0 + I_L^0 + I_{L_0}^0 + I_{C_0}^0 = 0 \\ I_R^1 + I_C^1 + I_L^1 + I_{L_0}^1 + I_{C_0}^1 = 0 \end{cases}, \quad (2.23)$$

where  $I_R^i = (-1)^{i-1} \gamma q_i$ ;  $I_C^i = \frac{dq_i}{dt}$ ;  $\frac{dI_L^i}{dt} = \alpha \omega_0^2 (q_i - \mu q_k)$ ;  $\frac{dI_{L_0}^i}{dt} = \alpha \nu \omega_0^2 (q_i - q_k)$ ;  $I_{C_0}^i = c \left( \frac{dq_i}{dt} - \frac{dq_k}{dt} \right)$ ;  $\gamma = \frac{1}{R} \sqrt{\frac{L}{C}}$ ;  $\alpha = \frac{1}{1-\mu^2}$ ;  $c = \frac{C_0}{C}$ ;  $\nu = \frac{L}{L_0}$ ;  $\mu = \frac{M}{L}$ ;  $\omega_0^2 = \frac{1}{LC}$ ;  $(i, k = 0, 1), \forall i \neq k$ .

Taking the derivative of the Eq. (2.23) with respect to the time  $t$ , we can derive a set of coupled second-order differential dimensionless equations for the charge capacitors  $Q_{i(i=0,1)}$  as:

$$\begin{cases} (1+c) \frac{d^2 Q_0}{d\tau^2} - c \frac{d^2 Q_1}{d\tau^2} + (\alpha + \nu) Q_0 - (\alpha \mu + \nu) Q_1 - \gamma \frac{dQ_0}{d\tau} = 0 \\ -c \frac{d^2 Q_0}{d\tau^2} + (1+c) \frac{d^2 Q_1}{d\tau^2} - (\alpha \mu + \nu) Q_0 + (\alpha + \nu) Q_1 + \gamma \frac{dQ_1}{d\tau} = 0 \end{cases}. \quad (2.24)$$

Each cell has a natural frequency  $\omega_0^2 = \frac{1}{LC}$  and a natural phase  $\tau = \omega_0 t$ ;  $\gamma = \frac{1}{R} \sqrt{\frac{L}{C}}$  is the dimensionless gain/loss parameter,  $Q_i = \frac{q_i}{Q}$ , and  $q_i$  is the charge at node  $i$ ,  $Q$  being a reference charge.

In the  $\mathcal{APTS}$  configuration, Eq. (2.24) is rewritten as :

$$\begin{cases} (1+c) \frac{d^2 Q_0}{d\tau^2} - c \frac{d^2 Q_1}{d\tau^2} + (\alpha + \nu) Q_0 - (\alpha \mu + \nu) Q_1 \pm \gamma \frac{dQ_0}{d\tau} = 0 \\ -c \frac{d^2 Q_0}{d\tau^2} + (1+c) \frac{d^2 Q_1}{d\tau^2} - (\alpha \mu + \nu) Q_0 + (\alpha + \nu) Q_1 \pm \gamma \frac{dQ_1}{d\tau} = 0 \end{cases}, \quad (2.25)$$

where  $(\pm \gamma)$  in Eq. (2.25) is associated to the  $\mathcal{APTS}$  dimer with the loss-loss  $(+\gamma)$  or the gain-gain  $(-\gamma)$  cells, respectively.

## 2.2.3 Description and modeling of the electrical transmission lines (ETLs)

### 2.2.3.1 Hermitian ZC ETL

The Hermitian ZC is a discrete one dimensional ( $1\mathcal{D}$ ) ETL made up of two components, one with impedance denoted by  $Z_n$ , located on the horizontal branch and another with impedance labelled as  $z_n$ , which is situated in the shunt branch. The two impedance values depend on the nature of the component used, which can be a capacitor or an imaginary resistance. Then, the ZC ETL is analyzed considering two possible configurations i.e right handed (RH) or left handed (LH). In the RH configuration,  $Z_n = jr_n$  and  $z_n = (j\omega C_n)^{-1}$ . On the contrary, in the LH configuration, we have  $Z_n = (j\omega C_n)^{-1}$ , and  $z_n = jr_n$ .

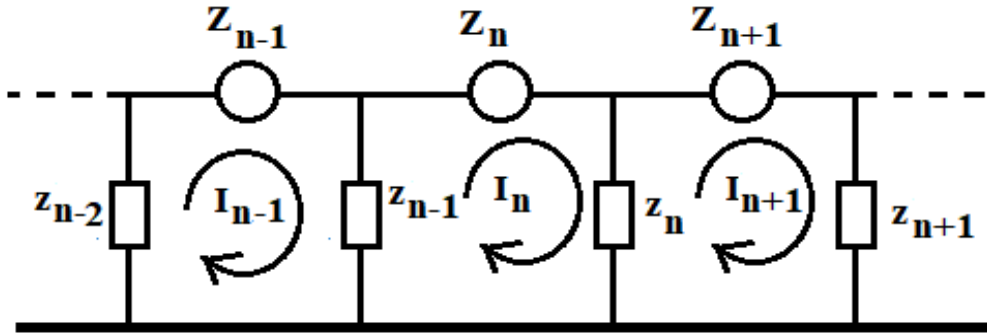


Figure 2.6: Diagram of a Hermitian ZC ETL.

Figure 2.6 shows a segment of a ZC LH or ZC RH ETL. Applying the Kirchhoff's law to the  $n$  th cell of the circuit, we obtain a linear relationship between the electric current circulating in the  $(n - 1)$  th,  $n$  th and  $(n + 1)$  th cells as follows:

$$(Z_n + z_n + z_{n-1}) I_n - z_{n-1} I_{n-1} - z_n I_{n+1} = 0 \quad (n = 1, \dots, 2N). \quad (2.26)$$

### 2.2.3.2 Non-Hermitian ZRC ETL

To transform the Hermitian ZC ETL into a non-Hermitian one, we add in series to each of the nodes  $n$  of Fig. 2.6, a dissipative component such as the linear resistance  $R_n$ , which can be positive (loss) or negative (gain). Hence, it results a cascade association of a ZRC unit cells so that for the ZRC RH TL, both the imaginary and the linear resistors are shunted by the capacitor whereas for the ZRC LH TL, both the capacitor in series with the real resistor, are shunted by the imaginary resistance. In what follows, we will consider systems of  $2N$  size. In this point of view, the ZRC ETL appears as a succession of  $2N$  oscillators ZRC, or as a succession of  $N$  dimers ZRC. Figure 2.7 illustrates a segment of a non-Hermitian ZRC RH/LH ETL. Applying the Kirchhoff loop rule to three successive unit cells of the ETL model allows us to obtain a dynamic equation relating the electric



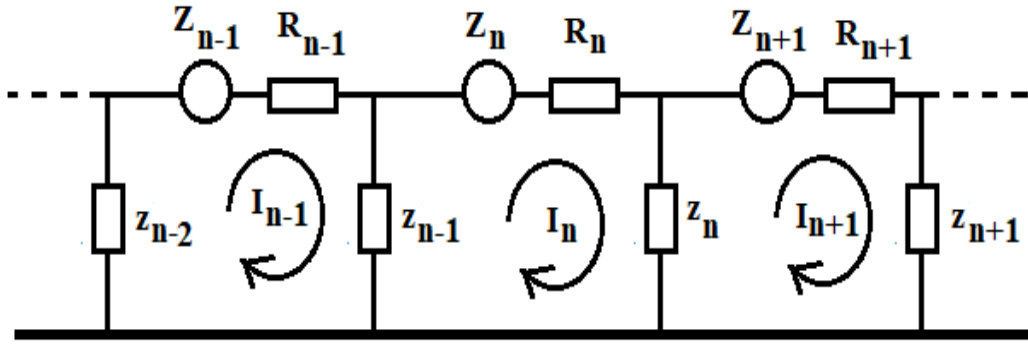


Figure 2.7: Segment of a non-Hermitian ZRC ETL.

current  $I$  in the  $n$  th,  $(n - 1)$  th and  $(n + 1)$  th cells as follows:

$$(Z_n + z_n + z_{n-1} + R_n) I_n - z_{n-1} I_{n-1} - z_n I_{n+1} = 0 \quad (n = 1, \dots, 2N). \quad (2.27)$$

Substituting for the ZRC RH TL  $Z_n = jr_n$  and  $z_n = (j\omega C_n)^{-1}$ , and for the ZRC LH TL  $Z_n = (j\omega C_n)^{-1}$  and  $z_n = jr_n$ , we obtain:

$$\text{(RH): } \lambda_n I_n - c_1 I_{n-1} - I_{n+1} = 0, \quad (2.28)$$

$$\text{(LH): } \varepsilon_n I_n - \alpha_1 I_{n-1} - I_{n+1} = 0, \quad (2.29)$$

where  $\lambda_n = a_1 + \omega(j\beta_n - 1)/\omega_n$ ;  $\varepsilon_n = b_1 - j\beta_n - (\omega/\omega_n)^{-1}$ ;  $a_1 = 1 + c_1$ ;  $b_1 = 1 + \alpha_1$ ;  $c_1 = \frac{C_n}{C_{n-1}}$ ;  $\alpha_1 = \frac{r_{n-1}}{r_n}$ ;  $\omega_n = \frac{1}{r_n C_n}$  and  $\beta_n = R_n/r_n$ .

## 2.3 Analytical methods

In the previous sections, we have shown that from Kirchhoff's laws, it is easy to describe the systems proposed by one or more differential equations. In this section we derive analytical methods used to investigate each proposed system.

### 2.3.1 Analytical methods for the analog models

As we said above, EIT is a quantum phenomenon occurring in atomic systems. However it can be developed and discussed using simple electrical analogies described in Figs. 2.1, 2.3 and 2.4, which allows it to be performed in an undergraduate physics laboratory. The dynamic equations of the classical analog models studied are found in Eqs. (2.18), (2.21) and (2.22). Therefore, the induced transparency is investigated analyzing the frequency dependence of the active power transferred from the voltage source  $u(t)$  to the resonant circuit simulating the atom. The analytical calculation methods are detailed below.

### 2.3.1.1 Dimer MLC series

The dimer MLC series can be described by the  $\mathcal{H}$  non-Hermitian Hamiltonian (NHH) when inserting harmonic solutions  $q_k(t) = A_k e^{-j\omega t} + \text{c.c.}$  ( $k = 1, 2$ ) into Eq. (2.18) which, can therefore be rewritten in the absence of the voltage into the matrix form given as:

$$(\mathcal{H} - \omega \mathbf{1}) = 0, \quad (2.30)$$

where

$$\mathcal{H} = \begin{pmatrix} 1 - \frac{j\gamma_1}{2} & \frac{C_T}{2} \\ \frac{C_T}{2} & 1 - \frac{j\gamma_2}{2} \end{pmatrix}, \quad (2.31)$$

with  $C_T = \frac{\mu + \nu_C}{1 + \nu_C} - \kappa$ ;  $\kappa = \frac{C_e}{C_C}$ ;  $\frac{1}{C_e} = \frac{1}{C} + \frac{1}{C_c}$ ;  $\gamma_k = \frac{\Gamma_k}{\omega_0}$ ;  $\Gamma_k = \frac{R_k}{l}$ ; ( $k = 1, 2$ );  $\mu = \frac{M}{L}$ ;  $\nu_C = \frac{L_C}{L}$ ;  $\kappa = \frac{C_e}{C_c}$ ;  $\mu, \kappa \in [0; 1[$ ;  $\nu_C \in [0; \infty[$ ,  $\mathbf{1}$  is the  $2 \times 2$  identity matrix and  $C_T$  is the effective coupling constant of the dimer. This effective coupling can be cancelled if the coupling less condition given below is fulfilled:

$$C_T = 0. \quad (2.32)$$

Solving the characteristic equation  $\det(\mathcal{H} - \omega \mathbf{1}) = 0$ , we find the eigenvalues of the system as:

$$\omega_{\pm} = \frac{\omega_0}{2} \left( 2 - j\eta \pm \sqrt{\Lambda} \right), \quad (2.33)$$

where  $\Lambda = -\zeta^2 + C_T^2$ ;  $\eta = \gamma_2 \frac{\varepsilon + 1}{2}$ ;  $\zeta = \gamma_2 \frac{\varepsilon - 1}{2}$  and  $C_T = d - \kappa$ .

#### ★ Analysis of the electric power

Let's consider again the Eq. (2.18) in presence of the voltage. According to Eq. (2.14), the instantaneous power transferred from the voltage source to the resonant circuit  $L_2$ ,  $R_2$ ,  $C_2$ ,  $L_C$  and  $C_C$  can be defined as:

$$p_2(t) = u(t) i_2(t) = u(t) \dot{q}_2(t). \quad (2.34)$$

Inserting  $u(t) = v_0 e^{-j\omega t} + \text{c.c.}$ ,  $q_k(t) = A_k e^{-j\omega t} + \text{c.c.}$  ( $k = 1, 2$ ) where  $v_0$ ,  $A_k$  are the complex amplitudes and c.c is the complex conjugate, the expression of the instantaneous power can be rewritten as:

$$p_2(t) = \left( v_0 e^{-j\omega t} + \text{c.c.} \right) \dot{q}_2(t). \quad (2.35)$$

By using Eq. (2.19), the average of the electric power during one period  $T = \frac{\omega}{2\pi}$  of oscillation reads as:

$$P_2(\omega) = \frac{\int_{t_0}^{t_0+T} (v_0 e^{-j\omega t} + \text{c.c.}) \dot{q}_2(t) dt}{2\pi/\omega}. \quad (2.36)$$

Replacing  $\dot{q}_2(t) = -j\omega A_2 e^{-j\omega t} + \text{c.c}$  into the Eq. (2.36), we get:

$$P_2(\omega) = j\omega v_0 A_2^* - j\omega A_2 v_0^* + \frac{\omega}{2\pi} \int_{t_0}^{t_0+T} j\omega v_0 A_2 e^{-j2\omega t} dt + \frac{\omega}{2\pi} \int_{t_0}^{t_0+T} j\omega v_0^* A_2^* e^{j2\omega t} dt, \quad (2.37)$$

which can be reduces to:

$$P_2(\omega) = -j\omega A_2 v_0^* + \text{c.c.} \quad (2.38)$$

Equation (2.38) is equivalent to  $P_2(\omega) = u^* \dot{q}_2 + \text{c.c.}$  We could have also used the expression  $P_2(\omega) = u \dot{q}_2^* + \text{c.c}$  to calculate that electric power. But, since both expressions have the same real parts (active power), which is of particular interest to us for reproduce quantum behavior of EIT, the choice of one or the other expression is not a problem. Solving Eq. (2.18), the expression of the amplitude  $A_2$  is found as:

$$A_2 = \frac{v_0}{l} \frac{\omega_0^2 - \omega^2 - j\omega\Gamma_1}{(\omega_0^2 - \omega^2 - j\omega\Gamma_1)(\omega_0^2 - \omega^2 - j\omega\Gamma_2) - (\Omega^2 - \omega^2 d)^2}, \quad (2.39)$$

Hence, the expression of  $P_2(\omega)$  is found as:

$$P_2(\omega) = -j\omega \frac{|v_0|^2}{l} \frac{\omega_0^2 - \omega^2 - j\omega\Gamma_1}{(\omega_0^2 - \omega^2 - j\omega\Gamma_1)(\omega_0^2 - \omega^2 - j\omega\Gamma_2) - (\Omega^2 - \omega^2 d)^2} + \text{c.c.}, \quad (2.40)$$

where  $\Gamma_k = \gamma_k \omega_0$  ( $k = 1, 2$ ),  $\Omega = \kappa \omega_0$  and  $d = \frac{\mu + \nu_C}{1 + \nu_C}$ .

Near or at the resonance, we assume that for  $|\omega - \omega_0| \ll \omega$ , i.e.,  $\omega \approx \omega_0$ ,  $\gamma_k \omega \approx \gamma_k \omega_0$  and,

$$\omega_0^2 - \omega^2 = (\omega_0 + \omega)(\omega_0 - \omega) \simeq 2\omega_0(\omega_0 - \omega). \quad (2.41)$$

Using the above approximation, the complex power is obtained from Eq. (2.40) as:

$$P_2(\omega) = -jp_0 \frac{f_1}{2f_1 f_2 - C_T^2/2}, \quad (2.42)$$

where  $f_k = \delta/\omega_0 - j\gamma_k/2$ , ( $k = 1, 2$ ),  $p_0 = |v_0|^2/l\omega_0$ ;  $C_T = d - \kappa$  and  $\delta = \omega_0 - \omega$  is the detuning frequency.

### ★ Partial fraction decomposition method

Partial fraction decomposition is used when we have a fraction  $\frac{P(x)}{Q(x)}$ , where  $P$  and  $Q$  are polynomials, and the degree of  $P$  is less than the degree of  $Q$ . (Note that if the degree of the numerator is larger than the denominator, then perform long division first). Assume  $Q$  is fully factored, i.e.,

$$Q(x) = (a_1 x + b_1)(a_2 x + b_2) \dots (a_k x + b_k). \quad (2.43)$$

Then a fraction  $\frac{P(x)}{Q(x)}$  can be rewritten as:

$$\frac{P(x)}{Q(x)} = \frac{A_1}{a_1x + b_1} + \frac{A_2}{a_2x + b_2} + \dots + \frac{A_k}{a_kx + b_k}. \quad (2.44)$$

The denominator of the complex power found in Eq. (2.42), i.e.,  $2f_1f_2 - C_T^2/2$  can be factorized. Its roots are the eigenfrequencies  $\omega_+$  and  $\omega_-$  expressed in Eq. (2.33). Hence, applying the partial fraction decomposition method, the complex power can be decomposed as a sum of two resonants terms,  $P_{2k}(\omega)$  ( $k = 1, 2$ ) as:

$$P_{21}(\omega) = -j \frac{p_0}{2(\omega_+ - \omega_-)} \cdot \frac{f_+}{\omega - \omega_+}, \quad (2.45)$$

$$P_{22}(\omega) = j \frac{p_0}{2(\omega_+ - \omega_-)} \cdot \frac{f_-}{\omega - \omega_-}, \quad (2.46)$$

where  $f_{\pm} = \omega_0 - \omega_{\pm} - j\varepsilon\gamma_2/2$ ,  $p_0 = |v_0|^2/l\omega_0$ .

Therefore,

$$P_2(\omega) = P_{21}(\omega) + P_{22}(\omega). \quad (2.47)$$

### 2.3.1.2 ZRC dimer

We consider that both ZRC loops have the same natural frequency  $\omega_0 = 1/rC$ , where  $r = r_{ei}$  and  $C = C_{ei}$ ,  $\omega_0$  being positive or negative (see Table 2.1 for the conditions). Assuming for the charges the harmonic solutions  $q_i(t) = A_i e^{j\omega t} + \text{c.c}$  (where c.c is a complex conjugate), the Eq. (2.21) leads to the following matrix representation in absence of the voltage:

$$\begin{pmatrix} \delta + j\omega\beta_0 & \omega\beta_C - \Omega \\ \omega\beta_C - \Omega & \delta + j\omega\beta_1 \end{pmatrix} \begin{pmatrix} A_0 \\ A_1 \end{pmatrix} = \begin{pmatrix} 0 \\ 0 \end{pmatrix}, \quad (2.48)$$

where  $\beta_C = r_C/r$ ,  $\Omega = 1/rC_C = \kappa\omega_0$ ,  $r = r_{0,1} + r_C$ ,  $\kappa = C/C_C$ ,  $\omega_0 = 1/rC$ ,  $C = \frac{C_{0,1}C_C}{C_{0,1} + C_C}$  and  $\delta = \omega_0 - \omega$  is the frequency detuning.

We are interested in the behavior of the system near the resonance. For that, we use the approximation  $|\omega - \omega_0| \ll \omega$ ,  $\beta\omega \approx \beta\omega_0$ . Therefore, Eq. (2.48) can be rewritten as:

$$\left[ \omega_0 \begin{pmatrix} 1 + j\beta_0 & c \\ c & 1 + j\beta_1 \end{pmatrix} - \omega \begin{pmatrix} 1 & 0 \\ 0 & 1 \end{pmatrix} \right] \begin{pmatrix} A_0 \\ A_1 \end{pmatrix} = \begin{pmatrix} 0 \\ 0 \end{pmatrix}, \quad (2.49)$$

where  $c = \beta_C - \kappa$  is the effective coupling of the system. Equation (2.49) has non-trivial solutions if the determinant of the left-most term vanishes. Then, we need to solve the characteristic equation  $|\mathcal{H} - \omega I| = 0$ , where  $I$  is the  $2 \times 2$  identity matrix and  $\mathcal{H}$  is a non-Hermitian Hamiltonian written as:

$$\mathcal{H} = \omega_0 \begin{pmatrix} 1 + j\beta_0 & c \\ c & 1 + j\beta_1 \end{pmatrix}. \quad (2.50)$$

The  $2 \times 2$  matrix  $\mathcal{H}$  has a form of a two state non-Hermitian Hamiltonian describing open quantum systems. One of its particularity is to admit a pair of two complex conjugate mode frequencies instead of four, as with the LRC coupled systems. For this later case, the eigenfrequencies are those of an effective Hamiltonian  $\mathcal{H}_{eff}$ , which results from the similarity transformation of the  $4 \times 4$  matrix  $\mathcal{L}$  as we will describe below for the dimer MLC parallel.

Through diagonalization of  $\mathcal{H}$ , the eigenfrequencies  $\omega_{\pm}$  of the ZRC dimer can be expressed as follows:

$$\omega_{\pm} = \omega_0 \left( 1 + jB \pm \sqrt{c^2 - \beta^2} \right), \quad (2.51)$$

where  $\kappa = C / (C + C_C)$ ;  $B = (\beta_1 + \beta_0) / 2 = \beta_0 (\varepsilon + 1) / 2$ ;  $\beta = (\beta_1 - \beta_0) / 2 = \beta_0 (\varepsilon - 1) / 2$  and  $c = \beta_C \pm \kappa$  is the effective coupling parameter. Here  $\varepsilon = \beta_1 / \beta_0$  is the gain/loss ratio.

#### ★ Energy in a single oscillator ZRC

The charge capacitor in Eq. (2.19), oscillates according to  $q_0(t) = q_0(0) \exp(-\omega_0 t / (\beta_0 + j))$  where  $q_0(0)$  is the initial charge amplitude. Then, substituting  $I_0 = dq_0/dt$ , the expression of the current through the loop is obtained as:

$$I_0(t) = I_0(0) \exp(-\omega_0 t / (\beta_0 + j)), \quad (2.52)$$

where the amplitude  $I_0(0)$  is found thanks to the initial conditions of the loop.

#### ★ Power in a single oscillator ZRC

In the absence of any coupling (SW off), the first row of Eq. (2.21) can be rewritten for a single oscillator ( $Z_0, R_0, C_0, Z_C, C_C$ ) as:

$$(\beta_0 + j) \frac{dq_0}{dt} + \omega_0 q_0 = u / r_{e0}, \quad (2.53)$$

where  $r_{e0} = r_0 + r_C$ ,  $u(t) = v_0 e^{j\omega t} + \text{c.c.}$ , c.c. is the complex conjugate.  $\omega$  is the voltage frequency,  $v_0$  its amplitude and  $\beta_0^{-1} = (R_0 / r_{e0})^{-1}$  is the circuit's quality factor. The general solution of Eq. (2.53) can be written in the form:

$$q_0(t) = \alpha e^{-\omega_0 t / (\beta_0 + j)} + (A e^{j\omega t} + \text{c.c.}), \quad (2.54)$$

where  $A = v_0 / [r_{e0} (\delta + j\beta_0 \omega)]$  is a complex amplitude,  $\delta = \omega_0 - \omega$  is the frequency detuning and  $\alpha$  is a constant amplitude. In the steady state regime, the first term of  $q_0(t)$  can be neglected and we can only consider that  $q_0(t) \approx A e^{j\omega t} + \text{c.c.}$  Hence, we can

evaluate the instantaneous power  $P_0(t)$  through the loop using Eq. (2.14), i.e.  $P_0(t) = (v_0 e^{j\omega t} + \text{c.c.}) \dot{q}_0(t)$ . Then, the average power  $P_0(\omega)$  transferred to the circuit during one period  $T = 2\pi/|\omega|$  of oscillation can then be evaluated using Eq. (2.15):

$$P_0(\omega) = \frac{1}{2\pi/\omega} \int_0^{2\pi/\omega} [P_0(t)] dt = \frac{1}{2\pi/\omega} \int_0^{2\pi/\omega} [(v_0 e^{j\omega t} + \text{c.c.}) \dot{q}_0(t)] dt. \quad (2.55)$$

Under the approximation  $|\omega - \omega_0| \ll \omega$ ,  $\beta\omega \approx \beta\omega_0$ , and using a few step of algebra, the complex power is finally obtained as:

$$P_0(\omega) \approx j \frac{p_0}{\chi_0}, \quad (2.56)$$

where  $j^2 = -1$ ,  $p_0 = |v_0|^2/r$ ,  $\chi_0 = \delta_0/\omega_0 + j\beta_0$  and  $\delta_0 = \omega_0 - \omega$ .

### ★ Energy in a dimer ZRC

In absence of the voltage, the eigenvectors  $A_{i+}, A_{i-}$  ( $i = 0, 1$ ) which describes the normal modes of the ZRC dimer verify:

$$A_{1\pm} = \alpha_{\pm} A_{0\pm}, \quad (2.57)$$

where  $\alpha_{\pm} = \frac{\omega_0 + (j\beta_0 - 1)\omega_{\pm}}{\Omega - \omega_{\pm}\beta_c} = \frac{\Omega - \omega_{\pm}\beta_c}{\omega_0 + (j\beta_1 - 1)\omega_{\pm}}$ . Hence, the general solution  $q_{0,1}(t)$  for the dimer is given by:

$$q_i(t) = A_{i+} e^{j\omega_+ t} + A_{i-} e^{j\omega_- t}, \quad (i = 0, 1). \quad (2.58)$$

Where the amplitudes  $A_{0\pm}$  are found from the initial conditions of the oscillators as:

$$A_{0+} = (\alpha_- q_0(0) - q_1(0)) / (\alpha_- - \alpha_+), \quad (2.59)$$

and

$$A_{0-} = (q_1(0) - \alpha_+ q_0(0)) / (\alpha_- - \alpha_+), \quad (2.60)$$

$q_i(0)$  being the initial charges of the capacitors. We calculated the amplitude squared  $|q_i|^2$  associated to each oscillator and the response is significantly describing the transfer of energy from one oscillator to another.

### ★ Power in a dimer ZRC series

Let's investigate the system dimer taking into account the external voltage source  $u(t)$ . In this case, the exact solutions  $q_i(t)$  of Eq. (2.21) can be written as a sum of two terms  $q_0(t) = q_0^C(t) + q_0^P(t)$ .  $q_0^C(t)$  is the complementary solution which linearly combines the two normal modes frequencies of the dimer i.e.  $q_0^C(t) = A_{0+} e^{j\omega_+ t} + A_{0-} e^{j\omega_- t}$ , where the eigenfrequencies  $\omega_{\pm}$  were obtained in Eq. (2.51).  $A_{0\pm}$  are the complex amplitudes.  $q_0^P(t)$  is a particular solution. It can be taken in the form of the voltage as  $q_0^P(t) =$

$\rho_0 e^{j\omega t} + \text{c.c.}$ , where  $\rho_0$  is the amplitude. In the steady state in general, only a particular solution remains. It is interesting to analyze the power transferred to the oscillators by the external voltage. Hence, substituting  $q_0^P(t)$  into Eq. (2.15), the steady state electric power transferred to the main loop ( $Z_0, R_0, C_0, C_C, Z_C$ ),  $P_0(\omega)$  is found to be:

$$P_0(\omega) = \frac{|V_0|^2}{r_{e0}} \frac{j\omega(\delta + j\beta_1\omega)}{(\delta + j\beta_0\omega)(\delta + j\beta_1\omega) - (\Omega - \beta_c\omega)^2}, \quad (2.61)$$

where  $\delta = \omega_0 - \omega$  and  $\Omega = \kappa\omega_0$ . Therefore, using the approximation  $|\omega - \omega_0| \ll \omega$ ,  $\beta\omega \approx \beta\omega_0$ , the electric complex power through the loop is obtained as:

$$P_0(\omega) \approx j \frac{p_0\chi_1}{\chi_0\chi_1 - c^2}, \quad (2.62)$$

where  $p_0 = |v_0|^2/r$ ,  $c = \beta_c \pm \kappa$ ,  $\chi_i = \delta_i/\omega_0 + j\beta_i$  and  $\delta_i = \omega_i - \omega$  is the detuning.

### 2.3.1.3 ZRC multi dimer

Considering the harmonic solutions  $q_i(t)$  for the loop  $i$ , ( $i = 0..N$ ) the Eq. (2.22) can be rewritten in the following matrix, in the absence of a voltage source:

$$\begin{pmatrix} \chi_0 & c_0 & c_0 & \cdots & c_0 \\ c_1 & \chi_1 & -c_1 & \cdots & -c_1 \\ c_2 & -c_2 & \chi_2 & \cdots & -c_2 \\ \vdots & \vdots & \vdots & \ddots & \vdots \\ c_N & -c_N & -c_N & \cdots & \chi_N \end{pmatrix} \begin{pmatrix} A_0 \\ A_1 \\ A_2 \\ \vdots \\ A_N \end{pmatrix} = \begin{pmatrix} 0 \\ 0 \\ 0 \\ \vdots \\ 0 \end{pmatrix}, \quad (2.63)$$

where ( $i = 0..N$ ),  $c_i = \beta_{c_i} - \kappa_i$ ,  $\beta_{c_i} = r_C/r_{ei}$ ,  $\kappa_i = \Omega_i/\omega_0$ ,  $\chi_i = \delta_i/\omega_0 + j\beta_i$ ,  $\delta_i = \omega_i - \omega$ ,  $\beta_i = R_i/r_{ei}$ ,  $r_{ei} = r_i + r_C$ , and  $C_{ei} = C_i C_C / (C_i + C_C)$ .

The eigenfrequencies of the system can be investigated assuming identical values of the imaginary resistances in the circuit  $r_{i(i=0..N)} = r$  while the capacitances are distinct, i.e.,  $\beta_{c_i} = \beta_C$ ,  $\kappa_i = \kappa$ , and  $c_i = c = \beta_C - \kappa$ .

Using the approximation  $|\omega - \varpi| \ll \omega$ ,  $\beta_i\omega \approx \beta_i\varpi = \beta_i\omega_0$  (where  $\varpi = \omega_0$  is the mean frequency), after a few steps of algebra, the determinant of the left most term in Eq. (2.63) is found to be:

$$D(\omega) = \prod_{i=0}^N \chi_i - Nc^{N+1} - \sum_{p=1}^N \sum_{i=0}^{N-p+1} \sum_{k=i+1}^{N-p+2} \cdots \sum_{s=i+q}^{N-p+q} (N-p)c^{N-p+1} \chi_i \chi_k \cdots \chi_s, \quad (2.64)$$

where  $1 \leq p \leq N$ ,  $2 \leq n \leq N$ ,  $N \geq 1$ ,  $q \geq 2$ ,  $u \geq 3$ .

Then, the eigenfrequencies of the system are the roots of  $D(\omega)$ , which can be obtained numerically with Matlab.

### ★ Power in a ZRC multi dimer

Adding the voltage term  $u(t) = v_0 e^{j\omega t} + c.c$  in the right term of Eq. (2.63), and solving such equation, the amplitudes  $A_i$  ( $i = 0 \dots N$ ) can be obtained, and accordingly, the charge solution  $q_0(t)$  through the central loop. Thanks to Eq. (2.14), we have calculated the expression of the steady state frequency-dependence power  $P_0(\omega)$ , which is dissipated by the main loop as a function of the  $N$  number ( $N \geq 1$ ) of multipod loops.

Under the approximation  $|\omega - \varpi| \ll \omega$ ,  $\beta_i \omega \approx \beta_i \varpi$ , where  $\varpi = \omega_0$  is the mean frequency of the system and, using steps of algebra, the steady state power  $P_0(\omega)$  is found to be:

$$P_0(\omega) = \frac{j}{D(\omega)} \left( \prod_{l=1}^N \chi_l - (N-1)c^N - \sum_{n=2}^N \sum_{m=1}^{N-n+2} \sum_{h=m+1}^{N-n+3} \dots \sum_{v=m+u}^{N-n+u} (N-n)c^{N-n+1} \chi_m \chi_h \dots \chi_v \right), \quad (2.65)$$

where  $1 \leq p \leq N$ ,  $2 \leq n \leq N$ ,  $N \geq 1$ ,  $q \geq 2$ ,  $u \geq 3$  and the expression of the denominator  $D(\omega)$  is given in Eq. (2.64).

## 2.3.2 Scattering formalism

Wave propagation phenomena have been discussed in several settings. Despite different languages, the fundamental process and the underlying physics coincide. In this section, we develop a formalism of one-dimensional ( $1\mathcal{D}$ ) scattering problems. Considering plane wave solutions and standard oscillating linearity, the scattering problems can be fully described by the wave amplitudes given by a transfer and scatter matrix. To develop this

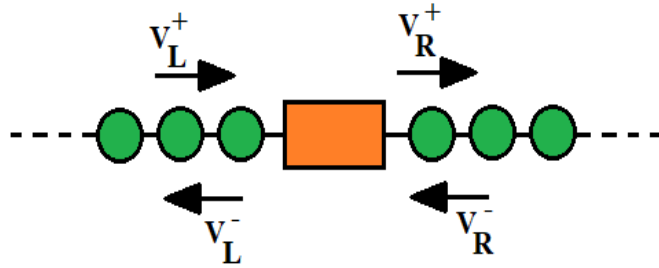


Figure 2.8: Schematic of a generic one-dimensional scattering system.

formalism, let us consider a linear circuit illustrated by the orange color block (defect) of Fig. 2.8, which interrupts the continuity by its left (L) and its right (R), of the conservative TL signal. We can characterize the scattering properties by defining a scattering matrix  $\mathcal{S}$  which relates the outgoing ( $V_R^+$  and  $V_L^-$ ) wave amplitudes to the incoming ( $V_L^+$  and  $V_R^-$ ) ones,

$$\begin{pmatrix} V_R^+ \\ V_L^- \end{pmatrix} = \mathcal{S} \begin{pmatrix} V_L^+ \\ V_R^- \end{pmatrix}, \quad (2.66)$$



where

$$\mathcal{S} = \begin{pmatrix} t_L & r_R \\ r_L & t_R \end{pmatrix}. \quad (2.67)$$

Another useful quantity is the transfer matrix  $\mathcal{M}$ , which relates the wave amplitudes on the right to those on the left:

$$\begin{pmatrix} V_R^+ \\ V_R^- \end{pmatrix} = \mathcal{M} \begin{pmatrix} V_L^+ \\ V_L^- \end{pmatrix}, \quad (2.68)$$

with

$$\mathcal{M} = \begin{pmatrix} \mathcal{M}_{11} & \mathcal{M}_{12} \\ \mathcal{M}_{21} & \mathcal{M}_{22} \end{pmatrix}. \quad (2.69)$$

Therefore, elements of the  $\mathcal{M}$  and  $\mathcal{S}$  matrices can be linked as follows:

$$t_L = \frac{\det \mathcal{M}}{\mathcal{M}_{22}} ; r_L = -\frac{\mathcal{M}_{21}}{\mathcal{M}_{22}} ; t_R = \frac{1}{\mathcal{M}_{22}} ; r_R = \frac{\mathcal{M}_{12}}{\mathcal{M}_{22}}. \quad (2.70)$$

The transmission and reflection amplitudes established above can be complex. Another way of presenting them is the exponential form which brings out their different phases. In this way it comes that:

$$t_L = |t_L| e^{j\phi_{TL}} ; r_L = |r_L| e^{j\phi_{RL}} ; t_R = |t_R| e^{j\phi_{TR}} ; r_R = |r_R| e^{j\phi_{RR}}. \quad (2.71)$$

Therefore, in the following the transmission  $T$  and the reflection  $R$  are defined in terms of dimensionless normalized power.

$$T_L = |t_L|^2 ; R_L = |r_L|^2 ; T_R = |t_R|^2 ; R_R = |r_R|^2. \quad (2.72)$$

### Application: A dimer MLC as a defect in a LC Hermitian ETL

To study scattering properties of our systems we linearly couple the left and the right sides of a  $\mathcal{PT}/\mathcal{APT}$  dimer MLC to a Hermitian ETL depicted in Fig. 2.9. The ETL

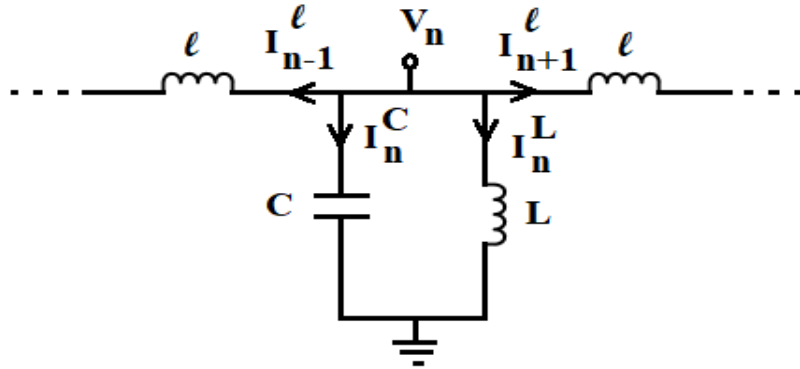


Figure 2.9: Diagram of a Hermitian LC ETL.

consists of inductively coupled parallel LC cells via an inductance  $l$ .

Applying Kirchhoff's laws to such a system leads to the following dimensionless charges of the capacitors at any point along a TL:

★  $\mathcal{PT}$  dimer MLC:

$$\begin{cases} a \frac{d^2 q_0}{dt^2} - c \frac{d^2 q_1}{dt^2} = -\vartheta \omega_0^2 q_{-1} - b \omega_0^2 q_0 + d \omega_0^2 q_1 + \gamma \omega_0 \frac{dq_0}{dt} \\ -c \frac{d^2 q_0}{dt^2} + a \frac{d^2 q_1}{dt^2} = d \omega_0^2 q_0 - b \omega_0^2 q_1 + \vartheta \omega_0^2 q_2 - \gamma \omega_0 \frac{dq_1}{dt} \\ \frac{d^2 q_n}{dt^2} = \vartheta \omega_0^2 q_{n-1} + \vartheta \omega_0^2 q_{n+1} - (1 + 2\vartheta) \omega_0^2 q_n, \text{ for } n \neq 0, 1 \end{cases}, \quad (2.73)$$

★  $\mathcal{APT}$  dimer MLC

$$\begin{cases} a \frac{d^2 q_0}{dt^2} - c \frac{d^2 q_1}{dt^2} = -\vartheta \omega_0^2 q_{-1} - b \omega_0^2 q_0 + d \omega_0^2 q_1 \pm \gamma \omega_0 \frac{dq_0}{dt} \\ -c \frac{d^2 q_0}{dt^2} + a \frac{d^2 q_1}{dt^2} = d \omega_0^2 q_0 - b \omega_0^2 q_1 + \vartheta \omega_0^2 q_2 \pm \gamma \omega_0 \frac{dq_1}{dt} \\ \frac{d^2 q_n}{dt^2} = \vartheta \omega_0^2 q_{n-1} + \vartheta \omega_0^2 q_{n+1} - (1 + 2\vartheta) \omega_0^2 q_n, \text{ for } n \neq 0, 1 \end{cases}, \quad (2.74)$$

where  $\vartheta = \frac{L}{l}$ ,  $a = 1 + c$ ,  $b = \alpha + \nu + \vartheta$  and  $d = \alpha\mu + \nu$ .

We are interested in investigating the transmission, reflection, and amplification properties of the different dimers MLC. For this purpose, we put the solutions of Eqs. (2.73) and (2.74) into the form:

$$\begin{cases} Q_n = I e^{j(k \cdot n - \omega \tau)} + R_g e^{j(-k \cdot n - \omega \tau)}, & n \leq 0 \\ Q_n = T_g e^{j(k \cdot n - \omega \tau)} & , n \geq 1 \end{cases} \quad (2.75)$$

where  $I$ ,  $R_g$  and  $T_g$  are respectively, the incident, the reflected, and the transmitted coefficients from the gain side; and  $k$  is the wave number of the incident wave. It is important to note that the dispersion frequency of the wave in a TL far away from the dimer MLC defect is defined as:

$$\omega^2 = 1 + 4\vartheta \sin^2 \left( \frac{k}{2} \right). \quad (2.76)$$

After substitution of Eq. (2.75) into Eqs. (2.73) and (2.74), the scattering coefficients for an incidence from the gain/loss side are derived to be:

★  $\mathcal{PT}$  dimer MLC

$$\begin{cases} T_g = j \frac{2\vartheta B \sin(k) e^{jk}}{D} I \\ R_g = \frac{B^2 - (A - \vartheta e^{jk})(A^* - \vartheta e^{-jk})}{D} I \\ R_l = \frac{(B^2 - (A - \vartheta e^{-jk})(A^* - \vartheta e^{jk})) e^{-2jk}}{D} I \end{cases}, \quad (2.77)$$

where  $D = (A - \vartheta e^{jk})(A^* - \vartheta e^{-jk}) - B^2$ ;  $A = b - a\omega^2 - j\gamma\omega$ ;  $B = c\omega^2 - d$ , with  $a = 1 + c$ ,  $b = \alpha + \nu + \vartheta$ ,  $d = \alpha\mu + \nu$  and the subscripts  $g$  and  $l$  refer to the incident wave arriving on the  $\mathcal{PTS}$  dimer MLC from the gain or lossy cell sides, respectively.

 ★  $\mathcal{APT}$  dimer MLC

$$\begin{cases} T_{L,R}^\pm = j \frac{2\vartheta B \sin(k) e^{-jk}}{D^\pm} I \\ R_L^\pm = \frac{B^2 - (A^\pm - \vartheta e^{jk})(A^\pm - \vartheta e^{-jk})}{D^\pm} I \\ R_R^\pm = \frac{B^2 - (A^\pm - \vartheta e^{jk})(A^\pm - \vartheta e^{-jk})}{D^\pm} e^{-2jk} I \end{cases}, \quad (2.78)$$

where  $D^\pm = (A^\pm - \vartheta e^{jk})^2 - B^2$ ,  $A^\pm = b - a\omega^2 - j\gamma^\pm\omega$ ,  $B = c\omega^2 - d$ , with  $a = 1 + c$ ,  $b = \alpha + \nu + \vartheta$ ,  $d = \alpha\mu + \nu$ . The subscripts  $L/R$  refer to the incident wave from Left/Right while  $(\pm)$  are associated to  $(\pm\gamma)$  which correspond to the incident wave arriving on the  $\mathcal{APTS}$  dimer MLC made from lossy  $(+\gamma)$  or gain  $(-\gamma)$  cells, respectively. All the scattering coefficients share a common denominator,  $D$  for  $\mathcal{PTS}$  dimer or  $D^\pm$  for  $\mathcal{APTS}$  dimer.

Solving  $D = 0$  or  $(D^\pm = 0)$ , we find the lasing gain/loss parameter  $\gamma_r$  operating at the some critical wavenumber  $k_r$  as:

 ★  $\mathcal{PT}$  dimer MLC:

$$\cos k_r = \frac{b - a(1 + 2\vartheta)}{(1 - 2a)\vartheta}, \quad (2.79)$$

$$\gamma_r = \frac{1}{\omega} \sqrt{B^2 + \vartheta^2 \sin^2 k_r}. \quad (2.80)$$

 ★  $\mathcal{APT}$  dimer MLC:

$$\cos k_r = \frac{(1 + 2\vartheta)(1 + 2c) - (b + d)}{\vartheta(1 + 4c)}, \quad (2.81)$$

$$\gamma_r^\pm = \mp \frac{\vartheta \sin k_r}{\omega}, \quad (2.82)$$

where  $\gamma_r^\pm$  is associated to  $(\pm\gamma)$ .

## 2.3.3 Analytical methods for the non-Hermitian ZRC ETLs

### 2.3.3.1 Schrödinger equation

The Eq. (2.21) describing the general dimer ZRC series is easier to handle. In absence of the external voltage, the action of the  $\mathcal{PT}$  operation on it swaps the indices 0 and 1, and reverses the sign of the pure imaginary number  $j$ . One of the advantages of this circuit is that it can exhibit both a  $\mathcal{PT}$  or  $\mathcal{APT}$  symmetric. In fact, The  $\mathcal{PT}$  operations in conjunction can lead the equations unaltered ( $\mathcal{PTS}$ ) or to its reversal ( $\mathcal{APTS}$ ) according to specific conditions. It is interesting to define in this case the state vector as,  $\psi = (q_0, q_1)^T$  and, using few steps of algebra, Eq. (2.21) is successfully transformed into a Schrödinger-like equation, where we have introduced an effective Hamiltonian  $\mathcal{H}_{eff}$  as follows:

$$j \frac{d\psi}{dt} = \mathcal{H}_{eff} \psi, \quad (2.83)$$

where

$$\mathcal{H}_{eff} = \begin{pmatrix} \frac{\Omega_1 \beta_{c0} - \omega_0 (1 - j\beta_1)}{\Delta} & \frac{\Omega_0 (1 - j\beta_1) - \omega_1 \beta_{c0}}{\Delta} \\ \frac{\Omega_1 (1 - j\beta_0) - \omega_0 \beta_{c1}}{\Delta} & \frac{\Omega_0 \beta_{c1} - \omega_1 (1 - j\beta_0)}{\Delta} \end{pmatrix}, \quad (2.84)$$

with  $\Delta = (1 - j\beta_{c0})(1 - j\beta_{c1}) - \beta_{c0}\beta_{c1}$ ,  $i = 0, 1$ ;  $\beta_i = \frac{R_i}{r_{ei}}$ ;  $r_{ei} = r_i + r_c$ ;  $\beta_{ci} = \frac{r_c}{r_{ei}}$ ;  $\omega_i = \frac{1}{r_{ei}C_{ei}}$ ;  $\Omega_i = \frac{1}{r_{ei}C_c}$ ;  $\frac{1}{C_{ei}} = \frac{1}{C_i} + \frac{1}{C_c}$ .

Let us interest ourselves to the following particular cases:

$$\text{Right - Handed (RH) dimer : } r_c = 0, \text{ i.e } \beta_{ci} = 0, \quad (2.85)$$

and

$$\text{Left - Handed (LH) dimer : } C_c \rightarrow \infty, \text{ i.e } \Omega_i \rightarrow 0. \quad (2.86)$$

Hence, the effective Hamiltonian in Eq. (2.84) can be rewritten according to the dimer in the following form:

$$\mathcal{H}_{eff}^{RH} = \begin{pmatrix} \frac{-\omega_0(1+j\beta_0)}{1+\beta_0^2} & \frac{\Omega_0(1+j\beta_0)}{1+\beta_0^2} \\ \frac{\Omega_1(1+j\beta_1)}{1+\beta_1^2} & \frac{\omega_1(1+j\beta_1)}{1+\beta_1^2} \end{pmatrix}, \quad (2.87)$$

and

$$\mathcal{H}_{eff}^{LH} = -\frac{1}{\Delta} \begin{pmatrix} \omega_0(1-j\beta_1) & \omega_1\beta_{c0} \\ \omega_0\beta_{c1} & \omega_1(1-j\beta_0) \end{pmatrix}. \quad (2.88)$$

Applying now the  $\mathcal{PT}$  symmetry operator in  $2\mathcal{D}$ ,  $\mathcal{PT} = \sigma_x \mathcal{K}$ , where  $\sigma_x$  is the first Pauli matrix and  $\mathcal{K}$  is the complex conjugation operation, we can demonstrate that these Hamiltonians commute i.e  $[\mathcal{PT}, \mathcal{H}_{eff}^{RH/LH}] = 0$ , or anti commute  $\{\mathcal{PT}, \mathcal{H}_{eff}^{RH/LH}\} = 0$ , with the join  $\mathcal{PT}$  operator if the following conditions are fulfilled:

- **$\mathcal{PTS}$  conditions**

$$\text{ZRC RH dimer : } \omega_0 = \omega_1 ; \Omega_0 = \Omega_1 ; \beta_0 = -\beta_1 , \quad (2.89)$$

$$\text{ZRC LH dimer : } \omega_0 = \omega_1 ; \beta_{c0} = \beta_{c1} ; \beta_0 = -\beta_1 . \quad (2.90)$$

- ***APTS* conditions**

$$\text{ZRC RH dimer : } \omega_0 = -\omega_1 ; \Omega_0 = -\Omega_1 ; \beta_0 = -\beta_1 , \quad (2.91)$$

$$\text{ZRC LH dimer : } \omega_0 = -\omega_1 ; \beta_{c0} = \beta_{c1} ; \beta_0 = -\beta_1 . \quad (2.92)$$

### 2.3.3.2 Eigenvalues for a non-Hermitian ZRC ETL

Considering a system of  $2N$  size, the ZRC ETL appears as a cascade association of  $2N$  oscillators ZRC, or as a cascade association of  $N$  dimers ZRC. Therefore, the system becomes *PTS* or *APTS* under the conditions similar as those from Eq. (2.89) to Eq. (2.92) in the cases of both RH and LH dimers. To find the eigenvalues of the system, we solve Eq. (2.28) for RH TL and Eq. (2.29) for LH TL. We look for this, the amplitudes  $I_n$  ( $1 \leq n \leq 2N$ ) in the solutions form proposed for *PT* problems [218],

$$I_n = \begin{cases} ae^{ink} + be^{-ink} & , \quad n \text{ even} \\ \rho (ae^{ink} + be^{-ink}) & , \quad n \text{ odd} \end{cases} \quad (2.93)$$

where  $a$ ,  $b$ , and  $\rho$  are constants and  $k$  is the wave number. In addition, we consider zero boundary conditions in both ETLs on sites  $n = 0$  and  $n = 2N + 1$  which lead to:

$$I_{(n=0)} = I_{(n=2N+1)} = 0 , \quad (2.94)$$

Taking into account these boundary conditions, the solutions given in Eq. (2.93) allow to obtain the discrete values  $k_p$  for the wave number  $k$  as:

$$k_p = \frac{p\pi}{2N + 1} , \quad (2.95)$$

with  $p = 1 \dots N$ . Inserting Eq. (2.93) into Eqs. (2.28) and (2.29), and using few steps of algebra lead to the normalized eigenfrequencies  $\Omega_{\pm}^{RH}(\beta, k_p)$  and  $\Omega_{\pm}^{LH}(\beta, k_p)$  describing the normalized modes frequencies of the RH and LH ETLs, respectively.

- ***PTS* conditions**

$$\Omega_{\pm}^{RH}(\beta, k_p) = \frac{2}{\Delta} \left( 1 \pm \sin(k_p) \sqrt{(\beta_{cr}^{RH})^2 - \beta^2} \right) , \quad (2.96)$$

$$\Omega_{\pm}^{LH}(\beta, k_p) = \frac{2}{\Delta'} \left( 1 \pm \sqrt{(\beta_{cr}^{LH})^2 - \beta^2} \right) , \quad (2.97)$$

where  $\Delta = \beta^2 + 1$  ;  $\Delta' = \beta^2 + 4\sin^2(k_p)$ .

The breaking values are found to be:

$$\beta_{cr}^{RH} = 1/\tan(k_p), \quad (2.98)$$

$$\beta_{cr}^{LH} = 2\cos(k_p). \quad (2.99)$$

- ***APTS* conditions**

$$\Omega_{\pm}^{RH}(\beta, k_p) = \frac{2}{\Delta} \left( j\beta \pm \cos(k_p) \sqrt{(\beta_{cr}^{RH})^2 - \beta^2} \right), \quad (2.100)$$

$$\Omega_{\pm}^{LH}(\beta, k_p) = \frac{1}{\Delta'} (j\beta \pm \cos(k_p)), \quad (2.101)$$

where the threshold reads as

$$\beta_{cr}^{RH} = \tan(k_p), \quad (2.102)$$

with  $\Delta = \beta^2 + 1$  ;  $\Delta' = \beta^2 + 4\sin^2(k_p)$ .

### 2.3.3.3 Electric current function in a non-Hermitian ZRC ETL

To investigate on the exact solutions of the electric current flowing on the  $n$  site through each ETL, we rewrite the solution (2.93) for the amplitude of the electric current using boundaries conditions as:

$$I_n = \begin{cases} 2a\rho \sin(nk_p), & \text{for } n \text{ odd} \\ 2a \sin(nk_p), & \text{for } n \text{ even} \end{cases} \quad (2.103)$$

where the constant  $a$  is obtained from the normalized condition, namely  $\sum_{n=1}^{2N} |I_n|^2 = 1$  as:

$$|a| = \left( 2\sqrt{S_n} \right)^{-1}, \quad S_n = \sum_{n=1}^N \left( \sin^2(2nk_p) + |\rho|^2 \sin^2((2n-1)k_p) \right). \quad (2.104)$$

The parameter  $\rho$  is found according to the given configuration:

- ***PTS* configuration**

$$\rho = e^{j\vartheta}, \quad (2.105)$$

where

$$\text{(RH)} : \vartheta = \tan^{-1} \left( \beta \Omega_{\pm}^{RH}(\beta, k_p) / (2 - \Omega_{\pm}^{RH}(\beta, k_p)) \right), \quad (2.106)$$

$$\text{(LH)} : \vartheta = \tan^{-1} \left( \beta \Omega_{\pm}^{LH}(\beta, k_p) / (1 - 2\Omega_{\pm}^{LH}(\beta, k_p)) \right). \quad (2.107)$$

- ***APTS* configuration**

$$\text{(RH): } \rho^2 = (2 + \Omega(j\beta - 1))/(2 + \Omega(j\beta + 1)), \quad (2.108)$$

$$\text{(LH): } \rho^2 = (-1 + (2 - j\beta)\Omega)/(1 + (2 + j\beta)\Omega). \quad (2.109)$$

### 2.3.3.4 Diagnostic tools to study the localization behavior

We remember that the  $1\mathcal{D}$  tight-binding Anderson model equation is written as :

$$(E - \xi_n) \phi_n - V_{n-1} \phi_{n-1} - V_n \phi_{n+1} = 0, \quad (2.110)$$

where  $E$  is the eigenenergy,  $\xi_n$  is the site energy,  $V_n$  the hopping between neighboring sites, and  $\phi_n$  is the eigenfunction.

A correspondence between the tight-binding Eq. (2.110) and Eq. (2.28) or (2.29) exists. For example, if we apply the following transformations,

$$\begin{aligned} E &= \omega; \quad \phi_n = [(j\beta_n - 1) r_n]^{1/2} I_n; \quad V_n = C_n^{-1} [r_n r_{n+1} (j\beta_n - 1) (j\beta_{n+1} - 1)]^{-1/2}, \\ \xi_n &= -[r_n (j\beta_n - 1)]^{-1} (C_{n-1}^{-1} + C_n^{-1}), \quad \forall n, \end{aligned} \quad (2.111)$$

in tight-binding model equation, we obtain Eq. (2.28) which describes the ZRC RH ETL. A similar correspondence can also be established with the ZRC LH TL. These correspondences between the tight-binding quantum model and our ETLs allows checking the localization behavior of quantum disordered  $1\mathcal{D}$  systems using a non-Hermitian ZRC ETLs.

Among the tools often used for checking the localization behavior, is the normalized localization function

$$\Lambda(\beta, \omega) = \frac{1}{M \lambda(\beta, \omega)}, \quad (2.112)$$

where  $M = 2N$  is the size of the system under study and  $\lambda(\beta, \omega)$  is the Lyapunov exponent given as:

$$\lambda(\beta, \omega) = \lim_{M \rightarrow \infty} \frac{1}{M} \sum_{n=1}^M \ln \left| \frac{I_{n+1}}{I_n} \right|, \quad (2.113)$$

where  $I_n(\beta, \omega)$  is the amplitude of the electric current function in each  $n$ th cell of the TL. To calculate  $\lambda(\beta, \omega)$ , we solve Eqs. (2.28) and (2.29) through an iterative process that deploys the transfer function  $\gamma_n$  defined as:

$$\gamma_n = \frac{I_{n+1}}{I_n}, \quad (2.114)$$

Using Eq. (2.114), the Eq. (2.28) can be written in the following iterative way for  $\gamma_n$ ,

$$\text{(RH): } \gamma_n = \lambda_n - (\gamma_{n-1})^{-1}, \quad (2.115)$$

$$\text{(LH): } \gamma_n = \varepsilon_n - j\beta_n - (\gamma_{n-1})^{-1}, \quad (2.116)$$

where  $\lambda_n = 2 + \omega(j\beta_n - 1)/\omega_n$  and  $\varepsilon_n = 2 - j\beta_n - (\omega/\omega_n)^{-1}$ . Iterating this equation, and starting with  $\gamma_1$ , the full set of  $\gamma_n$  values is obtained. Therefore for an arbitrary initial amplitude value, for example  $I_1$ , the full set of amplitudes  $\{I_n\}$  of the electric current function, can be calculated, i.e.,

$$I_{n+1} = \gamma_n I_n \quad , \quad (2.117)$$

where  $1 \leq n \leq N - 1$ . After that, the electric current function is normalized, i.e.,

$$\sum_{n=1}^N |I_n|^2 = 1. \quad (2.118)$$

Hence, the normalized localization function  $\Lambda(\beta, \omega)$  can be easily evaluated.

## 2.4 Numerical methods

The equations in this thesis are solved mainly using analytical methods. When the later does not allow the analytical solutions to be obtained, we resorted to numerical methods. Thus, in addition to plot analytical solutions, some functions, in particular, the square of the modulus of the electric current  $|I_n|^2$ , the normalized localization function  $\Lambda(\beta, \omega)$  and certain eigenvalues  $\omega$ , have been found using syntaxes predefined in Matlab (version 2016) or Maple (version 18) source programs and subroutines.

## 2.5 Simulations with LTSpice

It is important to do an experimental simulation before real-world electronic circuit is developed. Elaborated by analog devices, the LTSpice simulator is, like most analog simulators, a product of Spice, as PSpice, often used to simulate the devices for industrial applications. The LTSpice simulator presented as a teaching tool, is widely used by electrical and electronics students around the world. In this way, the latter free themselves from the manual resolution of tedious systems of equations and concentrate on the understanding of complex electrical models with complex devices. The electronic analogical simulation method presented here is based on LTSpice XVII program. It has the aim to consolidate the theoretical results obtained analytically within the framework of the study on EIT and related phenomena. To do so, let's consider a simple LRC series loop in presence of a harmonic voltage source  $u(t)$ . The electric current flowing through the inductor has the same frequency dependence as the power transferred from the voltage source to the LRC loop. Therefore, it is sufficient for example, to measure such a current under LTSpice, to qualitatively reproduce the absorption behavior and the dispersion profile expected with the real atomic system.



## Conclusion

In this chapter we have presented different models of non-Hermitian systems to investigate the quantum phenomena of Electromagnetically Induced Transparency (EIT) and Anderson Localization (AL). The analytical and numerical methods used to describe the analog systems and to solve the equations were presented. Finally, some results based on the analytical and numerical methods in this work can be completed by the analogical LTSpice simulation method also described in this chapter. The next chapter of the thesis deals with presentation of the results obtained and the discussions.

---

## Results and Discussions

---

### Introduction

In the previous chapter, we have presented the computational methods needed to address some wave transport phenomena and solved the equations governing them. The present chapter deals with the presentation of our results and the discussions. In section 3.1, Electromagnetically Induced Transparency (EIT) and related phenomena are investigated by analyzing close to the resonance, the effect of the non-Hermiticity on the dispersive properties in a dimer/multi dimer driven by a harmonic voltage source. In section 3.2, the scattering properties of the MLC dimer are also investigated when it is inserted as a defect in a Hermitian  $LC$  conservative electrical transmission line (ETL). In section 3.3, we focus on energy transport and Anderson-like localization behavior in the non-Hermitian ETLs resulting to a successive repetition of ZRC dimers. After that, we conclude the chapter.

### 3.1 Analysis close to the resonance of the effect of non-Hermiticity on dispersive properties in coupled LRC/ZRC oscillators driven by a harmonic voltage: EIT and multiple EIT behavior and related phenomena

As described in chapter 2, the phenomenology observed in EIT can be reproduced using resonant coupled oscillators [58, 59]. Our results will allow to confirm the analogy between the electronic circuits and the atomic systems. The analog model has the advantage that it helps to understand some elementary aspects of the underlying physics and can also be used as an introductory prototype, when introducing coherent systems to beginners and laymen.

The models considered here consist of dimers obtained by coupling LRC and ZRC series oscillators as shown in Fig. 2.1(a), Fig. 2.3 and 2.4(a), respectively. The induced transparency and the related phenomena are investigated by analyzing the frequency de-

pendence power  $P(\omega)$  transferred from the voltage source  $u(t)$  to the resonant circuits, that is, around the natural frequency  $\omega_0$  of the driven circuits. We begin with the eigenmodes analysis of the non-Hermitian systems in absence of the voltage. Here, a structural characterization allows to identify for the systems a weak and a strong coupling regimes, and then to emphasize the couplingless point (CPLP). In particular, we intend to reveal the ranges of frequencies that could exhibit EIT, EIA and ATS quantum phenomena.

### 3.1.1 Eigenmodes analysis

#### 3.1.1.1 Eigenmodes of the dimer MLC series

Equation (2.31) defines in units of  $\hbar = 1$ , the two states non-Hermitian Hamiltonian (NHH) describing the dimer, where  $C_T = d - \kappa$ , has been defined as the effective coupling of the system. This effective coupling can be cancelled, i.e.  $C_T = 0$  (see Eq. (2.32)), if the capacitive coupling parameter obeys to Eq. (3.1), and the dimer is said to be couplingless (CPL).

$$\kappa = d = \frac{\mu + \nu_C}{1 + \nu_C}. \quad (3.1)$$

Then, according to the couplings in place, the different dimers can be classified in two groups: the effective coupling dimers ( $C_T \neq 0$ ) and the effective couplingless dimers ( $C_T = 0$ ).

- The first group, effective coupling (CP) dimers is subdivided in two categories :

**The category 1** consisting of dimers made from a single type of coupling, as the dimer C, dimer L and the dimer M.

**The category 2**, including dimers formed at least of two types of couplings as dimer ML, dimer LC ( $\kappa \neq \nu_C/(1 + \nu_C)$ ), dimer MC ( $\mu \neq \kappa$ ) and dimer MLC ( $\kappa(1 + \nu_C) \neq \nu_C/(\mu + \nu_C)$ ). Except the case of dimer ML, all dimers of this category use capacitive coupling.

- The second group, effective couplingless (CPL) dimers includes dimer LC ( $\kappa = \nu_C/(1 + \nu_C)$ ), dimer MC ( $\mu = \kappa$ ) and dimer MLC ( $\kappa(1 + \nu_C) = \nu_C/(\mu + \nu_C)$ ). The eigenvalues of all types of dimers are expressed in Eq. (2.33)).

The eigenfrequencies  $\omega_{\pm}$  (Eq. (2.33)) are complex. Their real parts are associated to the peak frequencies' whereas their imaginary parts or linewidths are known as the decay rate of the resonant state, and determine the width of the resonance line at its half maximum. The expression of  $\omega_{\pm}$  reveals a transition at a effective coupling threshold  $C_{Tcr} = |\zeta|$  occurring when the square root in equation Eq. (2.33) vanishes. Then, we can define the region where  $C_T^2 - C_{Tcr}^2 < 0$  as the weak-driving regime and the region  $C_T^2 - C_{Tcr}^2 > 0$  as the strong-driving regime.  $C_T = C_{Tcr}$  is the transition point also

known as the exceptional point (EP) [13, 220].

### (1) Effective coupling (CP) dimers

#### a) Category 1

As we said, the category 1 consists of dimers made from a single type of coupling. For illustration, we restrict the eigenmodes analysis in this category, by considering only the case of the effective CP dimer L. For such a dimer, the real and the imaginary parts of the normal modes frequencies  $\omega_{\pm}/\omega_0$  are reported in Figs. 3.1(a) and 3.1(b) as a function of the normalized active coupling  $\nu_C/\nu_{Ccr}$ , for different values of the gain/loss ratio  $\varepsilon$  defined in Eq.(3.2). The corresponding normalized frequency splitting  $((\omega_+ - \omega_-)/\omega_0)$  is also presented in Figs. 3.1(c) and 3.1(d) as a function of  $\nu_C$  and  $\varepsilon$ .

$$\varepsilon = \gamma_1/\gamma_2, \quad (3.2)$$

where  $\gamma_1$  and  $\gamma_2$  are the normalized gain/loss for the mesh simulating the pump and the atom, respectively. The plots reveal one EP,  $\nu_{Ccr}$  which separates the weak to the strong coupling regime. The evolution of the coupling threshold  $\nu_{Ccr}$  as function of  $\varepsilon$  is indicated in green curves on Figs. 3.1(c) and 3.1(d).

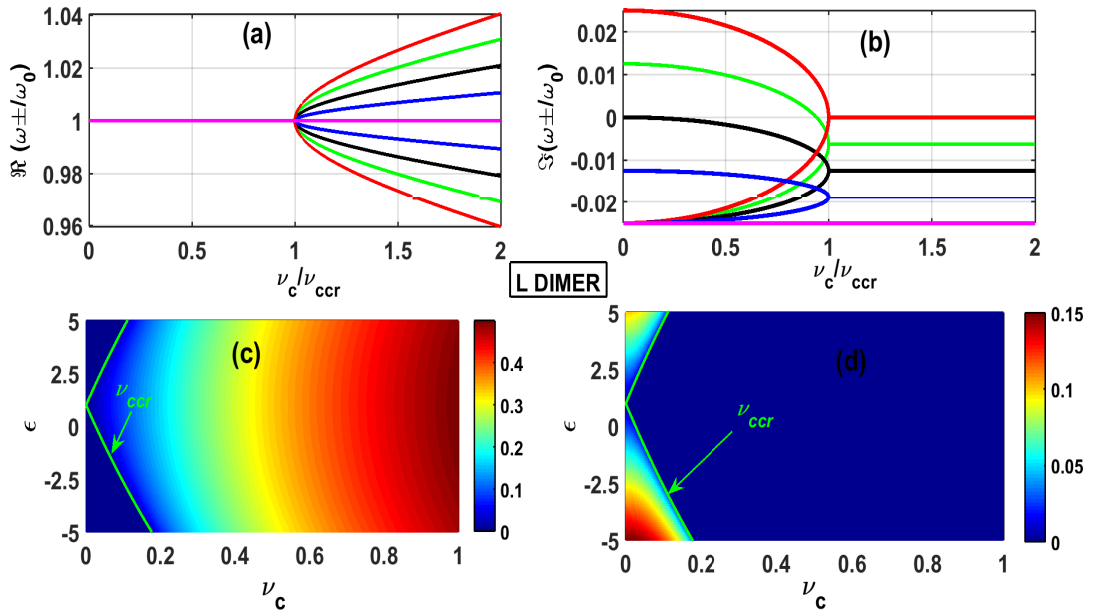


Figure 3.1: Effective CP dimer L. (a, b): Variation of the real and imaginary parts of  $\omega_{\pm}/\omega_0$  as function of  $\nu_C/\nu_{Ccr}$  for different values of  $\varepsilon$ .  $\varepsilon = -1$  (red);  $\varepsilon = -0.5$  (green);  $\varepsilon = 0$  (black);  $\varepsilon = 0.5$  (blue);  $\varepsilon = 1$  (magenta). (c, d): The real and imaginary parts of the eigenfrequencies splitting.

Indeed, in the regime of weak coupling where  $\nu_C < \nu_{Ccr}$ , we find that the two modes of frequencies have the same real part  $\Re(\omega_{\pm}) = \omega_0$ , but, show splitting in the imagi-

nary part  $\Im(\omega_{\pm}) = \frac{\omega_0}{2}(-\eta \pm \sqrt{-\Lambda})$ ; in fact, as we can see from Figs. 3.1(c) and 3.1(d),  $\Re((\omega_+ - \omega_-)/\omega_0) = 0$  while  $\Im((\omega_+ - \omega_-)/\omega_0) \neq 0$ . On contrary, in the strong-driving regime where  $\nu_C > \nu_{Ccr}$ , we find  $\Re(\omega_{\pm}) = \frac{\omega_0}{2}(2 \pm \sqrt{\Lambda})$  and  $\Im(\omega_{\pm}) = -\eta \frac{\omega_0}{2}$ . So, the imaginary parts are crossing while the real parts do not (see again Figs. 3.1(c) and 3.1(d)) where the splitting is real (i.e.  $\Re((\omega_+ - \omega_-)/\omega_0) \neq 0$  and  $\Im((\omega_+ - \omega_-)/\omega_0) = 0$ ). At the EP where  $\nu_C = \nu_{Ccr}$ , the frequencies  $\omega_{\pm}$  are complex with  $\Re(\omega_{\pm}) = \omega_0$  and  $\Im(\omega_{\pm}) = -\eta \frac{\omega_0}{2}$ . The splitting frequency is there equal to zero. Remarkably, the coupling threshold decreases as  $\varepsilon$  tends toward the value  $\varepsilon = 1$  where it is annuls, leading to a vanishing of the weak-driving regime. There,  $\Re(\omega_{\pm}) = \frac{\omega_0}{2}(2 \pm \sqrt{\Lambda})$  and  $\Im(\omega_{\pm}) = -\eta \frac{\omega_0}{2}$ . All results obtained here with the dimer L are generalized to other effective CP dimer belonging to this category.

### b) Category 2

As mentioned above, the dimer of this category are made at least of two couplings. We

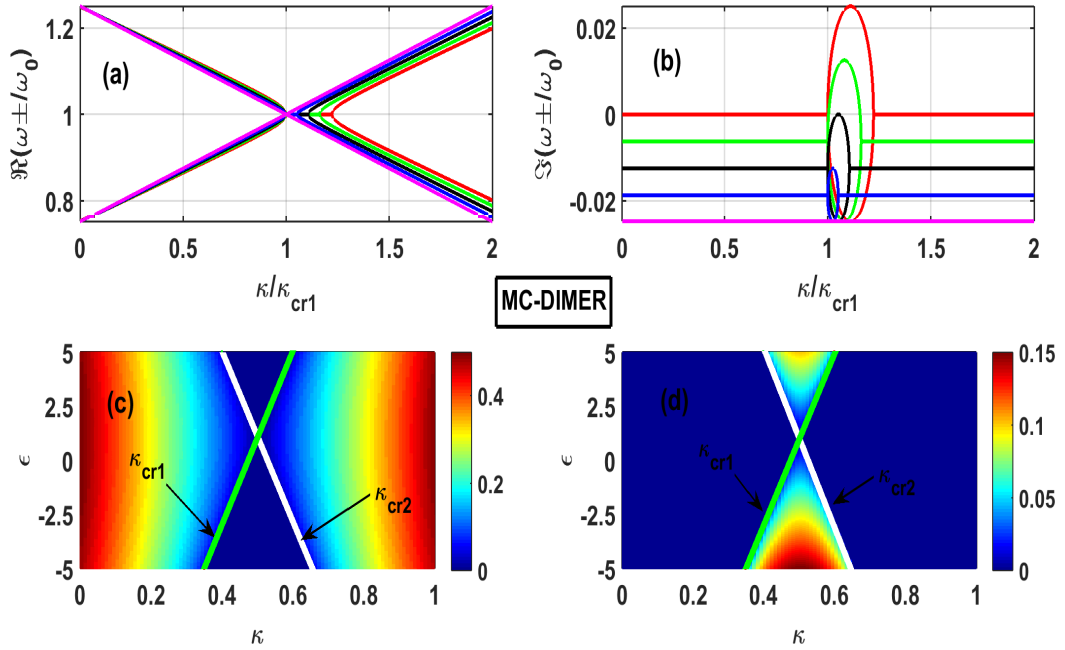


Figure 3.2: Effective CP dimer MC (when  $\mu = 0.50$ ,  $\kappa \neq \mu$ ). (a, b): Variation of the real and imaginary parts of  $\omega_{\pm}/\omega_0$  as function of  $\kappa/\kappa_{cr1}$  for different values of  $\varepsilon$ .  $\varepsilon = -1$  (red);  $\varepsilon = -0.5$  (green);  $\varepsilon = 0$  (black);  $\varepsilon = 0.5$  (blue);  $\varepsilon = 1$  (magenta). (c, d): The real and imaginary parts of the eigenfrequencies splitting and coupling threshold evolution. The coupling thresholds are indicated in green and white color as  $\kappa_{cr1}$  and  $\kappa_{cr2}$  with ( $\kappa_{cr1} < \kappa_{cr2}$ ) between which is located the weak coupling regime. Both critical values merge to only one point for  $\varepsilon = 1$  when  $\kappa = \mu$ . At this last point the weak regime vanishes. The color bar indicates the magnitude of the splitting. For all plots  $\gamma_2 = 0.05$ . The first and second column represent the real and imaginary parts, respectively. Except for dimer ML, all plots obtained here qualitatively describe what is observed in other types of CP dimers of category 2.

consider the case of dimer MC to illustrate the eigenmodes of this category of CP dimers. In Figs. 3.2(a) and 3.2(b), we have plotted the real and the imaginary parts of the eigenfrequencies  $\omega_{\pm}/\omega_0$  respectively as a function of the normalized active coupling  $\kappa/\kappa_{cr}$  for different values of the parameter  $\varepsilon$ . The plots parameters are  $\mu = 0.5$  and  $\gamma_2 = 0.05$ . In Figs. 3.2(c) and 3.2(d), we have also plotted the frequency splitting as a function of  $\varepsilon$  and the active coupling  $\kappa$ . Unlike dimers of category 1, those of this second category present two EPs, EP1 and EP2 given as  $\kappa_{cr1,2} = \mu \pm \gamma_2 (\varepsilon - 1) / 2$  (with  $\kappa_{cr1} < \kappa_{cr2}$ ) between which there is the weak-driving regime. The domain outside of the EPs ( $0 < \kappa < \kappa_{cr1}$  and  $\kappa_{cr2} < \kappa < 1$ ) constitutes the strong coupling regime. The variation of these EPs are shown in green and white curves as a function of  $\varepsilon$  in Figs. 3.2(c) and 3.2(d). Both EPs coalesce when  $\varepsilon = 1$  to form only one EP resulting in the disappearance of the weak regime. We can notice as in the case of dimers of category 1 that, in the weak-driving regime, the real parts of eigenfrequencies cross while their imaginary parts split. The similar behavior is observed in the strong-driving regime, where it is rather the imaginary parts which are crossing while the real parts split. In all cases, the frequency splitting increases when one moves away from the boundary between the two regimes and from the value  $\varepsilon = 1$ . At the EPs ( $\kappa = \kappa_{cr1,2}$ ), the splitting frequency is equal to zero. The case of dimer ML (with  $\mu = 0.2$ ) (not shown in Figure), presents a peculiarity of the dimers made with multiple couplings, thus, making of it an exception of this category. Indeed, the dimer L and the dimer M taken separately, each possess a weak-driving regime. However the association of their active couplings into dimer ML contributes to shift this driving-regime on the side of the negative couplings (that are not the objective of the study in this section). This leads only to the strong-driving regime, where, the imaginary parts of the eigenmodes coalesce while the real parts are avoiding. We can thus say with certainty that the appearance of the weak regime and the possibility of cancelation of the effective coupling in the dimers of category 2, is due only to the capacitive coupling  $C_C$ .

## (2) Effective coupling less (CPL) dimer

Effective coupling less (CPL) dimers are characterized by the vanishing of their effective coupling  $C_T$  ( $C_T = 0$ ). Remarkably, the couplingless occurs in the dimers whose coupling combines in series the capacitive coupling  $C_C$  with at least one of the coupling  $M$  or  $L$ . Then, the coupling parameters should obey to Eq. (2.32) that we called coupling cancelation condition. The particular point where this occurs is called the couplingless point (CPLP). Since  $C_T = 0$  at the CPLP, the parts of the dimer although coupled, behaves like two uncoupled circuits of eigenfrequencies  $\omega_{\pm} = (1 - j\gamma_k) \omega_0 / 2$  ( $k = 1, 2$ ). The real parts of the two modes frequencies share the same value but show splitting in their imaginary parts as we can identify in Fig. 3.2 when  $\kappa = \mu = 0.5$ . When  $\varepsilon = 1$ , both eigenmodes coalesce and the CPLP becomes the EP evoked above where the weak-driving regime completely disappears. Finally, note that the analysis made here with the dimer

MC remains valid for all other effective CPL dimers.

The aim of the next section is to give details on the structural characterization of the ZRC systems in the absence of an external voltage source.

### 3.1.1.2 Eigenmodes of the ZRC dimer

Before any analysis of the eigenfrequencies expressed in Eq. (2.51), it is instructive to note that the structural characterization done here consists in studying the behavior of the eigenfrequencies  $\omega_{\pm}$ . This allows us to analyze the real and the complex energy band frequencies which definitively have impact on the quantum interference dynamic.

- It is obvious that when  $\beta_0 = 0, \forall \varepsilon$  (no gain or loss in the loops),  $\omega_{\pm} = \omega_0 (1 \pm c)$ , all frequencies are real. The Hamiltonian  $\mathcal{H}$  is Hermitian.
- In the non-Hermitian case,  $\beta_0 \neq 0, \forall \varepsilon$ . The eigenfrequencies in Eq. (2.51) can be real or complex in general, depending on the  $\varepsilon$  parameter. In particular, three cases can be considered:
  - If  $\varepsilon = -1$ , i.e.  $\beta_1 = -\beta_0 \neq 0$ , the loss and the gain are exactly compensated. This gives rise to a particular class of non-Hermitian systems called the parity time symmetric  $\mathcal{PTS}$  of which the Hamiltonian  $H$  commutes with the join Parity-Time symmetry operator  $\mathcal{PT} = \sigma_x \mathcal{K}$  (where  $\sigma_x$  is the first Pauli matrix and  $\mathcal{K}$  is the complex conjugation operation). Under the  $\mathcal{PTS}$  conditions, the eigenfrequencies in Eq. (2.51) are reduced to  $\omega_{\pm} = \omega_0 \left( 1 \pm \sqrt{c^2 - \beta_0^2} \right)$ . Then, the eigenspectrum displays a spontaneous symmetry breaking at the coupling threshold  $c = c_{th}$ , where  $c_{th} = |\beta_0|$  known as the EP separates two phases: the  $\mathcal{PT}$  unbroken phase ( $\beta_0 < |c|$ ) where the frequencies are totally real, and the  $\mathcal{PT}$  broken phase ( $\beta_0 > |c|$ ) for which the frequencies are complex. It is important to mention that  $\mathcal{PTS}$  systems have demonstrated many intriguing features in several areas of physics.
  - If  $\varepsilon = 1$ , i.e.  $\beta_1 = \beta_0 \neq 0$ , the system is either amplifying or dissipative. The eigenfrequencies are complex and can be expressed as  $\omega_{\pm} = \omega_0 (1 \pm c + j\beta_0)$ . The imaginary part of the frequencies  $\omega_{\pm}$  are constant and the real parts coalesce at the particular point where the effective coupling vanishes.

$$c = 0 \quad \Leftrightarrow \quad \beta_C = \kappa \neq 0. \quad (3.3)$$

This point is referred to as the couplingless point (CPLP) in the case of the dimer ZC.

- The third case  $\varepsilon \neq \pm 1, \forall \beta_0 \neq 0$ , the gain and the loss are not compensated in the non-Hermitian system. As a consequence, the eigenfrequencies  $\omega_{\pm}$  remains complex and display a phase transition at two EPs which separate complex phases.

At the transition points, the effective coupling strength satisfies to  $c = c_{th}$ , where  $c_{th} = |\beta| = \beta_0 |\varepsilon - 1|/2$ .

In what follows we will illustrate the analysis made above considering two coupled systems, one with the single coupling, and another with a double coupling. The aim is to demonstrate that a double coupling gives rise as in the case of a dimer MLC, to a new phenomenon that we cannot observe in the simple coupling. In particular, we want to emphasize the couplingless point (CPLP) that we have illustrated in Eq. (3.3). For a double coupled system, the coupling parameters are non-zero, i.e.  $\beta_C \neq 0$ ,  $\kappa \neq 0$  (dimer ZC), for example, we set  $\kappa = 0.75$  which remains constant; whereas for a simple coupled system,  $\kappa = 0$  and  $\beta_C \neq 0$  (dimer Z). In both cases, we choose  $\beta_0 = 0.5 \neq 0$  and it can be easily verified from Eq. (2.51) that these systems are non-Hermitian.

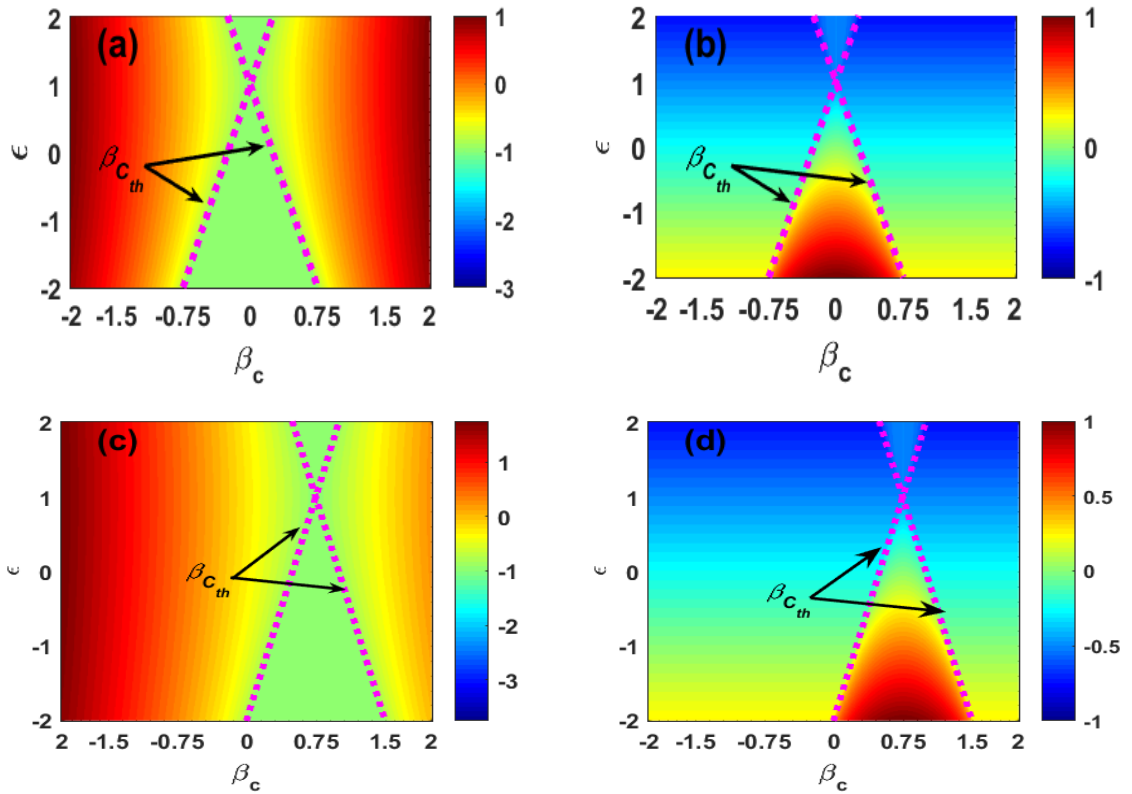


Figure 3.3: 3D top view of the real (first column) and imaginary (second column) parts of the normalized eigenfrequencies  $\omega_{\pm}/|\omega_0|$  of the ZRC dimer as function of the controlling coupling parameter  $\beta_c$  and the gain/loss ratio  $\varepsilon$ , in the case of dimer Z of which  $c = \beta_c$  ((a), (b)) and of the dimer ZC when fixed  $\kappa = 0.75$  ((c), (d)). The coupling threshold  $\beta_{C_{th}}$  is indicated with the dashed magenta color. For all plots  $\beta_0 = 0.5$ .

In Fig. 3.3, the real (first column) and the imaginary (second column) parts of the normalized eigenfrequencies  $\omega_{\pm}/|\omega_0|$  are shown as a function of the controlling coupling parameter  $\beta_c$  and the gain/loss ratio  $\varepsilon$ . The spectra are obtained with the negative frequency  $\omega_0 < 0$ , since the eigenfrequencies are the odd function of  $\omega_0$ . The exceptional points are indicated as a coupling threshold  $\beta_{C_{th}}$  with a dashed magenta curves in 3D



(top view) plots ((a), (b) for the dimer Z, and (c), (d) for the dimer ZC). As it can be expected, the frequencies  $\omega_{\pm}$  come in complex conjugate pairs and two coupling regimes are exhibited: the weakly driving regime ( $|c| < |\beta|$ ), characterized by the coalescence of the real parts of the eigenfrequencies and the splitting of their imaginary parts; and the strongly coupling regime ( $|c| > |\beta|$ ), where the imaginary parts of the eigenfrequencies cross and the real parts split. The splitting analysis will be studied in detail in the following. In the case of the dimer ZC, the EPs are symmetric with respect to the CPLP. To further complete the understanding of the eigenanalysis, the cross section of both real (solid) and imaginary (dashed) parts is made in the third column (see Fig. 3.4(a) for the dimer Z and Fig. 3.4(b) for the dimer ZC). The plots are obtained for different values of  $\varepsilon$  parameter and agree well the observations made from the 3D plots. Indeed, in the  $\mathcal{PTS}$  case  $\varepsilon = -1$  (red color), we note that, whether for the dimer Z or for the dimer ZC, the EPs separate exactly the real modes from the complex ones. When  $\varepsilon \neq -1$  these modes are complex (see  $\varepsilon = 0$  (green color) or  $\varepsilon = 1.5$  (blue color)). The case  $\varepsilon = 1$  (black color) supports the discussions made above on the CPLP, as a point of zero effective coupling of the dimer ZC. This CPLP effectively occurs when  $\beta_C = \kappa = 0.75$ .

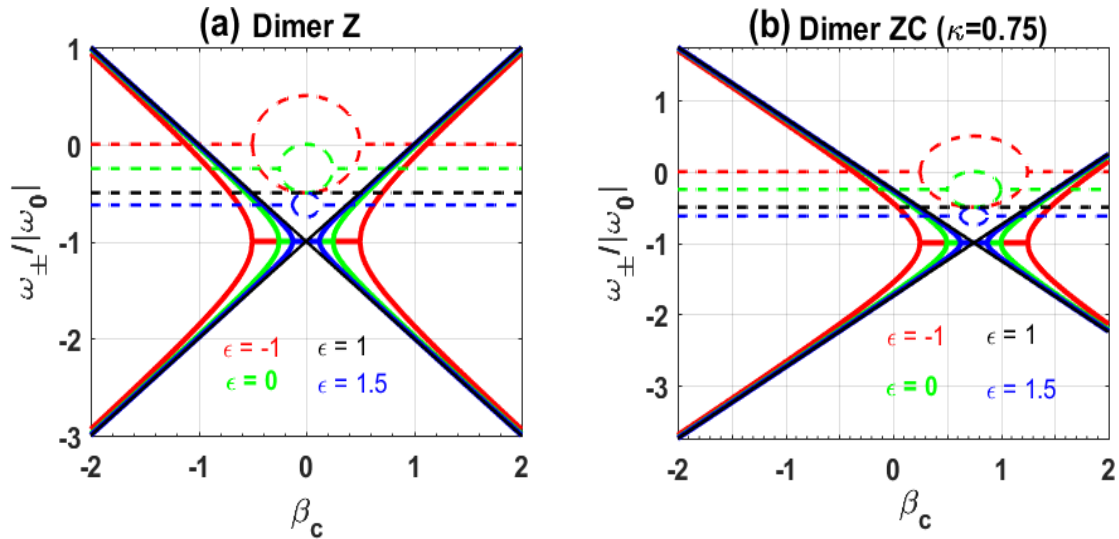


Figure 3.4: Cross section of the real (solid) and the imaginary (dashed) parts of the eigenfrequencies  $\omega_{\pm}/|\omega_0|$  shown in Fig. 3.3 for different values of  $\varepsilon$ : (e) the dimer Z and (f): dimer ZC ( $\kappa = 0.75$ ). The values of  $\varepsilon$  are indicated on the plots. For all plots  $\beta_0 = 0.5$ .

To emphasize on the structural characterization, we can as well predict the coupling range of the system for which quantum phenomena could occur using the splitting analysis. To do so, let's consider again the ZRC dimer. We assume that the coupled loops oscillate with different natural frequencies; for example  $\omega_0$  for the first oscillator and  $\omega_1 = \omega_0(1 + \Delta)$  for the second one, where  $\Delta$  is a small variation. After a little bit of algebra, the eigenfrequencies of the non-Hermitian system ( $\beta_0 \neq 0$ ) under these

considerations are found to be:

$$\omega_{\pm} = \omega_0 \left( 1 + \frac{\Delta}{2} + jB \pm \frac{1}{2} \sqrt{\Delta^2 - 4\beta^2 + 4c^2 + j4\beta\Delta} \right) \quad (3.4)$$

where the parameters are defined as in Eq. (2.51).

In Fig. 3.5, the real parts of the frequencies obtained in Eq. (3.4) and the splitting  $\omega_+ - \omega_-$  are shown as a function of the variation  $\Delta$  when  $\varepsilon = 0$ .

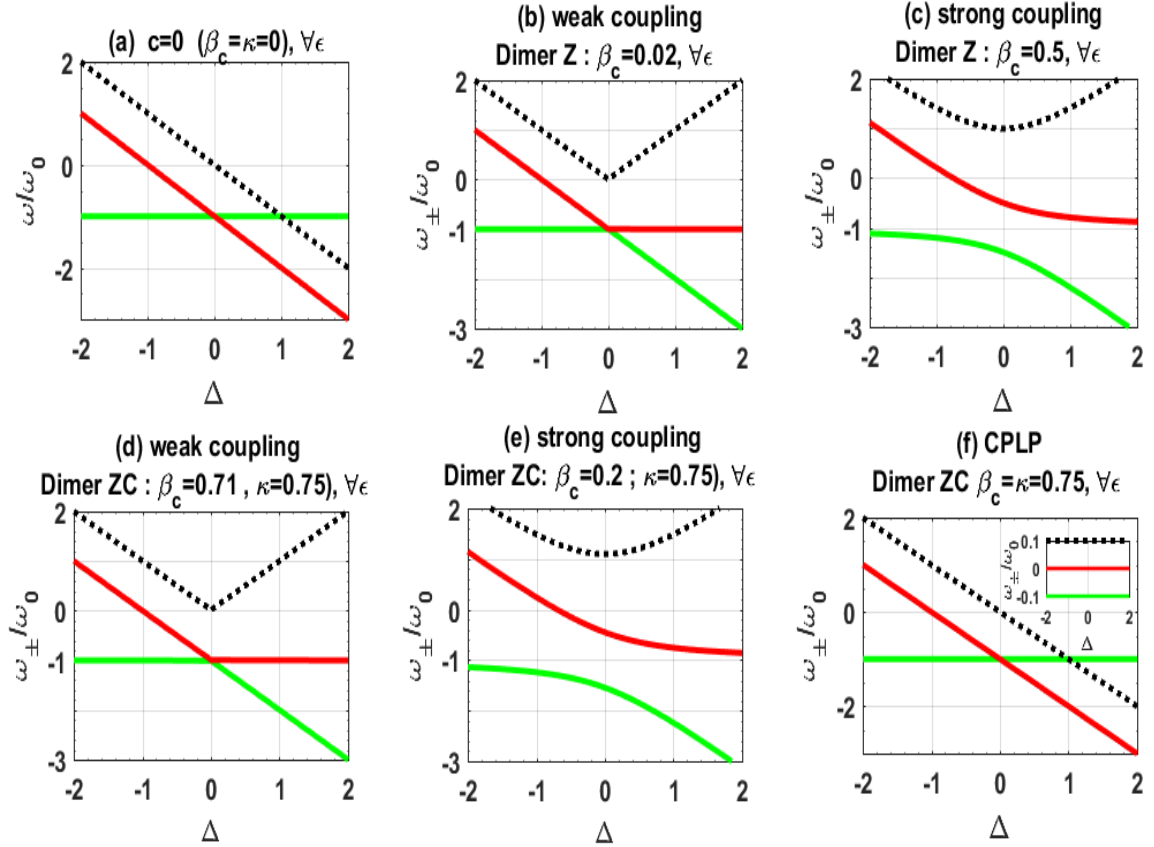


Figure 3.5: Eigenfrequencies of the dimer as function of the variation  $\Delta$ . (a) Uncoupled loops ( $c = 0$ , with  $\beta_C = \kappa = 0$ ). Dimer Z in weak (b) and strong (c) coupling regime. Dimer ZC in weak (d) and strong (e) coupling regime. (f) Dimer ZC at the couplingless point ( $c = 0$ , with  $\beta_C = \kappa = 0.75$ ). In all plots,  $\beta_0 = 0.5$ ,  $\omega_0 < 0$  and  $\varepsilon = 0$ .

In absence of the coupling i.e.,  $\beta_C = \kappa = 0$  (Fig. 3.5(a)), the frequency  $\omega_0$  (solid green) remains constant, while both  $\omega_1$  (solid red) and the splitting (dashed black) decrease as  $\Delta$  increases. The splitting cancels when  $\Delta = 0$ , where the two frequencies intersect. Once the weak coupling is established between loops, for example in the case of the dimer Z when  $\beta_C = 0.02$  (Fig. 3.5(a)) and for the dimer ZC when  $\beta_C = 0.71$  (Fig. 3.5(d)), one of the eigenfrequencies decreases while another remains constant of  $\omega_0$  as  $\Delta$  is increasing. The two frequencies cross at  $\Delta = 0$ . There, the splitting is also equal to zero. We will show in the following that the crossing of frequencies induces destructive or constructive interferences in the system, which favor to mimic EIT or EIA quantum phenomena, respectively. On the contrary, when the coupling becomes strong, for example

in the case of the dimer Z when  $\beta_C = 0.5$  (Fig. 3.5(c)) and for the dimer ZC when  $\beta_C = 0.2$  (Fig. 3.5(e)), both eigenfrequencies  $\omega_{\pm}$  decrease as  $\Delta$  is increasing. Remarkably, it can be seen that the two frequencies do not intersect at  $\Delta = 0$  as in the previous case, however a splitting is observed between them. This reveals the well-known anticrossing behavior, a fingerprint of strong coupling. We will also show later that the modes separation is responsible to the appearance of the doublets of Autler Townes splitting phenomenon. For the double coupled system at the CPLP, that is the dimer ZC when  $\beta_C = \kappa = 0.75$  (Fig. 3.5(f)), one of the eigenvalues remains equal to  $\omega_0$  while another decreases as  $\Delta$  is increasing from  $-2$  to  $0$ . The two curves intersect each other at  $\Delta = 0$ , exactly as in the absence of the coupling, even if the imaginary part of the splitting does not vanishes as shown in inset. At the CPLP, system then seems as an uncoupled one. Later on, we will see that the CPLP favors the disappearance of quantum interferences phenomena. In the next section, the structural analysis will be discussed in the case of the ZRC multi dimer system.

### 3.1.1.3 Eigenmodes of the ZRC multi dimer

It is obvious that the system is non-Hermitian when  $\beta_0 \neq 0$ ,  $\forall \varepsilon$  such that  $\beta_i = \varepsilon \beta_0$ . As the number N of the coupled loops increases from  $N=2$  to  $N > 2$ , the complex roots of  $D(\omega)$  can be numerically calculated. The real parts  $\text{Re}(\omega/|\omega_0|)$  of the roots  $D(\omega)$  determine the positions of the normal modes of the system; the imaginary parts  $\text{Im}(\omega/|\omega_0|)$ , describe their widths. We investigate the eigenmodes of the multi dimer ZC ( $\kappa = 0.75$ ,  $\beta_0 = 0.5$  and  $\varepsilon = 0$ ). The other system parameters are setting as follows (see Eq. (3.5)):

$$\begin{aligned}
 \text{bidimer (N = 2)} : \quad & \omega_1 = \omega_0 - 0.1\omega_0, \quad \omega_2 = \omega_0 + 0.1\omega_0; \\
 \text{tridimer (N = 3)} : \quad & \omega_1 = \omega_0 - 0.1\omega_0, \quad \omega_2 = \omega_0 + 0.02\omega_0, \quad \omega_3 = \omega_0 + 0.1\omega_0; \\
 \text{tetradimer (N = 4)} : \quad & \omega_1 = \omega_0 - 0.1\omega_0, \quad \omega_2 = \omega_0 + 0.1\omega_0, \quad \omega_3 = \omega_0 - 0.2\omega_0, \\
 & \omega_4 = \omega_0 + 0.2\omega_0.
 \end{aligned} \tag{3.5}$$

It can be seen from Eq. (3.5) that, with this choice of parameters the natural frequencies of the multipod loops are distinct, and the system is non-Hermitian. Fig. 3.6 shows the real ((a), (b) and (c)), and the imaginary ((d), (e) and (f)) parts of the roots of  $D(\omega)$  as a function of  $\beta_C$  in the case of the multi dimer ZC. As illustrated, the spectrum of the roots of  $D(\omega)$  can be analyzed as a function of  $\beta_C$ , in three domains as  $\beta_C$  is increasing from  $-1$  to  $2$  :

- Before the CPLP, the real parts of the normal modes  $\text{Re}(\omega_{i(i \neq 0)})$  related to the multipod loops evolve almost linearly compared to the central mode  $\text{Re}(\omega_0)$ . They undergo an abrupt transition after which, all the modes of the coupled system converge through the CPLP.
- At the CPLP ( $\beta_C = \kappa = 0.75$ ), the modes match with the natural frequencies of the uncoupled system.

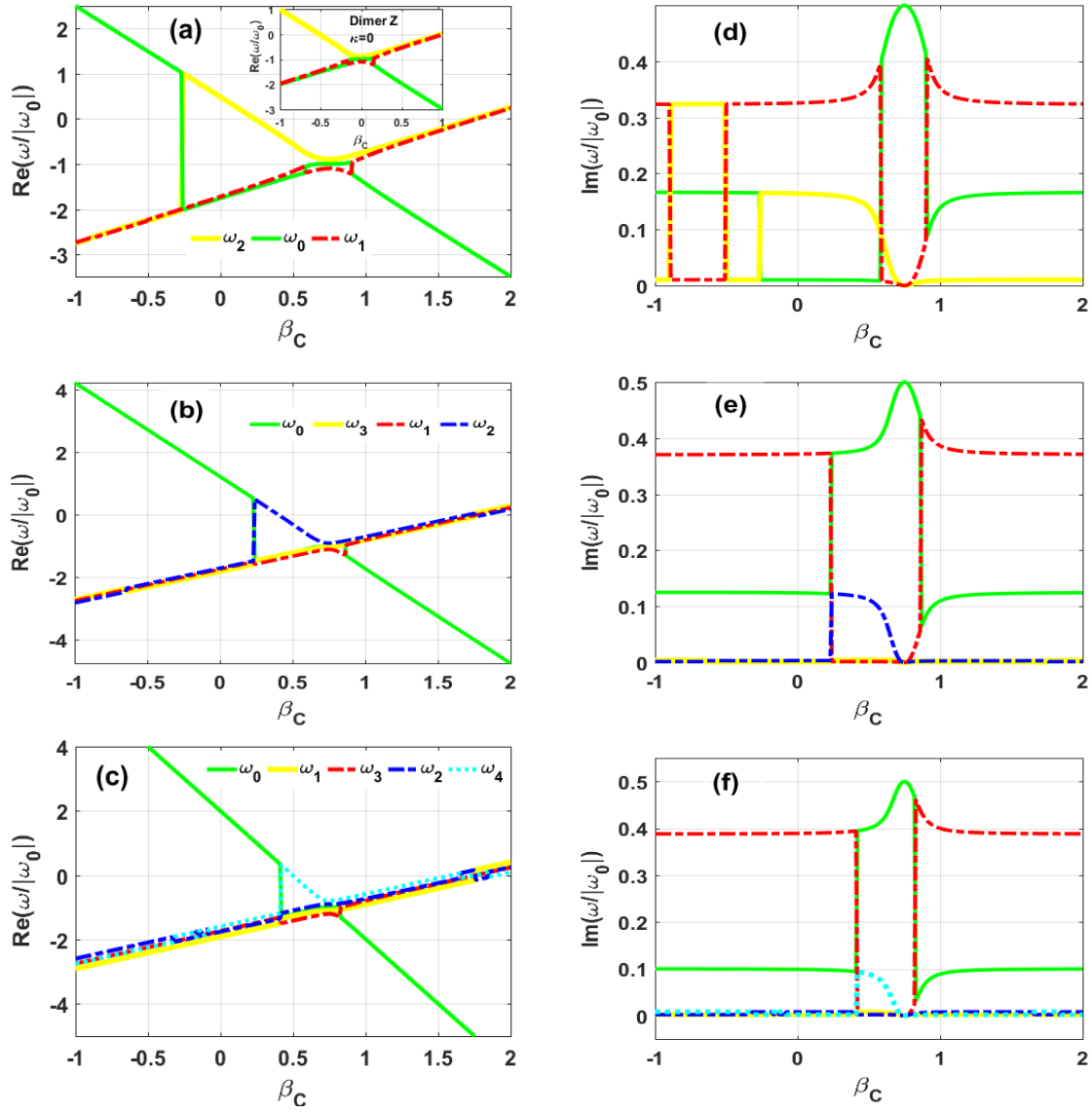


Figure 3.6: The normalized roots of  $D(\omega)$  as function of the imaginary resistive coupling parameter  $\beta_C$  for the multi dimer ZC (when  $\kappa = 0.75$ ). First row: the bi dimer ZC ( $N=2$ ). Second row: the tri dimer ZC ( $N=3$ ) and in third row: the tetra dimer ZC ( $N=4$ ). The first column shows the real parts of the roots ( $\text{Re}(\omega/|\omega_0|)$ ) and the second column shows their imaginary parts ( $\text{Im}(\omega/|\omega_0|)$ ). The other plot parameters are:  $\varepsilon = 0$ ,  $\beta_0 = 0.5$  and  $\omega_0 < 0$ . The inset in (a) corresponding to the case of the bi dimer Z ( $\kappa = 0$ ), allows to show the robustness of the multiple coupling.

- After the CPLP, the frequencies undergo a second transition less abrupt than the first, and return to their behavior before the first transition. This leads to the splitting of the central mode with respect to those of the multipod. These features are also well observed in the imaginary parts of the roots of  $D(\omega)$ .

Remarkably, the eigenfrequencies of the multi dimer are not symmetric with respect to the CPLP. The transition points become closer as the  $N$  number of the multipods increases. The frequencies' phase transitions are of great interest in quantum interferences phenomena in physics. For example, we demonstrate in the following that, the reduction of the

gap observed between them is consequent to the increasing of the number of interferences, giving rise to multiple EIT/EIA phenomena. These observations for the multi dimer with double coupling (multi dimer ZC) around the CPLP, is exhibited in the uncoupled multi dimer system, such as illustrated in the inset Fig. 3.6(a), the case of bi dimer Z. Note that this CPLP was already analyzed in the ZRC single dimer. This demonstrates the efficiency in the cancellation of the coupling modulation of the capacitive coupling ( $\kappa$ ) by the imaginary resistor ( $\beta_C$ ) coupling. In other words, the cancellation is robust throughout the N multipod coupling system.

To better understand the interference phenomena, we will focus in the next subsection on the steady state dynamics of the systems.

## 3.1.2 Steady state dynamic and dispersive properties

### 3.1.2.1 Dispersive properties of a dimer MLC

As EIT and related phenomena occur at (or near) resonance, we are interested in the response of the system around the zero frequency detuning. So, assuming harmonic solutions for the charges, we have calculated the complex electric power delivered to the mesh (2) during one period of oscillation  $P_2(\omega)$  as given by Eq. (2.42). It is well known that the real part  $\Re(P_2(\omega))$  of the complex power (i.e. active power) determines the absorption, while its imaginary part  $\Im(P_2(\omega))$  (i.e. reactive power) refers to the dispersion properties of the medium. When the coupling is not acting (i.e. SW Off), the meshes are uncoupled and, it is clearly seen in Fig. 3.7(a) where the mesh (2) is passive ( $\gamma_2 = 0.05 > 0$ ) that, the absorbed power is maximal when the loop is resonantly driving by the voltage source. However if the mesh (2) is active ( $\gamma_2 = 0.05 < 0$ ), Fig. 3.7(c) shows a negative absorption i.e. the power transferred by the voltage source to the oscillator is amplified instead of being absorbed and the maximal amplification occurs at the resonance. We have easily experimentally simulated the total power feature  $\Re(P_2(\omega))$  and  $\Im(P_2(\omega))$  with the LTspice program. The current flowing through the inductor  $L_2$  has the same frequency dependence as the power transferred from the voltage source to the loop. Therefore, it is sufficient for us to measure such a current of which the real (Re) and the imaginary (Im) parts are perfectly match with the absorption and the dispersion curves that we obtained theoretically. For the LTspice simulations, the parameters of the circuit have been chosen such that the resonant frequency  $f_0$  of the mesh (2) approaches  $7\text{ kHz}$  (see Figs. 3.7(b) and 3.7(d)). The amplitude of the voltage  $v_0$  is unity and remains constant through this thesis. The other circuitry elements used for the simulations are  $R_2 = 50\ \Omega$ ;  $L_2 = 5\ \text{mH}$ ;  $L_C = 0.272\ \text{mH}$ ;  $C_2 = 0.1\ \mu\text{F}$ .

Once the coupling is established (i.e. SW On), a dip is observed at the zero frequency detuning ( $\delta = 0$ ) where the maximum absorption/amplification is expected in absence of the coupling and a transparency window occurs in the profile. However, EIT and Autler Townes Splitting (ATS) are manifested by the dip, leading thus a transparency

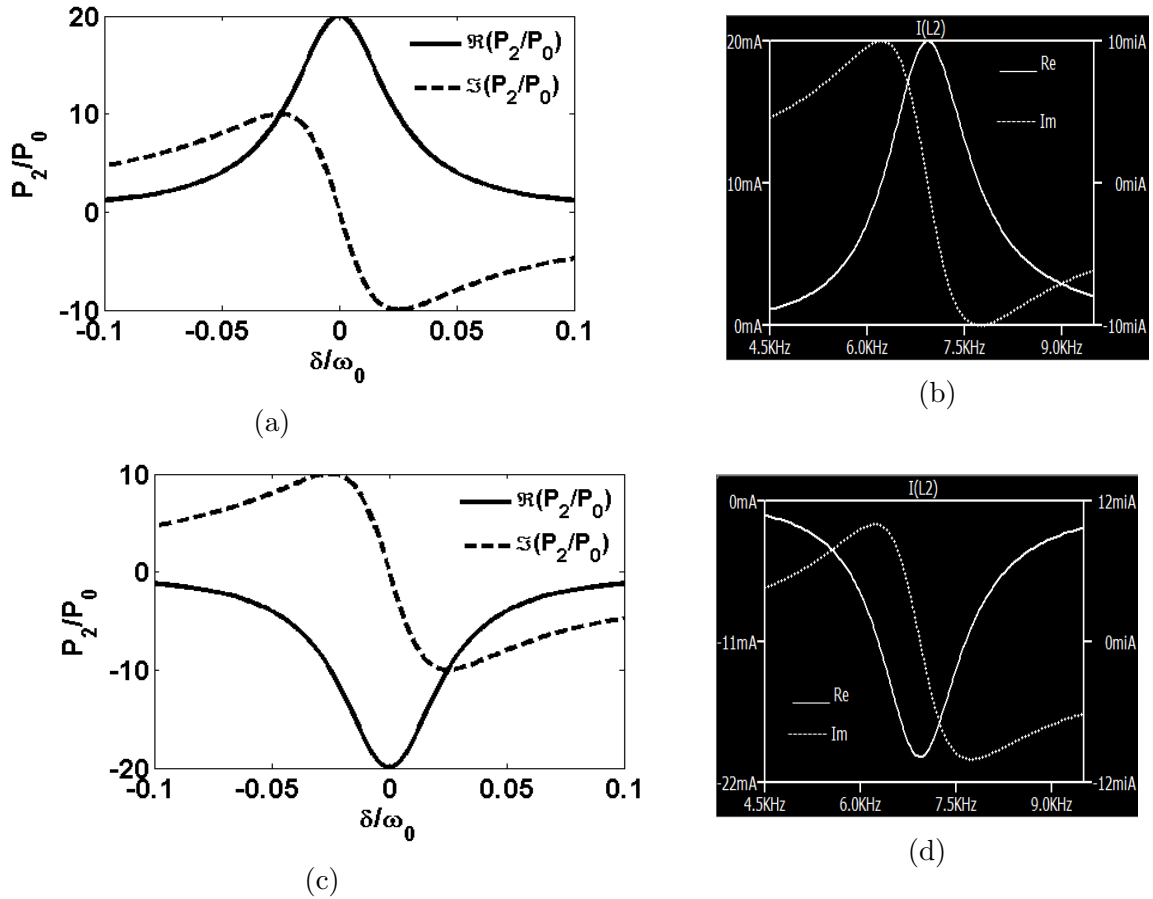


Figure 3.7: The solid black (white) curve is the absorption spectrum of the mesh (2) as function of the normalized frequency detuning  $\delta/\omega_0$  (frequency  $\omega$ ) when SW is off. The dashed black (white) is the corresponding dispersion curve. The first and second column represent the theoretical and the experimental LTspice results, respectively. (a, b): the mesh (2) is passive ( $\gamma_2 = 0.05$ ). (c, d): the mesh (2) is active ( $\gamma_2 = -0.05$ ). The experimental parameters are  $R_2 = 50 \Omega$ ;  $L_2 = 5 \text{ mH}$ ;  $L_C = 0.272 \text{ mH}$ ;  $C_2 = 0.1 \mu\text{F}$ .

window in the absorption profile. Therefore, these similarities create many confusions to discriminate them. Indeed, EIT has always been interpreted as a result of destructive interference between two excitation pathways [142] while ATS is analogous to the emergence of two dressed states caused by a strong control field [226] that is the splitting of normal-mode frequencies [58]. The analysis of the normal modes made above indicates that a spectrum is very different on both sides of the EPs. Then, we need to clarify in which coupling regime, the appearance of a dip in absorption has a consequence of EIT or ATS. To achieve this, we investigated the complex power using the resonant pole method introduced in this context by P. Anisimov [227] consisting to write the total power given in Eq. (2.42) as a sum of two resonant terms  $P_{2k}(\omega)$  ( $k = 1, 2$ ) (see Eqs.(2.45), (2.46) and (2.47)). We have separately plotted the two resonances as a function of the normalized frequency detuning  $\delta/\omega_0$  and the total absorbed power  $\text{Re}(P_2(\omega))$  (in red) is shown as the superposition of these two resonances. The blue (solid) and green (solid) curves correspond to the resonances  $\text{Re}(P_{21}(\omega))$  and  $\text{Re}(P_{22}(\omega))$  respectively, and remain the same throughout this work.

## a) Absorption in weak-driving regime

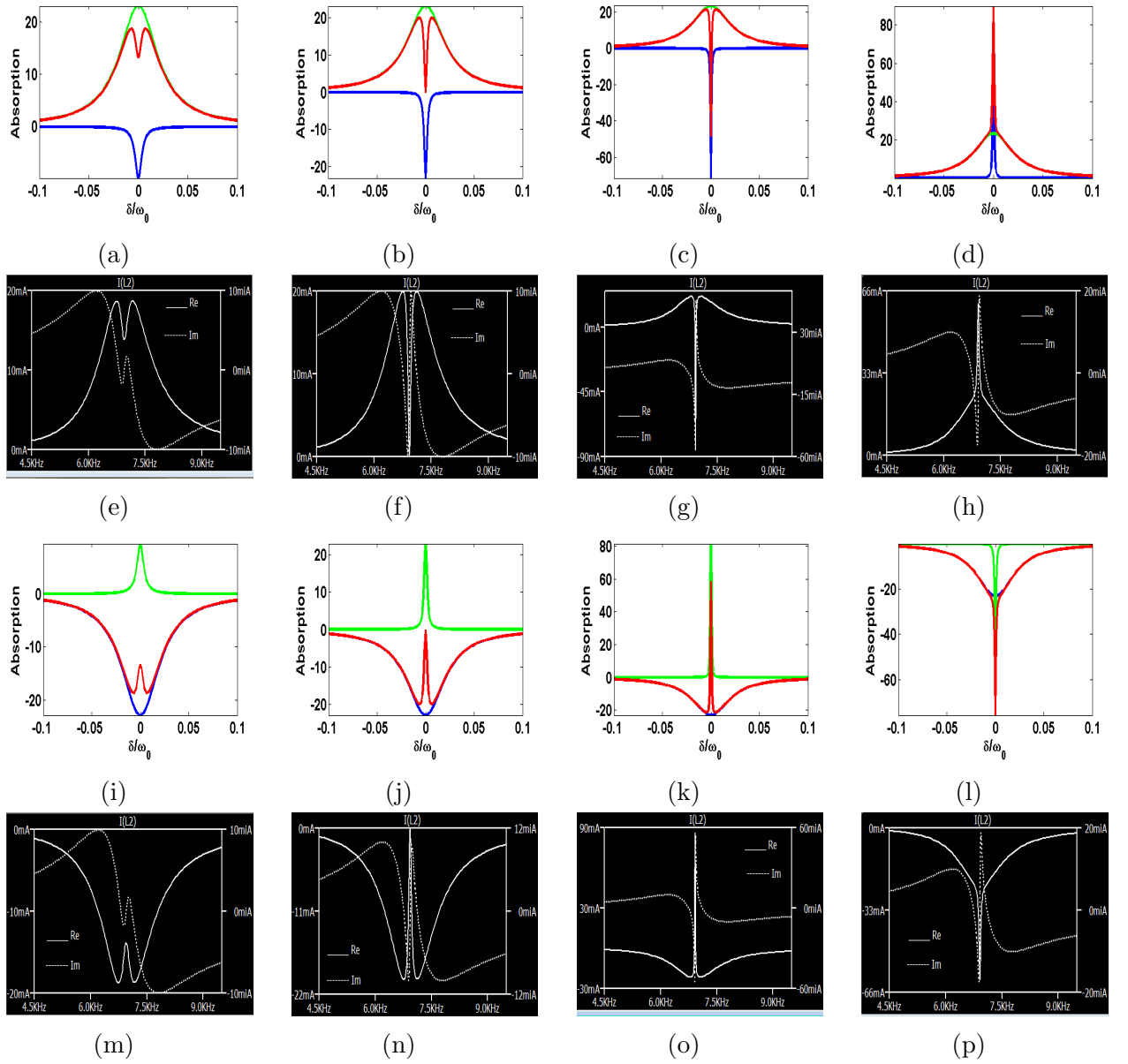


Figure 3.8: Absorption spectrum of the mesh (2) in Effective CP dimers as function of  $\delta/\omega_0$  for different values of  $\varepsilon$ . We assume coupling in the weak driving regime. For illustration, we have considered the case of CP dimer L where  $\nu_C/\nu_{Ccr} = 0.5$ . The solid blue, green and red curves are the real parts of the resonances  $P_{21}/p_0$ ,  $P_{22}/p_0$  and the total dissipated power  $P_2/p_0$ . From (a)-(d) and from (i)-(l) are theoretical results. From (e)-(h) and from (m)-(p) are experimental LTspice simulation results. The experimental parameters are indicated in Table 3.1. first column:  $\varepsilon = 0.1$ ; second column:  $\varepsilon = 0$ ; third column:  $\varepsilon = -0.05$ ; last column:  $\varepsilon = -0.1$ . In the first and second rows, the mesh (2) is passive ( $\gamma_2 = 0.05$ ), while in the third and last row it is active ( $\gamma_2 = -0.05$ ).

In Fig. 3.8, we show the evolution of the real parts of the two normalized resonances  $P_{2k}/p_0$  ( $k = 1, 2$ ) and their superposition  $P_2(\omega)/p_0$  as a function of the normalized frequency detuning  $\delta/\omega_0$ , when a weak coupling is established between parts of the effective CP dimers, the switch SW being closed. To illustrate, we have consider the case of the effective CP dimer L when  $\nu_C/\nu_{Ccr} = 0.5$ . From subplots 3.8 (a) to 3.8(h), the mesh (2)

weak driving regime					
$R_2$	$R_1$	$\varepsilon$	$L_C$	$L$	$C$
$\pm 50 \Omega$	$0 \Omega$	0.0	0.272 mH	5 mH	0.1 $\mu\text{F}$
	$5 \Omega$	0.1	0.245 mH		
	$2.5 \Omega$	-0.05	0.285 mH		
	$-5 \Omega$	-0.1	0.298 mH		

Table 3.1: Electronic components used in LTspice experimental simulations with the CP dimer L in the weak driving regime.

of which the dissipated power is calculated, is passive ( i.e.  $\gamma_2 > 0$  ) while from subplots 3.8(i) to 3.8(p), it is active (i.e.  $\gamma_2 < 0$ ). In the first column where  $\varepsilon = 0.5$ , the two resonances overlap each other with  $P_{21} < 0$  and  $P_{22} > 0$ . Their superposition leads to two positive (resp. negative) absorption peaks in subplot 3.8(a) (resp. in subplot 3.8(i)), separated by a narrow dip (resp. dome) appearing at  $\delta = 0$  instead of the single peak expected there, in absence of the coupling (SW off). The depth (resp. height) of this dip (resp. dome) increases and allows a zero absorption, when  $\varepsilon$  decreases to  $\varepsilon = 0$  (second column). We then note a totally transparency (see subplots 3.8(b) and 3.8(j)).

In the above situations, the dip (dome) in the profile can be interpreted as a destructive interference between the two resonances which are centered at the same frequency  $\Re(\omega_{\pm}) = \omega_0$ . So, the transparency window is precisely what is meant by EIT (subplots 3.8(a) and 3.8(b)) and EIT with Amplification (EITA) (subplots 3.8(i) and 3.8(j)) [228]. Now decreasing the value of  $\varepsilon$  so that one of the meshes become active, for example, taking  $\varepsilon = -0.05$  (third column), we note an appearance of a negative (resp. positive) absorption at the zero detuning in subplot 3.8(c) (resp. in subplot 3.8(k)) when the mesh (2) is passive (resp. active). Then, it appears in the profile, a transparency accompanied of a small amplification (resp. positive absorption) of the power. We called these selective behavior electromagnetically Induced Amplified Transparency (EIAT) (see subplot 3.8(c)) and EITA with absorption (see subplot 3.8(k)). The response of our circuit is very sensitive so that when  $\varepsilon$  decreases to  $\varepsilon = -0.1$  (last column), a drastic change is observed in the phenomena shown respectively in subplots 3.8(c) and 3.8(k). Then, with a passive mesh (2), we switch from EIAT to another behavior called Electromagnetically Induced Absorption (EIA) (subplot 3.8(d)) [181, 183], characterized by a notable enhancement of a total absorption with a sub natural linewidth. The two resonances  $P_{2k}(\omega)/p_0$  ( $k = 1, 2$ ) have the same sign, with one of the peak more pronounced than other which is rather broadened; thus, EIA appears as a consequence of constructive interference between resonances. It has potential applications such as ultra-narrow band perfect absorbers, optical modulation, and absorptive switching [229]. Likewise, if the mesh (2) is keeping active, the negative absorption is notably enhanced at the zero detuning so that we pass to Electromagnetically Induced Absorption Amplified (EIAA)(subplot 3.8(l)). When  $\varepsilon$  is increased (resp. decreased) to higher positive (resp. negative) values (not represented here), one of the resonance becomes very flat thus preventing the possibility to see a dip



(resp. dome) in the absorption spectrum; The superposition of both resonances no more gives two peaks but only one, which is similar to those of uncoupled mesh (2) shown in Figs. 3.7(a) and 3.7(c). We successfully reproduced all these theoretical results via the LTspice program. The experimental simulation curves are shown in subplots from Figs. 3.8(e) to 3.8(h) and from Figs. 3.8(m) to 3.8(p) where the real (Re) and the imaginary (Im) parts of the current through the inductor  $L_2$  are plotted as a function of the voltage source frequency. The simulation parameters are given in Table 3.1 and the results match perfectly with those we presented above. Finally, it is instructive to notice that, all conclusions made in this coupling regime with the effective CP dimer L are also valid for other dimers belonging to the group of Effective CP dimers.

### b) Absorption in strong-driving regime

We are now investigate the dissipated power through the effective CP dimers assuming the strong-coupling between parts of the dimers. To elucidate that, we consider again the case of the effective CP dimer L when  $\nu_C = 2\nu_{Cr}$ . Figure 3.9 represents the evolution of real part of the total absorption  $P_2(\omega)/p_0$  and the resonances  $P_{2k}(\omega)/p_0$  ( $k = 1, 2$ ) as a function of the normalized detuning  $\delta/\omega_0$  for different values of  $\varepsilon$ . From the subgraphs 3.9(a) to 3.9(d), the mesh (2) is assumed passive ( $\gamma_2 > 0$ ) while from subgraphs 3.9(i) to 3.9(l), it is active (i.e.  $\gamma_2 < 0$ ). In subplots 3.9(a) and 3.9(i) (see first column) where we used the value  $\varepsilon = 0.5$ , and in subplots 3.9(b) and 3.9(j) (see second column) of which  $\varepsilon = 0$ , it is observed once SW is closed, a reduction in the total power around the zero detuning, instead of the single lorentzian peak expected in absence of the coupling. This dip is much wider compared to that encountered in Figs. 3.8(a) and 3.8(b). Hence, it is interpreted as a gap between the two positive (resp. negative) Lorentzians centered at  $\Re(\omega_{\pm}) = \frac{\omega_0}{2} (2 \pm \sqrt{\Lambda})$  respectively. Therefore, the behavior observed in subplots 3.9(a) and 3.9(b) are referred as Autler-Townes Splitting (ATS) [230]. Similarly to what we termed EITA, we named the phenomena illustrated in subplots 3.9(i) and 3.9(j), where the total absorption is negative, as Autler-Townes Splitting with Amplification (ATSA). This later behavior as our knowledge, has never been addressed. In the third column ( $\varepsilon = -0.5$ ) where one mesh of the so-called dimer is active, we note around the zero detuning that, a negative (resp. positive) absorption appears into the spectrum in subplot 3.9(c) (resp. subplot 3.9(k)) where the mesh (2) is passive (resp. active). In all cases, the reduction (resp. enhancement) of the absorption observed in the transparency zone, is also interpreted as the gap between the resonances  $P_{2k}(\omega)$  ( $k = 1, 2$ ) and is a consequence of a constructive interference. Remarkably, the behavior found in subplot 3.9(c) (resp. subplot 3.9(k)) is a feature of ATS (resp. ATSA) accompanied by an amplification (resp. positive absorption). In the last column,  $\varepsilon = -1$ . The amount of gain or loss into parts of the dimer is balanced. We are in situation of the parity Time symmetric ( $\mathcal{PTS}$ ). In this case, the NHH  $\mathcal{H}$  that we derived in Eq. (2.31) features the invariance under the combined operation of space and time reflection symmetry. As we have mentioned above,

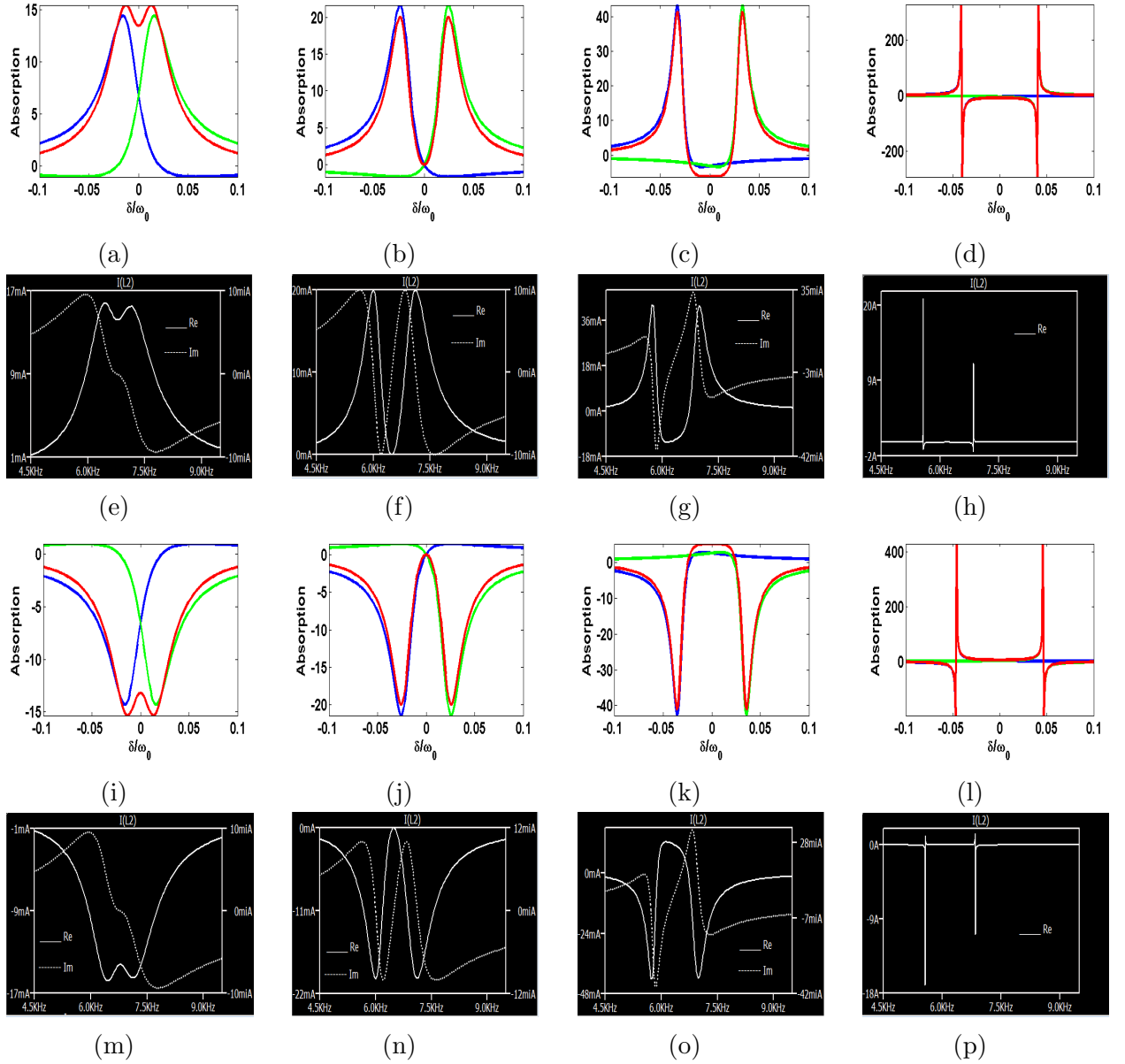


Figure 3.9: Absorption spectrum of the mesh (2) in Effective CP dimers as function of  $\delta/\omega_0$  for different values of  $\epsilon$ . We assume coupling in the strong driving regime. For illustration, we have considered the case of CP dimer L where  $\nu_C/\nu_{Ccr} = 2$ . The solid blue, green and red curves are the resonances  $P_{21}/p_0$ ,  $P_{22}/p_0$  and the total dissipated power  $P_2/p_0$ . From (a)-(d) and from (i)-(l) are theoretical results. From (e)-(h) and from (m)-(p) are experimental LTspice simulation results. The experimental parameters are indicated in Table 3.2. First column:  $\epsilon = 0.5$ ; second column:  $\epsilon = 0$ ; third column:  $\epsilon = -0.5$ ; last column:  $\epsilon = -1.0$ . In the first and second rows, the mesh (2) is passive ( $\gamma_2 = 0.05$ ) while in the third and last row it is active ( $\gamma_2 = -0.05$ ).

it produces entirely real and broken (complex) spectra as we are passing from the weak to the strong coupling through the EP (for details, see Fig. 3.1). Therefore, the resonance linewidths going to zero in the strong-driving regime, leading narrow and enhanced absorption peaks. All the theoretical results presented here, were once more been successfully obtained with the LTspice program. All the plot parameters are given in Table 3.2. The simulation curves can be confirmed from subplots 3.9(e) to 3.9(h) where the mesh

(2) is passive and from subplots 3.9(m) to 3.9(p), where it is active. Finally, notice that all the results and the conclusions obtained in the strong-coupling regime here with the effective CP dimer L are also valid for the other dimers of this category.

strong driving regime					
$R_2$	$R_1$	$\varepsilon$	$L_C$	$L$	$C$
$\pm 50 \Omega$	0.0 $\Omega$	0.0	1.019 mH	5 mH	0.1 $\mu\text{F}$
	25 $\Omega$	0.5	0.531 mH		
	-25 $\Omega$	-0.5	1.473 mH		
	-50 $\Omega$	-1.0	1.903 mH		

Table 3.2: Electronic components used in LTspice experimental simulations with the CP dimer L in the strong driving regime.

### c) Suppression of EIT and related phenomena in effective CPL dimer MLC

As mentioned in the previous section, the CPLP is characterized as a point of the weak-driving regime for which the effective coupling of the dimer vanishes ( $C_T = 0$ ). At the CPLP, Eq. (2.42) allows to rewrite the complex power as  $P_2(\omega) = -jp_0/2f_2$  which is same as the power dissipated through the mesh (2) in absence of coupling (Figs. 3.7(a) and 3.7(c)). This indicates for the dimer that, although the coupling is present, at the CPLP, it exactly behaves like the uncoupled mesh (2). Therefore, this forces the disappearance of EIT and its related phenomena where they should expected to be. The non-appearance is due to the combination of the capacitive coupling  $C_C$  with at least one of the couplings M or L.

For illustration, we consider the case of effective CP dimer MC, when  $\varepsilon = 0$ ,  $\mu = 0.5$  and  $\gamma_2 = \pm 0.05$ . In Figs. 3.10(a) and 3.10(c), we show in 3D, the real part of the total dissipated power as function of  $\delta/\omega_0$  when assuming the mesh (2) passive and active respectively. The active coupling being in the weak-driving regime of which borders are  $\kappa_{cr1} = 0.4775$  and  $\kappa_{cr2} = 0.5225$ . The CPLP is obtained in this case when  $\kappa = \mu = 0.5$ . As we can see in the absorption profile, everywhere in the regime, a dip (or a dome) is observed between the two absorption peaks, except at the CPLP where we rather note a single peak, this, regardless of the value of  $\varepsilon$  used; Which shows that the EIT-like behavior and related phenomena (EIAT, EIA) we mentioned above disappear. A cross section at the CPLP in the 3D-plots is experimentally verified with the LTspice program (from the original model, i.e. without any approximation) where we confirm that the absorption and the dispersion profile are identical as those of Figs. 3.7(a) and 3.7(d). The circuitry elements used for the simulations are:  $R_2 = 50 \Omega$ ;  $R_1 = 0.0 \Omega$ ;  $L_2 = 5 \text{ mH}$ ;  $L_C = 0.986 \text{ mH}$ ;  $C_2 = 0.1 \mu\text{F}$ .

In conclusion, the decomposition method clearly shows that at the CPLP, the dissipated power is a consequence of a single resonant frequency mode, the contribution of the other resonant term being null. At the CPLP, the dimer exhibits what is found in single mode lasers [231]. In the next section, we analyze the dynamic and the dispersive properties of the ZRC system in presence of the harmonic voltage source  $u(t)$ . In this

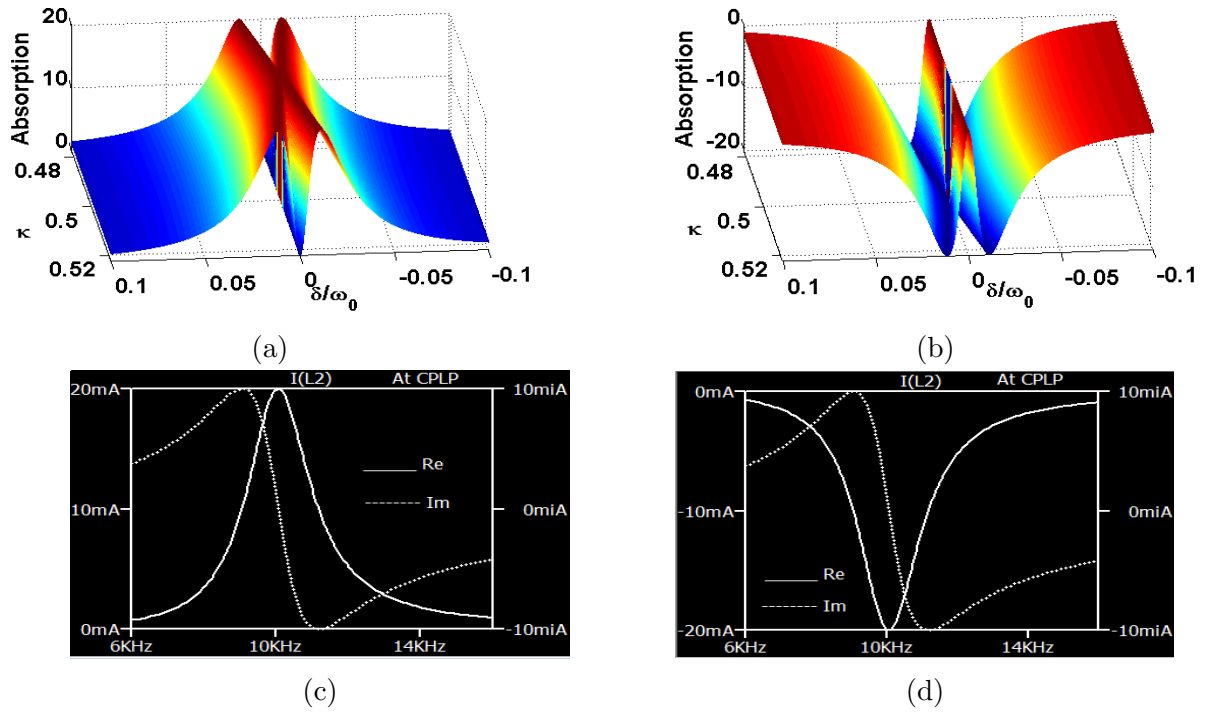


Figure 3.10: (a) and (b) Absorption spectrum of the mesh (2) in Effective CP dimers of category 2 (dimer MC with  $\mu = 0.5$  for illustration), as function of  $\delta/\omega_0$  and the active coupling ( $\kappa$  for illustration). We assume  $\varepsilon = 0$  and the active coupling  $\kappa$  evolves in the weak driving regime. We note a particular behavior at the center of this regime corresponding to the disappearance of EIT and related phenomena. (c) and (d) are experimental LTspice simulation results at the CPLP when  $\varepsilon = 0$ ,  $\kappa = \mu = 0.5$ . The experimental values used for the simulations are:  $R_2 = 50 \Omega$ ;  $R_1 = 55 \Omega$ ;  $L_2 = 5 \text{ mH}$ ;  $L_C = 0.986 \text{ mH}$ ;  $C_2 = 0.1 \mu\text{F}$ . In first column: the mesh (2) is passive ( $\gamma_2 = 0.05$ ) while in the second column it is active ( $\gamma_2 = -0.05$ ).

way, we first study the dynamic of the free single ZRC oscillator. Then, we discuss about the ZRC coupled systems.

### 3.1.2.2 Dispersive properties in a single ZRC oscillator

#### a) Temporal solutions

The particularity of the ZRC oscillator as we described in chapter 2, is among others that, it can generate negative frequencies according to the sign of the circuit parameters. Its temporal behavior can be analyzed via the capacitor charge  $q_0(t)$  or the electric current  $I_0(t)$  through the circuit as given in Eq. (2.52) in absence of any voltage source. This solution presents one oscillating part and one exponential part of which the increasing or the decreasing depends to the non-Hermitian parameter  $\beta_0$ . Fig. 3.11 shows the transient variation of the normalized current  $I_0(t)/I_0(t_0)$  through the loop for different values of the quality factor  $\beta_0^{-1}$ . When the natural frequency of the circuit,  $\omega_0$ , is positive ( $\omega_0 > 0$ ), the oscillations are decreasing during the time for the loss loop where  $\beta_0^{-1} = 10$  (see Fig. 3.11(a)) while increasing for the gain loop where  $\beta_0^{-1} = -10$  (see Fig. 3.11(c)). However, in Figs. 3.11(d) and 3.11(f) when  $\omega_0$  becomes negative ( $\omega_0 < 0$ ), the roles of gain and

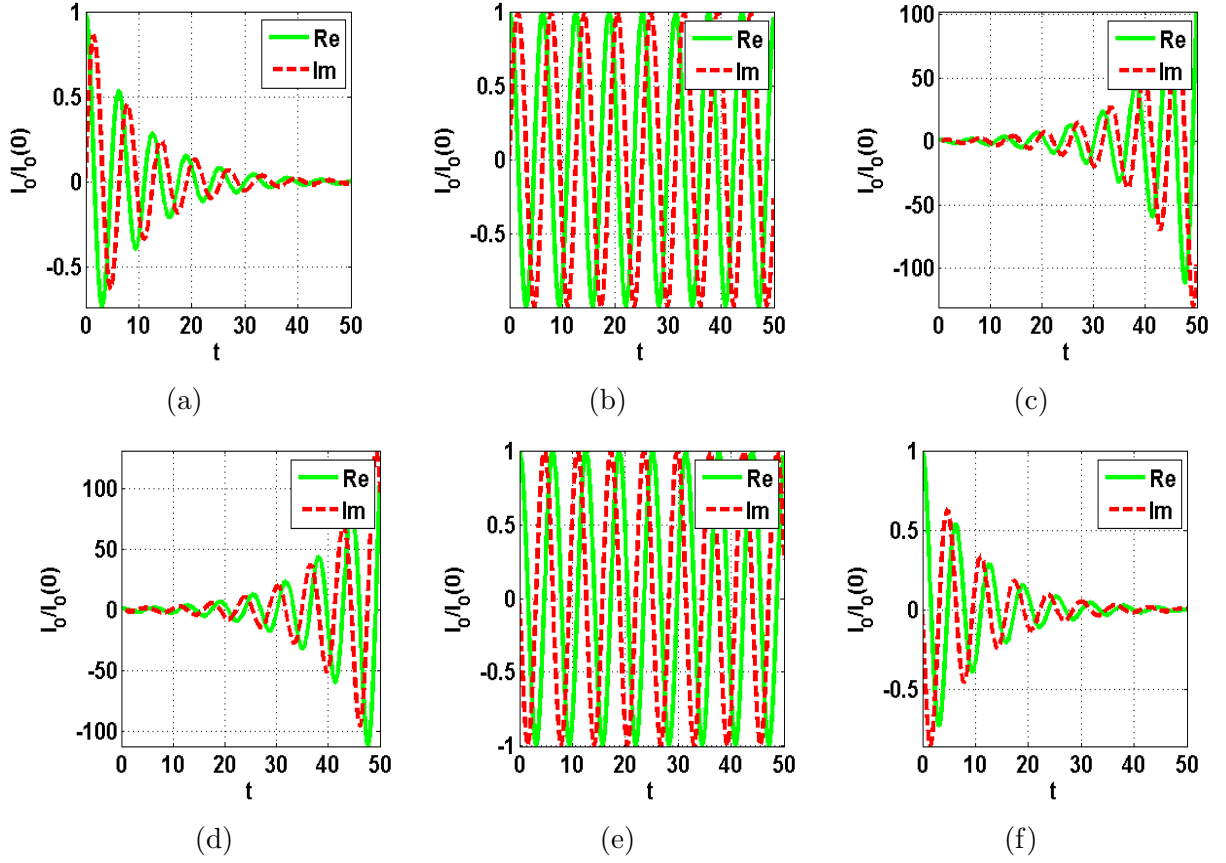


Figure 3.11: Transient evolution of the normalized current into the loop in absence of the harmonic voltage for different values of the quality factor (a, d):  $\beta_0^{-1} = 10$  ; (b, e):  $\beta_0^{-1} \rightarrow \infty$  ; (c, f):  $\beta_0^{-1} = -10$ . From (a)-(c):  $\omega_0 > 0$  ; from (d)-(f):  $\omega_0 < 0$ .

loss are reversed. We rather note the amplification of oscillations for a loss loop (see Fig. 3.11(d)) and the attenuation of oscillations in a gain loop (see Fig. 3.11(f)) where the amplification was expected. This shows that the negative natural frequency of the loop plays a determining role in the response of the gain or loss loop. It is interesting to also note that in the case of neutral loop for which the non-Hermitian parameter is almost null ( $\beta_0^{-1} \rightarrow \infty$ ), the amplitude of oscillations are not affected as we pass from positive to negative frequencies, since the real resistance tends toward zero while the imaginary resistance amplitude tends towards infinity implying to the frequency to go towards 0. The behavior of the gain and loss then becomes similar. It is why the oscillations remain regular over time (see Figs. 3.11(b) and 3.11(e)).

### b) Steady state dynamic: Absorption in an oscillator ZRC

In Fig. 3.12, the real (solid) and the imaginary (dash/dot) parts of the steady state normalized electric power ( $P_0/p_0$ ) dissipated by the  $Z_0R_0C_0$  loop are depicted as a function of the normalized voltage frequency  $\omega/\omega_0$  for given values of the non-Hermitian parameter  $\beta_0$ . The green and the blue curves are used for the loss loop ( $\beta_0 = 0.5 > 0$ ) while the purple and the red colors refer to the gain loop ( $\beta_0 = -0.5 < 0$ ). As it can

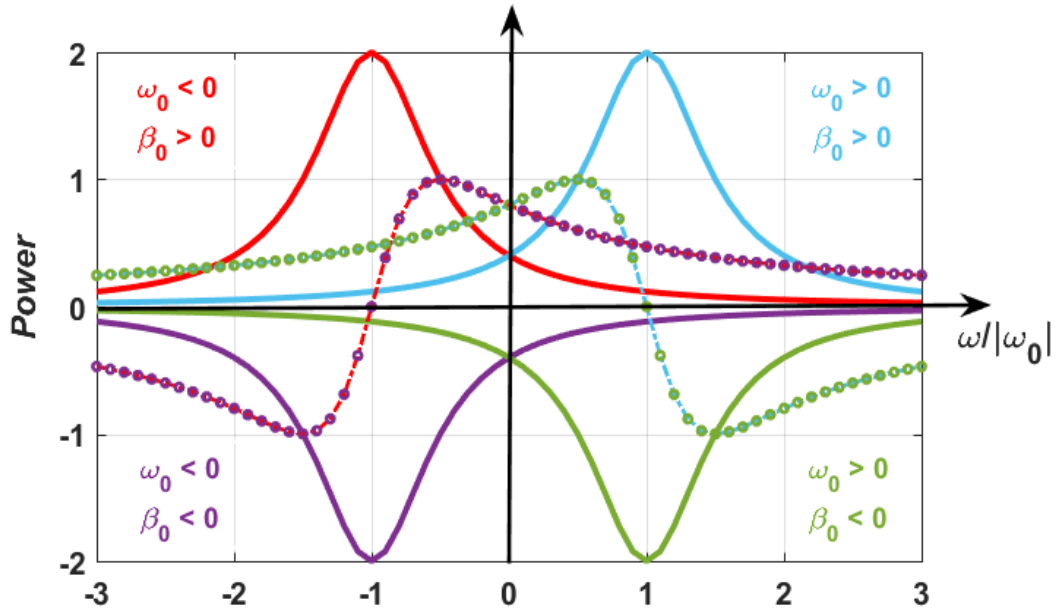


Figure 3.12: The real (solid lines) and the imaginary (dashes/dots lines) parts of the steady state normalized power dissipated by the  $Z_0R_0C_0$  loop as a function of the normalized frequency  $\omega/\omega_0$  for different values of the non-Hermitian parameter  $\beta_0$ . The plot parameters are shown in the figure. In all plots, green and blue curves correspond to the loss loop ( $\beta_0 = 0.5$ ) whereas purple and red curves are associated to the gain loop ( $\beta_0 = -0.5$ ), respectively.

be noticed, the absorption profile presents a lorentzian form with the maximum of the absorption centered at  $\omega = \omega_0$ . Remarkably, for a loss loop the lorentzian is positive, corresponding to a typical absorption in a real atomic system. On the contrary, it is negative in the case of the gain loop, which can be interpreted as enhancement of the power. Indeed, the power is amplified instead of being absorbed. The imaginary part of the power represents the dispersion in an atomic systems. In the  $Z_0R_0C_0$  oscillator, the slope of a dispersion around the absorption's peak is positive or negative depending on the sign of  $\omega_0$ . It is positive when  $\omega_0 < 0$ , indicating that, the maximum of absorption (or amplification of a power) is obtained at the resonance, where the voltage frequency is equal to the natural loop's frequency. The negative frequencies have been suggested to many past researches [232–236]. However, their use in the context of quantum analog system is often overlook.

### 3.1.2.3 Dispersive properties in a ZRC dimer

#### a) Temporal solutions

From the eigenfrequencies of the ZRC dimer illustrated in Figs. 3.3 and 3.4, two main coupling regimes have emerged and border by the EPs of the non-Hermitian system. We now attempt to understand the physical significance of the coupling regimes on the dynamic of two coupling ZRC oscillators.

Firstly the dynamic of the system can be investigated in the absence of the external

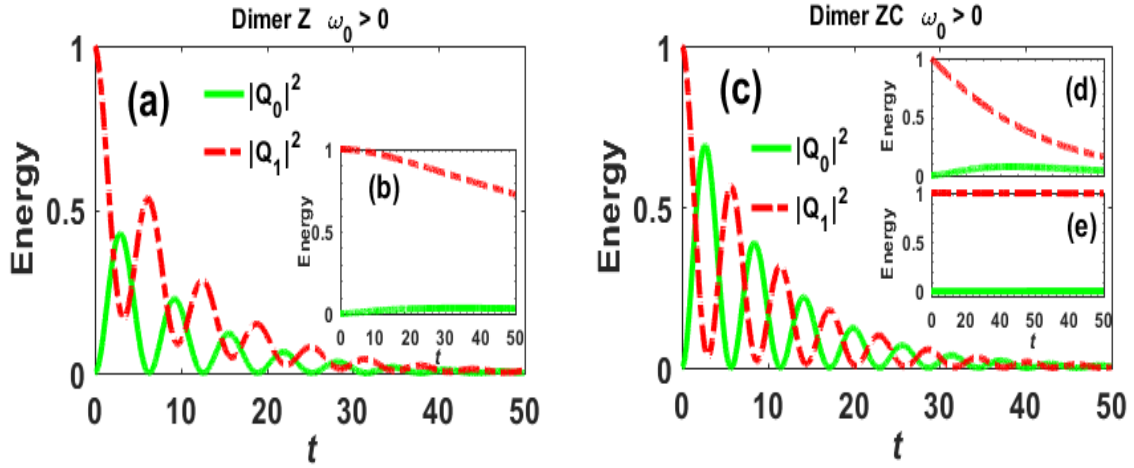


Figure 3.13: Time evolution of the energy in each cell of the dimer Z (first column) and the dimer ZC (second column). (a) and (b) correspond to dimer Z in presence of strong ( $\beta_C = 0.5$ ) and weak ( $\beta_C = 0.02$ ) coupling regimes, respectively. (c) and (d) represent the dimer ZC (when  $\kappa = 0.75$ ) in the strong ( $\beta_C = 0.2$ ) and the weak ( $\beta_C = 0.71$ ) couplings, respectively. (e) correspond to the dimer ZC at the CPLP ( $\beta_C = \kappa = 0.75$ ). For all plots  $\varepsilon = 0$  and  $\beta_0 = 0.1$  and  $\omega_0 = 1 \text{ rad.s}^{-1} > 0$ . The solid green and red dashes curves represent the energies  $|Q_0|^2$  and  $|Q_1|^2$ , respectively.

voltage. According to Eq. (2.49), the eigenvectors  $A_{i+}$ ,  $A_{i-}$  ( $i = 0, 1$ ) describing the normal modes of the coupled system satisfy to Eq. (2.57).

If  $c \neq c_{th} = \beta_0(\varepsilon - 1)/2$ , the general solution  $Q_{0,1}(t)$  for the ZRC dimer can be written as in Eq. (2.58). The amplitudes  $A_{i\pm}$  are found from the initial conditions of the oscillators (see Eqs. (2.59) and (2.60)),  $Q_i(0)$  being the initial charges of the capacitors. We have calculated the amplitude squared  $|Q_i|^2$  associated to each loop of the dimer and the response is significantly describing the transfer of energy from one oscillator to another.

Let's discuss the dynamics of the dimer by considering the following parameter for the non-Hermitian system  $\beta_0 = 0.1$  and  $\varepsilon = 0$ . With these considerations, the EPs are found to be  $\beta_{C1} = -0.05$  and  $\beta_{C2} = 0.05$  in the case of the dimer Z. In the case of the dimer ZC ( $\kappa = 0.75$ ), they are obtained as  $\beta_{Cth1} = 0.7$  and  $\beta_{Cth2} = 0.8$ . Then, the weakly coupled regimes are in the ranges  $-0.05 < \beta_C < 0.05$  for the dimer Z and  $0.7 < \beta_C < 0.8$  for the dimer ZC, respectively. In both cases, the strongly coupled regime is found everywhere else.

In Figs. 3.13 and 3.14, the quantities  $|Q_0|^2$  and  $|Q_1|^2$  are plotted as a function of time  $t$  for different values of the active coupling  $\beta_C$  taken from each of the coupling regimes. The initial conditions of the dimer were chosen such as to introduce the signal into the coupling  $Z_1R_1C_1$  loop (oscillator 1),  $Q_0(0) = 0$  and  $Q_1(0) = 1$ . As illustrated, in presence of a strong coupling, once a signal is put into oscillator 1, it is noticed a rapid periodic exchange of energy between both oscillators loops. This exchange is made in an oscillatory process so that, when the energy of one oscillator reaches its maximum value, the energy

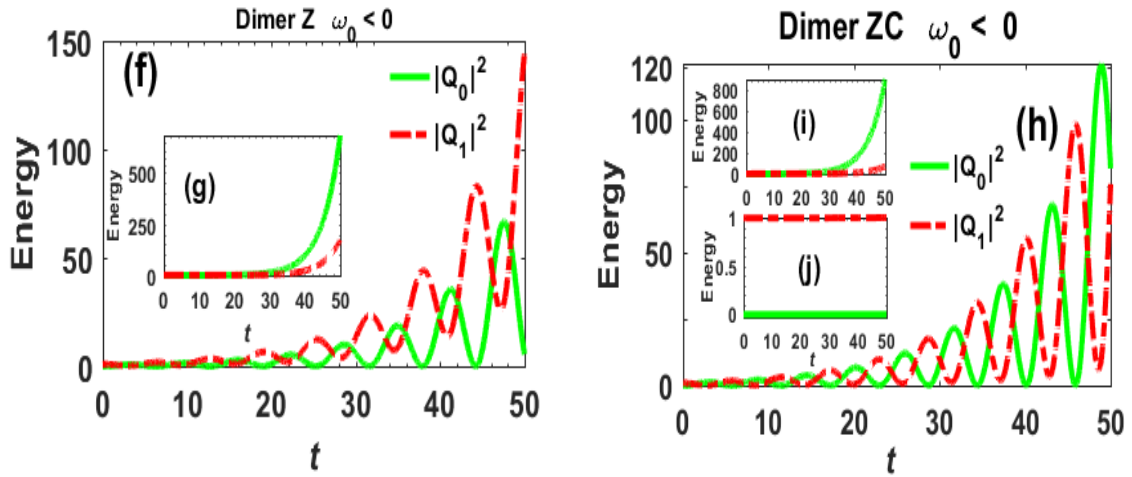


Figure 3.14: Time evolution of the energy in each cell of the dimer Z (first column) and the dimer ZC (second column). (f) and (g) correspond to dimer Z in presence of strong ( $\beta_C = 0.5$ ) and weak ( $\beta_C = 0.02$ ) coupling regimes, respectively. (h) and (i) represent the dimer ZC (when  $\kappa = 0.75$ ) in the strong ( $\beta_C = 0.2$ ) and the weak ( $\beta_C = 0.71$ ) couplings, respectively. (j) correspond to the dimer ZC at the CPLP ( $\beta_C = \kappa = 0.75$ ). For all plots  $\varepsilon = 0$  and  $\beta_0 = 0.1$  and  $\omega_0 = -1\text{rad.s}^{-1} < 0$ . The solid green and red dashes curves represent the energies  $|Q_0|^2$  and  $|Q_1|^2$ , respectively.

of the other oscillator is minimum. Also, note that these oscillations are very fast in the dimer ZC. On the contrary in presence of the weak coupling, it is noticed when  $\omega_0$  is positive that, the energy is irreversibly transferred from oscillator 1 to oscillator 0 of which the energy remains almost closed to zero. However, if  $\omega_0$  is negative, the energy of oscillator 1 takes a relatively long time to reach oscillator 0, of which the energy increases exponentially. At the CPLP, a particular point of a weak coupling regime, a different behavior is remarkable. Indeed, once the signal is introduced in oscillator 1, it remains there. There is no exchange of the energy with the oscillator 0 whose the amplitude remains zero. This confirms that at this point, the system seems effectively as it is uncoupled.

### b) Steady state dynamic: Absorption in a ZRC dimer

In the context of electronics, it is well known that the real part of the complex power (i.e. the active power) determines the absorption. Its imaginary part (i.e. the reactive power) simulates the dispersion properties of the atomic medium. Considering the central loop as a loss loop ( $\beta_0 = 0.1 > 0$ ), and modulating the non-Hermitian parameter ratio  $\varepsilon$  from the positive to negative values, the complex power can be investigated according to the coupling strength of dimers formed by a double and single coupling. In Fig. 3.15, the real (solid blue) and the imaginary (dashed red) parts of the normalized dissipated power ( $P_0/p_0$ ) are reported as a function of the normalized voltage frequency  $\omega/\omega_0$ . As it can be seen, if a weak coupling is established in the dimer ZC ( $\kappa = 0.75$ ,  $\beta_C = 0.71$ ,  $\omega_0 > 0$ ), a narrow dip appears in the absorption spectrum of the  $Z_0R_0C_0$  loop when  $\varepsilon = 0.2$ , leading two absorption peaks (Fig. 3.16(a)). The dispersion curve is



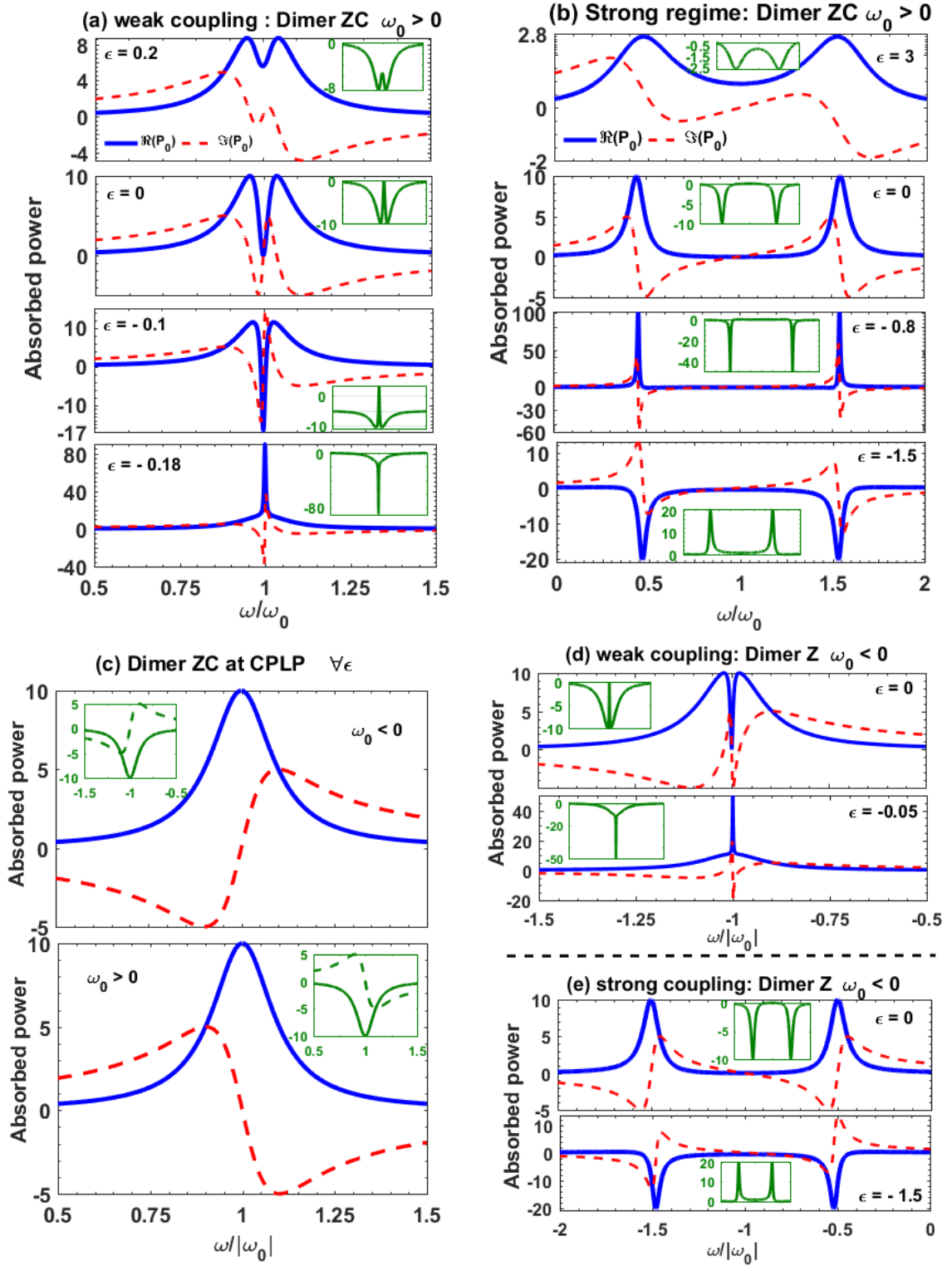


Figure 3.15: Absorbed power (dissipated) by the main loop of the dimer ZC (from (a) to (c)) when the natural frequencies of the loops are positive  $\omega_0 > 0$  and the one of the dimer Z (d) when natural frequencies are negative  $\omega_0 < 0$ . The solid blue and dashed red correspond to the real and imaginary parts of the absorbed power when the main loop is loss ( $\beta_0 = 0.1 > 0$ ). The insets in green show the real part of the power corresponding to the main loop gain ( $\beta_0 = -0.1 < 0$ ). The other parameters used to plot the graphs are the same as those used in Fig. 3.12.

also modified around the resonance (zero detuning). When  $\varepsilon = 0$ , a zero absorption, so a transparency domain occurs in the spectrum at a zero frequency detuning  $\delta = 0$ . Then, the dispersion curve becomes much steeper near the central frequency. This behavior is similar to the EIT effect. In atomic context, it has been interpreted as a direct manifestation of destructive interferences between the normal modes of oscillations of the system. This description matches perfectly with the experimental demonstrations made previously with classical systems. When a small negative dissipation ( $\varepsilon = -0.1$ ) is introduced into the pumping  $Z_1R_1C_1$  loop, a negative absorption occurs in the transparency zone. The negative absorption refers to the amplification. The later behavior is referred as the Electromagnetically Induced Amplified Transparency (EIAT). For a further decrease of  $\varepsilon$  until the value  $\varepsilon = -0.18$ , an enhanced absorption peak occurs in the profile where the dip was expected to be. This mimics the absorption spectrum of atomic systems with three energy levels in lambda ( $\Lambda$ ) configuration, in the regime of Electromagnetically Induced Absorption (EIA). EIA has been interpreted for atomic systems, as a manifestation of constructive interferences between the normal modes of oscillations. Fig. 3.16(b) shows the absorption profile of the  $Z_0R_0C_0$  loop when a strong coupling ( $\kappa = 0.75$ ,  $\beta_C = 0.2$ ,  $\omega_0 > 0$ ) is established in the dimer system. If much losses are introduced into the pumping loop ( $\varepsilon = 3$ ), it is observed in the spectrum, two absorption peaks separated by a large transparency window. These peaks are clearly identified when the losses decrease to zero (i.e.  $\varepsilon = 0$ ). The phenomenon is similar to the well-known Autler-Townes Splitting (ATS) effect which is generally interpreted as a consequence of a gap between two atomic resonances peaks. The peaks are located on both sides of the central frequency  $\omega_0$ . For a further decreasing of the damping, such as to introduce a negative dissipation into a pumping oscillator ( $\varepsilon = -0.8$ ), a negative absorption occurs in the spectrum. This leads the enhancement of the absorption peaks. Such a behavior can be generalized to the values of  $\varepsilon$  in the domain between 0 and  $-1$ , where  $\varepsilon = -1$  corresponds to the Parity Time Symmetric ( $\mathcal{PTS}$ ) case. However, when  $\varepsilon$  is less than  $-1$ , the peaks become inverted so that, only a negative absorption (amplification) is observed in the profile. The behavior can be called Autler-Townes splitting with amplification (ATSA).

*The question we can ask now is: what happens at the CPLP where the effective coupling cancels?*

To answer to this question, we substitute the couplingless condition given in Eq. (3.3) into the Eq.(2.61) and the expression of the absorbed power by the main loop is reduced to that dissipated by a free  $Z_0R_0C_0$  loop which was obtained in Eq. (2.56). As we could predict, the cancellation of the effective coupling has the effect to decouple parts of the system such that, no exchange of energy can be observed between them. Therefore, no interference could be obtained. The absorption spectrum is then reduced to that of a free oscillator, a lorentzian curve illustrated in Fig. 3.16(c). Accordingly, all

the other replicated atomic phenomena disappear. These results indicate that operating at the CPLP could be an efficient way to control applications of EIT with real atomic systems. Except for the CPLP, all the results discussed here with the ZC dimer when  $\omega_0 > 0$ , can also be obtained with a single coupled dimer. For example, Fig. 3.16(d) illustrates the absorption spectrum in the case of the dimer Z ( $\beta_C = 0.02$  and  $\beta_0 = 0.5$ ) when  $\omega_0 < 0$ . The transparent window observed agrees well the observation made with the dimer ZC when  $\omega_0 > 0$ . This demonstrates that EIT and related phenomena can be observed with negative frequencies of the system, and show a wide range of frequency for investigations with ZRC circuits. Also mention that the green curves illustrated in the insets show the active power obtained in the same conditions, however with the main loop gain ( $\beta_0 = -0.1 < 0$ ).

Knowing the dynamics in the dimer, the next paragraph will be focused on the multidimer systems.

### 3.1.2.4 Dispersive properties in a ZRC multi dimer

Let us consider the multi dimer circuit. In the previous section, we have seen from the absorption spectrum of the ZRC dimer ( $N=1$ ) that, the circuit allows to reproduce EIT, EIAT, EIA or ATS windows.

*What happens in the spectrum when  $N > 1$ ? Is the multi dimer circuit could be used to replicate a multiple EIT, EIA or ATS windows?*

Indeed it has been demonstrated that, to obtain multiple transparency windows, each part of the circuit must oscillates with its own natural frequency  $\omega_i$  ( $i = 0..N$ ), which differs from one loop to another. Considering harmonic solutions for the charges, the dynamic of the multidimer can be described by the Eq. (2.63) when adding the voltage term  $u(t) = v_0 e^{j\omega t} + c.c$  in its right term. Solving such equation, the amplitudes  $A_i$  ( $i = 0..N$ ) can be obtained and accordingly, the charge solution  $Q_0(t)$  through the central loop. Thanks to Eq. (2.15), we have calculated the expression of the steady state frequency-dependence power  $P_0(\omega)$ , which is dissipated by the main loop as a function of the  $N$  number ( $N \geq 1$ ) of multipod loops under the resonance conditions. Its expression is found in Eq. (2.65).

In the following, we will focus the analysis on three cases of the multi dimer ZC circuits: the bi dimer, the tri dimer and the tetra dimer. The aim is to show that the interferences in the system can allow to reproduce the multiple EIT, EIA and ATS, with the number of windows consistent with the  $N$  number of the multipods. Assuming Eq. (3.5) for the multipod loops frequencies' and the central loop as a loss one ( $\beta_0 = 0.5 > 0$ ), the steady state power  $P_0(\omega)$  can be investigated when controlling the coupling parameter  $\beta_C$  and the non-Hermitian parameter ratio  $\varepsilon$ . In Figs. 3.16, 3.17 and 3.18, the real (solid blue) and the imaginary (dashed red) parts of the normalized dissipated power  $P_0(\omega)/p_0$  are

reported as a function of the normalized frequency  $\omega/|\omega_0|$  for different values of the  $\varepsilon$  parameter.

**Case 1: the bi dimer ZC ( $N = 2$ )**

As illustrated in Figs. 3.16(a), in presence of the weak coupling ( $\kappa = 0.75$ ,  $\beta_C = 0.85$ ), it is noticed in the absorption spectrum when  $\varepsilon = 0$ , the occurrence of two symmetric dips centered at  $\omega = 0.9\omega_0$  and  $\omega = 1.1\omega_0$  on both sides of the central peak. This gives rise to two EIT windows. The behavior is similar to the quantum phenomenon of a double Electromagnetically Induced Transparency (DEIT). Accordingly, two steep slopes are observed in the dispersion curve near the transparency domain. It is interesting to note that these results are consistent with DEIT demonstrated in the previous works, where the LRC circuits have been used.

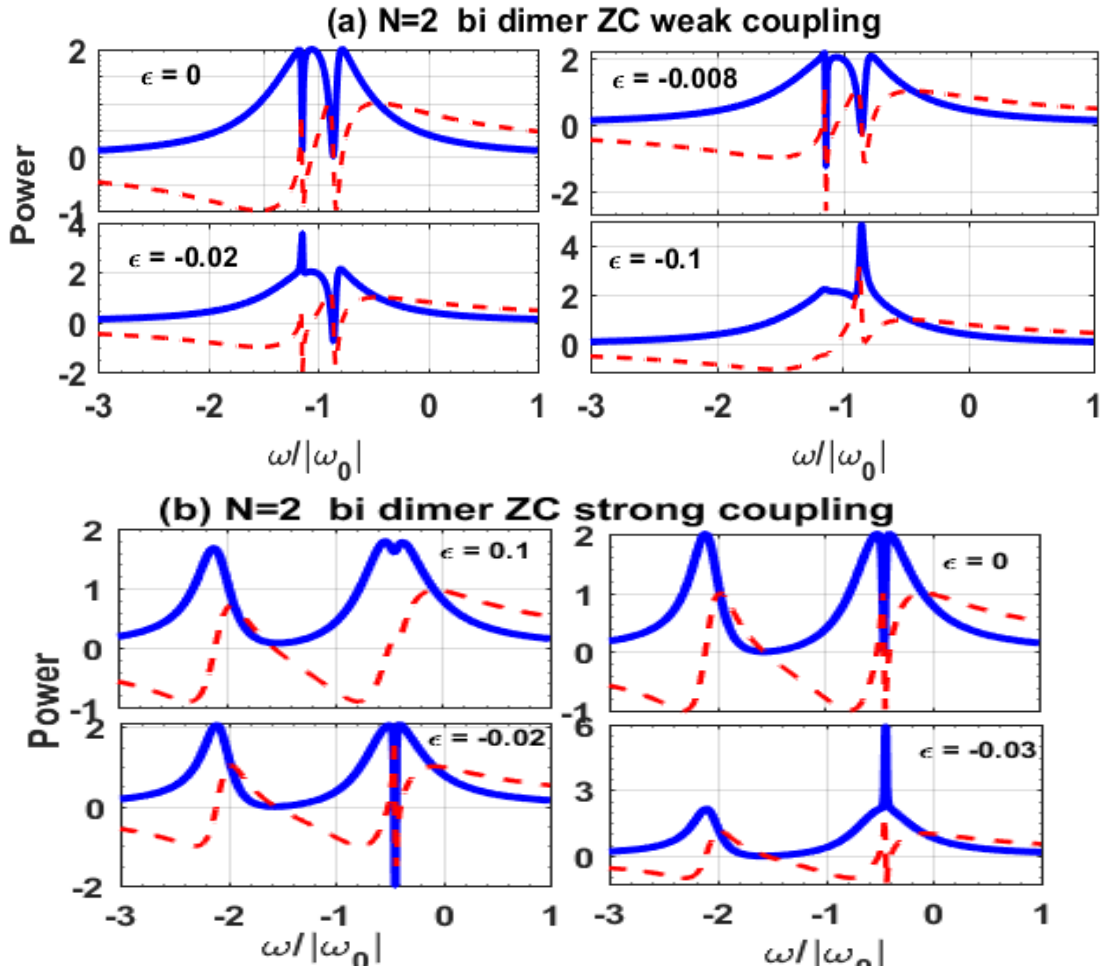


Figure 3.16: The real and imaginary parts of the steady state normalized dissipated power  $P_0/p_0$  as a function of the normalized frequency  $\omega/|\omega_0|$  in the case of the bi dimer ZC ( $N=2$ ) according to the coupling regime: (a) weak coupling, (b) strong coupling. In all plots, we set  $\omega_0 < 0$ ,  $\beta_0 = 0.5$  and  $\kappa = 0.75$ . The other parameters used to plot the graphs are inserted in text.

However, notice that one difference between our results and the previous ones is that for the previous ones, the frequencies of the system were only positive, while for our system, the frequencies can be as well positive or negative, as described above. By decreasing  $\varepsilon$

to the value  $\varepsilon = -0.008$ , a phenomenon similar to the EIAT appears in the absorption spectrum. However it is centered at two frequencies, where a negative power is observed. Accordingly, this new behavior is called double EIAT (DEIAT). For a further decreasing of  $\varepsilon$  to  $-0.02$ , and then to the value  $-0.1$ , it is remarked in the spectrum the occurrence of one EIA peak where the first EIT dip was observed and then another one, where the second dip was expected to be. As a consequence, it results two enhanced absorption peaks. Then, the bi dimer ZC circuit allows to replicate double EIA (DEIA). So, the bi dimer allows the replication of two EIT, EIAT or EIA windows in the weak coupling regime.

Fig. 3.16(b) shows in presence of the strong coupling ( $\kappa = 0.75$ ,  $\beta_C = 0.2$ ) that, when a dissipation is introduced into the coupling fields  $\varepsilon = 0.1$ , it is observed two dips inside the absorption profile. One of the dips is more pronounced and centered at the frequency  $\omega_0$  while the other one is very narrow. Both dips are separated by a large transparency domain, similar to the ATS effect described above. The location of the peaks is in perfect accordance with the eigenmodes behavior presented in Fig. 3.6, where the multipod modes frequencies are closed together while the central mode splits. A further decrease of  $\varepsilon$  to the value  $\varepsilon = 0$  reduces the dips to zero, leading to the phenomenology of EIT. The system then allows to reproduce simultaneously EIT and ATS windows instead of two ATS windows as we could expected in the strong coupling regime. As one would imagine, by lowering  $\varepsilon$  to negative values for example  $\varepsilon = -0.02$ , a negative power, typical to the EIAT effect observed in the weak coupling for  $\varepsilon = 0$ , occurs in the region of transparency between the two EIT peaks. For  $\varepsilon = -0.03$ , it is not surprising to note that the spectrum just pass from EIAT to the EIA behavior exhibited in the case of the dimer ZC. In all cases, the dispersion curve is modified according to the phenomenon reproduced. The bi dimer can then allow to replicate simultaneously ATS and EIT, EIAT or EIA windows in the strong coupling regime.

### ***Case 2: the tri dimer ZC ( $N = 3$ )***

In the presence of the weak coupling ( $\kappa = 0.75$ ,  $\beta_C = 0.803$ ) as illustrated in Fig. 3.17(c), if  $\varepsilon = 0$ , the absorption spectrum shows three narrow dips centered at the natural loops frequencies  $0.9\omega_0$ ,  $1.02\omega_0$  and  $1.1\omega_0$  (see Eq. (3.5)), thus exhibiting three EIT windows. This behavior is similar to the Triple EIT (TEIT) effect, which was observed in atomic contexts. TEIT was also studied in a superconducting quantum circuit with a four-level V-type energy spectrum. A further decreasing of  $\varepsilon$  to  $-0.003$ , then to  $-0.006$  and thereafter to  $-0.04$  allows to the spectrum to switch from the triple EIAT (TEIAT) to a double EIA (DEIA) and then to triple EIA (TEIA), respectively. So, a tri dimer can provides up to three EIT, EIAT or EIA windows in presence of the weak coupling.

In presence of a strong coupling ( $\kappa = 0.75$ ,  $\beta_C = 0.58$ ) as shown in Fig. 3.17(d), when  $\varepsilon$  takes respectively the values  $\varepsilon = 0$ ,  $\varepsilon = -0.0037$ ,  $\varepsilon = -0.002$ , and  $\varepsilon = -0.01$ , the spectrum presents similar behaviors as those obtained in the strong coupling regime with

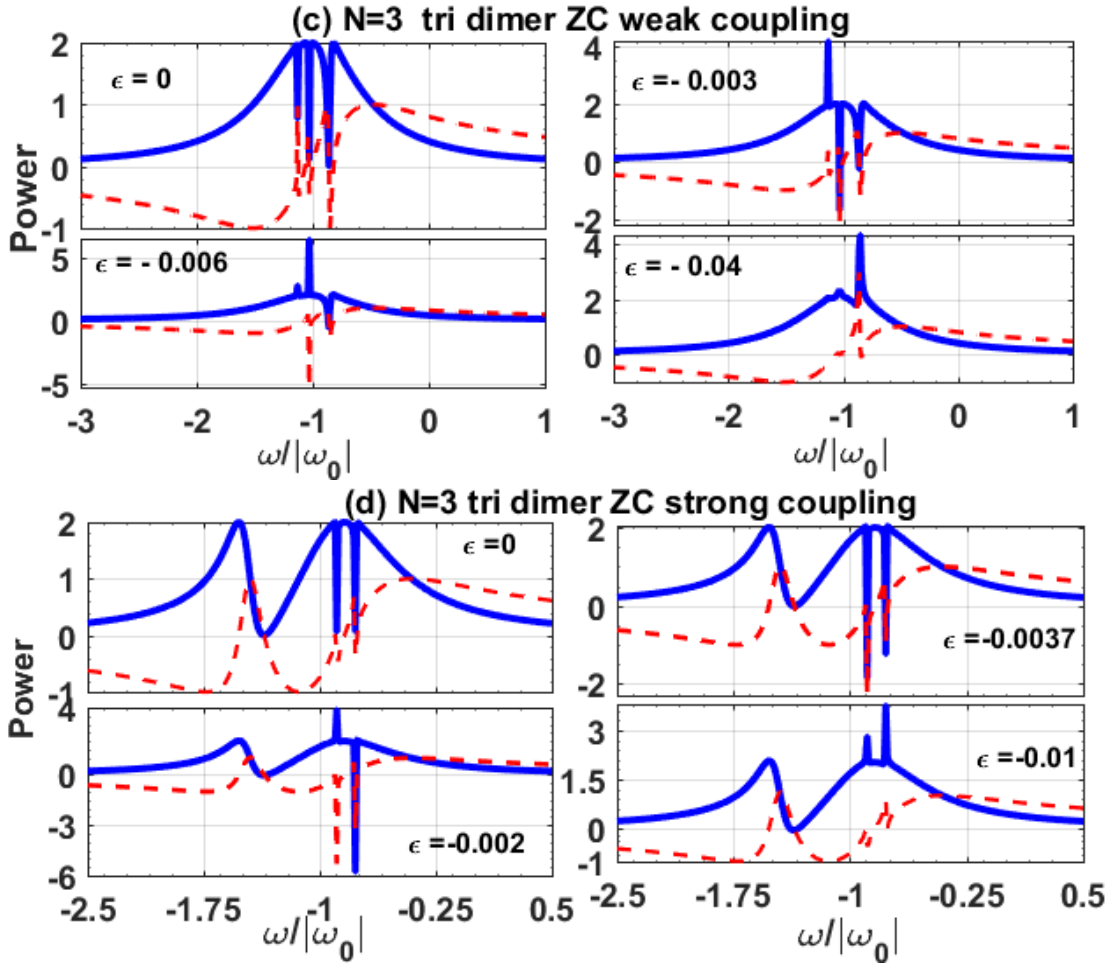


Figure 3.17: The real and imaginary parts of the steady state normalized dissipated power  $P_0/p_0$  as a function of the normalized frequency  $\omega/|\omega_0|$  in the case of the tri dimer ZC ( $N=3$ ) according to the coupling regime: c) weak coupling, d) strong coupling. In all plots, we set  $\omega_0 < 0$ ,  $\beta_0 = 0.5$  and  $\kappa = 0.75$ . The other parameters used to plot the graphs are inserted in text.

the bi dimer ZC. However, the number of EIT, EIAT dips or EIA peaks is increased to two, whereas the number of ATS window remains constant to one.

### ***Case 3: the tetra dimer ZC ( $N = 4$ )***

As illustrated in Fig. 3.18(e), in the presence of the weak coupling ( $\kappa = 0.75$ ,  $\beta_C = 0.78$ ), it is observed in the profile when  $\varepsilon = 0$ , four EIT windows, called a quadruple EIT (QEIT). By playing on the value of  $\varepsilon$ , the tetra dimer allowed also to reproduce quadruple EIAT (QEIAT) windows when  $\varepsilon = -0.0007$ , then a TEIA when  $\varepsilon = -0.004$  and finally quadruple EIA (QEIA) if  $\varepsilon = -0.01$ .

In Fig. 3.18(f) where the tetra dimer is in presence of the strong coupling ( $\kappa = 0.75$ ,  $\beta_C = 0.2$ ), the system allows again to mimic TEIT ( $\varepsilon = 0$ ), TEIAT ( $\varepsilon = -0.001$ ), DEIA ( $\varepsilon = -0.006$ ) and TEIA ( $\varepsilon = -0.0025$ ) simultaneously accompanied in each case by just an ATS dynamic.

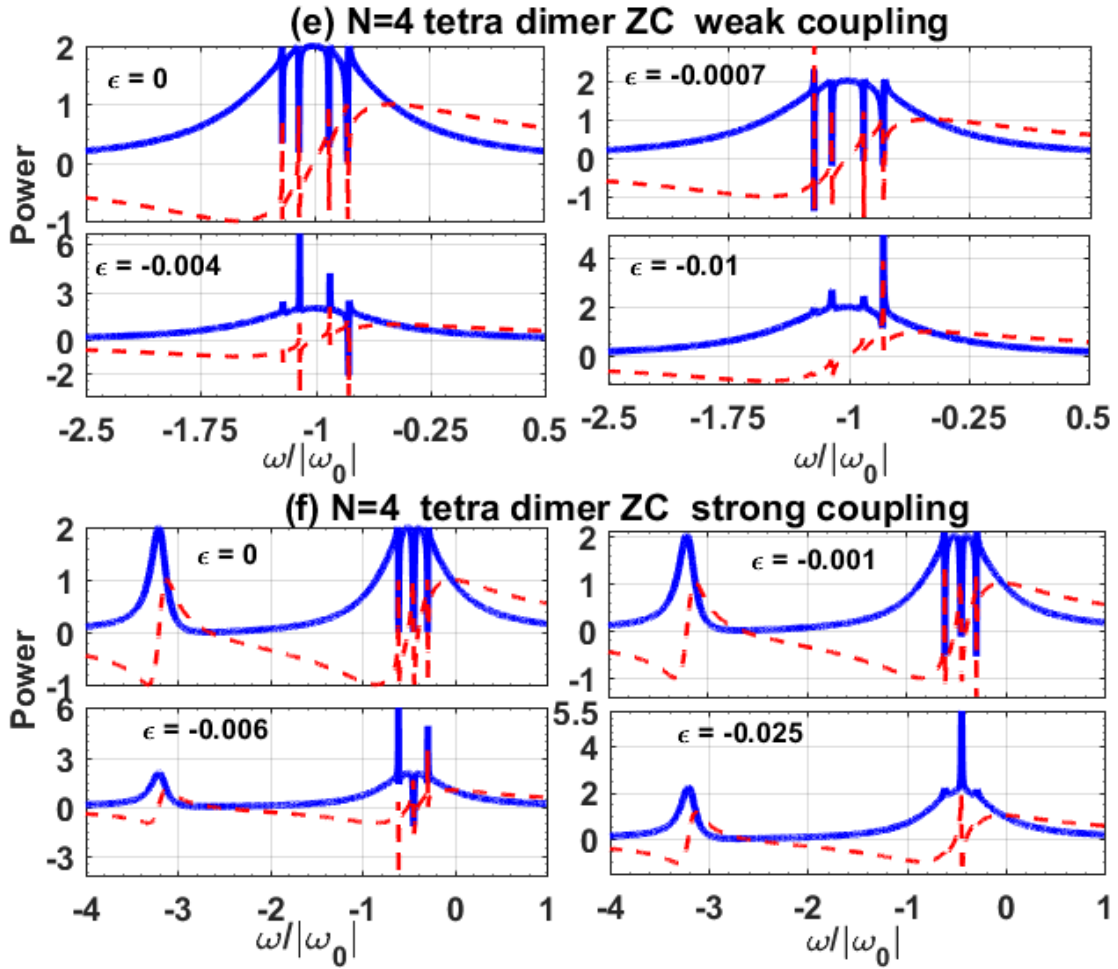


Figure 3.18: The real and imaginary parts of the steady state normalized dissipated power  $P_0/p_0$  as a function of the normalized frequency  $\omega/|\omega_0|$  in the case of the tetra dimer ZC ( $N=4$ ) according to the coupling regime: e) weak coupling, f) strong coupling. In all plots, we set  $\omega_0 < 0$ ,  $\beta_0 = 0.5$  and  $\kappa = 0.75$ . The other parameters used to plot the graphs are inserted in text.

### 3.1.3 Concluding remarks on the analysis close to the resonance of coupled LRC/ZRC oscillators driven by a harmonic voltage

In this part, we have proposed two models of electronic dimers as analog of a three-level atomic system with  $\Lambda$  type energy-level configuration. With the dimer MLC using a LRC series oscillator, we have derived a non-Hermitian Hamiltonian of which the effective coupling  $C_T$  allowed to group the system in the effective CP and the effective CPL dimers characterized by a CPLP. In CP dimers, we distinguish the weak coupling regime where the phenomenology of EIT and related phenomena is observed. However, in the strong regime, the model made it possible to reproduce ATS type behavior which could be modified into other similar effects. On the contrary, in CPL dimers the EIT like behavior and all related phenomena are vanishing since at the CPLP, the parts of the dimer seem as uncoupled. All these results match well with the experimental LTspice simulations.

We have also proposed a non-Hermitian electronic dimers, based on the imaginary resistor, which is analog to a  $(N+2)$  level atomic system in the multipod type configuration. The so-called ZRC multi dimer system is described by the equations of the first order. Under the resonance approximations, we have successfully investigated on the structural characterization. Two main coupling regimes have emerged revealing a couplingless point (CPLP) associated to multiple couplings. In the weakly coupling regime, the eigenfrequencies cross. This demonstrates a non-reversible energy transfer between the coupled oscillators. On the other hand, in the strong coupling regime, the eigenfrequencies exhibit a splitting behavior. This indicates exchange between energy in the coupling oscillators in a periodical way. The proposed model is highly desired to develop quantum interference dynamic in dispersive media. When the central loop is coupled to  $N$  multipod loops, its absorption profile replicates the N-EIT, N-EIAT or N-EIA dynamic in the weakly coupling. When the strong coupling is established, the  $(N-1)$  EIT,  $(N-1)$  EIAT or  $(N-1)$  EIA with the ATS dynamic is simultaneously observed. It is remarkable that, at the CPLP all the quantum phenomena disappears. This reveals the efficiency of the imaginary resistive coupling in the cancellation of the capacitive coupling effect. We hope that our model will be a better prototype that can help researchers in understanding quantum phenomena observable in atomic media and could find farther ideas for future works.

In the next section, we study scattering properties of non-Hermitian  $\mathcal{PT}/\mathcal{APT}$  symmetric systems.

## 3.2 Scattering properties of non-Hermitian electronic dimers

The scattering is achieved by embedding a non-Hermitian  $\mathcal{PT}/\mathcal{APT}$  symmetric dimer MLC presented in Fig. 2.5, as a defect into a  $LC$  Hermitian ETL (Fig. 2.6). The wave propagation at any point of the system is governed by Eqs. (2.73) and (2.74). Far away from the defect, the dispersion frequency of the wave in a TL can be written as in Eq. (2.76). Such dispersion indicates that the TL is a bandpass with a lower cutoff frequency of  $f_1 = 1/2\pi$  and an upper cutoff frequency of  $f_2 = \sqrt{1 + 4\vartheta}/2\pi$ , which occur at wavenumbers  $k = 0$  and  $k = \pi$ , respectively. The scattering coefficients for an incidence from the gain/loss side of the dimer were calculated using the  $S$ -scattering matrix defined in Eq. (2.67). Such coefficients are obtained in Eqs. (2.77) and (2.78).

### 3.2.1 Scattering properties of the $\mathcal{PT}$ symmetric dimer MLC

Due to the reciprocity of transmission for any linear stationary and nonmagnetic medium [66, 220], the transmission coefficients coincide for the left and right propagations ( $T_g = T_l$ ). The reflection coefficients are nonreciprocal ( $R_g \neq R_l$ ), and the corresponding scattering signals satisfy the generalized unitary conservation relation  $||T|^2 - 1| =$



$|R_l \cdot R_g^*|$ , which reveals the underlying symmetries of the scattering  $\mathcal{PTS}$  dimer defect. The active  $\mathcal{PTS}$  dimer MLC allows for a direct observation for a transition from exact phase to the broken phase controlled by a gain and loss parameter. Hence, we distinguish between two groups of dimers: the TH dimers (C, L, M and ML) for which the first gain/loss breaking value  $\gamma_{PT}$  remains non-zero whatever the circuit parameters combinations of the isolated dimer, and the THL dimer (LC, MC and MLC) for which  $\gamma_{PT}$  vanishes if the capacitance coupling obeys Eq. (3.6).

$$c = \frac{\nu + \alpha\mu}{\alpha(1 - \mu)} \quad (3.6)$$

The TH or THL characteristic of the dimer plays an interesting role in the scattering features, such as lasing modes, unidirectional transparency, mirror-like behavior, etc. The lasing modes properties of the dimer systems are investigated by analyzing the lasing gain/loss parameter  $\gamma_r$  operating at a critical wavenumber  $k_r$ . Their expressions are obtained in Eqs. (2.79) and (2.80) when the common denominator  $D$  of the scattering coefficients turns to zero.

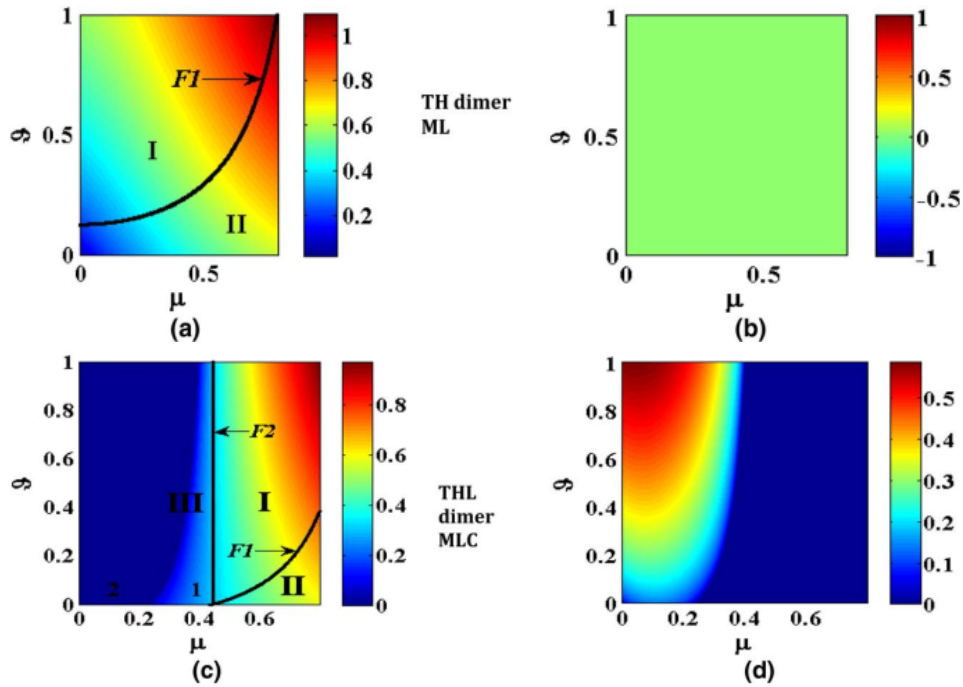


Figure 3.19: Spectra of  $\gamma_r$  for which  $D = 0$ . The case TH dimer ML is depicted in (a) and (b), and the case THL dimer MLC is plotted in (c) and (d). The first column is the real part representation, while the imaginary part is depicted in the second column. F1 and F2 define the frontiers of regions I (real  $k$ ), II (complex  $k$ ), and III (purely imaginary  $k$ ). The TH dimer does not allow imaginary wave propagation;  $\gamma_r$  is either real or complex. The THL dimer allows control of real, complex, and imaginary propagation wavenumbers. The existence of region III-2 implies that lasing modes occur for imaginary  $\gamma_r$  and  $k_r$ .

The lasing mode spectra for the TH dimer ML are plotted in Figs. 3.19(a) and 3.19(b), while the ones of THL dimer MLC are represented in Figs. 3.19(c) and 3.19(d). The first

column is the real part of  $\gamma_r$ , and the second column represents its imaginary part. We derive the boundaries of the values of  $k$ , F1, and F2 from Eq. (2.79) as:

$$\vartheta = (1 - \mu^2) (\nu - c - 1) + 1 / \left[ 2(1 + 2c) (1 - \mu^2) \right], \quad \text{for F1,} \quad (3.7)$$

$$1 / (1 - \mu^2) + \nu = 1 + c, \quad \text{for F2.} \quad (3.8)$$

As indicated by the graphs, F1 and F2 delimit three regions: I, II, and III. F2 is independent of  $\vartheta$ . Region I corresponds to purely real and positive values of the wavenumbers  $k$  and frequencies  $\omega$  (i.e.,  $-1 < \cos k < 1$  and  $1 < \omega < \sqrt{1 + 2\vartheta}$ ). These are the allowed frequencies from the TL dispersion relation expressed in Eq. (2.76); we can then see that the values of  $\gamma_r$  for which lasing modes occurs are real. Region II is the upper forbidden gap where  $\cos(k) < -1$  and  $\omega > \sqrt{1 + 2\vartheta}$ . The wavenumbers are complex, with a constant real part (equal to  $\pi$ ) and a varying negative imaginary part,  $k = \pi - i\kappa$ . The frequencies are also complex in this region, but the lasing modes exist for real values of  $\gamma_r$  (Eq. (2.80)). Region III is the lower forbidden bandgap for which  $\cos(k) > 1$  and the wavenumbers  $k$  are purely imaginary (i.e.,  $k = +i\kappa$ ). Therefore, the frequency propagation ( $\omega < 1$ ) is real for  $2\vartheta (\cosh k - 1) > 1$  and purely imaginary for  $2\vartheta (\cosh k - 1) < 1$ . From Figs. 3.19(c) and 3.19(d), it can be clearly seen that the lasing parameter  $\gamma_r$  can be either real region III-1 or purely imaginary region III-2. These analyses indicate three regions of wavenumber propagation and subsequently lasing modes operation in THL dimers, the third region being the region of purely imaginary  $k$ , while TH dimer can only operate in two regions in which  $k$  is either real or complex. It is interesting that there are two exceptions for these rules: The TH dimer C does not have real or complex operating modes. Regions II and I are not observed. F2 frontier occurs at  $C = 0$ . Therefore,  $\gamma_r$  is purely imaginary, so the lasing modes could only be observed for purely imaginary values of the wavenumbers. The second exception is that in the THL dimer LC, the frontier F2 coincides with the THL transition of the isolated dimer LC; consequently, region III-1 does not exist.

In what follows, the scattering coefficients' dependence on the different regions detailed above are analyzed. Whenever a region is observed in the  $k$  spectrum of a dimer, the behavior is dictated by the related scattering coefficients. Specifically, for the dimer MLC, which includes all regions in the spectrum (Figs. 3.19(c) and 3.19(d)), the value of  $\mu$  can be taken as the region-selective parameter and thus be tuned from one region to another while the other parameters  $\vartheta = 0.1$ ,  $c = 0.5$ , and  $\nu = 0.25$  remain unchanged unless otherwise specified. As predicted from the above analysis, we identify in Figs. 3.20 and 3.21 spectral singularities of zero-width resonances ( $D = 0$ ) [99] corresponding to intense scattering coefficients amplifications (i.e.,  $T_{g,l} = R_{g,l} = \infty$ ) in all the propagation regions except at the frontiers, where the waves are perfectly reflected (i.e.,  $T_{g,l} = 0$  and  $R_{g,l} = 1$ ). These spectral singularities give rise to lasing modes  $k_r$  at  $\gamma_r$ . Notwithstanding this analysis, the scattering coefficients have specific features in each region depending on the nature of

$k$ . In region I (Fig. 3.20(a)), for example, at  $\mu = 0.5$ , the wavenumbers are all real and positive (allowed frequencies), two close EPs emerge ( $\gamma_g = 0.282$ ,  $\gamma_l = 0.438$ ) as gain/loss values at which the gain/loss reflected wave vanishes, i.e.,  $R_g = 0$  ( $R_l \neq 0$ ) and  $R_l = 0$  ( $R_g \neq 0$ ), respectively. The parameters  $\gamma_{g,l}$  are the gain/loss reflectionless points. Due to the unitary transmission ( $T_{g,l} = 1$ ), moreover, at these points, the transmission phase is not affected, as indicated in Fig. 3.20(c), which refers to as anisotropic transmission resonances. And these points correspond to regions of unidirectional invisibility [106,222] from left and right, respectively. In the range between unidirectional invisibility from the left ( $R_g = 0$ ,  $T = 1$ ) and unidirectional invisibility from the right ( $R_l = 0$ ,  $T = 1$ )(i.e.,  $\gamma_g < \gamma < \gamma_l$ ) the transmission is superunitary ( $T > 1$ ); otherwise, the transmission is subunitary ( $T < 1$ ). These unidirectional reflectionlessness and invisibility are the characteristics of any  $\mathcal{PTS}$  scattering system. They are of technological interest, as they offer the means of one-way designing of linear optical devices [106,222,223]. It was demonstrated [99,224,225], that in  $\mathcal{PTS}$  systems, the transition from the  $\mathcal{PTS}$  phase to the  $\mathcal{PTS}$  broken phase is dictated by the unitary related transmission. In particular, it was shown that  $T < 1$  corresponds to the  $\mathcal{PTS}$  phase, where the eigenvalues of the scattering  $S$ -matrix are unimodular and non degenerated, while  $T > 1$  induces a  $\mathcal{PTS}$  broken phase of which the eigenvalues are degenerated and non-unimodular. Thus our scattering system is phase-broken  $\mathcal{PT}$  symmetric between  $\gamma_g$  and  $\gamma_l$ .

Importantly, we find a critical value of the TL coupling parameter  $\vartheta_c$  above which the reflection scattering coefficient from the right does not vanish any longer, but the left reflection vanishes at two different points. This critical value is obtained by solving the equation  $R_{g,l} = 0$ . For the set of parameters we have considered, the calculated critical value is  $\vartheta_c = 1.719$ . In Fig. 3.20(b), we have taken  $\vartheta = 4 > \vartheta_c$ , the scattering plots exhibit two far-apart EPs at  $\gamma_{L1} = 0.7156$  and  $\gamma_{L2} = 2.042$  for which  $R_l = 0$  ( $T = 1$ ). In Fig. 3.20(d), the spectrum of  $\vartheta$  is numerically plotted for the parameters  $c = 0.5$ ,  $\mu = 0.5$ . The green color identifies the region where  $R_{g,l} = 0$  admits one solution each. Consequently, there are two EPs, one in each direction, giving rise to the  $\mathcal{PTS}$  behavior in the gain/loss direction. In the red region, there are two solutions for  $R_l = 0$  and no solution for  $R_g = 0$ . Likewise, there are two EPs but only in the loss direction and no EP in the right direction. Moreover, the right reflection is greater than the transmission and the EPs are very far apart. This behavior has drastic consequence on the scattering system, as this latter becomes non- $\mathcal{PTS}$  and mainly mirrors in the gain direction. The  $\mathcal{PTS}$  behavior is observed only in the allowed values of real frequency as defined by the frontiers F1 and F2. It is useful to reveal that this transmission tends to vanish as both reflections (from gain and loss sides) tend to unity far away from the inner region of unidirectionality  $R_{l,g} \rightarrow 1$  when  $T \rightarrow 0$ .

At the two frontiers, the transmission vanishes completely and the dimer behaves like a perfect mirror throughout the  $\gamma$  range (i.e.,  $R_{l,g} = 1$  and  $T = 0$ ) as predicted by the combined Eqs. (3.7) and (3.8) in Eq. (2.77). For example, in Fig. 3.21(a), the scattering

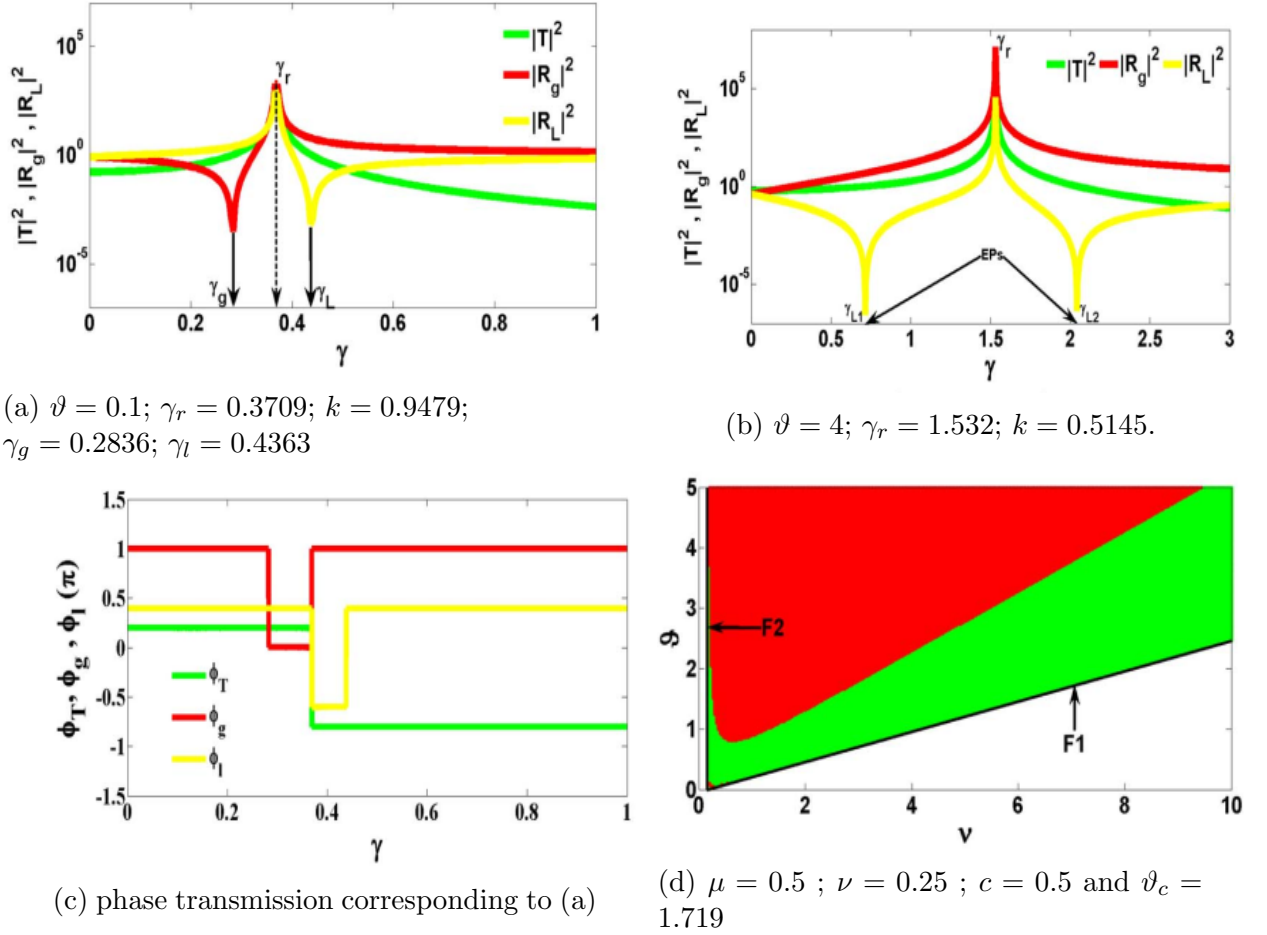


Figure 3.20: Scattering normalized coefficient  $T$  and  $R$  of THL dimer MLC versus the gain/loss parameter in region I.  $\nu = 0.25$ ,  $c = 0.5$  and  $\vartheta = 0.1$ . (a)  $k$  and  $\gamma$  are real; EPs occur for the gain/loss incidence while in (b)  $\vartheta = 4$ , and the EP occurs only for the loss incidence at two different points.  $T > 1$  in between the EP in both cases. Lasing modes are observed inside the EPs, where the transmission is superunitary. (c) At  $\gamma_g$  and  $\gamma_l$ , the phase transmission corresponding to (a) does not change. In (d), the spectrum of  $\vartheta$  is plotted for  $c = 0.5$  and  $\mu = 0.5$ ; the green color indicates the region where the dimer is  $\mathcal{PTS}$  in two opposite directions (at  $\gamma_{g/l}$ ), while in the red region, the dimer is  $\mathcal{PTS}$  in one direction (two distinct values of  $\gamma_l$ ).

parameters are plotted at F1 for  $\mu = 0.447$ ,  $k = 0$ , and at F2 for  $\mu = 0.627$ ,  $k = \pi$ . In region II, the upper forbidden gap with complex wavenumbers ( $k = \pi - i\kappa$ ), the scattering coefficients are plotted for  $\mu = 0.75$  in Fig. 3.20(b). As indicated in the graph,  $\gamma_r$  exists and is real and  $T > R_g > R_l$ . It is, however, instructive that far from this lasing zone, the left reflection is totally attenuated while the gain reflection is unity; likewise there is a critical value of  $\gamma = \gamma_c$  where  $R_g = T = 1$ , below which the  $(T + R)$  is superunitary and subunitary above. In region III, the lower forbidden gap having purely imaginary wavenumbers, we distinguish the plot in region III-1 where  $\gamma_r$  is real (Fig. 3.21(c)) and in region III-2 where  $\gamma_r$  is purely imaginary (Fig. 3.21(d)). For real  $\gamma_r$  (for example,  $\mu = 0.3$ ), there is a resonant mode indicated by  $\gamma_r$  and  $R_l > R_g > T$  and outside the resonant mode, the transmission is completely attenuated while the reflection scatterings are constants,  $R_g = 1$  and  $R_l > R_g$ . For imaginary values of  $\gamma_r$  (for example,  $\mu = 0.2$ ), the

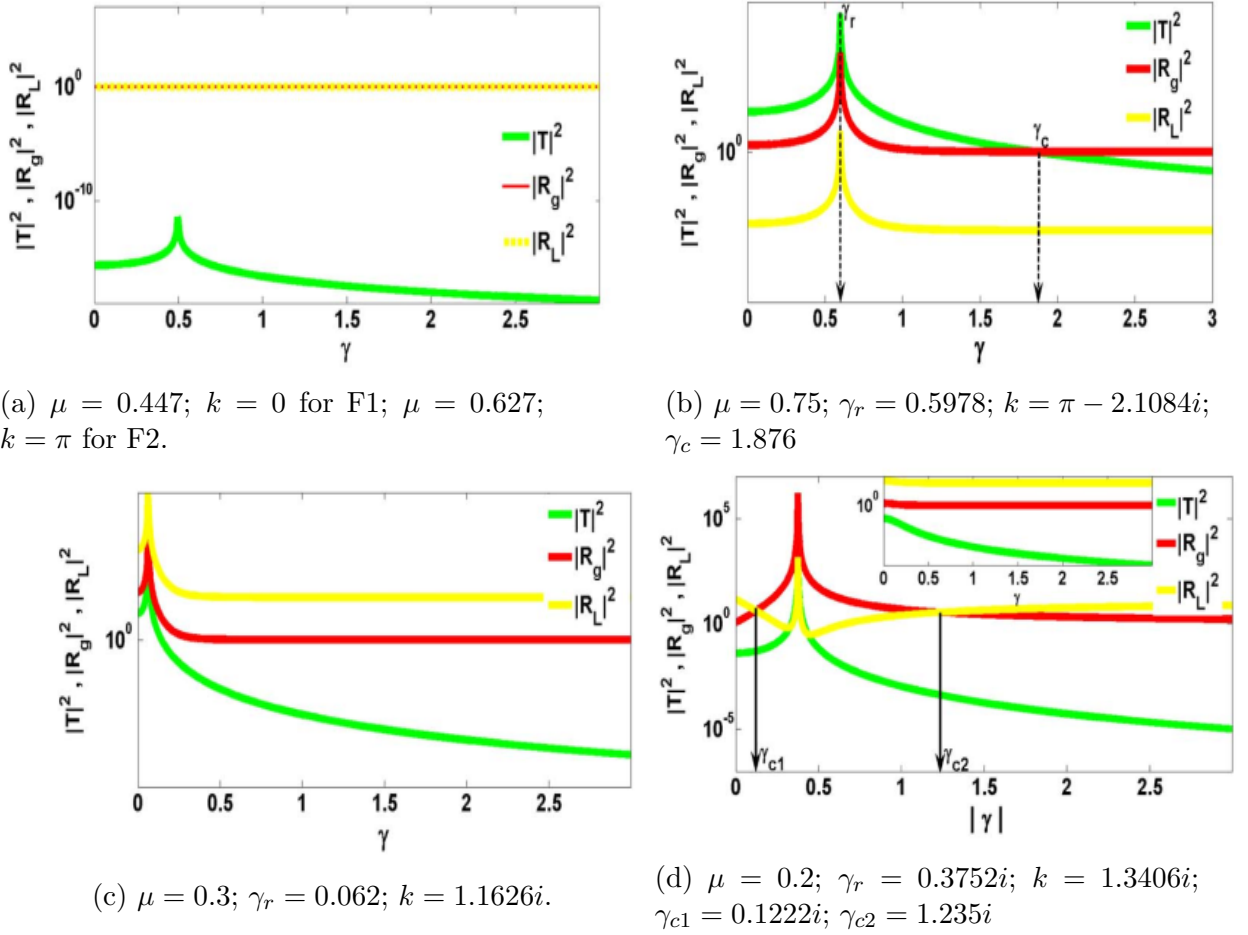


Figure 3.21: Scattering normalized coefficient  $T$  and  $R$  of THL dimer MLC versus the gain/loss parameter  $\nu = 0.25$ ,  $c = 0.5$  and  $\vartheta = 0.1$ . (a) At the frontiers F1 ( $\mu = 0.447$ ,  $k = 0$ ) and F2 ( $\mu = 0.627$ ,  $k = \pi$ ), the transmission vanishes completely:  $T = 0$ ;  $R_g = R_l = 1$ . (b) In region II,  $\mu = 0.75$ ,  $k$  is complex and  $\gamma$  is real,  $\gamma_c$  occurs at  $R_g = T = 1$  below which  $T > 1$  and  $T < 1$  above. Lasing modes occur in the region of superunitary transmission. Far from  $\gamma_r$ ,  $R_l = 0$ . (c) Region III-1,  $k$  is imaginary but  $\gamma$  is real. Lasing mode occurs around  $\gamma_r = 0.062$ . The transmission vanishes completely, i.e.,  $T = 0$  and  $R_g = 1 (< R_l)$ . (d) Region III-2,  $\mu = 0.75$ ;  $k$  and  $\gamma$  are both imaginary.  $|\gamma|$  is the magnitude of the imaginary gain/loss parameter  $\gamma$ . Lasing mode is observed inside the region defined by  $\gamma_{c1}$  and  $\gamma_{c2}$  where  $R_g = R_l$ . Far from  $\gamma_c$ ,  $T = 0$  and  $R_l > R_g$ . The inset indicates that all real  $\gamma$  incidences are totally attenuated in transmission and perfectly reflected in the gain side ( $R_g = 1$ ), while the loss reflected wave is amplified ( $R_l > R_g$ ).

scattering coefficients are plotted in the imaginary plane. There are two critical points at which  $R_g = R_l$  ( $T = 0$ ), inside which the gain reflection is amplified and the loss reflection is attenuated;  $R_g > R_l$  with  $R_l < 1$  except at the resonance. Indeed, a lasing mode does exist where all the scattering coefficients are intensely amplified simultaneously with the reflections are more amplified than the transmission. Outside the region of simultaneously left and right unitary reflection, the loss reflection is slightly amplified, while the gain reflection is slightly attenuated, and thus  $R_l > R_g$ . As indicated at the inset of the curve, all real  $\gamma$  incidences are totally attenuated in transmission and perfectly reflected in the gain side ( $R_g = 1$ ), while the loss reflected wave is amplified ( $R_l > R_g$ ). This indicates

the absence of lasing states for real values of  $\gamma_r$ .

### 3.2.2 Scattering properties of the $\mathcal{APT}$ symmetric dimer MLC

We are now interested on the scattering properties of the  $\mathcal{APT}$  dimer MLC. A rapid analysis of the scattering coefficients obtained in Eq. (2.78) indicates a reciprocity in the transmittance and the reflectances for the real wave number  $k$ . The spectral singularities of the system are investigated by solving the equation  $D^\pm = 0$ , where  $D$  is the common denominator of the scattering coefficients and the signs  $\pm$  are associated to  $\pm\gamma$ . Solving this, leads to a critical gain/loss  $\gamma_r$  and wave number  $k_r$  at the resonance whose the expressions are found in Eqs. (2.81) and (2.82), respectively. The spectrum of  $\gamma_r$  indicates three domains similar to domains (I), (II) and (III) obtained in the  $\gamma_r$  spectra of the  $\mathcal{PT}$  scattering system. The corresponding frontiers can be expressed as follows:

$$\vartheta = \frac{2c\mu + \mu + 2\nu - 2\mu\nu - 2c}{2(1 - \mu)(1 + 4c)}, \text{ for F1} \quad (3.9)$$

$$2(1 - \mu)c - 2\nu - \mu + 2\mu\nu = 0, \text{ for F2.} \quad (3.10)$$

Nest, we analyze the scattering coefficients in the mentioned domains and the frontiers. We use the following parameter values:  $\nu = 1$ ,  $\mu = 0.5$  and  $\vartheta = 0.5$ , for the  $\mathcal{APT}$  dimer MLC in loss  $(+\gamma) - \text{loss } (+\gamma)$  configuration. Only the variation of the coupling parameter  $c$  allows to pass from one domain to another one.

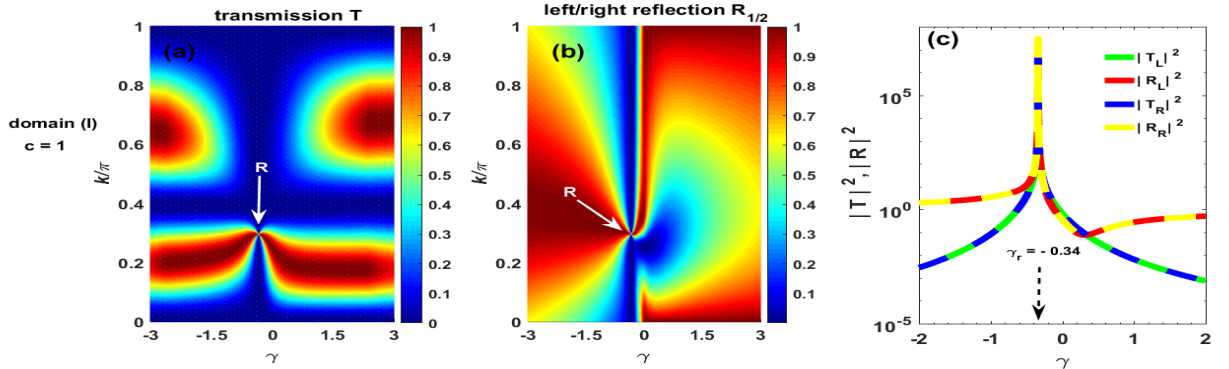


Figure 3.22: (a), (b): 3D (top view) representation of  $T = \left|T_{R/L}\right|^2 / \left|T_{R/L}\right|_{\max}^2$  and (c):  $R_{1/2} = \left|R_{L/R}\right|^2 / \left|R_{L/R}\right|_{\max}^2$  for the  $\mathcal{APT}$  dimer MLC ( $\nu = 1$ ,  $\mu = 0.5$ ,  $\vartheta = 0.5$  and  $c = 1$ ) in the domain (I). The lasing mode occurs at  $\gamma_r \approx -0.34$ , for  $k_r \approx 0.3\pi$ . we note a reciprocity in both reflection and transmission. (d): Scattering normalized coefficient for  $k = k_r$ .

In Figs. 3.22 and 3.23, the 3D (top view) representation of the quantities  $T = \left|T_{R/L}\right|^2 / \left|T_{R/L}\right|_{\max}^2$  and  $R_{1/2} = \left|R_{L/R}\right|^2 / \left|R_{L/R}\right|_{\max}^2$  are depicted as a function of the normalized wave number  $k/\pi$  and the gain/loss parameter  $\gamma$ . As we can see in Figs. 3.22

(a), (b) and (c) illustrating the scattering properties in domain (I) ( $c = 1$ ), one observe a reciprocity in the reflectances and the transmittances from the left and the right. We also note a presence of the lasing (resonance) point  $R$  where it is observed an amplification of the scattering coefficients ( $T_{L/R} = R_{L/R} = \infty$ , i.e.,  $T = R_{1/2} = 1$ ). This point occurs at a negative value of  $\gamma_r \approx -0.34$ , corresponding to  $k_r \approx 0.3\pi$ . This indicates that the loss  $(+\gamma) - \text{loss } (+\gamma)$   $\mathcal{APT}$  scatterer systems displays either lasing mode for negative gain/loss parameter. The reflectances tend to vanishes for positive gain/loss value. In the case of the  $\mathcal{APT}$  dimer in gain  $(-\gamma) - \text{gain } (-\gamma)$  configuration, the lasing mode would occurred for positive gain/loss parameter. These properties suggest alternatives ways of designing novel linear optoelectronics devices. A cross section made from Figs. 3.22(a) and 3.22(b) at  $k = k_r$  is shown in 2D plot on Fig. 3.22(c), where the resonance point is clearly observed. Indeed, when  $\gamma < \gamma_r = -0.34$ , both reflections amplitudes are amplified  $R_{L/R} > 1$  and the transmissions tend to zero  $T_{L/R} \rightarrow 0$ . The systems thus behaves as a mirror from both sides. After the resonance point, all scattering coefficients begin to decrease. While the transmission continues to tend towards 0, we see that the reflections reach a minimum value but not completely zero (on contrary to what observed in the  $\mathcal{PTS}$  case, where they completely disappear), from which we note a sudden rise in their value to tend to one.

The Figs. 3.23 (a), (b) and (c) obtained when  $c = 0.1$ , illustrate the behavior of the reflected and transmitted wave in the domain (II). Indeed, the resonance point does not occurs. The wave number  $k$  is complex (i.e.,  $k = \pi - 1.76j$ ). The reflectances from left and right sides become non-reciprocal. Whatever the gain/loss parameter  $\gamma$  value, the reflection from the left is always amplified while the one from the right side and the transmission remain attenuated as shown by Fig. 3.23(d). This means that from one direction a system behaves as a mirror while from the other direction it looks as an absorber.

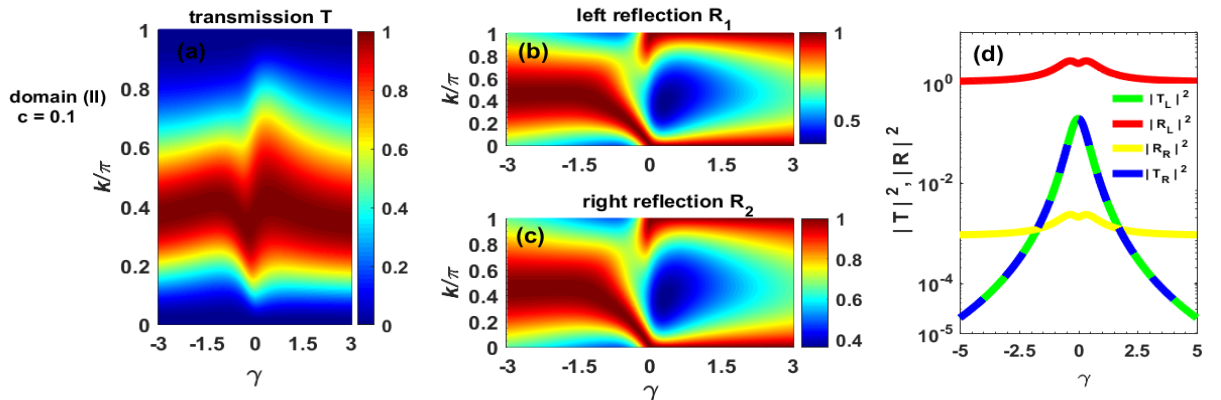


Figure 3.23: (a), (b) and (c): 3D top view of  $T = |T_{R/L}|^2 / |T_{R/L}|_{\max}^2$  and  $R_{1/2} = |R_{L/R}|^2 / |R_{L/R}|_{\max}^2$  in the domain (II) for the  $\mathcal{APT}$  dimer MLC ( $\nu = 1$ ,  $\mu = 0.5$ ,  $\vartheta = 0.5$  and  $c = 0.1$ ). There is not reciprocity in reflections since the wave number is complex and the lasing mode does not occurs. (d): Scattering normalized coefficient for  $k = \pi - 1.76j$ .

Finally, when the value of  $c$  respects the Eq. (3.10), that is for example  $c = c_{cr} = 1.5$ , it is observed a total attenuation of the transmission and the reciprocity in the two reflections, as in the  $\mathcal{PT}$  case (see Fig. 3.21(a)). So, the system behaves as a perfect mirror for the left and right incidences.

### 3.2.3 Concluding remarks on scattering properties of a $\mathcal{PT}/\mathcal{APT}$ dimer MLC

In this section, we have investigated on the scattering properties of the general model of  $\mathcal{PT}/\mathcal{APT}$  symmetric dimer MLC. When inserted it into a Hermitian ETL, the scattering system admits real waves in the allowed band, complex waves in the upper forbidden gap, and purely imaginary waves in the lower gap. This corresponds either to a real or an imaginary gain/loss parameter. We have demonstrated that when the  $\mathcal{PTS}$  dimer scattering system propagates real wave number, it undergoes a spontaneous breaking symmetry at the EPs inside which the transmission is superunitary ( $T > 1$ ) and subunitary outside. This corresponds to three types of regimes in the context of Anderson localization behavior: the extended states regime ( $T > 1$ ); the localized states regime ( $T < 1$ ), and the unidirectional invisibility or transparency ( $T = 1$ ) at the EPs. Interestingly, the  $\mathcal{PTS}$  scattering system exhibits qualitative new behavior, such as the canceling of the  $\mathcal{PTS}$  property in one direction, which arises when  $\vartheta$ , the TL coupling parameter, exceeds a TH limit  $\vartheta_c$ .

The  $\mathcal{APT}$  scattering systems are generally behave as mirrors, and absorbers when propagating complex and imaginary wave numbers. For the real wave numbers propagation, the lasing modes always occur at the negative gain/loss values for loss-loss  $\mathcal{APT}$  dimers and at the positive gain/loss values otherwise. The results demonstrate promising applications in wave manipulations for artificial structures, which exhibit novel properties and control mechanisms.

Finally, it is remarkable that the insertion of the  $\mathcal{PT}/\mathcal{APTS}$  dimer into a conservative ETL as a defect, in addition to reveal intriguing features, intrinsically inspires us to investigate the wave transport phenomena in disordered media. We are therefore tempted to repeat the defect in the TL in order to study other properties. In this logic, we investigate in the next section, the quantum behavior of Anderson localization (AL) in non-Hermitian ETL systems.

## 3.3 Energy transport and Anderson-like localization in non-Hermitian electrical transmission lines

In this section, we analyze the effect of a cascade association of  $2N$  size oscillators ZRC or  $N$  dimers ZRC, so as to obtain a discrete  $1\mathcal{D}$  non-Hermitian ETL schematically shown in Fig. 2.7. The non-Hermiticity in the TL is introduced by the linear resistance



$R_n$  whose value, as for other components of the circuit, can be positive or negative. Given that the resistance is dissipative by nature, we used it to simulate the disorder effect, which will allow us to check the quantum localization behavior of  $1\mathcal{D}$  disordered systems using the ETLs. To do so, we will focus ourselves to the ETL systems in  $\mathcal{PT}$  or in  $\mathcal{APT}$  configuration. The resonance approximations made above within the framework of the EIT and related phenomena effects are not valid here.

In particular, we focus on  $1\mathcal{D}$  ETLs in the Right-handed (RH) or the Left-handed (LH) configurations representing a succession of dimers RH or LH such as required by Eqs. (2.85) and (2.86), respectively. It is then instructive for us, to first analyze as an example, the equations dynamic and symmetries of a pair of unit cells number 0 and 1. The effective Hamiltonian describing the so-called dimers RH and LH are found in Eqs. (2.87) and (2.88), and the conditions of commutation of these later with the joint  $\mathcal{PT}$  operator are given in Eqs. (2.89) and (2.90) respectively. In the same way, the conditions of anti-commutation can be found in Eqs. (2.91) and (2.92), respectively. These necessary  $\mathcal{PT}$  and  $\mathcal{APT}$  conditions can be generalized to a dimer formed from a pair of unit cells,  $n$  and  $(n + 1) \forall n$  (odd or even) in Tables 3.2 and 3.3.

Configuration	$\mathcal{PT}^{RH}$		$\mathcal{APT}^{RH}$	
	odd	even	odd	even
$C_n$	$C$	$C$	$C$	$C$
$r_n$	$r$	$r$	$-r$	$r$
$R_n$	$-R$	$R$	$R$	$R$
$\beta_n$	$-\beta$	$\beta$	$-\beta$	$\beta$
$\omega_n$	$\omega_0$	$\omega_0$	$-\omega_0$	$\omega_0$

Table 3.3: RH ETL characteristics

Configuration	$\mathcal{PT}^{LH}$		$\mathcal{APT}^{LH}$	
	odd	even	odd	even
$r_n$	$r$	$r$	$r$	$r$
$C_n$	$C$	$C$	$-C$	$C$
$R_n$	$-R$	$R$	$-R$	$R$
$\beta_n$	$-\beta$	$\beta$	$-\beta$	$\beta$
$\omega_n$	$\omega_0$	$\omega_0$	$-\omega_0$	$\omega_0$

Table 3.4: LH ETL characteristics

Based on these findings, we can as well demonstrate the  $\mathcal{PT}$  and  $\mathcal{APT}$  symmetry behaviors of a bigger chain. Let's consider a chain of  $2N$  size, where  $N = 25$  remains constant throughout this thesis. The electric currents in any three successive cells  $(n - 1)$ ,  $n$  and  $(n + 1)$  obey to Eqs. (2.28) and (2.29) for the ETLs in the RH and LH configuration, respectively. In the following, the capacitances and resistances in each cell are considered constants and positive ( $C > 0$ ,  $r > 0$ ,  $R > 0$ ). In addition, the gain/loss parameter,  $\beta = R/r$  and the reference frequency,  $\omega_0 = 1/rC$  are also restricted to positive values. Therefore, the eigenfrequencies of the systems can be found when taking into account

the solutions given in Eq. (2.93) and the zero boundaries conditions (Eq. (2.94)). It is necessary to notice that, the Hermitian ETLs are governed by the dispersion relations  $\omega = 2\omega_0(1 - \cos k)$  for the LH TL and  $\omega = \frac{\omega_0}{2(-1 + \cos k)}$  for the RH TL. Such dispersion indicates that the TLs are a bandpass of which the allowed frequencies are given by  $0 < \omega < 4\omega_0$  and  $-\frac{\omega_0}{4} < \omega < \infty$ , for the ideal LH and RH ETL, respectively.

In what follow, we investigate on the vibration frequency on each site of the TLs.

### 3.3.1 Modes dynamic

#### 3.3.1.1 $\mathcal{PTS}$ configuration

The Eqs. (2.96) and (2.97) give us the normalized frequencies  $\Omega_{\pm}^{RH}(\beta, k_p)$  and  $\Omega_{\pm}^{LH}(\beta, k_p)$  in  $\mathcal{PT}$  configuration (see tables 3.2 and 3.3 for more details), for the RH and for the LH ETLs, respectively. In these expressions, one easily identifies the square root singularity

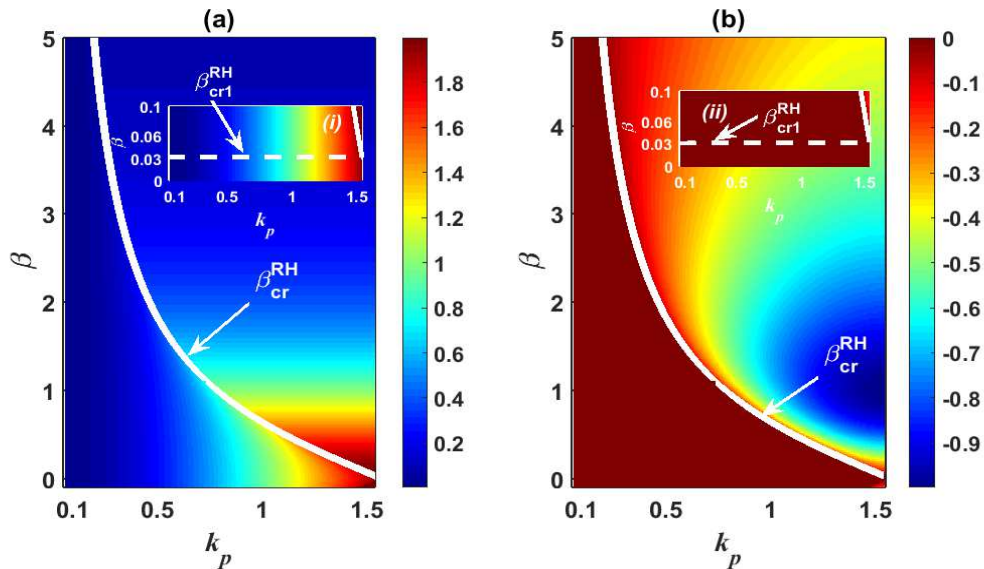


Figure 3.24: 3D top view ETLs normalized frequencies spectra  $\Omega_{\pm}^{RH}(\beta, k_p)$  as function of  $k_p$  and  $\beta$  in  $\mathcal{PTS}$  configuration. Column (a) for the real parts and column (b) for the imaginary parts.  $\beta_{cr1} < \beta_{cr} < \beta_{cr2}$  is the transition range values separating the real and the complex modes. Beyond this range the modes are thresholdless. The insets (i) and (ii) highlight the domain situated before  $\beta_{cr1}$ .

$\Omega \propto \sqrt{(\beta_{cr})^2 - \beta^2}$ , a characteristic of the  $\mathcal{PTS}$  modes expansion.  $\beta_{cr}$ , is the threshold value of  $\beta$  at which the  $\mathcal{PTS}$  breaking occurs [221]. Consequently, for  $\beta < \beta_{cr}$ , the system is in the  $\mathcal{PTS}$  phase with real frequencies and for  $\beta > \beta_{cr}$ , the system is in the broken symmetry phase with complex frequencies. At the transition point also called exceptional point (EP) [13, 220], there is a coalescence of the eigenfrequencies. In our models, the thresholds depend on the wave number  $k_p$ ,  $\beta_{cr} = \beta_{cr}(k_p)$ . Their expressions are given in Eqs. (2.98) and (2.99). The  $\mathcal{PTS}$  phase exists for real frequencies, and this condition is fulfilled for the values of the wave numbers  $k_1 < k_p < k_N$ , corresponding to the critical transitions domain defined by  $\beta_{cr1} < \beta_{cr} < \beta_{cr2}$ . The two limiting values  $\beta_{cr1}$  and  $\beta_{cr2}$  for

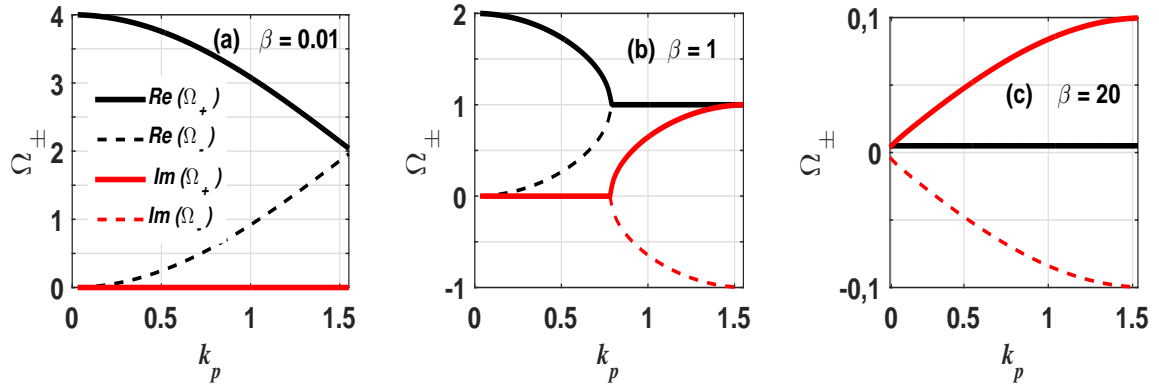


Figure 3.25: The real (black color) and the imaginary parts (red color) of the eigenvalues  $\Omega_{\pm}^{RH}$  as function of the wave number  $k_p$  for several values of the gain/loss  $\beta$  in  $\mathcal{PTS}$  configuration. The values of  $\beta$  used correspond to the domains illustrated in Fig. 3.24. (a)  $\beta = 0.01 < \beta_{cr1}^{RH}$ ; (b)  $\beta_{cr1}^{RH} < \beta = 1 < \beta_{cr2}^{RH}$ ; (c)  $\beta = 20 > \beta_{cr2}^{RH}$ .

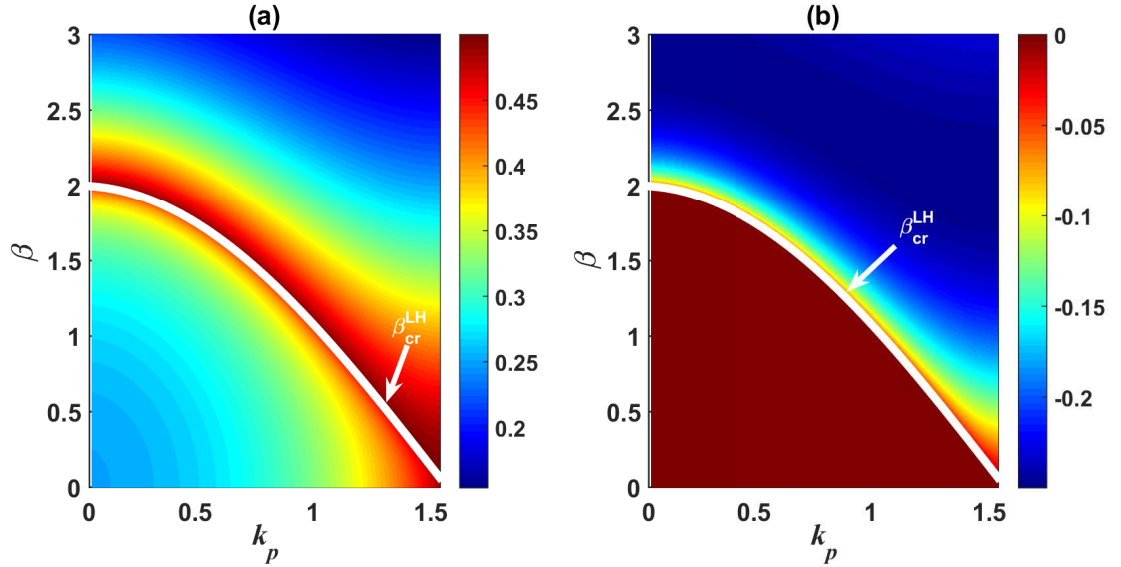


Figure 3.26: 3D top view ETLs normalized frequencies spectra  $\Omega_{\pm}^{LH}(\beta, k_p)$  as function of  $k_p$  and  $\beta$  in  $\mathcal{PTS}$  configuration. Column (a) for the real parts and column (b) for the imaginary parts.  $\beta_{cr1} < \beta_{cr} < \beta_{cr2}$  is the transition range values separating the real and the complex modes. Beyond this range the modes are thresholdless.

the RH and LH configurations are given by Eqs. (2.98) and (2.99) for  $k_p = k_N$  and  $k_p = k_1$ , respectively. In other words, for  $\beta < \beta_{cr1}^{RH} = 1/\tan(k_N)$  (resp.  $\beta < \beta_{cr1}^{LH} = 2 \cos(k_N)$ ), the eigenspectrum is entire real. When  $\beta > \beta_{cr2}^{RH} = 1/\tan(k_1)$  (resp.  $\beta > \beta_{cr2}^{LH} = 2 \cos(k_1)$ ), the eigenspectrum is totally complex. For values of  $\beta_{cr}$  in the range  $\beta_{cr1}^{RH} < \beta_{cr} < \beta_{cr2}^{RH}$  (resp.  $\beta_{cr1}^{LH} < \beta_{cr} < \beta_{cr2}^{LH}$ ), the spectrum displays two domains, one of which the frequencies are totally real and the other where they are complex, both domains being separated by a critical wave number  $k_{cr}^{RH} = \tan^{-1}(1/\beta_{cr}^{RH})$  (resp.  $k_{cr}^{LH} = \cos^{-1}(\beta_{cr}^{LH}/2)$ ). In Fig. 3.24, the real (a) and the imaginary (b) parts of normal modes frequencies and the threshold value  $\Omega_{\pm}^{RH}(\beta, k_p)$  (white curves) are reported as a function of the wave number  $k_p$  for the ETL in the  $\mathcal{PT}^{RH}$  configuration respectively. We find  $\beta_{cr1}^{RH} = 0.03$  and  $\beta_{cr2}^{RH} = 16.2$ .

For  $\beta < \beta_{cr1}^{RH}$ , as illustrated by the insets (i) and (ii), the spectrum is entirely real since the imaginary part  $\text{Im}(\Omega_{\pm}^{RH}) = 0$ . The value  $\beta = 0.01$  used in Fig. 3.25(a) agrees well this observation. On the contrary, for the values of  $\beta$  taken between 0.03 and 16.2, the plot in Fig. 3.25(b),  $\beta = 1$ , displays two domains: the first region where  $\Omega_{\pm}^{RH}$  is real and the second region where it is complex. The separation between the two regions occurs at  $k_{cr}^{RH} = \pi/4$ . The case  $\beta = 20$ , corresponds to the broken phase Fig. 3.25(c)). In the same logic, in Fig. 3.26 are shown in 3D top view, the real (a) and the imaginary (b) parts of the normal modes frequencies  $\Omega_{\pm}^{LH}(\beta, k_p)$  for the ETL in  $\mathcal{PT}^{LH}$  configuration. In this case, the boundary threshold values are found to be  $\beta_{cr1}^{LH} = 0.06$  and  $\beta_{cr2}^{LH} = 2$ . As shown in Fig. 3.27 (a) for  $\beta = 0.01 < \beta_{cr1}^{LH}$ , the frequencies are real. When  $\beta$  is increased to 1, Fig. 3.27(b) exhibits a domain where the frequencies are totally real and another one where they are complex. For the case  $\beta = 3 > \beta_{cr2}^{LH}$ , in Fig. 3.27(c), all frequencies are totally complex.

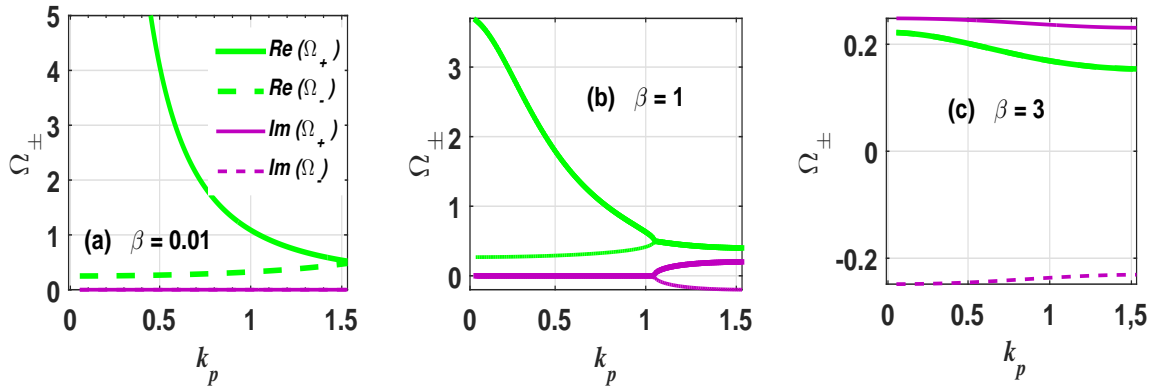


Figure 3.27: The real (green color) and the imaginary parts (purple color) of the eigenvalues  $\Omega_{\pm}^{LH}$  as function of the wave number  $k_p$  for several values of the gain/loss  $\beta$  in  $\mathcal{PTS}$  configuration. The values of  $\beta$  used correspond to the domains illustrated in Fig. 3.26. (a)  $\beta = 0.01 < \beta_{cr1}^{LH}$ ; (b)  $\beta_{cr1}^{LH} < \beta = 1 < \beta_{cr2}^{LH}$ ; (c)  $\beta = 3 > \beta_{cr2}^{LH}$ .

### 3.3.1.2 $\mathcal{APTS}$ configuration

The analysis of the eigenmodes  $\Omega_{\pm}^{RH}(\beta, k_p)$  for the RH ETL in  $\mathcal{APT}$  configuration given in Eq. (2.100) also reveals a square-root singularity  $\Omega \propto \sqrt{(\beta_{cr})^2 - \beta^2}$ , a fingerprint of non-Hermitian  $\mathcal{APTS}$  systems. The atypical  $\mathcal{APTS}$  breaking occurs at  $\beta = \beta_{cr}^{RH} = \tan(k_p)$  for any value of  $p$ . Since this expression depends on the wave number  $k_p$ , two critical points  $\beta_{cr1}^{RH} = \tan(k_1)$  and  $\beta_{cr2}^{RH} = \tan(k_N)$  are evinced to bind the region of the gain/loss parameter where the frequencies of the system result in a thresholdless operation regime. Thus, when  $\beta < \beta_{cr1}^{RH}$ , the eigenspectrum is characterized by complex frequencies, while for  $\beta > \beta_{cr2}^{RH}$ , the entire eigenspectrum become purely imaginary. As  $\beta$  moves in the range  $[\beta_{cr1}^{RH}, \beta_{cr2}^{RH}]$ , we can distinguish a region below  $k_{cr} = \tan^{-1}(\beta_{cr}^{RH})$  where the frequencies are purely imaginary and a region above where system is complex. Unlike the case of the  $\mathcal{APT}^{RH}$ , a quick analysis of Eq. (2.101) reveals that the  $\mathcal{APT}^{LH}$  is unbreakable.

In Fig. 3.28, the real (column (a)) and the imaginary (column (b)) parts of the

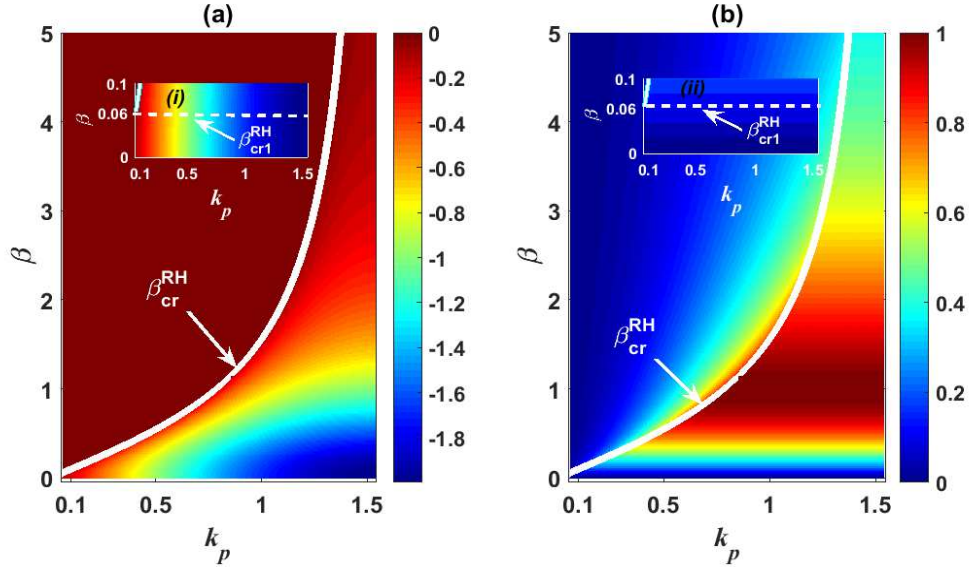


Figure 3.28: 3D top view ETLs normalized frequencies spectra  $\Omega_{\pm}^{RH}(\beta, k_p)$  as function of  $k_p$  and  $\beta$  in  $\mathcal{APT}^{RH}$  configuration. Column (a) for the real parts and column (b) for the imaginary parts. The threshold  $\beta_{cr}$  separates the complex and the purely imaginary mode regions. The insets (i) and (ii) highlight the domain situated before  $\beta_{cr1}$ .

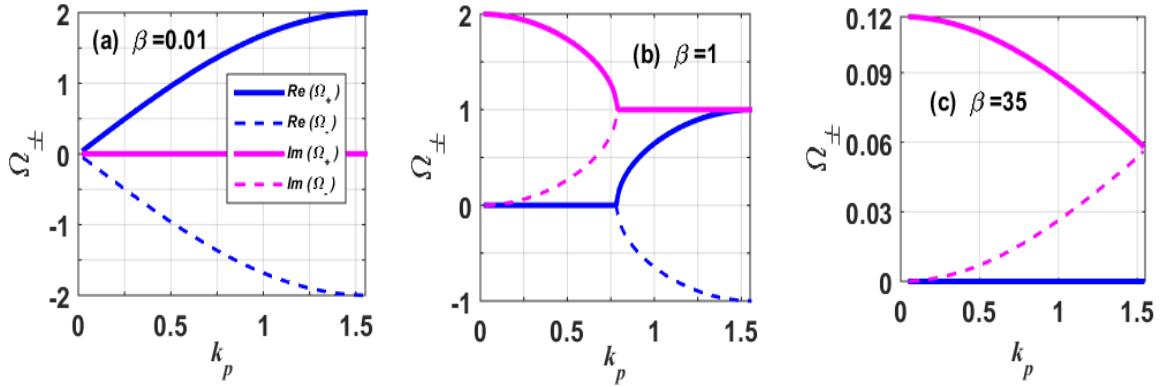


Figure 3.29: The real (blue color) and the imaginary parts (magenta color) of the eigenvalues  $\Omega_{\pm}^{RH}$  as function of the wave number  $k_p$  for several values of the gain/loss  $\beta$  in  $\mathcal{APTS}$  configuration. The values of  $\beta$  used correspond to the domains illustrated in Fig. 3.28. (a)  $\beta = 0.01 < \beta_{cr1}^{RH}$ ; (b)  $\beta_{cr1}^{RH} < \beta = 1 < \beta_{cr2}^{RH}$ ; (c)  $\beta = 20 > \beta_{cr2}^{RH}$

normalized eigenfrequencies  $\Omega_{\pm}^{RH}(\beta, k_p)$  of the ETL in the  $\mathcal{APT}^{RH}$  configuration and the threshold  $\beta_{cr}^{RH}$  (white curve) are plotted as function of  $k_p$ . We obtained the threshold values  $\beta_{cr1}^{RH} = 0.061$  and  $\beta_{cr2}^{RH} = 32.5$ . The plots are consistent with the analysis made above. Furthermore, for  $\beta = 0.01$  (Fig. 3.29(a)), the system is in the broken phase even when the imaginary part of the frequencies is closed to, but remains non zero. The value  $\beta = 1$  chosen in the range  $\beta_{cr1}^{RH} < \beta < \beta_{cr2}^{RH}$  (Fig. 3.29(b)) allows to obtain  $k_{cr}^{RH} = \pi/4$ , below which all the frequencies are imaginary and complex above. Here, as  $\beta \rightarrow \beta_{cr2}^{RH}$ ,  $k_{cr}^{RH} \rightarrow k_N$  and the imaginary phase dominates. However, when  $\beta \rightarrow \beta_{cr1}^{RH}$ ,  $k_{cr}^{RH} \rightarrow k_1$ , the broken phase becomes larger. Finally, when  $\beta = 35 > \beta_{cr2}^{RH}$  (see Fig. 3.29(c)), all frequencies are purely imaginary. The real (column a) and the imaginary (column b)

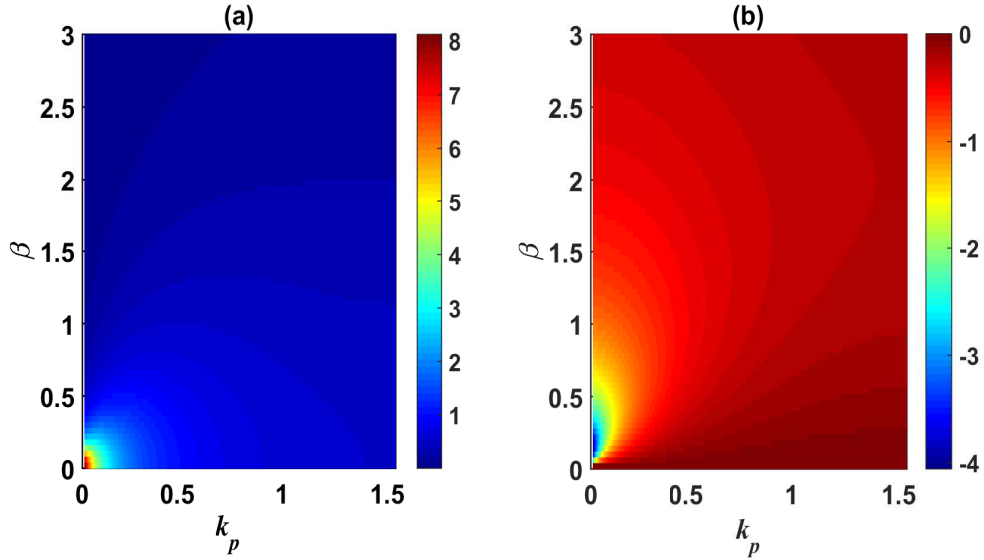


Figure 3.30: 3D top view ETLs normalized frequencies spectra  $\Omega_{\pm}^{LH}(\beta, k_p)$  as function of  $k_p$  and  $\beta$  in  $\mathcal{APTS}^{LH}$  configuration, where the system is unbreakable. Column (a) for the real parts and column (b) for the imaginary parts.

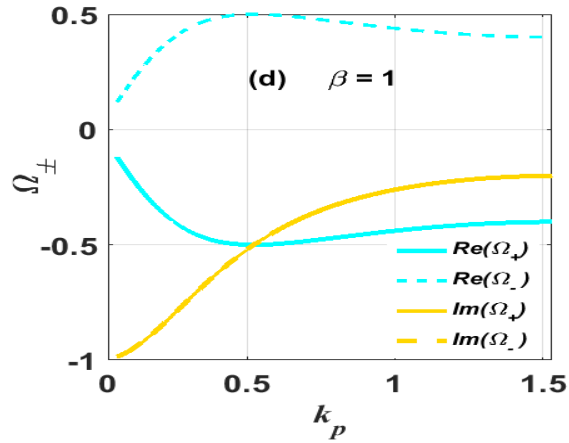


Figure 3.31: The real (cyan color) and the imaginary parts (orange color) of the eigenvalues  $\Omega_{\pm}^{LH}$  as function of the wave number  $k_p$  for the gain/loss  $\beta = 1$  in  $\mathcal{APTS}$  configuration. the frequencies are complex

parts of eigenfrequencies  $\Omega_{\pm}^{LH}(\beta, k_p)$  are shown in 3D top view in Fig. 3.30 for the ETL in  $\mathcal{APTS}^{LH}$  configuration. It can be seen in the plot that frequencies are complex and the system remains in the broken phase whatever the value of the wave number considered. This is also illustrated by Fig. 3.31 when taking  $\beta = 1$ .

### 3.3.2 Transport properties

#### 3.3.2.1 Transport in $\mathcal{PT}$ configuration

To investigate on the energy transport properties, we have interested ourselves to the modulus square  $|I_n(\beta, \Omega)|^2$  of the electric current  $I_n$  expressed in Eq. (2.103), since it is proportional to the light power and then to the energy in the ETL. Thanks to Maple and Matlab programs, we have calculated and plotted in two ways,  $|I_n(\beta, \Omega)|^2$  as a function of  $n$ , for different values of  $p$ : first, we have considered  $\Omega_{\pm}$  as a function of  $\beta$  and we have shown in the 3D top view (see Fig. 3.32(a, b) for the  $\mathcal{PT}^{RH}$  configuration and Fig. 3.33(a, b) for the  $\mathcal{PT}^{LH}$  configuration),  $|I_n(\beta, \Omega)|^2$  as function of  $n$  and  $\beta$  for different values of  $p$ . In the second case, the value of  $\Omega_{\pm}$  is calculated for a fixed value of  $\beta$  and

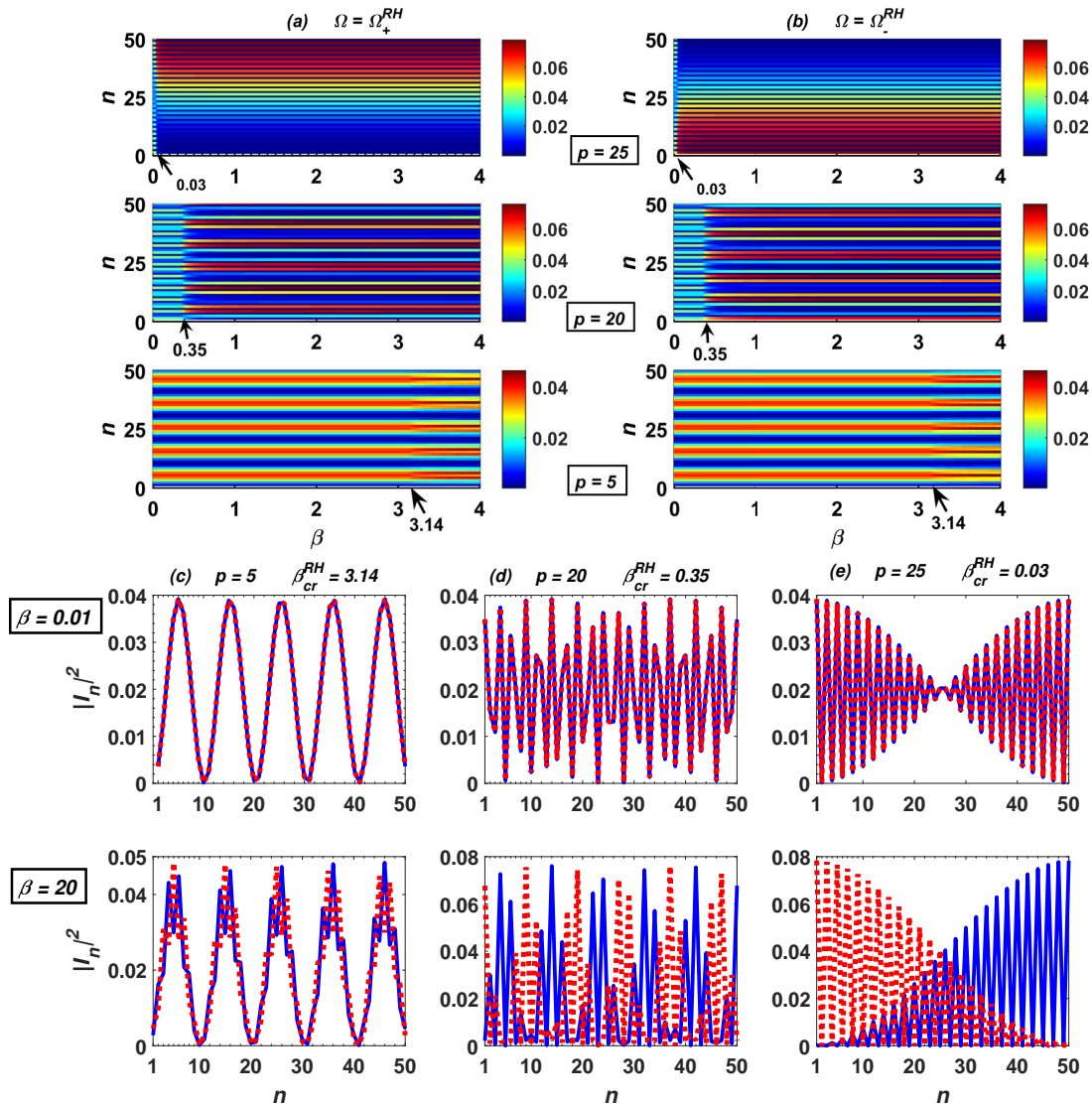


Figure 3.32: The modulus square  $|I_n(\beta, \Omega)|^2$  of the electric current in the  $\mathcal{PT}^{RH}$  configuration. Columns (a) and (b): 3D top view for several values of  $p$  as a function of  $\beta$  and  $n$ . Columns (c)–(e): 2D plot as function of  $n$  for different values of  $p$ ,  $\beta = 0.01$  in the 1st row and  $\beta = 20$  in the 2nd row. We note a symmetric energy transport of the  $\mathcal{PT}^{RH}$  exact phase whereas energy transport is asymmetrical in the  $\mathcal{PT}^{RH}$  broken phase.

is used to plot  $|I_n(\beta, \Omega)|^2$  as a function of  $n$  as illustrated in Fig. 3.32(c, d, e) for the  $\mathcal{PT}^{RH}$  and in Fig. 3.33(c, d, e) for the  $\mathcal{PT}^{LH}$ . As we can see in the 3D (top view), the plot of  $|I_n(\beta, \Omega)|^2$  clearly highlights two distinct behavioral regimes which are separated by the critical  $\mathcal{PT}$  breaking point. The values of  $p$  used and the corresponding thresholds are indicated in the plots. We note that, in the regime below the breaking points ( $\mathcal{PTS}$  phase) where the frequencies  $\Omega_{\pm}^{RH/LH}$  are real, the distribution of  $|I_n|^2$  is symmetrical for the frequencies  $\Omega_+^{RH/LH}$  (column (a)) and  $\Omega_-^{RH/LH}$  (column (b)) while it is asymmetric in the regime above the transition point where the frequencies are complex.

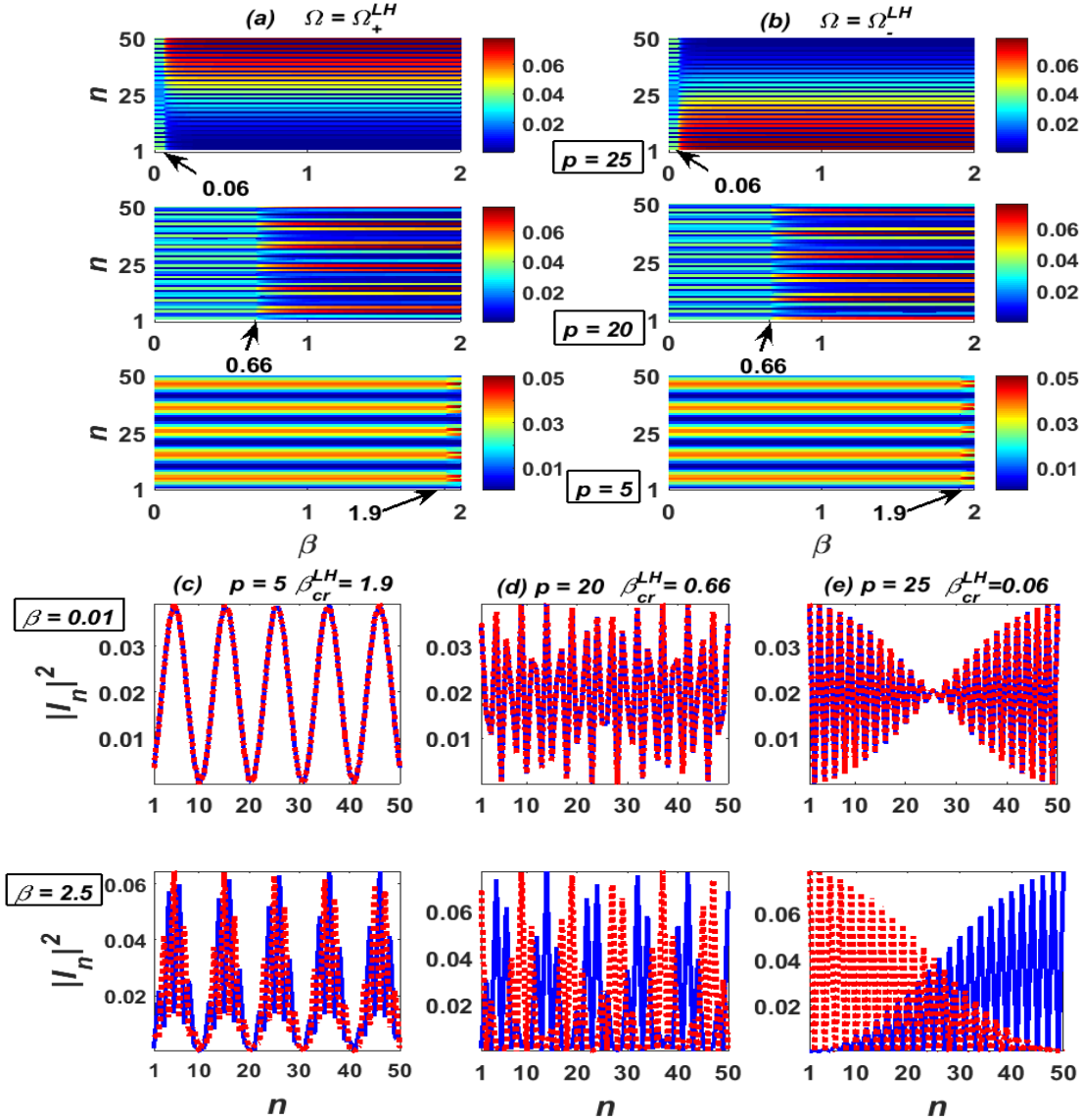


Figure 3.33: The modulus square  $|I_n(\beta, \Omega)|^2$  of the electric current in the  $\mathcal{PT}^{LH}$  configuration. Columns (a) and (b): 3D top view for several values of  $p$  as a function of  $\beta$  and  $n$ . Columns (c)–(e): 2D plot as function of  $n$  for different values of  $p$ ,  $\beta = 0.01$  in the 1st row and  $\beta = 2.5$  in the 2nd row. We note a symmetric energy transport of the  $\mathcal{PT}^{LH}$  exact phase whereas energy transport is asymmetrical in the  $\mathcal{PT}^{LH}$  broken phase.

The 2D plots of Figs. 3.32(c, d, e) and 3.33(c, d, e) agree well with the analysis made on the previous 3D figures. Indeed, for the value  $\beta = 0.01 < \beta_{cr1}^{RH/LH}$ , and whether



for  $p = 5; 20; 25$ , the current modulus square  $|I_n|^2$  is symmetric. However, when  $\beta$  is increased to  $\beta = 20 > \beta_{cr2}^{RH}$  or to  $\beta = 2.5 > \beta_{cr2}^{LH}$ ,  $|I_n|^2$  becomes asymmetric. The results obtained with frequencies  $\Omega_+^{RH/LH}$  and  $\Omega_-^{RH/LH}$  are represented in solid and dashed, respectively.

### 3.3.2.2 Transport in $\mathcal{APT}$ configuration

In Figs. 3.34(a, b) and 3.35(a, b), we have plotted the 3D (top view) of the  $|I_n(\beta, \Omega)|^2$  in the  $\mathcal{APT}^{RH}$  and in the  $\mathcal{APT}^{LH}$  configuration, in (a) for  $\Omega_+^{RH/LH}$  and in (b) for  $\Omega_-^{RH/LH}$ . Fig. 3.34(a, b) exhibits two domains for the energy transport: the  $\mathcal{APT}$  broken phase where the energy is asymmetric, and the exact phase where the energy distribution is symmetric. This energy distribution is sensitive to the chain size. For the  $\mathcal{APT}^{LH}$

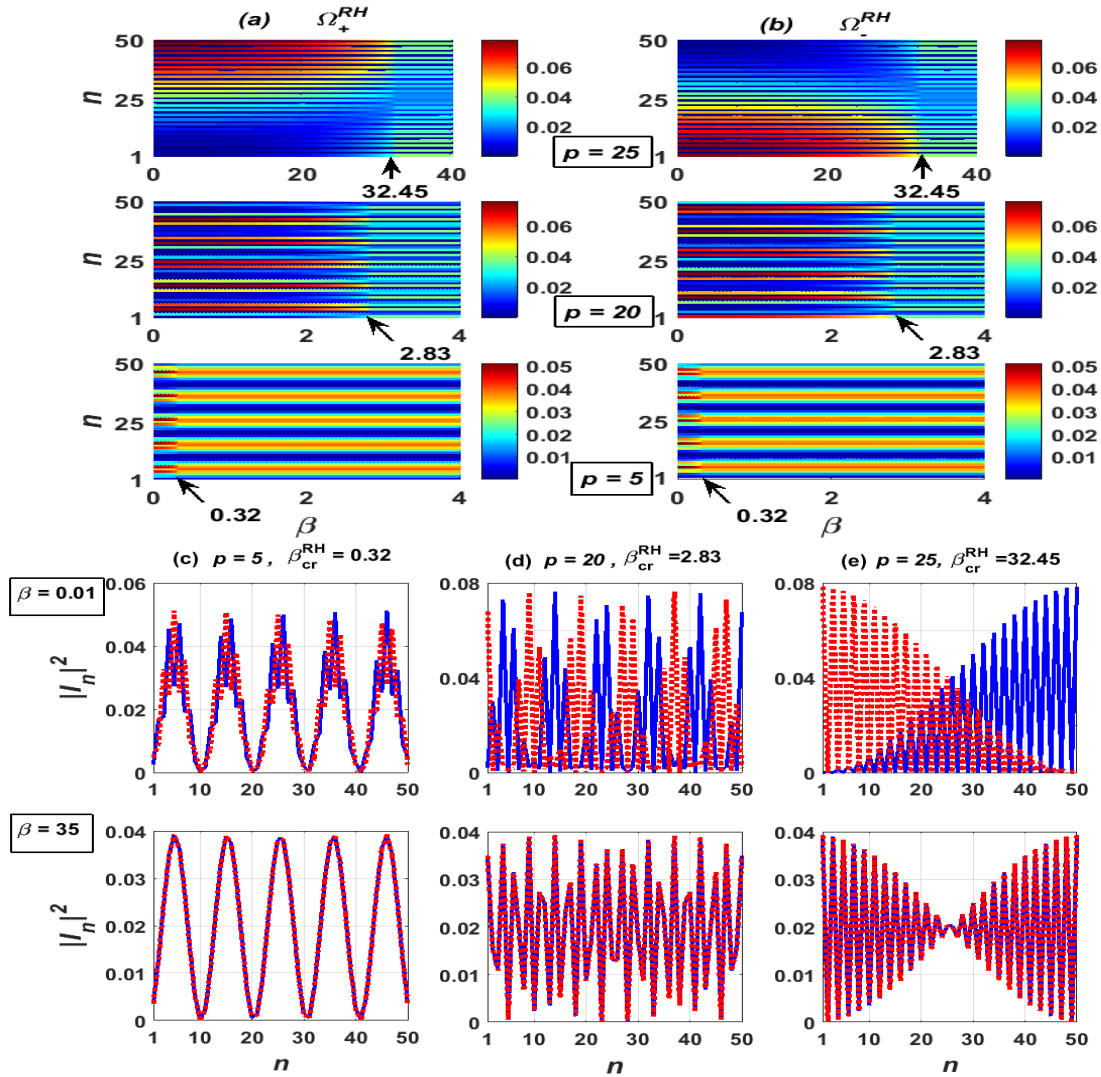


Figure 3.34: The modulus square  $|I_n(\beta, \Omega)|^2$  of the electric current in the  $\mathcal{APT}^{RH}$  configuration. Columns (a) and (b): 3D top view for several values of  $p$  as a function of  $\beta$  and  $n$ . Columns (c)–(e): 2D plot as function of  $n$  for different values of  $p$ ,  $\beta = 0.01$  in the 1st row and  $\beta = 35$  in the 2nd row. We note a symmetric energy transport of the  $\mathcal{APT}^{RH}$  exact phase whereas energy transport is asymmetrical in the  $\mathcal{APT}^{RH}$  broken phase.

configuration on contrary, Fig. 3.35(a, b) shows that the energy distribution being asymmetric for small values of the gain/loss  $\beta$  but becomes symmetric at higher values, despite be in the complex regime. In agreement with figs. 3.34(a, b), the 2D plots of the energy of Fig. 3.34(c, d, e), are illustrated for  $\beta = 0.01 < \beta_{cr1}^{RH}$  (first row) and for  $\beta = 35 > \beta_{cr2}^{RH}$  (second row), for different cell sizes as indicated. As we can see, in the  $\mathcal{APT}^{RH}$  broken phase, the energy is asymmetric whereas in the  $\mathcal{APT}^{RH}$  exact phase, its distribution is symmetric.

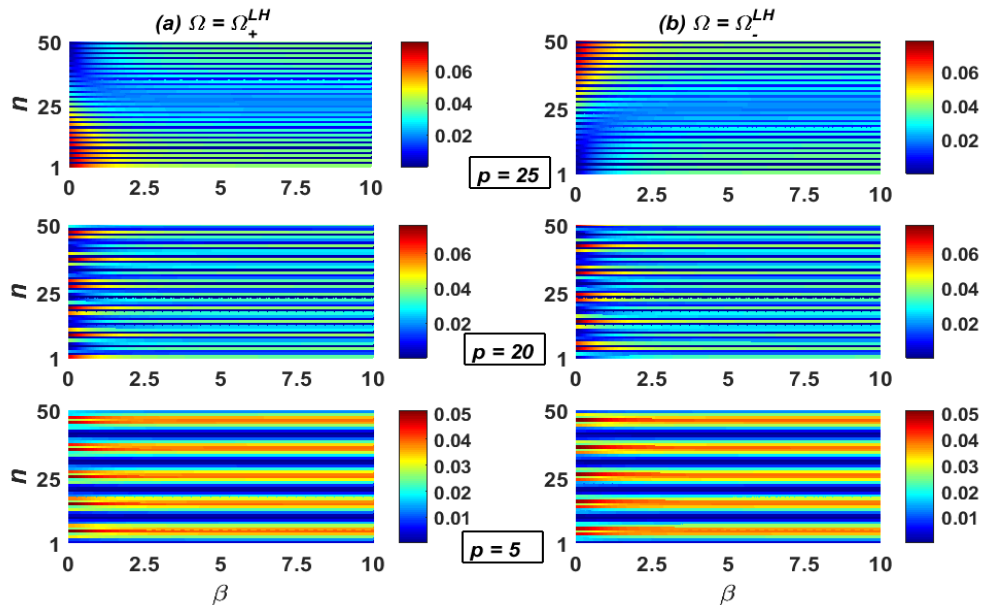


Figure 3.35: The modulus square  $|I_n(\beta, \Omega)|^2$  of the electric current in the  $\mathcal{APT}^{LH}$  configuration. In column (a):  $\Omega = \Omega_+^{LH}$  and in column (b):  $\Omega = \Omega_-^{LH}$ . In all plots, we are situated in the broken phase since the system is unbreakable and we note an asymmetry transport of energy for small values  $\beta$ , even if it becomes almost symmetry for higher values of  $\beta$

### 3.3.3 Anderson-like localization

In chapter 2, we have established equivalences between systems described here and a  $1D$  tight binding Anderson model, so that the non-Hermiticity introducing disorder in our electrical circuit allows us checking the localization behavior of quantum disordered  $1D$  systems using the so-called disordered ETLs. The tool used to study the localization behavior in this thesis as we said in chapter 2, is among many several other tools [60, 199–204, 206, 210, 213], the normalized localization length  $\Lambda(\beta, \omega)$ , whose the expression was totally defined using Eqs. (2.112) - (2.115). The expression of  $\Lambda(\beta, \omega)$  contains a recurrence sum which is not easy to solve analytically. Subsequently, we have numerically calculated it, i.e.,  $\Lambda(\beta, \Omega)$  as a function of both normalized frequencies  $\Omega(\beta, k_p)$  and the gain/loss  $\beta$  parameter.

3.3.3.1  $\mathcal{PT}$  configuration

In the  $\mathcal{PTS}$  configuration a general overview of the normalized localization length  $\Lambda(\beta, \omega)$  plotted in Figs. 3.36(a) and 3.36(b) allows to identify two zones: the first zone, where  $\Lambda(\beta, \Omega)$  describes an extended function ( $\Lambda(\beta, \Omega_{\pm}^{RH/LH}) > 1$ ) corresponding to the  $\mathcal{PT}$  unbroken phase and the localized function zone where  $\Lambda(\beta, \Omega_{\pm}^{RH/LH}) < 1$ , corresponding to the broken region. Interestingly, two striking differences appear between the ETL models. Thanks to the horizontal gray dashed curves corresponding to  $\Lambda(\beta, \Omega_{\pm}) = 1$ ,

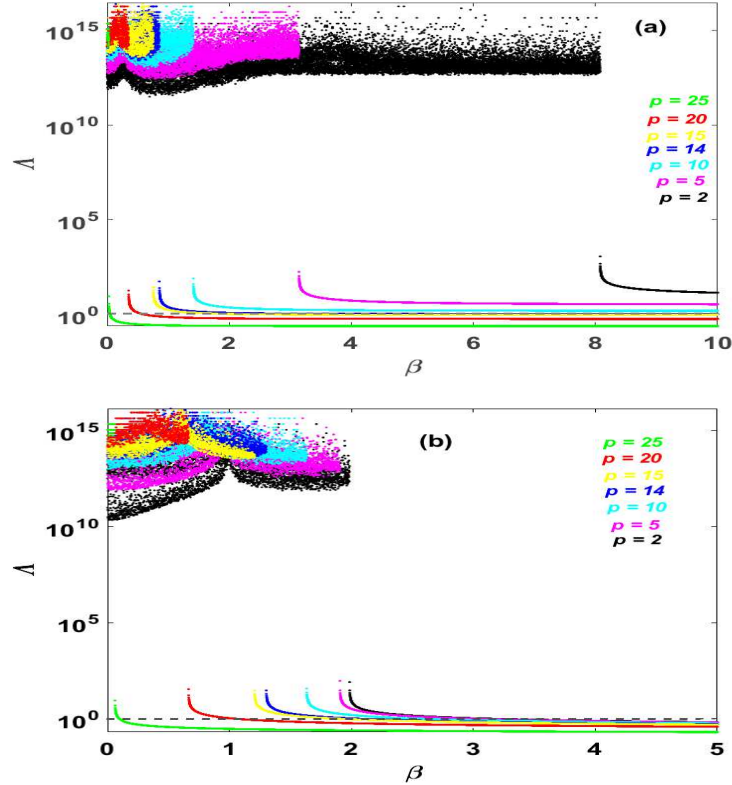


Figure 3.36: Normalized localization length  $\Lambda(\beta, \Omega_{\pm})$  in semi-log scale for the system in  $\mathcal{PTS}$  configuration as function of  $\beta$  for different values of  $p$  when  $N = 25$ . (a):  $\mathcal{PT}^{RH}$ , and (b):  $\mathcal{PT}^{LH}$ . For the values of  $p$  indicated in the plots, we observed extended modes (i.e  $\Lambda(\beta, \Omega_{\pm}) > 1$ ) in the  $\mathcal{PT}$  exact phase, while the localized modes (i.e  $\Lambda(\beta, \Omega_{\pm}) < 1$ ) occur in the  $\mathcal{PT}$  broken phase. Both localization behavior are separated by the gray curves which marks  $\Lambda(\beta, \Omega_{\pm}^{RH,LH}) = 1$ . In  $\mathcal{PT}^{RH}$ , the appearance of the localized modes in the broken phase required a minimum of cells ( $p = 15$ ) since below that value, all modes remain extended (i.e.  $\Lambda(\beta, \Omega_{\pm}^{RH}) > 1$ ). While,  $\mathcal{PT}^{LH}$  configuration, confined modes even for the smallest value  $p = 1$  (not shown).

it can be noticed that for the system in  $\mathcal{PT}^{RH}$  configuration (3.36(a)), the Anderson-like localized mode required a minimum of 15 cells to occur in the broken regime. In fact, when the value of  $\beta$  becomes greater than the transition point, there is a sharp decreased of the function  $\Lambda(\beta, \Omega_{\pm})$ , whereas, in the  $\mathcal{PT}^{LH}$  configuration (3.36(b)), the large cells number is not required for the mode localization. In this LH configuration, even for the smallest value  $p = 1$  (not shown in the plots), the localized mode can be identified. Such

results have been obtained for the LRC based ETLs and have demonstrated revealed applications in the field of information security [199]. Another important difference which emerges from the Localization behavior of the two ETLs is the conduction range. This range gets larger in extended state for  $\mathcal{PT}^{RH}$  at compared to  $\mathcal{PT}^{LH}$ . Moreover, this range can be widen upon tunneling the system parameters such as the real and imaginary resistances.

### 3.3.3.2 $\mathcal{APT}$ configuration

We have also numerically calculated  $\Lambda(\beta, \Omega_{\pm}^{RH})$  (resp.  $\Lambda(\beta, \Omega_{\pm}^{LH})$ ) in the  $\mathcal{APTS}$  configurations. The results are shown in Fig. 3.37(a) for the  $\mathcal{APT}^{RH}$  and in Fig. 3.37(b)

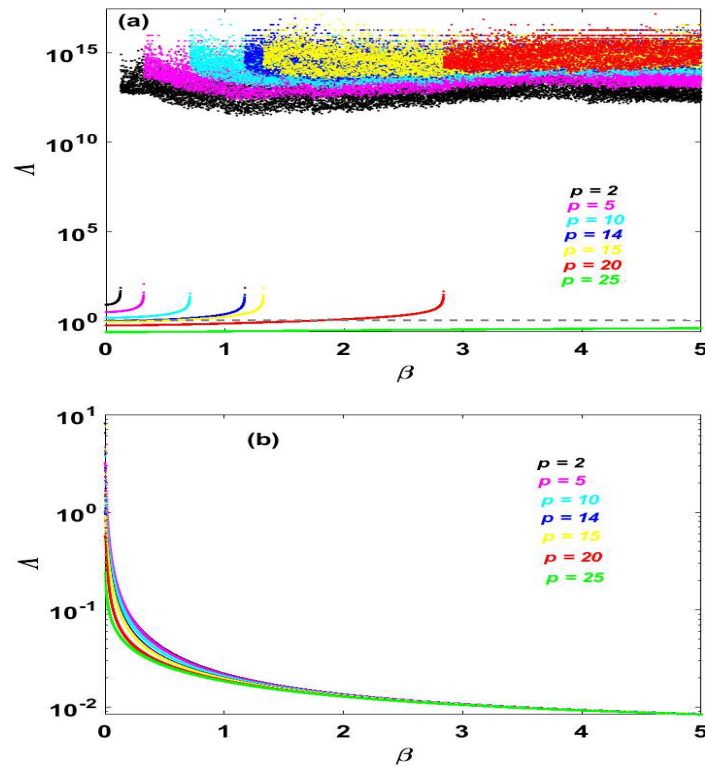


Figure 3.37: Normalized localization length  $\Lambda(\beta, \Omega_{\pm})$  in semi-log scale for the system in  $\mathcal{APTS}$  configuration as function of  $\beta$  for different values of  $p$  when  $N = 25$ . (a):  $\mathcal{APT}^{RH}$ , and (b):  $\mathcal{APT}^{LH}$ . For the values of  $p$  indicated in the plots, we observe in  $\mathcal{APT}^{RH}$  extended modes (i.e.  $\Lambda(\beta, \Omega_{\pm}^{RH}) > 1$ ) in the exact phase (pure imaginary frequencies), while the localized modes (i.e.  $\Lambda(\beta, \Omega_{\pm}^{RH}) < 1$ ) occur in the  $\mathcal{APT}$  broken phase (complex frequencies). Both localization behaviors are separated by the gray curve corresponding to  $\Lambda(\beta, \Omega_{\pm}^{RH,LH}) = 1$ . Also remark that for the  $\mathcal{APT}^{RH}$ , the appearance of the localized modes in the broken phase required a minimum of cells ( $p = 15$ ) since below that value, all modes become extended (i.e.  $\Lambda(\beta, \Omega_{\pm}^{RH}) > 1$ ) however in  $\mathcal{APT}^{LH}$  configuration, the modes are localized even for infinitesimal value  $p = 1$  (not shown).

for the  $\mathcal{APT}^{LH}$  configuration. Interestingly, Fig. 3.37(a) shows that for the structure in  $\mathcal{APT}^{RH}$ , there are two behavioral domains whatever the value of  $p$  used: the first

$\mathcal{APT}^{RH}$  domain (broken phase) characterized by the Anderson-like localized modes, and the second domain ( $\mathcal{APT}^{RH}$  exact phase) which is dominated by the extended state. The  $\mathcal{APT}^{RH}$  configuration exhibits a wider range of extended states in the purely imaginary phase. Finally, in  $\mathcal{APT}^{LH}$  configuration, we have seen in above section that the system is unbreakable and behaves in complex frequencies domain. The Fig. 3.37(b) shows that, the Anderson-like localized mode dominates the system whatever the values of  $p$  and  $\beta$  considered.

### 3.3.4 Concluding remarks on the analysis of a dimer ZRC based non-Hermitian electrical transmission line

In this section, we have proposed 1D ETLs of ZRC right/left handed (RH/LH) model of 2N size. This unit cell made it possible to simplify a description of the conventional direct and dual ETL with a simple first order differential equation. In our systems, components were distributed such as to have two non-Hermitian ETL models  $\mathcal{PT}^{RH}$  (resp.  $\mathcal{PT}^{LH}$ ) and  $\mathcal{APT}^{RH}$  (resp.  $\mathcal{APT}^{LH}$ ). We demonstrated that both ETL models are  $\mathcal{PT}$  breakable and allow a phase transition of the eigenfrequencies from real to complex domain. However, only the RH ETL is  $\mathcal{APT}$  breakable and allows frequencies from the complex to the exact phase where modes become totally imaginary. In the  $\mathcal{APT}$  configuration, the LH ETL remains in the broken phase and no phase transition is possible. On the other hand, the Anderson-like localized modes appears in the broken  $\mathcal{PT}/\mathcal{APT}$  phase while others regions evince extended modes with the localization length proportional to the cell numbers. Furthermore, the results indicate that the mode localization is most likely to occur in structures consisting of a large cells number for RH ETL while LH ETL will confine modes even for infinitesimal small cell numbers. Giving the ability of our system to exist in both  $\mathcal{PT}$  or  $\mathcal{APT}$  configurations, this may offer interesting applications in information encryption, optical switching and devices system control.

## Conclusion

Throughout this chapter, we have presented and discussed the results of our findings through this thesis work. We have reproduced and investigated on two main phenomena in the context of the wave transport using non-Hermitian electronic systems. Firstly, we have studied the effect of the non-Hermiticity on both dimers MLC and multi dimer ZRC series driven by an external voltage as electrical analogs of EIT, multiple EIT and related phenomena. Secondly, we have also analyzed the scattering properties of  $\mathcal{PTS}/\mathcal{APTS}$  dimer MLC parallel when inserted it as an impurity in a Hermitian conservative ETL which, finally served us to investigate on the energy transport and the Anderson-like localization in a repetition of dimers ZRC in non-Hermitian ETLs. The main results are summarized in the different concluding remarks.

---

# General Conclusion

---

## 1- Main results of the thesis

The main purpose of this work was twofold: Firstly, to extend the study made on the analog electronics models of the Electromagnetically Induced Transparency (EIT)/multiple EIT and related phenomena; this by analyzing the effect of the non-Hermiticity on the dispersive properties in a dimer/multi dimer driven by a harmonic voltage source. And, secondly to take more ownership of the Anderson localization (AL) phenomenon, this by analyzing on the one hand, the scattering properties of a  $\mathcal{PT}$  or  $\mathcal{APT}$  dimer embedded as a defect into a Hermitian conservative ETL; and on the other hand, to investigate on energy transport and the localization behavior in the repetitive sequence of dimers forming a non-Hermitian  $\mathcal{PT}/\mathcal{APT}$  symmetric electric transmission line (ETL).

We have presented in the first chapter the generalities on quantum Hermitian and non-Hermitian theories, and revisited literature on non-Hermitian electronics systems. Thereafter, we have described the imaginary resistor and given an overview on quantum theory of EIT and AL, followed by the state of art of the analog models proposed. In chapter 2, we have presented the mathematical modelling, analytical, numerical and experimental simulation methods used. Chapter 3 has been devoted to the results and the discussions. We have there analyzed on the one hand the EIT/multiple EIT and related phenomena behavior, followed by the AL behavior on the other.

★ **Concerning the study on EIT and related phenomena**, we first developed a general mutual inductive M, inductive L, and capacitive C couplings (dimer MLC series) electronic dimer model. We have established an analogy between the latter and an atomic system with three energy levels in  $\Lambda$  configuration. Under the resonance conditions, we derived the non-Hermitian Hamiltonian  $\mathcal{H}$  describing the system and highlighted an effective coupling ( $C_T$ ) for the system. The analysis of  $C_T$  suggested to distinguish between two groups of dimers: coupling (CP) dimers with  $C_T \neq 0$  and couplingless (CPL) dimers for which the combination of couplings in place allows  $C_T = 0$ . The dispersive properties of the system have been analysed by studying the absorbed power by the main cell (considered here as a loss cell), the one directly driven by a harmonic voltage. This absorption has been written as a combination of two resonances.

In the case of the **CP dimers**, the results show that the absorption spectrum behavior is modified when modulating the value of the non-Hermitian parameter  $\varepsilon$  which is

associated to the coupling regimes.

- **In the weak coupling regime:**

- When  $\varepsilon = 0$ , the absorption profile permitted to reproduce the EIT effect.
- For very lower values of  $\varepsilon$ , the absorption profile obtained described a behavior that we interpreted as the Electromagnetically Induced Amplified Transparency (EIAT).
- By further decreasing the negative value of  $\varepsilon$ , the absorption profile allowed the illustration of the Electromagnetically Induced Amplification (EIA) effect.

Whether for the EIT, EIAT or EIA behaviors, the absorbed power resulted of two resonances centered at the same frequency. Therefore, we have interpreted EIT and EIAT as the result of destructive interferences, whereas EIA results from constructive interferences.

- **In the strong coupling regime:**

- When  $\varepsilon = 0$ , the absorption profile allowed to reproduce the Autler-Townes Splitting (ATS) behavior.
- When  $\varepsilon < 0$ , the absorption profile described the ATS with amplification (ATSA) behavior.
- when  $\varepsilon = -1$  ( $\mathcal{PT}$  symmetric case) the two resonances are enhanced and the transparency zone becomes very large.

In all cases, the total absorbed power in the strong coupling regime was interpreted as the gap between the two resonances centered at different frequencies. The nature of interferences in this case, is either destructive or constructive.

- **At the couplingless point (CPLP)**, for which the effective coupling is zero ( $C_T = 0$ ), all the replicated phenomena disappear, the coupled system behaves as the decoupled one, and the absorption profile has a Lorentzian form. The CPLP occurs as a possible way to control EIT experiments and realize an optical switch.

The analogical LTSpice simulations curves obtained whether in the strong or the weak coupling regimes were in perfect agreement with the theoretical results shown by the Matlab plots.

Remaining in the EIT study, we have also proposed a non-Hermitian electronic dimers, based on the imaginary resistor. The so-called multi dimer was considered as an analog of the (N+2) level atomic system in the multipod type configuration. For this purpose, we have first studied the isolated ZRC cell. The temporal solutions well revealed the oscillations in the ZRC cell. Next, as in the previous case, two coupling regimes have emerged from the structural characterisation of the ZRC dimer, revealing a CPLP

associated to multiple couplings. In the weakly coupling regime, the eigenfrequencies crossed, demonstrating a non-reversible energy transfer between the coupled oscillators. However, in the strong coupling regime, the eigenfrequencies exhibited a splitting behavior indicating exchange between energy in the coupling oscillators in a periodical way. When the central loop was coupled to  $N$  multipod loops, its absorption profile replicated the  $N$ -EIT,  $N$ -EIAT or  $N$ -EIA dynamic in the weakly coupling. On the other hand, when the strong coupling was established, the  $(N-1)$  EIT,  $(N-1)$  EIAT or  $(N-1)$  EIA with the ATS dynamic were simultaneously observed. We also remarked that, at the CPLP of the multi dimer, all the quantum phenomena disappeared, revealing the efficiency of the imaginary resistive coupling in the cancellation of the capacitive coupling effect.

★ **Next, concerning the AL behavior**, we have used two approaches.

- First we analyzed the scattering properties of the Hermitian ETL embedding the  $\mathcal{PT}/\mathcal{APT}$  symmetric dimer MLC parallel as a defect. This first study revealed that:
  - When the  $\mathcal{PTS}$  dimer scattering system propagates real wave number, it undergoes a spontaneous breaking symmetry at the EPs inside which the transmission is superunitary ( $T > 1$ ) and subunitary outside ( $T < 1$ ). This corresponds to three types of regimes in the context of Anderson localization behavior: the extended states regime ( $T > 1$ ); the localized states regime ( $T < 1$ ), and the unidirectional invisibility/transparency also called anisotropic transmission resonance ( $T = 1$ ), at the EPs.
  - The study also revealed the suppression of unidirectional invisibility from the gain input when the Hermitian line coupling exceeds a critical point for the  $\mathcal{PTS}$  dimer system and such scattering system becomes unidirectional  $\mathcal{PTS}$ .
  - We also remarked that under the thresholdless conditions, lasing modes appeared for imaginary values of wave numbers corresponding to either real or purely imaginary values of the gain/loss modulation. This latter demonstrated the ability to control prohibited waves in the linear regime.
  - In the same ways, we shown that  $\mathcal{APT}$  symmetric scattering systems are generally behave as mirrors, and absorbers when propagating complex and imaginary wave numbers.
  - When propagating real wave numbers the  $\mathcal{APT}$  scattering systems are non-reciprocal.
- Second, we have analyzed the effect of a cascade association of the non-Hermitian dimers ZRC such as to form non-Hermitian ETLs. Two types were considered: Right-Handed (RH) and Left-Handed (LH) ETL. The Hamiltonian of each system was successfully derived in the framework of the tight-binding theory. We have discussed the underlying symmetries and calculated the breaking thresholds of the  $\mathcal{PTS}$  and  $\mathcal{APTS}$  phase transition. It results from this investigation that:



- The modes dynamic characterization revealed the existence of critical points beyond which operation requires thresholdless transition and the eigen modes are either real or complex.
- The analysis of the transport properties of the electric current reveals that in the  $\mathcal{PT}/\mathcal{APT}$  unbroken phase, the electric current is always a symmetrical function. This symmetrical behavior disappears when the system goes to the broken  $\mathcal{PT}/\mathcal{APT}$  phase.
- The scattering properties shown that the Anderson-like localized modes mostly emerged in the broken phase where eigen modes are complex with the localization length proportional to the cell numbers.
- Importantly, we have shown that the mode localization is most likely to occur in structures consisting of a large cells number for RH ETL while LH ETL confined modes even for infinitesimal small cell numbers. These results unveil embryonic applications in cryptography, switching and system control.

## 2- Future works

Despite the results that were obtained in this thesis, other points of interest may be solved in the future to complete and get a better understanding on topics discussed here.

- It would be interesting to do the analogical LTSpice simulations for both dispersive properties in the ZRC multi dimer and the scattering behavior of the dimer MLC parallel. This would consolidate our theoretical results.
- It would be also interesting to study on the energy transport and the localization behavior of the proposed ETL models by taking into account the other topological repartitions of the gain/loss, as trimer or pseudo-trimer arrangement for example.
- The thresholdless effect would also be interesting in the framework of the energy transport and Anderson-like localization.
- In addition to this work, it would be interesting to study the influence of the non-linear inductances, capacitances and imaginary resistances on all the results discussed in this thesis.

---

# Bibliography

---

- [1] C. M. Bender and S. Boettcher, *Phys. Rev. Lett.*, **80**, 5243 (1998)
- [2] C. M. Bender, S. Boettcher and P. N. Meisinger, *J. Math. Phys*, **40**, 2201 (1999).
- [3] C. M. Bender, M. V. Berry and A. Mandilara, *J. Phys. A*, **35**, L467 (2002).
- [4] A. Mostafazadeh, *J. Math. Phys*, **43**, 205 (2002).
- [5] A. Mostafazadeh and A. Batal, *J. Phys. A*, **37**, 11645 (2004).
- [6] A. Mostafazadeh, *J. Math. Phys*, **46**, 102108 (2005).
- [7] C. E. Rüter, K. G. Makris, R. El-Ganainy, D. N. Christodoulides, M. Segev and D. Kip, *Nat. Phys*, **6**, 192 (2010)
- [8] S. Nixon and J. Yang, *Phys. Rev. A*, **93**, 031802 (2016).
- [9] R. El-Ganainy, K. G. Makris, M. Khajavikhan, Z. H. Musslimani, S. Rotter and D. N. Christodoulides, *Nat. Phys*, **14**, 11 (2018).
- [10] H. Zhao and L. Feng, *Natl. Sci. Rev.*, **5**, 183 (2018).
- [11] M. A. Miri and A. Alù, *Science*, **363**, eaar7709 (2019).
- [12] K. Özdemir, S. Rotter, F. Nori and L. Yang, *Nat. Mater.*, **18**, 783 (2019).
- [13] K. G. Makris, R. El-Ganainy, D. N. Christodoulides and Z. H. Musslimani, *Phys. Rev. Lett.*, **100**, 103904 (2008).
- [14] P. Tassin, L. Zhang, T. Koschny, E. N. Economou and C. M. Soukoulis, *Phys. Rev. Lett.*, **102**, 053901 (2009).
- [15] A. Alù and N. Engheta, *Phys. Rev. Lett.*, **103**, 143902 (2009).
- [16] H. Alaeian and J. A. Dionne, *Phys. Rev. A.*, **89**, 033829 (2014).
- [17] A. Baev, P. N. Prasad, H. Ågren, M. Samoć and M. Wegener, *Phys. Rep.*, **594**, 1 (2015).
- [18] C. M. Bender, B. K. Berntson, D. Parker and E. Samuel, *Am. J. Phys.*, **81**, 173 (2013).

- [19] E. N. Tsoy, *Phys. Lett. A*, **381**, 462 (2017).
- [20] X.-W. Xu, Y. Liu, C.-P. Sun and Y. Li, *Phys. Rev. A*, **92**, 013852 (2015).
- [21] W. Li, Y. Jiang, C. Li and H. Song, *Sci. Rep.*, **6**, 1 (2016).
- [22] L.-Y. He, *Phys. Rev. A*, **99**, 033843 (2019).
- [23] C. Jiang, Y. Cui, Z. Zhai, H. Yu, X. Li and G. Chen, *Opt. Expr.*, **26**, 28834 (2018).
- [24] X. Zhu, H. Ramezani, C. Shi, J. Zhu and X. Zhang, *Phys. Rev. X*, **4**, 031042 (2014).
- [25] R. Fleury, D. Sounas and A. Alu, *Nat. Commun.*, **6**, 5905 (2015).
- [26] C. Shi, M. Dubois, Y. Chen, L. Cheng, H. Ramezani, Y. Wang and X. Zhang, *Nat. Commun.*, **7**, 11110 (2016).
- [27] E.-M. Graefe, *J. Phys. A*, **45**, 444015 (2012).
- [28] J. Schindler, A. Li, M. C. Zheng, F. M. Ellis and T. Kottos, *Phys. Rev. A*, **84**, 040101 (2011).
- [29] J. Schindler, Z. Lin, J. M. Lee, H. Ramezani, F. M. Ellis and T. Kottos, *J. Phys. A: Math. Theor.*, **45**, 444029 (2012).
- [30] Z. H. Musslimani, R. El-Ganainy, K. G. Makris and D. N. Christodoulides, *Phys. Rev. Lett.* **100**, 030402 (2008).
- [31] S. V. Suchkov, D. I. Borisov, A. A. Sukhorukov and Y. S. Kivshar, *Lett. Mater.*, **4**, 222 (2014).
- [32] A. A. Sukhorukov, S. V. Dmitriev, S. V. Suchkov and S. Yuri, *Opt. Lett.*, **37**, 2148 (2012).
- [33] M. C. Zheng, D. N. Christodoulides, R. Fleischmann and T. Kottos, *Phys. Rev. A*, **82**, 010103 (2010).
- [34] S. Longhi, *Phys. Rev. Lett.*, **103**, 123601 (2009).
- [35] A. Mostafazadeh, *J. Phys. A*, **45**, 444024 (2012).
- [36] S. Longhi, *Phys. Rev. A*, **82**, 031801 (2010).
- [37] Y. D. Chong, L. Ge and A. D. Stone, *Phys. Rev. Lett.*, **106**, 093902 (2011).
- [38] X. Wang and J.-H. Wu, *Opt. Expr.*, **24**, 4289 (2016).
- [39] P. Peng, W. Cao, C. Shen, W. Qu, J. Wen, L. Jiang and Y. Xiao, *Nat. Phys.*, **12**, 1139 (2016).

- [40] C. Zheng, *EPL*, **126**, 30005 (2019).
- [41] B. Lu, X.-F. Liu, Y.-P. Gao, C. Cao, T.-J. Wang and C. Wang, *Opt. Expr.*, **27**, 22237 (2019).
- [42] Y. Li, Y. Peng, L. Han, M.-A. Miri, W. Li, M. Xiao, X.-F. Zhu, J. Zhao, A. Alù, S. Fan and C.-W. Qiu, *Science*, **364**, 170 (2019).
- [43] J. Zhao, Y. Liu, L. Wu, C.-K. Duan and J. Du, **13**, 1 (2020).
- [44] J. Wen, G. Qin, C. Zheng, S. Wei, X. Kong, T. Xin and G. Long, **6**, 1 (2020).
- [45] D. A. Antonosyan, A. S. Solntsev and A. A. Sukhorukov, *Opt. Lett.*, **40**, 4575 (2015).
- [46] F. Yang, Y.-C. Liu and L. You, *Phys. Rev. A*, 96, 053845 (2017).
- [47] S. Longhi, *Opt. Lett.*, **43**, 4025 (2018)
- [48] J.-H. Wu, M. Artoni, and G. C. La Rocca, *Phys. Rev. Lett.* **113**, 123004 (2014).
- [49] S. B. Tabeu, F. Fotsa-Ngaffo, and A. Kenfack-Jiotsa, *EPL*, **125**, 24002 (2019).
- [50] Y. Choi, C. Hahn, J.W. Yoon, S. H. Song, *Nat. Commun.*, **9**, 2182 (2018).
- [51] P.-Y. Chen, M. Sakhdari, M. Hajizadegan, Q. Cui, M. M.-C. Cheng, R. ElGanainy and A. Alù, *Nat. Electron.*, **1**, 297 (2018).
- [52] M. Hajizadegan, M. Sakhdari, S. Liao and P.-Y. Chen, *IEEE T. Antenn. Propag.*, **67**, 3445 (2019).
- [53] L. O'Brien, *Science*, **318**, 1567 (2007).
- [54] P. Kok, W. J. Munro, K. Nemoto, T. C. Ralph, J. P. Dowling and G. J. Milburn, *Rev. Mod. Phys.*, **79**, 135 (2007).
- [55] M. G. Thompson, A. Politi, J. C. F. Matthews and J. L. O'Brien, *IET Circuits, Devices Syst.*, **5**, 94 (2011).
- [56] C. Zheng, *EPL*, **126**, 30005 (2019).
- [57] L. J. Matthew, *Honors theses—All* (Wesleyan University, **2014**), 1285.
- [58] S. Satpathy, A. Roy and A. Mohapatra, *Eur. J. Phys.*, **33**, 863 (2012).
- [59] C. L. G. Alzar, M. A. G. Martinez and P. Nussenzveig, *Am. J. Phys.* **70**, 37 (2002).
- [60] F. R. Humire and E. Lazo, *Phys. Rev. E*, **100**, 022221 (2019).
- [61] A. S. Elwakil and B.J. Maundy, *Circuits Syst Signal Process*, **35**, 2610 (2016).

- [62] S. B. Tabeu, F. Fotsa-Ngaffo and A. Kenfack-Jiotsa, *Opt. Quantum Electron.*, **51**, 1 (2019).
- [63] S. B. Tabeu, F. Fotsa-Ngaffo, S. Tagouegni, K. Shouno and A. Kenfack-Jiotsa, *arXiv:2007.01999 [physics.class-ph]* (2020).
- [64] I. B. Njike-Njike, F. Fotsa-Ngaffo, S. B. Tabeu, A. Kenfack-Jiotsa. *Arab. J. Sci. Eng.* **47**, 3659 (2022).
- [65] L. Ge and A. D. Stone, *Phys. Rev. X*, **4**, 031011 (2014).
- [66] A. Cerjan, A. Raman and S. Fan, *Phys. Rev. Lett.* **116**, 203902 (2016).
- [67] C. M. Bender, M. V. Berry, and A. Mandilara, *J. Phys. A: Math. Gen.*, **35**, L467 (2002).
- [68] B. Khantoul, La Pseudo hermiticité et sa généralisation aux systèmes dépendants du temps, archives.umc.edu.dz, (2010)
- [69] N. Moiseyev, Non-Hermitian Quantum Mechanics, (2011).
- [70] D. J. Griffiths, Introduction to quantum mechanics, (2010).
- [71] C. M. Bender, *Rep. Prog. Phys.*, **70**, 947 (2007).
- [72] Z. Ahmed, *Phys. Lett. A*, **286**, 231 (2001).
- [73] B. Bagchi, C. Quesne and M. Znojil, *Mod. Phys. Lett. A*, **16**, 2047 (2001).
- [74] A. Mostafazadeh, *J. Math. Phys.*, **43**, 2814 (2002).
- [75] C. M. Bender, D. C. Brody and H. F. Jones, *Phys. Rev. Lett.*, **89**, 270401 (2002).
- [76] A. Mostafazadeh, *J. Phys. A: Math. Gen.*, **36**, 7081 (2003).
- [77] S. Weigert, *Phys. Rev. A*, **68**, 062111 (2003).
- [78] W. D. Heiss, *J. Phys. A: Math. Gen.*, **37**, 2455 (2004).
- [79] C. M. Bender, *Contemp. Phys.*, **46**, 277 (2005).
- [80] Z. Lin, J. Schindler, F. M. Ellis and T. Kottos, *Phys. Rev. A*, **85**, 050101(R) (2012).
- [81] E. Schrödinger, *Ann. Phys.* **384**, 489 (1926).
- [82] R. El-Ganainy, K. G. Makris, D. N. Christodoulides and Z. H. Musslimani, *Opt. Lett.*, **32**, 2632 (2007).
- [83] A. Guo, G. J. Salamo, D. Duchesne, R. Morandotti, M. Volatier Ravat, V. Aimez, G. A. Siviloglou and D. N. Christodoulides, *Phys. Rev. Lett.*, **103**, 093902 (2009).

- [84] L. Feng, R. El-Ganainy and L. Ge, *Nat. Photon.*, **11**, 752 (2017).
- [85] V. V. Konotop, J. Yang and D. A. Zezyulin, *Rev. Mod. Phys.*, **88**, 035002 (2016).
- [86] C. H. Lee, S. Imhof, C. Berger, F. Bayer, J. Brehm, L.W. Molenkamp, T. Kiessling and R. Thomale, *Commun. Phys.*, **1**, 39 (2018).
- [87] J. Schindler, Z. Lin, J. M. Lee, H. Ramezani, F. M. Ellis, and T. Kottos, *J. Phys. A Math. Theor.*, **45**, 444029 (2012).
- [88] H. Benisty, A. Degiron, A. Lupu, A. D. Lustrac, S. Forget, M. Besbes, G. Barbillon, A. Bruyant, S. Blaize and G. Lerondel, *Opt. Expr.*, **19**, 3567 (2011).
- [89] S. Bittner, B. Dietz, U. Gunther, H. L. Harney, M. Miski-Oglu, A. Richter and F. Schafer, *Phys. Rev. Lett.*, **108**, 024101 (2012).
- [90] C. M. Bender, B. K. Berntson, D. Parker and E. Samuel, *Am. J. Phys.*, **81**, 173 (2013).
- [91] K. Bertoldi, V. Vitelli, J. Christensen and M. van Hecke, *Nat. Rev. Mater.*, **2**, 17066 (2017).
- [92] X. Zhu, H. Ramezani, C. Shi, J. Zhu and X. Zhang, *Phys. Rev. X*, **4**, 031042 (2014).
- [93] R. Fleury, D. Sounas and A. Alu, *Nat. Commun.*, **6**, 5905 (2015).
- [94] X.-Y. Lu, H. Jing, J.-Y. Ma and Y. Wu, *Phys. Rev. Lett.*, **114**, 253601 (2015).
- [95] H. Xu, D. Mason, L. Jiang and J. G. E. Harris, *Nature*, **80**, 537 (2016).
- [96] P. Tassin, L. Zhang, T. Koschny, E. N. Economou and C. M. Soukoulis, *Phys. Rev. Lett.*, **102** (2009).
- [97] T. Chou, K. Mallick, and R.K.P. Zia, *Rep. Prog. Phys.*, **74**, 116601 (2011).
- [98] M. Wimmer, A. Regensburger, M.-A. Miri, C. Bersch, D. N. Christodoulides and U. Peschel, *Nat. Commun.*, **6**, 7782 (2015).
- [99] A. Mostafazadeh, *Phys. Rev. Lett.*, **102**, 220402 (2009).
- [100] H. Ramezani, H.-K. Li, Y. Wang and X. Zhang, *Phys. Rev. Lett.*, **113**, 263905 (2014).
- [101] A. A. Sukhorukov, Z. Y. Xu and Y. S. Kivshar, *Phys. Rev. A*, **82**, 043818 (2010).
- [102] Y. Lumer, Y. Plotnik, M. C. Rechtsman and M. Segev, *Phys. Rev. Lett.*, **111**, 263901 (2013).
- [103] K. G. Makris, R. El-Ganainy and D. N. Christodoulides, *Phys. Rev. A*, **81**, 063807 (2010).

- [104] C. T. West, T. Kottos and T. Prosen, *Phys. Rev. Lett.*, **104**, 054102 (2010).
- [105] Y. D. Chong, L. Ge and A. D. Stone, *Phys. Rev. Lett.*, **106**, 093902 (2011).
- [106] Z. Lin, H. Ramezani, T. Eichelkraut, T. Kottos, H. Cao and D. N. Christodoulides, *Phys. Rev. Lett.*, **106**, 213901 (2011).
- [107] H. Ramezani, D. N. Christodoulides, V. Kovanis, I. Vitebskiy and T. Kottos, *Phys. Rev. Lett.*, **109**, 033902 (2012).
- [108] A. Regensburger, M.-A. Miri, C. Bersch, J. Nager, G. Onishchukov, D. N. Christodoulides and U. Peschel, *Phys. Rev. Lett.*, **110**, 223902 (2013).
- [109] B. Peng, S. K. Ozdemir, S. Rotter, H. Yilmaz, M. Liertzer, F. Moni, C. M. Bender, F. Nori and L. Yang, *Science*, **346**, 328 (2014).
- [110] V. A. Vysloukh and Y. V. Kartashov, *Opt. Lett.*, **39**, 5933 (2014).
- [111] S. Savoia, G. Castaldi and V. Galdi, *Phys. Rev. B*, **89**, 085105 (2014).
- [112] M. Turduev, M. Botey, I. Giden, R. Herrero, H. Kurt, E. Obzay and K. Staliunas, *Phys. Rev. A*, **91**, 023825 (2015).
- [113] B. Peng, S. K. Ozdemir, M. Liertzer, W. Chen, J. Kramer, H. Yilmaz, J. Wiersig, S. Rotter and L. Yang, *Proc. Natl. Acad. Sci.*, **113**, 6845 (2016).
- [114] A. U. Hassan, B. Zhen, M. Soljačić, M. Khajavikhan and D. N. Christodoulides, *Phys. Rev. Lett.*, **118**, 093002 (2017)
- [115] P. E Dorey, C. Dunning and R. Tateo, *J. Phys. A: Math. Gen.*, **34**, L391 (2001).
- [116] P. E Dorey, C. Dunning and R. Tateo, *J. Phys. A: Math. Gen.*, **34**, 5679 (2001).
- [117] C. M. Bender, S. Boettcher and V. M. Savage, *J. Math. Phys. (N.Y)*, **41**, 6381 (2000);
- [118] M. Znojil, *J. Phys. A*, **36**, 7639 (2003).
- [119] C. M. Bender, *Phys. Rep.*, **315**, 27 (1999).
- [120] B. Peng, S. K. Ozdemir, F. Lei, F. Moni, M. Gianfreda, G. L. Long, S. Fan, F. Nori, C. M. Bender and L. Yang, *Nat. Phys.*, **10**, 394 (2014).
- [121] L. Chang, X. Jiang, S. Hua, C. Yang, J. Wen, L. Jiang, G. Li, G. Wang and M. Xiao, *Nat. Photon.*, **8**, 524 (2014).
- [122] J. Li, R. Yu, C. Ding and Y. Wu, *Phys. Rev. A*, **93**, 023814 (2016).
- [123] Z.-P. Liu, J. Zhang, S.K. Ozdemir, B. Peng, H. Jing, X.-Y. Lü, C.-W. Li, L. Yang, F. Nori and Y.-X. Liu, *Phys. Rev. Lett.*, **117**, 110802 (2016).

- [124] J. Schindler, *PT-Symmetric Electronics*, honor thesis, Wesleyan University, (2013).
- [125] H. Ramezani, J. Schindler, F. M. Ellis, U. Guenther and T. Kottos, *Phys. Rev. A*, **85**, 062122 (2012).
- [126] L. Ge and H. E. Tureci, *Phys. Rev. A*, **88**, 053810 (2013).
- [127] J.-H. Wu, M. Artoni and G. C. La Rocca, *Phys. Rev. Lett.*, **113**, 123004 (2014).
- [128] F. Yang, Y.-C. Liu and L. You, *Phys. Rev. A*, **96**, 053845 (2017).
- [129] X. Wang and J.-H. Wu, *Opt. Expr.*, **24**, 4289 (2016).
- [130] S. Longhi, *Ann. Phys.*, **360**, 150 (2015).
- [131] S. Longhi, *Opt. Lett.*, **41**, 4518 (2016).
- [132] K. Shouno and Y. Ishibashi, *IEICE Trans. Fundamentals*, **E84-A**, 1536 (2001).
- [133] K. Shouno and Y. Ishibashi, *book: 2008 51st Midwest Symposium on Circuits and Systems*, 550 (2008).
- [134] K. Shouno and Y. Ishibashi, *IEEE*, **55**, 1897 (2008).
- [135] A. S. Elwakil and B. J. Maundy, *Circ. Syst. Signal Process.*, **35**, 2610 (2016).
- [136] T. Nakagawa, K. Shouno and K. Kuniya, *Analog Integr. Circuits Signal Process.*, **78**, 33 (2013).
- [137] J. O. Voorman, Y. P. Tsivids and J. O. Voorman, *IEEE*, 15 (1993).
- [138] M. A. Nielsen and I. L. Chuang, *book: Quantum Computation and Quantum Information*, 528 (2000).
- [139] D. Mayers, *J. ACM*, **48**, 351 (2001).
- [140] V. Giovannetti, S. Lloyd and L. Maccone, *Phys. Rev. Lett.*, **96**, 010401 (2006).
- [141] K.-J. Boller and A. Imamoglu and S.E. Harris, *Phys. Rev. Lett.*, **66**, 2593 (1991).
- [142] S. E. Harris, *Phys. Today*, **50**, 36 (1997).
- [143] S. E. Harris and L.V. Hau, *Phys. Rev. Lett.*, **82**, 4611 (1999).
- [144] M. O. Scully and M. Fleischhauer, *Phys. Rev. Lett.*, **69**, 1360 (1992).
- [145] L. Hau, S. Harris, Z. Dutton and C. Behroozi, *Nature*, **397**, 594 (1999).
- [146] M. M. Kash, V. A. Sautenkov, A. S. Zibrov, L. Hollberg, G. R. Welch, M. D. Lukin, Y. Rostovtsev, E. S. Fry and M. O. Scully, *Phys. Rev. Lett.*, **82**, 5229 (1999).



- [147] D. Budker, D. F. Kimball, S. M. Rochester and V. V. Yashchuk, *Phys. Rev. Lett.*, **83**, 1767 (1999).
- [148] C. J. Chang-Hasnain, P.-C. Ku, J. Kim, and S.-L. Chuang, *Proc. IEEE.*, **9**, 1884 (2003).
- [149] C. Liu, Z. Dutton, C. H. Behroozi, and L. V. Hau, *Nature*, **409**, 490 (2001).
- [150] D. F. Phillips, A. Fleischhauer, A. Mair, R.L. Walsworth and M.D. Lukin, *Phys. Rev. Lett.*, **86**, 783 (2001).
- [151] E. E. Mikhailov, Y. V. Rostovstev and G. R. Welch, *J. Mod. Opt.*, **50**, 2645 (2003).
- [152] J. Appel, E. Figueroa, D. Korystov, M. Lobino and A. I. Lvovsky, *Phys. Rev. Lett.*, **100**, 9 (2008).
- [153] M. Fleischhauer and M. Lukin, *Phys. Rev. A*, **65**, 022314 (2000).
- [154] F. Vewinger, J. Appel, E. Figueroa and A. I. Lvovsky, *Opt. Lett.*, **32**, 2771 (2007).
- [155] K.-P. Marzlin, Z.-B. Wang and B. Sanders, *Phys. Rev. Lett.*, **97**, 063901 (2006).
- [156] J. Khurgin, *J. Opt. Soc. Am. B*, **22**, 1062 (2005).
- [157] K. Murali, *Electromagnetically Induced Transparency and electron spin dynamics using superconducting quantum circuits*, Doctoral dissertation, Massachusetts Institute of Technology (2006).
- [158] C. C. Tannoudji, B. Diu, and F. Laloe, *book: Quantum Mechanics, J. Wiley and Sons Inc.*, (1973).
- [159] N. F. Ramsey, *Phys. Rev.*, **78**, 695 (1950).
- [160] Y. Aharonov and D. Bohm, *Phys. Rev.*, **115**, 485, (1959).
- [161] W. D. Oliver, Y. Yu, J.C.Lee, K. K. Berggren, L. S. Levitov and T.P. Orlando, *Science*, 1653 (2005).
- [162] M. Fleischhauer, A. Imamoglu and J. P. Marangos, *Rev. Mod. Phys.*, **77**, 633 (2005).
- [163] A. G. Litvak and M. D. Tokman, *Phys. Rev. Lett.*, **88**, 095003 (2002).
- [164] J. Harden, A. Joshi and J. D. Serna, *Eur. J. Phys.*, **32**, 541 (2011).
- [165] Z. Bai, C. Hang, G. Huang, *Opt. Commun.*, **291** 253 (2013).
- [166] S. Weis, R. Rivière, S. Deléglise, E. Gavartin, O. Arcizet, A. Schliesser and T. J. Kippenberg, *Science*, **330**, 1520 (2010).
- [167] C. Dong, V. Fiore, M. C. Kuzyk and H. Wang, *Science*, **338**, 1609 (2012).

- [168] Y. Xiaodong, M. Yu, D.-L. Kwong and C. H. Wong, *Phys. Rev. Lett.*, **102**, 173902 (2009).
- [169] S. Zhang, D. A. Genov, Y. Wang, M. Liu, and X. Zhang, *Phys. Rev. Lett.*, **101**, 047401 (2008).
- [170] J. Gu, R. Singh, X. Liu, X. Zhang, Y. Ma, S. Zhang, S. A. Maier, Z. Tian, A. K. Azad, H.-T. Chen, A. J. Taylor, J. Han and W. Zhang, *Nat. Commun.*, **3**, 1151 (2012).
- [171] Z. Han, and S. I. Bozhevolnyi, *Opt. Expr.*, **19**, 3251 (2011).
- [172] Z. Dong, H. Liu, J. Cao, T. Li, S. Wang, S. Zhu and X. Zhang, *Appl. Phys. Lett.*, **97**, 114101 (2010).
- [173] N. Papasimakis, V. A. Fedotov, N. I. Zheludev and S. L. Prosvirnin, *Phys. Rev. Lett.*, **101**, 253903 (2008).
- [174] J. B. Pendry, A. J. Holden, D. J. Robbins and W. J. Stewart, *IEEE Trans. Microw. Theory Tech.*, **47**, 2075 (1999).
- [175] R. A. Shelby, *Science*, **292**, 77 (2001).
- [176] D. Petrosyan and Y. P. Malakyan, *Phys. Rev. A*, **70**, 023822 (2004).
- [177] S. Rebić, D. Vitali, C. Ottaviani, P. Tombesi, M. Artoni, F. Cataliotti and R. Corbalán, *Phys. Rev. A*, **70**, 032317 (2004).
- [178] Z.-B. Wang, K.-P. Marzlin and B. C. Sanders, *Phys. Rev. Lett.* **97**, 063901(2006).
- [179] A. MacRae, G. Campbell, and A. I. Lvovsky, *Opt. Lett.*, **33**, 2659 (2008).
- [180] S. Li, X. Yang, X. Cao, C. Zhang, C. Xie and H. Wang, *Phys. Rev. Lett.*, **101**, (2008).
- [181] A. Lezama, S. Barreiro and A. M. Akulshin, *Phys. Rev. A*, **59**, 4732 (1999).
- [182] A. M. Akulshin, S. Barreiro, and A. Lezama, *Phys. Rev. A*, **57**, 2996 (1998).
- [183] C. Goren, A. D. Wilson-Gordon, M. Rosenbluh and H. Friedmann, *Phys. Rev. A*, **69** (2004).
- [184] A. V. Taichenachev, A. M. Tumaikin and V. I. Yudin, *Phys. Rev. A*, **61**, 011802 (1999).
- [185] P. W. Anderson, *Phys. Rev.*, **109**, 1492 (1958).
- [186] F. R. Allen and C. J. Adkins, *Philos. Mag.*, **26**, 1027 (1972).

- [187] R. Dalichaouch, J. P. Armstrong, S. Schultz, P. M. Platzman and S. L. McCall, *Nature*, **354**, 53, (1991).
- [188] H. Hu, A. Strybulevych, J. H. Page, S. E. Skipetrov and B. A. van Tiggelen, *Nat. Phys.*, **4**, 945 (2008).
- [189] S. Faez, A. Strybulevych, J. H. Page, A. Lagendijk, and B. A. van Tiggelen, *Phys. Rev. Lett.*, **103**, (2009).
- [190] D. S. Wiersma, P. Bartolini, A. Lagendijk and R. Righini, *Nature*, **390**, 671 (1997).
- [191] S. Mookherjea, J. S. Park, S.-H. Yang, and P. R. Bandaru, *Nat. Photonics*, **2**, 90 (2008).
- [192] K. Hashimoto, C. Sohrmann, J. Wiebe, T. Inaoka, F. Meier, Y. Hirayama, R. A. Römer, R. Wiesendanger and M. Morgenstern, *Phys. Rev. Lett.*, **101**, (2008)
- [193] A. Richardella, P. Roushan, S. Mack, B. Zhou, D. A. Huse, D. D. Awschalom and A. Yazdani, *Science*, **327**, 665 (2010).
- [194] Y. Lahini, A. Avidan, F. Pozzi, M. Sorel, R. Morandotti, D. N. Christodoulides and Y. Silberberg, *Phys. Rev. Lett.*, **100**, 013906 (2008).
- [195] U. Naether, S. Stützer, R. A. Vicencio, M. I. Molina, A. Tünnermann, S. Nolte, T. Kottos, D. N. Christodoulides and A. Szameit, *New J. Phys.*, **15**, 013045 (2013).
- [196] M. Segev, Y. Silberberg and D. N. Christodoulides, *Nat. Photon.*, **7**, 197 (2013).
- [197] G. Roati, C. D’Errico, L. Fallani, M. Fattori, C. Fort, M. Zaccanti, G. Modugno, M. Modugno and M. Inguscio, *Nature*, **453**, 895 (2008).
- [198] J. Billy, V. Josse, Z. Zuo, A. Bernard, B. Hambrecht, P. Lugan, D. Clément, L. Sanchez-Palencia, P. Bouyer, and A. Aspect, *Nature*, **453**, 891 (2008).
- [199] E. Lazo and E. Diez, *Phys. Lett. A*, **374**, 3538 (2010).
- [200] E. Lazo and E. Diez, *Phys. Lett. A*, **375**, 2122 (2011).
- [201] E. Lazo, F. Mellado and E. Saavedra, *Phys Lett. A*, **376**, 3423 (2012).
- [202] E. Lazo and E. Diez, *Physica B Condens. Matter*, 419, 19 (2013).
- [203] E. Lazo, *Physica B Condens. Matter*, 432, 121 (2014).
- [204] E. Lazo, F. R. Humire and E. Saavedra, *Physica B Condens. Matter*, **452**, 74 (2014).
- [205] E. Lazo, F. R. Humire and E. Saavedra, *Int. J. Mod. Phys. C*, **25**, 1450023 (2014).
- [206] E. Lazo, E. Saavedra, F. Humire, C. Castro and F. Cortés-Cortés, *Eur. Phys. J. B*, **88**, (2015).

- [207] E. Lazo, C. E. Castro and F. Cortés-Cortés, *Phys. Lett. A*, **380**, 3284 (2016).
- [208] E. Lazo, A. Garrido and F. Neira, *Eur. Phys. J. B*, **89**, (2016).
- [209] E. Lazo, *Eur. Phys. J. D*, **71**, 1 (2017).
- [210] E. Lazo and F. Cortés-Cortés, *Eur. Phys. J. Plus*, **134**, 1 (2019).
- [211] E. Lazo, *Physica E Low Dimens. Syst. Nanostruct.*, **114**, 113628 (2019).
- [212] E. Lazo, *Symmetry*, **11**, 1257 (2019).
- [213] E. Diez, F. Izrailev, A. Krokhin and A. Rodriguez, *Phys. Rev. B*, **78**, 035118 (2008).
- [214] A. Rényi and A. Renyi, *ISR*, **33**, 1 (1965).
- [215] E. Maciá, *Ann. Phys.*, **529**, 1700079 (2017).
- [216] M. I. Molina, *Phys. Rev. E*, **89**, 033201 (2014).
- [217] Y. J. Zhang, H. Kwon, M.-A. Miri, E. Kallos, H. Cano-Garcia, M. S. Tong, and A. Alu, *Phys. Rev. Appl.*, **11**, 044049 (2019).
- [218] O. Vázquez-Candanedo, J. C. Hernández-Herrejón, F. M. Izrailev, and D. N. Christodoulides, *Phys. Rev. A*, **89**, 013832 (2014).
- [219] S. V. Suchkov, B. A. Malomed, S. V. Dmitriev, and Y. S. Kivshar, *Phys. Rev. E*, **84**, 046609 (2011).
- [220] S. V. Suchkov, F. Fotsa-Ngaffo, A. Kenfack-Jiotsa, A. D. Tikeng, T. C. Kofane, Y. S. Kivshar and A. A. Sukhorukov, *New J. Phys.* **18**, 065005 (2016).
- [221] T. Kottos, *Nat. Phys.*, **6**, 166 (2010).
- [222] A. Mostafazadeh, *Phys. Rev. A*, **90**, 023833 (2014).
- [223] L. Feng, Y.-L. Xu, W. S. Fegasolli, M.-H. Lu, J. E. B. Oliveira, V. R. Almeida, Y.-F. Chen and A. Scherer, *Nat. Mater.*, **12**, 108 (2012).
- [224] L. Ge, Y. D. Chong and A. D. Stone, *Phys. Rev. A* **85**, 023802 (2012).
- [225] Y. Fu, Y. Xu, and H. Chen, *Opt. Expr.*, **24**, 1648 (2016).
- [226] H. Li, G. Ge, L. Liao, and Shunbin Feng, *Found. Phys.*, **45**, 198 (2014).
- [227] P. Anisimov and O. Kocharovskaya, *J. Mod. Opt.*, **55**, 3159 (2008).
- [228] H.-C. Li and G.-Q. Ge, *Chin. Phys. B*, **23**, 054206 (2014).
- [229] J. He, P. Ding, J. Wang, C. Fan and E. Liang, *Opt. Expr.*, **23**, 6083 (2015).

- [230] L. S. Molella, Nonlinear spectroscopy of closed degenerate two-level systems, *Dissertation*, Leibniz Universität Hannover, (2006).
- [231] C. Shi, M. Dubois, Y. Chen, L. Cheng, H. Ramezani, Y. Wang and X. Zhang, *Nat. Commun.*, **7**, 11110 (2016).
- [232] M. V. Nezlin, *Sov. Phys. Usp*, **19**, 946 (1976).
- [233] E. Rubino, J. McLenaghan, S. C. Kehr, F. Belgiorno, D. Townsend, S. Rohr, C. E. Kuklewicz, U. Leonhardt, F. König, and D. Faccio, *Phys. Rev. Lett.*, **108**, 253901 (2012).
- [234] M. Conforti, N. Westerberg, F. Baronio, S. Trillo, and D. Faccio, *Phys. Rev. A*, **88**, 013829 (2013).
- [235] C. R. Lourés, D. Faccio, and F. Biancalana, *Phys. Rev. Lett.*, **115**, 193904 (2015).
- [236] S. Pendharker, Y. Guo, F. Khosravi and Z. Jacob, *Phys. Rev. A*, **95**, 033817 (2017).

---

# List of Publications

---

---

## Publications in International Refereed Journals

---

- 1- **Tagouegni, S.**, Fotsa-Ngaffo, F., Kenfack-Jiotsa, A.: Non-Hermitian electronics multipods of Electromagnetically Induced Transparency (EIT) and Absorption (EIA). *Opt. Quantum Electron.* **54**, **3** (2022)
- 2- **Tagouegni, S.**, Fotsa-Ngaffo, F., Tabeu, S.B., Kenfack-Jiotsa, A.: Energy transport and Anderson-like localization in non-Hermitian electrical transmission line. *Phys. Scr.* **95(9)** **095808** (2020)
- 3- Fotsa-Ngafo, F., Tabeu, S.B., **Tagouegni, S.**, Kenfack-Jiotsa, A.: Thresholdless characterization in space and time reflection symmetry electronic dimers. *J. Opt. Soc. Am. B* **34(3)**, **658–667** (2017)

---

## Other publications

---

- 1- Tabeu, S.B, Fotsa-Ngaffo, F., **Tagouegni, S.**, Kazuhiro Shouno, Kenfack-Jiotsa, A.: Experimental observation of real spectra in Parity-Time symmetric ZRC dimers with positive and negative frequencies. *arXiv:2007.01999v1 [physics.class-ph]* , (2020)



# Non-Hermitian electronics multipods of electromagnetically induced transparency (EIT) and absorption (EIA)

Senghor Tagouegni<sup>1,2</sup> · Fernande Fotsa-Ngaffo<sup>2,3</sup> · Aurélien Kenfack-Jiotsa<sup>2</sup>

Received: 7 March 2020 / Accepted: 5 February 2022

© The Author(s), under exclusive licence to Springer Science+Business Media, LLC, part of Springer Nature 2022

## Abstract

We study a non-Hermitian electronic dimers system based on an imaginary resistor ( $Z$ ) in a  $(N+2)$  level atomic multipod configuration. Non-Hermitian systems depend on a gain/loss parameter and are specifically marked by a degeneracy exhibited at an exceptional point separating different phases of complex modes dynamics. Interestingly, the structural characterization and the dispersive properties reveal a broad range of strong coupling where the interplay between the control and the probe field induce a simultaneous EIT, EIA and ATS. Here, by identifying the underlying physical mechanisms, we show that multiple windows of transparency can be strongly enhanced by the incorporation of several dimers in the multipod network. On the other hand, if the pumping field is resonant in the weak regime, multiple EIT and EIA windows result in the number of dimers. Remarkably, the proposed system embedded a multiple coupling mechanism whose modulation induces a couplingless point (CPLP) whereby the energy cross. At this point EIT and related phenomena vanish.

**Keywords** Non-Hermitian · Couplingless · Multiple EIT · Multiple EIA · ATS

## 1 Introduction

Electromagnetically Induced Transparency (EIT) and related phenomena are prominent examples of coherent interactions between optical fields and multilevel atoms which have spurred the development of new materials with optimized optical properties (Harris et al.

---

✉ Senghor Tagouegni  
stagouegni@yahoo.fr

Fernande Fotsa-Ngaffo  
ngafotsa@yahoo.com

Aurélien Kenfack-Jiotsa  
kenfack@yahoo.com

<sup>1</sup> Laboratory of Mechanics, Materials and Structures, Department of Physics, Faculty of Science, University of Yaoundé I, P.O. Box 812, Yaoundé, Cameroon

<sup>2</sup> Nonlinear Physics and Complex Systems Group, Department of Physics, The Higher Teacher's Training College, University of Yaoundé I, P.O. Box 47, Yaoundé, Cameroon

<sup>3</sup> Institute of Wood Technologies, University of Yaoundé I, P.O. Box 306, Mbalmayo, Cameroon

1990; Harris 1997; Scully 1992; Matsko et al. 2001; Fleischhauer et al. 2005). The coherent preparation produces remarkable changes in the dispersive properties of a medium which leads to quantum interference, namely the Fano interferences, between the excitation pathways that control the optical response. The EIT has also been demonstrated to occur via the splitting of energy levels into dressed states by strong coupling fields. In general the transparency of the absorbing medium is increased at large control intensity of the pumping field, leading to the appearance of two dressed states which correspond to the Autler–Townes splitting (ATS) phenomenon (Autler and Townes 1955; Cohen-Tannoudji 1996). Such phenomena have given rise to a range of properties including lasing without inversion (Mompert and Corbalán 2000), ultra-slow light (Totsuka et al. 2007), stopping of light pulses (Liu et al. 2001; Phillips et al. 2001) quantum memory (Hétet et al. 2008), enhanced nonlinear optical processes (Wang et al. 2001), plasmonic sensing with narrow linewidths (Liu et al. 2010), optical switches (Bermel et al. 2006), just to name but a few. These possibilities opened new avenues for optical information storage and quantum information processing. While EIT renders a narrow spectrum of perfect transmission, its complementary effect known as electromagnetically induced absorption (EIA) defines a band of frequency in which enhanced absorption due to the wave coherence is observed. Traditionally, EIA occurs in a degenerated two-level system (Lezama et al. 1999). The EIA effect supports some exciting wave propagation concept like the anomalous dispersion, detection of foliage moisture and other types of sensing (Ramzan et al. 2016, 2018; Siddiqui et al. 2016).

The realization of EIT in atomic systems has been a difficult task imposed by some restrictions (Wang et al. 2016). Interestingly, the EIT effect was demonstrated in classical optical coupled resonators due to its flexible design and easy implementation (Smith et al. 2004). However, most of these can be tuned by mechanical alignment making it difficult to realize the dynamic control of the transparency window, which limits the practical application of EIT-like effect. In addition to a three-level type configuration (Dastidar and Dutta 2008), EIT has also been realized in various multilevel configurations (Petrosyan and Malakyan 2004; Huy et al. 2019; Bharti and Wasan 2014; Paspalakis and Knight 2002), and quite recently, it was extended to the  $N$  and  $(N+1)$ -level systems (Paspalakis and Knight 2002; McGloin et al. 2001). These systems exhibited multiple EIT with highly desired applications in the bifurcation of quantum information in multiple channels.

Experimental realizations were carried on by Garrido Alzar et al. (Garrido Alzar et al. 2002) who reproduced the EIT behavior using two linearly coupled LRC circuits. By changing the strength of the coupling parameter, the authors have successfully controlled the response of the system going from the analog of EIT to that of the ATS effect. Joshua Harden et al. (Harden et al. 2011), Zhengyang Bai et al. (Bai et al. 2013), reproduced double EIT (DEIT) through coupled LRC circuits, in a four-level atomic system, in the Y-inverted and tripod configurations, respectively.

In practice, manipulating the LRC circuits in higher frequency regimes may in general lead to miniaturization of devices, higher storage capacities, and larger data transfer rates, but introduces a frequency dependent phase shift and delay effects in two different points of the circuit (Tagouegni et al. 2020; Tabeu et al. 2019) which can hinder the judicious control of EIT.

In this paper, we present an alternative approach of designing electrical analogs of multiple Electromagnetically Induced Transparency (EIT) and/or Absorption (EIA) and related phenomena. Our models are based on  $(N+1)$  coupled ZRC circuits in which the inductor  $L$  is merely replaced by the imaginary resistor of an impedance  $Z$  ( $Z = jr$ , with  $j^2 = -1$ ). This later presents a major asset with the ability to generate a frequency independent phase



shift, unlike the inductor/capacitor reactive elements (Tagouegni et al. 2020; Tabeu et al. 2019). The experimental realizations of the imaginary resistor have been suggested in the literature using a gyrator (Shouno and Ishibashi 2008; Fujii and Shouno 2019; Nakagawa et al. 2013; Elwakil and Maundy 2015). The imaginary resistor allows an efficient manipulation between the lower and higher frequencies. In addition, the ZRC oscillator has a natural frequency  $\omega_0 = 1/rC$ , which can be positive or negative according to the real value of the resistance  $r$  associated to the imaginary resistor and the capacitance  $C$  of the circuit. Within this concept, the ZRC multi dimer can exhibits quantum interference phenomena such as EIT, EIA and ATS with an optimal modulation of the couplings and the gain/loss parameter.

Our paper is organized as follows: in Sect. 2, we present the model equations and the eigenmodes analysis. Here, a structural characterization allows to identify for the system a weak and a strong coupling regimes, and then to emphasize the couplingless point (CPLP). In Sect. 3, the steady state dynamic and dispersive properties of the systems are investigated.

## 2 Equations of model and eigenmodes analysis

We consider a ZRC multi dimer obtained by coupling  $(N + 1)$  oscillators ZRC as shown in Fig. 1a. Each  $Z_iR_iC_i$  circuit consists of a linear capacitor  $C_i$ , a real resistor  $R_i$  and an imaginary resistor of impedance  $Z_i$ , where  $Z_i = jr_i$  ( $j^2 = -1$ ), all arranged in series. The sub-index  $i = (0...N)$  indicates the oscillator's number, and  $N$  ( $N \geq 1$ ) is the total number of cells coupled to the main loop oscillator  $Z_0R_0C_0$  for which a harmonic voltage source  $u(t)$  has been added in series with the resistor  $R_0$ . The coupling between loops is realized thanks to the capacitor  $C_c$  and another imaginary resistor  $Z_c$  ( $Z_c = jr_c$ ), also arranged in series and belonging to the set of circuit meshes.

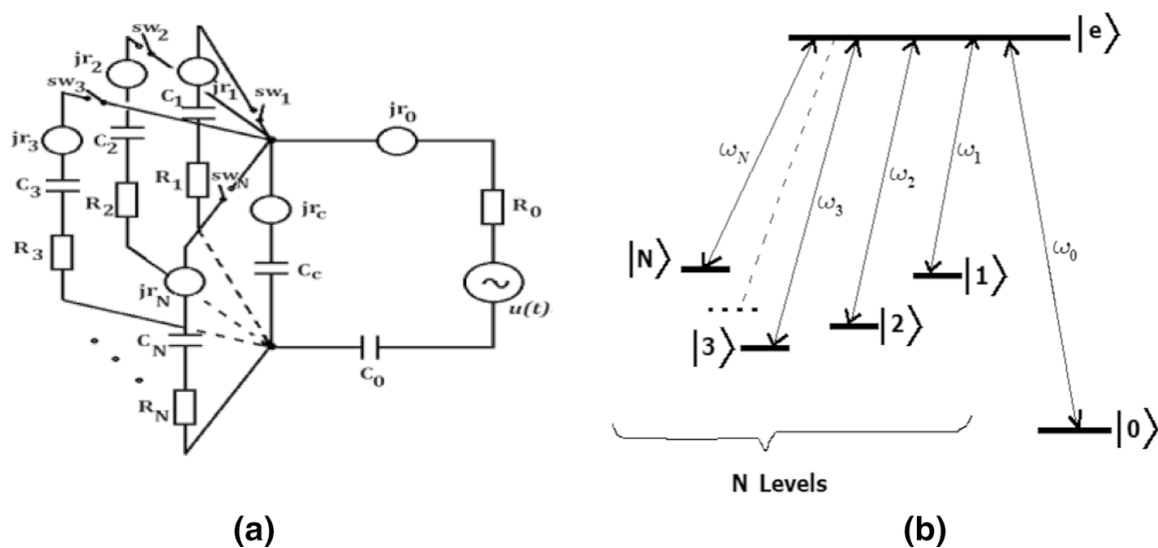


**Fig. 1** **a** ZRC Multi dimer circuit used for a single and multiple EIT, ATS and EIA windows. **b** Energy diagram of a  $(N + 2)$  level atomic system in a multi-pod type configuration consisting of  $(N + 1)$  lower levels  $|i\rangle$  ( $i = 0 \dots N$ ) of which  $N$  pumping lasers couple near resonantly each state to the upper state  $|e\rangle$ , while a probe laser couples level  $|0\rangle$  to  $|e\rangle$

In this model, the inductor has been replaced by an imaginary resistor as compared to the analog models using LRC circuits (Garrido Alzar et al. 2002; Harden et al. 2011; Bai et al. 2013).

Figure 1b illustrates a (N + 2) level atomic system in a multipod type configuration, where the (N + 1) lower states |i⟩ which can be degenerated or not, are coupled to a single excited upper level state |e⟩. The atomic system is initially prepared in a particular state |0⟩ and interacts with a probe laser that couples the lower state |0⟩ to an excited state |e⟩. Adding a total number of N light sources (each being in a state |i⟩) induces an atomic transition of frequency ω<sub>i</sub> from |i⟩ to |e⟩. The absorption spectrum of the probe laser is modified once the N control fields simultaneously interact with the medium, which results in the interferences between the different transitions pathways of the atom.

In what follows, our objective is to demonstrate that the ZRC multi dimer circuit (Fig. 1a) is analog to the (N + 2) level atomic system in a multipod type configuration (Fig. 1b). In this analogy, the loop Z<sub>0</sub>R<sub>0</sub>C<sub>0</sub> of frequency ω<sub>0</sub> models the atom. This represents the central loop where the other loops are connected to. The harmonic voltage u(t) is the probe laser field. Once the switch SW i is closed, each loop of frequency ω<sub>i</sub> acts as a control field to the central loop.

If the switches SW i, i = (0...N) are closed, the Kirchhoff's laws leads to the following coupled equations:

$$\begin{cases} (\beta_0 + j) \frac{dQ_0}{dt} - j\beta_{c0} \sum_{n=1}^N \frac{dQ_n}{dt} + \omega_0 Q_0 - \Omega_0 \sum_{n=1}^N Q_n = u/r_{e0}, & \text{for } i = 0 \\ (\beta_i + j) \frac{dQ_i}{dt} - j\beta_{ci} \left( \frac{dQ_0}{dt} - \sum_{\substack{n=1, \\ n \neq i}}^N \frac{dQ_n}{dt} \right) + \omega_i Q_i - \Omega_i \left( Q_0 - \sum_{\substack{n=1, \\ n \neq i}}^N Q_n \right) = 0, & \text{for } i \neq 0 \end{cases} \quad (1)$$

where  $j = \sqrt{-1}$ ,  $i = 0 \dots N$ ,  $\beta_i = R_i/r_{ei}$ ,  $\beta_{C_i} = r_C/r_{ei}$ ,  $\omega_i = 1/r_{ei}C_{ei}$ ,  $\Omega_i = 1/r_{ei}C_C$ ,  $r_{ei} = r_i + r_C$  and  $C_{ei} = C_i C_C / (C_i + C_C)$ .

Q<sub>i</sub> and dQ<sub>i</sub>/dt represent the charge and the current in each loop, respectively. The so-called ZRC multi dimer system leads to first order coupled ordinary differential equations, which can be easily analyzed. Moreover, the system can support negative frequencies, without altering its operating mode, therefore it opens an avenue to investigate various quantum phenomena through positive and negative frequencies. Table 1 summarizes the different possible combinations of the circuit elements to have positive or negative charges in the loop. The experimental realization of the negative resistor can be found in ref. (Schindler et al. 2012).

One of the key parameters of the system is the gain/loss parameter  $\beta_i = R_i/r_{ei}$ . This parameter defines the energy state of the system which can be Hermitian or non-Hermitian depending on the nature of  $\beta_i$ . The system is Hermitian when  $\beta_i = 0$ . As soon as  $\beta_i \neq 0$ , the system becomes non-Hermitian.  $\beta_i$  is thus called the non-Hermitian parameter responsible

**Table 1** Combination of circuit elements for either positive or negative charges

	$r_C$		$C_C$		$C_{ei}$		$R_i$	
	$r_C > 0$	$r_C < 0$	$C_C > 0$	$C_C < 0$	$C_{ei} > 0$	$C_{ei} < 0$	$R_i > 0$	$R_i < 0$
$r_{ei} > 0$	$\beta_{C_i} > 0$	$\beta_{C_i} < 0$	$\Omega_i > 0$	$\Omega_i < 0$	$\omega_i > 0$	$\omega_i < 0$	$\beta_i > 0$	$\beta_i < 0$
$r_{ei} < 0$	$\beta_{C_i} < 0$	$\beta_{C_i} > 0$	$\Omega_i < 0$	$\Omega_i > 0$	$\omega_i < 0$	$\omega_i > 0$	$\beta_i < 0$	$\beta_i > 0$

to the amplification or the damping into the loop. When  $r_{ei}$  and  $R_i$  have the same signs (i.e.  $\beta_i > 0$ ), the loop is said ‘‘loss’’, otherwise, it is ‘‘gain’’. When  $\beta_i$  exceeds a threshold value, the system is marked by a degeneracy and the threshold is called the exceptional point (EP). Non-Hermitian electronic systems have been intensively investigated in the literature (Tagouegni et al. 2020; Tabeu et al. 2019; Schindler et al. 2012; Fotsa-Ngaffo et al. 2017). These systems have exhibited unconventional properties such as unidirectional invisibility, thresholdless transition (Fotsa-Ngaffo et al. 2017), simultaneously coherent perfect absorber lasing (Bai et al. 2016) and many more (Christodoulides and Yang 2018), with desired applications in the generation of new multifunctional optoelectronic devices.

The aim of the next section is to give details on the structural characterization of the different non-Hermitian systems. The circuits are investigated in the absence of an external source. In particular, we intend to reveal the ranges of frequencies that could exhibit EIT, EIA and ATS quantum phenomena.

### 2.1 The ZRC dimer

The ZRC dimer is obtained by coupling only two oscillators  $Z_i R_i C_i (i = 0, 1)$  as schematically described by the Fig. 1a when  $N = 1$ . We assume that both loops have the same natural frequency  $\omega_0 = 1/rC$ , where  $r = r_{ei}$  and  $C = C_{ei}$ ,  $\omega_0$  being positive or negative (see Table 1 for the conditions). As in Fotsa-Ngaffo et al. (2017), the active controlling coupling can be used to refer the ZRC dimer. For convenience, for the dimer Z, only the imaginary resistive coupling ( $Z_C$ ) is active while in the case of the dimer ZC, the series combination  $Z_C - C_C$  is active. Rewriting Eq. (1) for  $i = 0, 1$  and assuming the harmonic solutions  $Q_i(t) = A_i e^{j\omega t} + c.c$  (where c.c is a complex conjugate) for the charges leads to the following matrix representation:

$$\begin{pmatrix} \delta + j\omega\beta_0 & \omega\beta_C - \Omega \\ \omega\beta_C - \Omega & \delta + j\omega\beta_1 \end{pmatrix} \begin{pmatrix} A_0 \\ A_1 \end{pmatrix} = \begin{pmatrix} 0 \\ 0 \end{pmatrix} \tag{2}$$

where  $\beta_C = r_C/r$ ,  $\Omega = 1/rC_C = \kappa\omega_0$ ,  $r = r_{0,1} + r_C$ ,  $\kappa = C/C_C$ ,  $\omega_0 = 1/rC$ ,  $C = \frac{C_{0,1}C_C}{C_{0,1}+C_C}$  and  $\delta = \omega_0 - \omega$  is the frequency detuning.

We are interested in the behavior of the system near the resonance. For that, we use the approximation  $|\omega - \omega_0| \ll \omega$ ,  $\beta\omega \approx \beta\omega_0$  (Rodriguez 2016). Therefore, Eq. (2) can be rewritten as:

$$\left[ \omega_0 \begin{pmatrix} 1 + j\beta_0 & c \\ c & 1 + j\beta_1 \end{pmatrix} - \omega \begin{pmatrix} 1 & 0 \\ 0 & 1 \end{pmatrix} \right] \begin{pmatrix} A_0 \\ A_1 \end{pmatrix} = \begin{pmatrix} 0 \\ 0 \end{pmatrix} \tag{3}$$

where  $c = \beta_C - \kappa$  is the effective coupling of the system. Equation (3) has non-trivial solutions if the determinant of the left-most term vanishes. Then, we need to solve the characteristic equation  $|H - \omega I| = 0$ , where  $I$  is the  $2 \times 2$  identity matrix and  $H$  is a non-Hermitian Hamiltonian (Rodriguez 2016) written as:

$$H = \omega_0 \begin{pmatrix} 1 + j\beta_0 & c \\ c & 1 + j\beta_1 \end{pmatrix} \tag{4}$$

The  $2 \times 2$  matrix  $H$  has a form of a two state non-Hermitian Hamiltonian describing open quantum systems. One of its particularity is to admit a pair of two complex conjugate mode frequencies instead of four, as with the LRC coupled systems. For this later case, the

eigenfrequencies are those of an effective Hamiltonian  $H_{eff}$ , which results from the similarity transformation of the  $4 \times 4$  matrix  $L$  describing the system, i.e.  $H_{eff} = jL$  (Schindler et al. 2012).

Through diagonalization of  $H$ , the eigenfrequencies  $\omega_{\pm}$  of the ZRC dimer can be expressed as follows:

$$\omega_{\pm} = \omega_0 \left( 1 + jB \pm \sqrt{c^2 - \beta^2} \right) \quad (5)$$

with  $B = (\beta_1 + \beta_0)/2 = \beta_0(\varepsilon + 1)/2$ ,  $\beta = (\beta_1 - \beta_0)/2 = \beta_0(\varepsilon - 1)/2$ ,  $c = \beta_C - \kappa$ ,  $\beta_C = r_C/r$  and  $\kappa = \Omega/\omega_0$ . Here  $\varepsilon = \beta_1/\beta_0$  is the gain/loss ratio.

Before any analysis, it is instructive to note that the structural characterization done here consists in studying the behavior of the eigenfrequencies  $\omega_{\pm}$ . This allows us to analyze the real and the complex energy band frequencies which definitively have impact on the quantum interference dynamic.

It is obvious that when  $\beta_0 = 0$ ,  $\forall \varepsilon$  (no gain or loss in the loops),  $\omega_{\pm} = \omega_0(1 \pm c)$ , all frequencies are real. The Hamiltonian  $H$  is Hermitian.

In the non-Hermitian case,  $\beta_0 \neq 0$ ,  $\forall \varepsilon$ . The eigenfrequencies in Eq. (5) can be real or complex in general, depending on the  $\varepsilon$  parameter. In particular, three cases can be considered:

1. If  $\varepsilon = -1$ , i.e.  $\beta_1 = -\beta_0 \neq 0$ , the loss and the gain are exactly compensated. This gives rise to a particular class of non-Hermitian systems called the parity time symmetric (PTS) (Schindler et al. 2012; Fotsa-Ngaffo et al. 2017; Bai et al. 2016; Christodoulides and Yang 2018) of which the Hamiltonian  $H$  commutes with the join Parity-Time symmetry operator  $PT = \sigma_x K$  (where  $\sigma_x$  is the first Pauli matrix and  $K$  is the complex conjugation operation). Under the PTS conditions, the eigenfrequencies in Eq. (5) are reduced to  $\omega_{\pm} = \omega_0 \left( 1 \pm \sqrt{c^2 - \beta_0^2} \right)$ . Then, the eigenspectrum displays a spontaneous symmetry breaking at the coupling threshold  $c = c_{th}$ , where  $c_{th} = |\beta_0|$  known as the EP, separates two phases: The PT unbroken phase ( $\beta_0 < |c|$ ) where the frequencies are totally real, and the PT broken phase ( $\beta_0 > |c|$ ) for which the frequencies are complex. It is important to mention that PTS systems have demonstrated many intriguing features in several areas of physics (Christodoulides and Yang 2018).
2. If  $\varepsilon = 1$ , i.e.  $\beta_1 = \beta_0 \neq 0$ , the system is either amplifying or dissipative. The eigenfrequencies are complex and can be expressed as  $\omega_{\pm} = \omega_0(1 \pm c + j\beta_0)$ . The imaginary part of the frequencies  $\omega_{\pm}$  are constant and the real parts coalesce at the particular point where the effective coupling vanishes.

$$c = 0 \Leftrightarrow \beta_C = \kappa \neq 0 \quad (6)$$

This point is referred to as the couplingless point (CPLP) in the case of the dimer ZC.

3. The third case  $\varepsilon \neq \pm 1$ ,  $\forall \beta_0 \neq 0$ , the gain and the loss are not compensated in the non-Hermitian system. As a consequence, the eigenfrequencies  $\omega_{\pm}$  remains complex and display a phase transition at two EPs which separate complex phases. At the transition points, the effective coupling strength satisfies to  $c = c_{th}$ , where  $c_{th} = |\beta| = \beta_0|\varepsilon - 1|/2$ .

In what follows we will illustrate the analysis made above considering two coupled systems, one with the single coupling, and another with a double coupling. The aim is to demonstrate that a double coupling gives rise to a new phenomenon that we cannot observe in the simple coupling. In particular, we want to emphasize the couplingless point (CPLP) that we have illustrated in Eq. (6). For a double coupled system, the coupling parameters are non-zero, i.e.  $\beta_C \neq 0, \kappa \neq 0$  (dimer ZC), for example, we set  $\kappa = 0.75$  which remains constant through the paper; whereas for a simple coupled system,  $\kappa = 0$  and  $\beta_C \neq 0$  (dimer Z). In both cases, we choose  $\beta_0 = 0.5 \neq 0$  and it can be easily verified from Eq. (5) that these systems are non-Hermitian.

In Fig. 2, the real (first column) and the imaginary (second column) parts of the normalized eigenfrequencies  $\omega_{\pm}/|\omega_0|$  are shown as a function of the controlling coupling parameter  $\beta_C$  and the gain/loss ratio  $\epsilon$ . The spectra are obtained with the negative frequency  $\omega_0 < 0$ , since the eigenfrequencies are the odd function of  $\omega_0$ . The exceptional points are indicated as a coupling threshold  $\beta_{C_{th}}$  with a dashed magenta curves in 3D (top view) plots [(a), (b) for the dimer Z, and (d), (e) for the dimer ZC]. As it can be expected, the frequencies  $\omega_{\pm}$  come in complex conjugate pairs and two coupling regimes are exhibited: the weakly driving regime ( $|c| < |\beta|$ ), characterized by the coalescence of the real parts of the eigenfrequencies and the splitting of their imaginary parts; and the strongly coupling regime ( $|c| > |\beta|$ ), where the imaginary parts of the eigenfrequencies cross and the real parts split. The splitting analysis will be studied in detail in the following. In the case of the dimer ZC, the EPs are symmetric with respect to the CPLP. To further complete the understanding of the eigenanalysis, the cross section of both real (solid) and imaginary (dashed) parts is made in the third column (see Fig. 2c for the dimer Z and Fig. 2f for the dimer ZC). The plots are obtained for different values of  $\epsilon$  parameter and agree well the observations made from the 3D plots. Indeed, in the PTS case  $\epsilon = -1$  (red color), we note that, whether

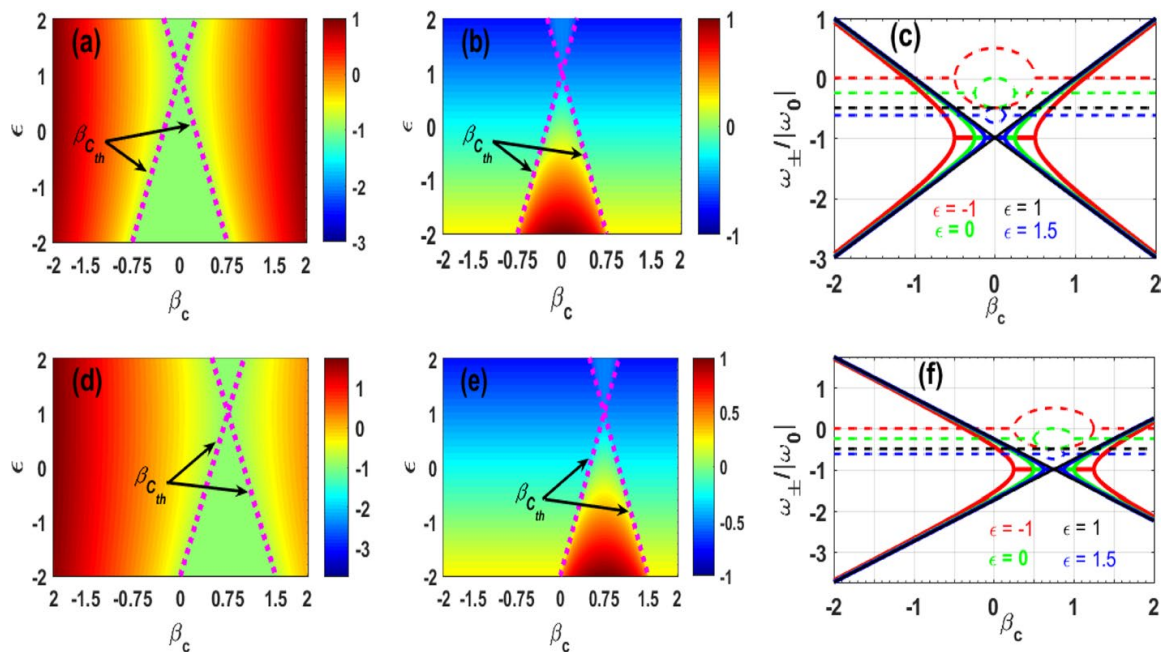


**Fig. 2** 3D top view of the real (first column) and imaginary (second column) parts of the normalized eigenfrequencies  $\omega_{\pm}/|\omega_0|$  of the ZRC dimer as function of the controlling coupling parameter and the gain/loss ratio  $\epsilon$ , in the case of dimer Z of which  $c = \beta_C$  [plots (a), (b)] and of the dimer ZC when fixed  $\kappa = 0.75$  [plots (d), (e)]. The coupling threshold  $\beta_{C_{th}}$  is indicated with the dashed magenta color. Third column: cross section of the real (solid) and the imaginary (dashed) parts of  $\omega_{\pm}$  with different values of  $\epsilon$ : c: dimer Z and f: dimer ZC (when  $\kappa = 0.75$ ). The values of  $\epsilon$  are indicated on the plots. For all plots  $\beta_0 = 0.5$

for the dimer Z or for the dimer ZC, the EPs separate exactly the real modes from the complex ones. When  $\epsilon \neq -1$  these modes are complex [see  $\epsilon = 0$  (green color) or  $\epsilon = 1.5$  (blue color)]. The case  $\epsilon = 1$  (black color) supports the discussions made above on the CPLP, as a point of zero effective coupling of the dimer ZC. This CPLP effectively occurs when  $\beta_c = \kappa = 0.75$ .

To emphasize on the structural characterization, we can as well predict the coupling range of the system for which quantum phenomena could occur using the splitting analysis. To do so, let's consider again the ZRC dimer. We assume that the coupled loops oscillate with different natural frequencies; for example  $\omega_0$  for the first oscillator and  $\omega_1 = \omega_0(1 + \Delta)$  for the second one, where  $\Delta$  is a small variation. After a little bit of algebra, the eigenfrequencies of the non-Hermitian system ( $\beta_0 \neq 0$ ) under these considerations are found to be:

$$\omega_{\pm} = \omega_0 \left( 1 + \frac{\Delta}{2} + jB \pm \frac{1}{2} \sqrt{\Delta^2 - 4\beta^2 + 4c^2 + j4\beta\Delta} \right) \tag{7}$$

where the parameters are defined as in Eq. (5).

In Fig. 3, the real parts of the frequencies obtained in Eq. (7) and the splitting  $\omega_+ - \omega_-$  are shown as a function of the variation  $\Delta$  when  $\epsilon = 0$ .

In absence of the coupling i.e.,  $\beta_c = \kappa = 0$  (see Fig. 3a), the frequency  $\omega_0$  (solid green) remains constant, while both  $\omega_1$  (solid red) and the splitting (dashed black) decrease as  $\Delta$  increases. The splitting cancels when  $\Delta = 0$ , where the two frequencies intersect.

Once the weak coupling is established between loops, for example in the case of the dimer Z when  $\beta_c = 0.02$  (see Fig. 3a) and for the dimer ZC when  $\beta_c = 0.71$  (Fig. 3d), one of the eigenfrequencies decreases while another remains constant of  $\omega_0$  as  $\Delta$  is increasing. The two frequencies cross at  $\Delta = 0$ . There, the splitting is also equal to zero. We will show in the following that the crossing of frequencies induces destructive or constructive interferences in the system, which favor to mimic EIT or EIA quantum phenomena, respectively.

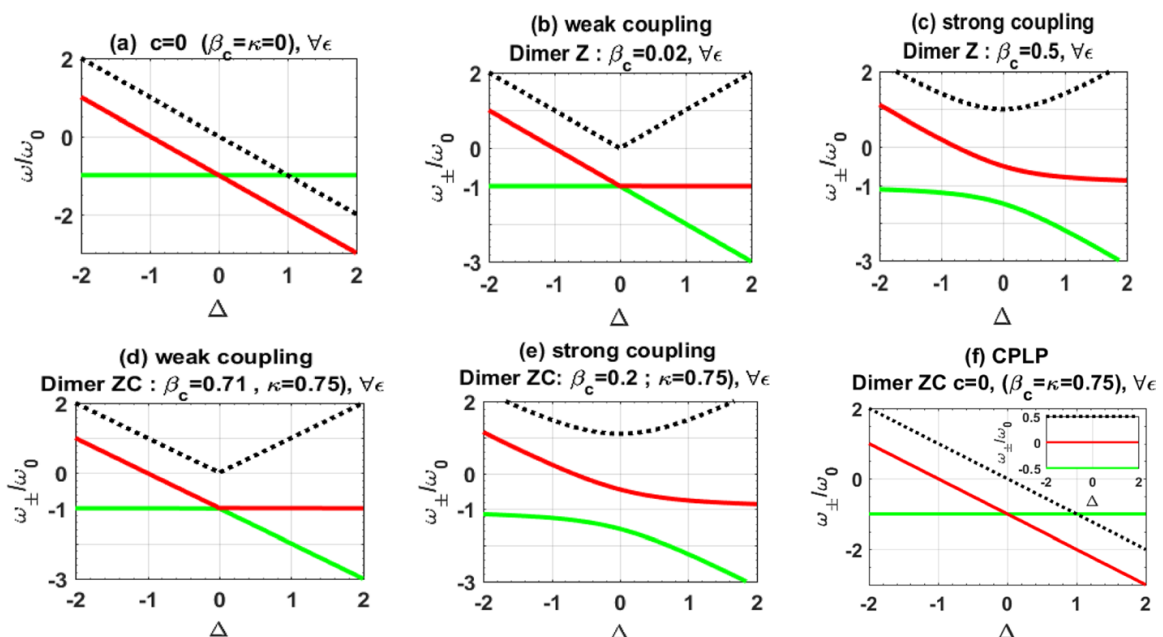


**Fig. 3** Eigenfrequencies of the dimer as function of the variation  $\Delta$ . **a** Uncoupled loops ( $c = 0$ , with  $\beta_c = \kappa = 0$ ). Dimer Z in weak **b** and strong **c** coupling regime. Dimer ZC in weak **d** and strong **e** coupling regime. **f** Dimer ZC at the couplingless point ( $c = 0$ , with  $\beta_c = \kappa = 0.75$ ). In all plots,  $\beta_0 = 0.5$ ,  $\omega_0 < 0$  and  $\epsilon = 0$

On the contrary, when the coupling becomes strong, for example in the case of the dimer Z when  $\beta_C = 0.02$  (Fig. 3a) and for the dimer ZC when  $\beta_C = 0.71$  (Fig. 3d), both eigenfrequencies  $\omega_{\pm}$  decrease as  $\Delta$  is increasing. Remarkably, it can be seen that the two frequencies do not intersect at  $\Delta = 0$  as in the previous case, however a splitting is observed between them. This reveals the well-known anticrossing behavior, a fingerprint of strong coupling (Frimmer and Novotny 2014). We will also show later that the modes separation is responsible to the appearance of the doublets of Autler Townes splitting phenomenon.

For the double coupled system at the CPLP, that is the dimer ZC when  $\beta_C = \kappa = 0.75$  (Fig. 3f), one of the eigenvalues remains equal to  $\omega_0$  while another decreases as  $\Delta$  is increasing from  $-2$  to  $0$ . The two curves intersect each other at  $\Delta = 0$ , exactly as in the absence of the coupling, even if the imaginary part of the splitting does not vanishes as shown in inset. At the CPLP, system then seems as an uncoupled one. Later on, we will see that the CPLP favors the disappearance of quantum interferences phenomena.

In the next section, the structural analysis will be discussed in the case of the ZRC multi dimer system.

### 2.2 The ZRC multi dimer

Let us now focus on the ZRC multi dimer circuit, as depicted in Fig. 1a when  $N > 1$ . The ZRC multi dimers are modeled so that the multipod loops are connected to the central one ( $Z_0R_0C_0$ ). For example, in the cases of the bi and the tri dimer,  $N=2$  and  $N=3$  loops are respectively connected to the central loop. Considering the harmonic solutions  $Q_i(t)$  for the loop  $i(i = 0..N)$ , the Eq. (1) can be rewritten in the following matrix, in the absence of a voltage source:

$$\begin{pmatrix} \chi_0 & c_0 & c_0 & \cdots & c_0 \\ c_1 & \chi_1 & -c_1 & \cdots & -c_1 \\ c_2 & -c_2 & \chi_2 & \cdots & -c_2 \\ \vdots & \vdots & \vdots & \ddots & \vdots \\ c_N & -c_N & -c_N & \cdots & \chi_N \end{pmatrix} \begin{pmatrix} A_0 \\ A_1 \\ A_2 \\ \vdots \\ A_N \end{pmatrix} = \begin{pmatrix} 0 \\ 0 \\ 0 \\ \vdots \\ 0 \end{pmatrix} \tag{8}$$

where  $(i = 0 \dots N)$ ,  $c_i = \beta_{c_i} - \kappa_i \beta_{C_i} = r_C / r_{ei}$ ,  $\kappa_i = \Omega_i / \omega_0$ ,  $\chi_i = \delta_i / \omega_0 + j\beta_i$ ,  $\delta_i = \omega_i - \omega_0$ ,  $\beta_i = R_i / r_{ei}$ ,  $\omega_i = 1 / r_{ei} C_{ei}$ ,  $r_{ei} = r_i + r_C$  and  $C_{ei} = C_i C_C / (C_i + C_C)$ .

The eigenfrequencies of the system can therefore be investigated assuming identical values of the imaginary resistances in the circuit  $r_{i(i=0..N)} = r$  while the capacitances are distinct. Thus  $\beta_{C_i} = \beta_C$ ,  $\kappa_i = \kappa$  and  $c_i = c = \beta_C - \kappa$ . Using the approximation  $|\omega - \omega_0| \ll \omega_0$ ,  $\beta_i \omega \approx \beta_i \omega_0$  (where  $\omega_0$  is the mean frequency), after a few steps of algebra, the determinant of the left most term in Eq. (8) is found to be:

$$D(\omega) = \prod_{i=0}^N \chi_i - Nc^{N+1} - \sum_{p=1}^N \sum_{i=0}^{N-p+1} \sum_{k=i+1}^{N-p+2} \cdots \sum_{s=i+p}^{N-p+q} (N-p)c^{N-p+1} \chi_i \chi_k \cdots \chi_s \tag{9}$$

where  $1 \leq p \leq N$ ,  $2 \leq n \leq N$ ,  $N \geq 1$ ,  $q \geq 2$ ,  $u \geq 3$ , and the other parameters are given as in Eq. (8). It is obvious that the system is non-Hermitian when  $\beta_0 \neq 0$ ,  $\forall \epsilon$  such that  $\beta_i = \epsilon \beta_0$ . As the number  $N$  of the coupled loops increases from  $N=2$  to  $N > 2$ , the complex roots of  $D(\omega)$  can be numerically calculated. The real parts  $\text{Re}(\omega / |\omega_0|)$  of the roots determine the positions of the normal modes of the system; the imaginary parts  $\text{Im}(\omega / |\omega_0|)$ , describe their widths. We investigate the eigenmodes of the multi dimer ZC ( $\kappa = 0.75$ ,  $\beta_0 = 0.5$  and  $\epsilon = 0$ ). The other system parameters are setting as follows [see Eq. (10)]:

bi dimer ( $N = 2$ ) :  $\omega_1 = \omega_0 - 0.1\omega_0$ ,  $\omega_2 = \omega_0 + 0.1\omega_0$ ;  
 tri dimer ( $N = 3$ ) :  $\omega_1 = \omega_0 - 0.1\omega_0$ ,  $\omega_2 = \omega_0 + 0.02\omega_0$ ,  $\omega_3 = \omega_0 + 0.1\omega_0$ ;  
 tetra dimer ( $N = 4$ ) :  $\omega_1 = \omega_0 - 0.1\omega_0$ ,  $\omega_2 = \omega_0 + 0.1\omega_0$ ,  $\omega_3 = \omega_0 - 0.2\omega_0$ ,  $\omega_4 = \omega_0 + 0.2\omega_0$ .  
 (10)

It can be seen from Eq. (10) that, with this choice of parameters the natural frequencies of the multipod loops are distinct, and the system is non-Hermitian.

Figure 4 shows the real [(a), (b) and (c)], and the imaginary [(d), (e) and (f)] parts of the roots of  $D(\omega)$  as a function of  $\beta_C$  in the case of the multi dimer ZC.

As illustrated, the spectrum of the roots of  $D(\omega)$  can be analyzed as a function of  $\beta_C$ , in three domains as  $\beta_C$  is increasing from  $-1$  to  $2$ :

1. Before the CPLP, the real parts of the normal modes  $\text{Re}(\omega_{i(i \neq 0)})$  related to the multipod loops evolve almost linearly compared to the central mode  $\text{Re}(\omega_0)$ . They undergo an abrupt transition after which, all the modes of the coupled system converge through the CPLP.
2. At the CPLP ( $\beta_C = \kappa = 0.75$ ), the modes match with the natural frequencies of the uncoupled system.
3. After the CPLP, the frequencies undergo a second transition less abrupt than the first, and return to their behavior before the first transition. This leads to the splitting of the central mode with respect to those of the multipod. These features are also well observed in the imaginary parts of the roots of  $D(\omega)$ . Remarkably, the eigenfrequencies of the multi dimer are not symmetric with respect to the CPLP. The transition points become

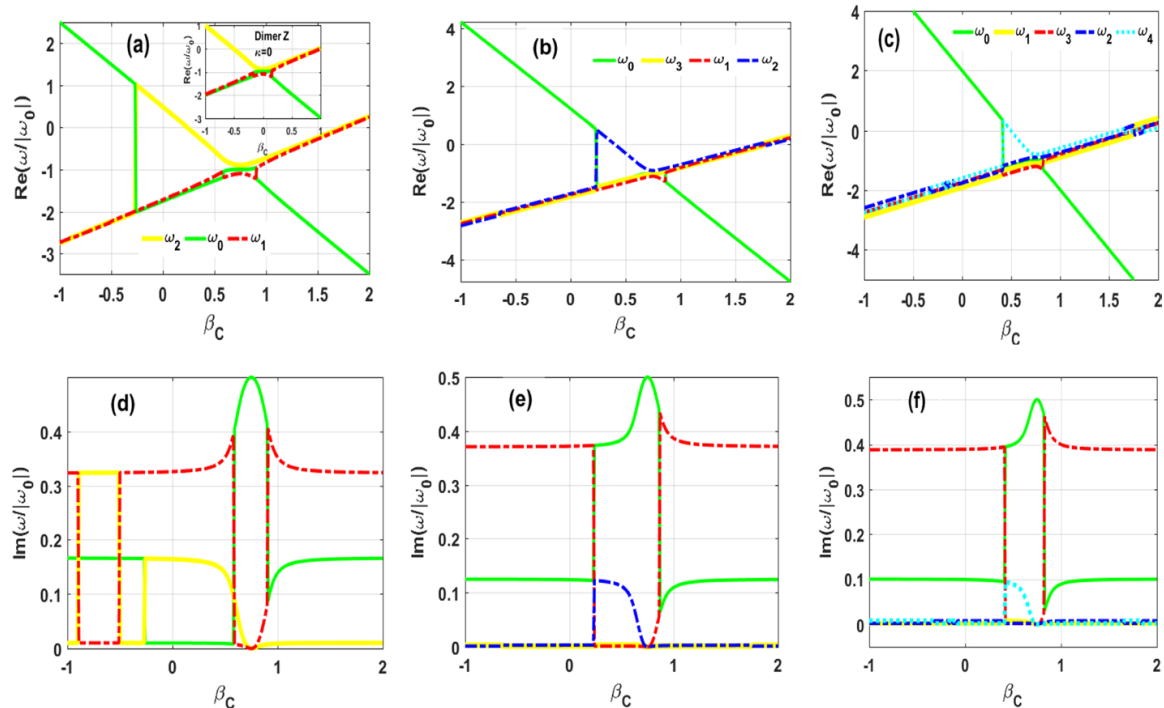


**Fig. 4** The normalized roots of  $D(\omega)$  as function of the imaginary resistive coupling parameter  $\beta_C$  for the multi dimer ZC (when  $\kappa = 0.75$ ). First column: The bi dimer ZC ( $N=2$ ). Second column: The tri dimer ZC ( $N=3$ ) and in last column: The tetra dimer ZC ( $N=4$ ). The upper row shows the real parts of the roots  $[\text{Re}(\omega/|\omega_0|)]$  and the down row shows their imaginary parts  $[\text{Im}(\omega/|\omega_0|)]$ . The other plot parameters are:  $\varepsilon = 0$ ,  $\beta_0 = 0.5$  and  $\omega_0 < 0$ . The inset in (a) corresponding to the case of the bi dimer Z ( $\kappa = 0$ ) allows to show the robustness of the multiple coupling



closer as the N number of the multipods increases. The frequencies' phase transitions are of great interest in quantum interferences phenomena in physics. For example, we demonstrate in the following that, the reduction of the gap observed between them is consequent to the increasing of the number of interferences, giving rise to multiple EIT/EIA phenomena. These observations for the multi dimer with double coupling (multi dimer ZC) around the CPLP, is exhibited in the uncoupled multi dimer system, such as illustrated in the inset Fig. 4a, the case of bi dimer Z. Note that this CPLP was already analyzed in the ZRC single dimer. This demonstrates the efficiency in the cancellation of the coupling modulation of the capacitive coupling ( $\kappa$ ) by the imaginary resistor ( $\beta_C$ ) coupling. In other words, the cancellation is robust throughout the N multipod coupling system.

To better understand the interference phenomena, we will focus in the next section on the steady state dynamics of the systems.

### 3 Steady state dynamic and dispersive properties

In this section, we analyze the dynamic and dispersive properties of the system in presence of the harmonic voltage source  $u(t)$ . In this way, we first study the dynamic of the free single ZRC oscillator. Then, we discuss the ZRC coupled systems.

#### 3.1 Single ZRC oscillator

Let us consider the  $Z_0R_0C_0$  central loop.

In the absence of any coupling (SW  $i$  off), the first row of Eq. (1) can be rewritten as:

$$(\beta_0 + j) \frac{dQ_0}{dt} + \omega_0 Q_0 = u/r_{e0} \tag{11}$$

where  $u(t) = V_0 e^{j\omega t} + c.c.$   $c.c$  is the complex conjugate,  $\omega$  is the voltage frequency,  $V_0$  its amplitude and  $\beta_0^{-1} = (R/r_{e0})^{-1}$  is the circuit's quality factor. It has been shown in ref. (Tabeu et al. 2019) that the quality factor displays an important role to determine the nature of the oscillations in a ZRC oscillator. If the quality factor becomes large ( $\beta_0^{-1} \rightarrow \infty$ ), the circuit oscillates with constant amplitude.

The general solution of Eq. (10) can be written in the form:

$$Q_0(t) = \alpha e^{-\omega_0 t / (\beta_0 + j)} + (A e^{j\omega t} + c.c) \tag{12}$$

where  $A = V_0 / [r_{e0} (\delta + j\beta_0 \omega)]$  is a complex amplitude,  $c.c$  is the complex conjugate,  $\delta = \omega_0 - \omega$  is the frequency detuning and  $\alpha$  is a constant amplitude. In the steady state regime, the first term of  $Q_0(t)$  can be neglected and we can only consider that  $Q_0(t) \approx A e^{j\omega t} + c.c$ . Hence, we can evaluate the dissipated power through the loop as  $P_0(t) = (V_0 e^{j\omega t} + c.c) \dot{Q}_0(t)$ . The average of a dissipated power during one period  $T = 2\pi/|\omega|$  of oscillation is calculated using the expression:

$$P_0(\omega) = \frac{1}{2\pi/\omega} \int_0^{2\pi/\omega} [P_0(t)] dt = \frac{1}{2\pi/\omega} \int_0^{2\pi/\omega} [(V_0 e^{j\omega t} + c.c) \dot{Q}_0(t)] dt \tag{13}$$

Since we are interested in the response of the system near (or at the resonance), we assume  $|\omega - \omega_0| \ll \omega$  and  $\beta\omega \approx \beta\omega_0$ . Under this approximation and using a few step of algebra, the electric power in Eq. (13) can be obtained as:

$$P_0(\omega) \approx j \frac{P_0}{\chi_0} \tag{14}$$

where  $j = \sqrt{-1}$ ,  $p_0 = |V_0|^2 / r_{e0}$ ,  $\chi_0 = \delta_0 / \omega_0 + j\beta_0$ ,  $\delta_0 = \omega_0 - \omega$ .

In Fig. 5, the real (solid) and the imaginary (dash/dot) parts of the steady state normalized electric power ( $P_0/p_0$ ) dissipated by the  $Z_0R_0C_0$  loop are depicted as a function of the normalized voltage frequency  $\omega/\omega_0$  for given values of the non-Hermitian parameter  $\beta_0$ . The green and the blue curves are used for the loss loop ( $\beta_0 = 0.5 > 0$ ) while the purple and the red colors refer to the gain loop ( $\beta_0 = -0.5 < 0$ ). As it can be noticed, the absorption profile presents a lorentzian form with the maximum of the absorption centered at  $\omega = \omega_0$ . Remarkably, for a loss loop the lorentzian is positive, corresponding to a typical absorption in a real atomic system. On the contrary, it is negative in the case of the gain loop, which can be interpreted as enhancement of the power. Indeed, the power is amplified instead of being absorbed (Hai-Chao and Guo-Qin 2014). The imaginary part of the power represents the dispersion in an atomic systems. In the  $Z_0R_0C_0$  oscillator, the slope of a dispersion around the absorption's peak is positive or negative depending on the sign of  $\omega_0$ . It is positive when  $\omega_0 < 0$ , indicating that, the maximum of absorption (or amplification of a power) is obtained at the resonance, where the voltage frequency is equal to the natural loop's frequency. The negative frequencies have been suggested to many past researches (Rubino et al. 2012; Conforti et al. 2013; Lourés et al. 2015; Pendharker et al. 2017; Nezhlin 1976). However, their use in the context of quantum analog system is often overlook.

### 3.2 The dynamic of the ZRC dimer

From the eigenfrequencies of the ZRC dimer illustrated in Fig. 2, two main coupling regimes have emerged and border by the EPs of the non-Hermitian system. We now

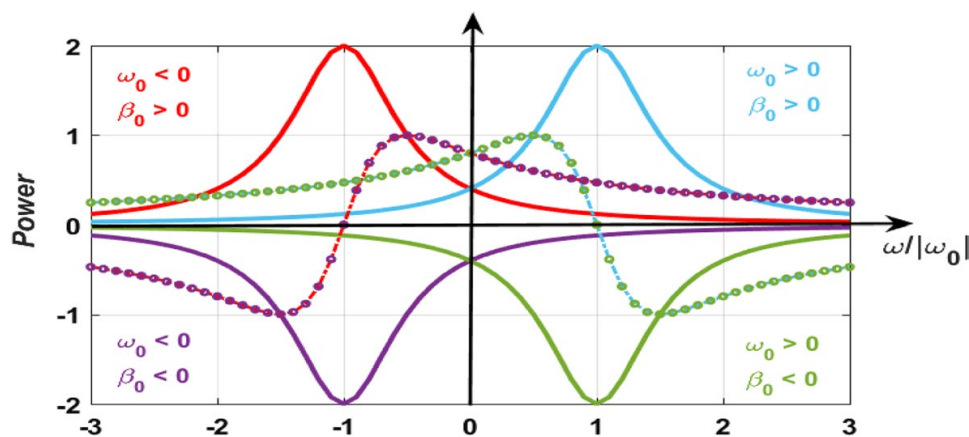


**Fig. 5** The real (solid lines) and the imaginary (dashes/dots lines) parts of the steady state normalized power dissipated by the  $Z_0R_0C_0$  loop as a function of the normalized frequency  $\omega/\omega_0$  for different values of the non-Hermitian parameter  $\beta_0$ . The plot parameters are shown in the figure. In all plots, green and blue curves correspond to the loss loop ( $\beta_0 = 0.5$ ) whereas purple and red curves are associated to the gain loop ( $\beta_0 = -0.5$ ), respectively

attempt to understand the physical significance of the coupling regimes on the dynamic of two coupling ZRC oscillators.

Firstly the dynamic of the system can be investigated in the absence of the external voltage. According to Eq. (3), the eigenvectors  $A_{i+}$ ,  $A_{i-}$  ( $i = 0, 1$ ) describing the normal modes of the coupled system satisfy to Dolfo and Vigué (2018):

$$A_{1\pm} = \alpha_{\pm} A_{0\pm} \tag{15}$$

where  $\alpha_{\pm} = \frac{\omega_0 + (j\beta_0 - 1)\omega_{\pm}}{\Omega - \omega_{\pm}\beta_C} = \frac{\Omega - \omega_{\pm}\beta_C}{\omega_0 + (j\beta_1 - 1)\omega_{\pm}}$ ,  $\beta_C = r_C/r$ ,  $\Omega = 1/rC_C = \kappa\omega_0$ ,  $r = r_{0,1} + r_C$  and  $\omega_0 = 1/rC$ . The eigenfrequencies  $\omega_{\pm}$  are given in Eq. (5).

If  $c \neq c_{th} = \beta_0(\epsilon - 1)/2$ , the general solution  $Q_{0,1}(t)$  for the ZRC dimer can be written as:

$$Q_i(t) = A_{i+}e^{j\omega_+t} + A_{i-}e^{j\omega_-t} \tag{16}$$

where  $i = (0, 1)$ . The amplitudes  $A_{i\pm}$  are found from the initial conditions of the oscillators:  $A_{0+} = [\alpha_-Q_0(0) - Q_1(0)]/(\alpha_- - \alpha_+)$  and  $A_{0-} = [Q_1(0) - \alpha_+Q_1(0)]/(\alpha_- - \alpha_+)$ ,  $Q_i(0)$  being the initial charges of the capacitors. We have calculated the amplitude squared  $|Q_i|^2$  associated to each loop of the dimer and the response is significantly describing the transfer of energy from one oscillator to another. Let's discuss the dynamic of the dimer by considering the following parameter for the non-Hermitian system  $\beta_0 = 0.1$  and  $\epsilon = 0$ . With these considerations, the EPs are found to be  $\beta_{C1} = -0.05$  and  $\beta_{C2} = 0.05$  in the case of the dimer Z. In the case of the dimer ZC ( $\kappa = 0.75$ ), they are obtained as  $\beta_{C_{th1}} = 0.7$  and  $\beta_{C_{th2}} = 0.8$ . Then, the weakly coupled regimes are in the ranges  $-0.05 < \beta_C < 0.05$  for the dimer Z and  $0.7 < \beta_C < 0.8$  for the dimer ZC, respectively. In both cases, the strongly coupled regime is found everywhere else. In Fig. 6, the quantities  $|Q_0|^2$  and  $|Q_1|^2$  are plotted as a function of the time  $t$  for different values of the active coupling  $\beta_C$  in each coupling regime. The initial conditions of the dimer were chosen such as to introduce the signal into the coupling  $Z_1R_1C_1$  loop (oscillator 1)  $Q_0(0) = 0$ ,  $Q_1(0) = 1$ . As illustrated, in presence of a strong coupling, once a signal is put into oscillator 1, it is noticed a rapid periodic exchange of energy between both oscillators loops. This exchange is made in an oscillatory process so that, when the energy of one oscillator reaches its maximum value, the energy of the other oscillator is minimum. Also, note that these oscillations are very fast in the dimer ZC. On the contrary in presence of the weak coupling, it is noticed when  $\omega_0$  is positive that, the energy is irreversibly transferred from oscillator 1 to 0 of which the energy remains almost closed to zero. However, if  $\omega_0$  is negative, the energy of oscillator 1 takes a relatively long time to reach oscillator 0, of which the energy increases exponentially. At the CPLP, a particular point of a weak coupling regime, a different behavior is remarkable. Indeed, once the signal is introduced in oscillator 1, it remains there. There is no exchange of the energy with the oscillator 0 whose the amplitude remains zero. This confirm that at this point, the system seems effectively as it is uncoupled.

Secondly, let's investigate the system taking into account the external voltage source. In this case, the exact solutions  $Q_i(t)$  of Eq. (1) can be written as a sum of two terms  $Q_0(t) = Q_0^C(t) + Q_0^P(t)$ .  $Q_0^C(t)$  is the complementary solution which linearly combines the two normal modes frequencies of the dimer i.e.  $Q_0^C(t) = A_{0+}e^{j\omega_+t} + A_{0-}e^{j\omega_-t}$ , where the eigenfrequencies  $\omega_{\pm}$  were obtained in Eq. (5).  $A_{0\pm}$  are the complex amplitudes.  $Q_0^P(t)$  is a particular solution. It can be taken in the form of the voltage as  $Q_0^P(t) = \rho_0 e^{j\omega t} + c.c$ , where  $\rho_0$  is the amplitude. In the steady state in general, only a particular solution remains. It is interesting to analyze the power absorbed or dissipated by the oscillators from the external

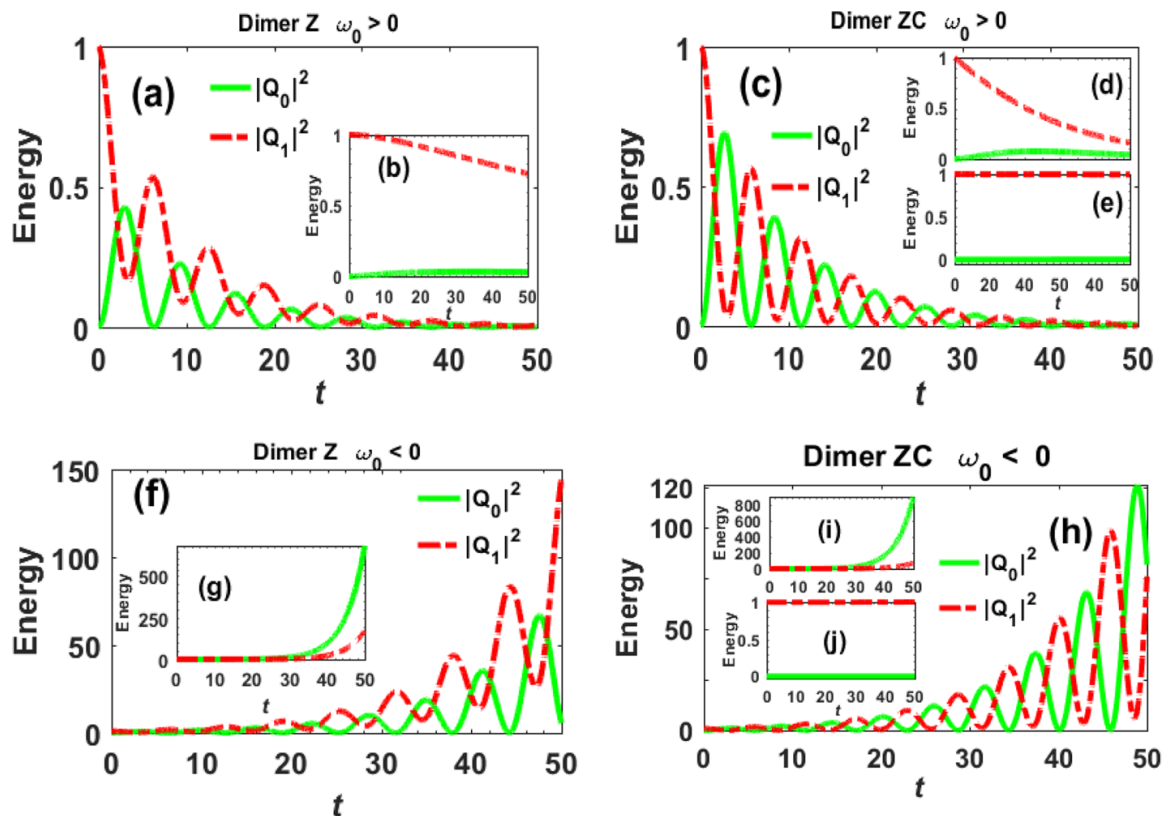


**Fig. 6** Time evolution of the energy in each cell of the dimer Z (first column) and the dimer ZC (second column). (a) and (f): dimer Z ( $\beta_C = 0.5$ ) in strong regime. (b) and (g) correspond to dimer Z ( $\beta_C = 0.02$ ) in the weak coupling regime. (c) and (h): dimer ZC ( $\kappa = 0.75, \beta_C = 0.2$ ) in the strong regime. (d) and (i): dimer ZC ( $\kappa = 0.75, \beta_C = 0.71$ ) in the weak coupling regime. (e) and (j): the dimer ZC at the CPLP ( $\beta_C = \kappa = 0.75$ ). From (a) to (e):  $\omega_0 = 1 \text{ rad.s}^{-1} > 0$  and from (f) to (j):  $\omega_0 = -1 \text{ rad.s}^{-1} < 0$ . For all plots  $\varepsilon = 0$  and  $\beta_0 = 0.1$ . The solid green and red dashes curves represent the energies  $|Q_0|^2$  of and  $|Q_1|^2$ , respectively

voltage. Hence, substituting  $Q_0^P(t)$  into Eq. (13), the steady state power dissipated by the loop  $Z_0 R_0 C_0$ ,  $P_0(\omega)$  is found to be:

$$P_0(\omega) = \frac{|V_0|^2}{r_{e0}} \frac{j\omega(\delta + j\beta_1\omega)}{(\delta + j\beta_0\omega)(\delta + j\beta_1\omega) - (\Omega - \beta_c\omega)^2} \tag{17}$$

where  $\delta = \omega_0 - \omega$  and  $\Omega = \kappa\omega_0$ .

Using the approximation  $|\omega - \omega_0| \ll \omega, \beta\omega \approx \beta\omega_0$ , Eq. (17) can be rewritten as:

$$P_0(\omega) \approx j \frac{p_0 \chi_1}{\chi_0 \chi_1 - c^2} \tag{18}$$

where  $j = \sqrt{-1}$ ,  $p_0 = V_0^2/r$ ,  $c = \beta_c - \kappa$ ,  $\chi_{0,1} = \delta/\omega_0 + j\beta_{0,1}$  and  $\delta = \omega_0 - \omega$  is the frequency detuning between the loops and the voltage frequencies.

In the context of electronics, it is well known that the real part of the dissipated power (i.e. the active power) determines the absorption. Its imaginary part (i.e. the reactive power) simulates the dispersion properties of the atomic medium. Considering the central loop as a loss loop ( $\beta_0 = 0.1 > 0$ ), and modulating the non-Hermitian parameter ratio  $\varepsilon$  from the positive to negative values, the dissipated power can be investigated according to the coupling strength of dimers formed by a double and single coupling.

In Fig. 7, the real (solid blue) and the imaginary (dashed red) parts of the normalized dissipated power ( $P_0/p_0$ ) are reported as a function of the normalized voltage frequency  $\omega/\omega_0$ .

As it can be seen, if a weak coupling is established in the dimer ZC ( $\kappa = 0.75$ ,  $\beta_C = 0.71$ ,  $\omega_0 > 0$ ), a narrow dip appears in the absorption spectrum of the  $Z_0R_0C_0$  loop when  $\epsilon = 0.2$ , leading two absorption peaks (Fig. 7a). The dispersion curve is also modified around the resonance (zero detuning). When  $\epsilon = 0$ , a zero absorption, so a transparency domain occurs in the spectrum at a zero frequency detuning  $\delta = 0$ . Then, the dispersion curve becomes much steeper near the central frequency. This behavior is similar to the EIT effect. In atomic context, it has been interpreted as a direct manifestation of destructive interferences between the normal modes of oscillations of the system. This description matches perfectly with the experimental demonstrations made previously with classical systems (Garrido Alzar et al. 2002; Harden et al. 2011; Bai et al. 2013). When a small negative dissipation ( $\epsilon = -0.1$ ) is

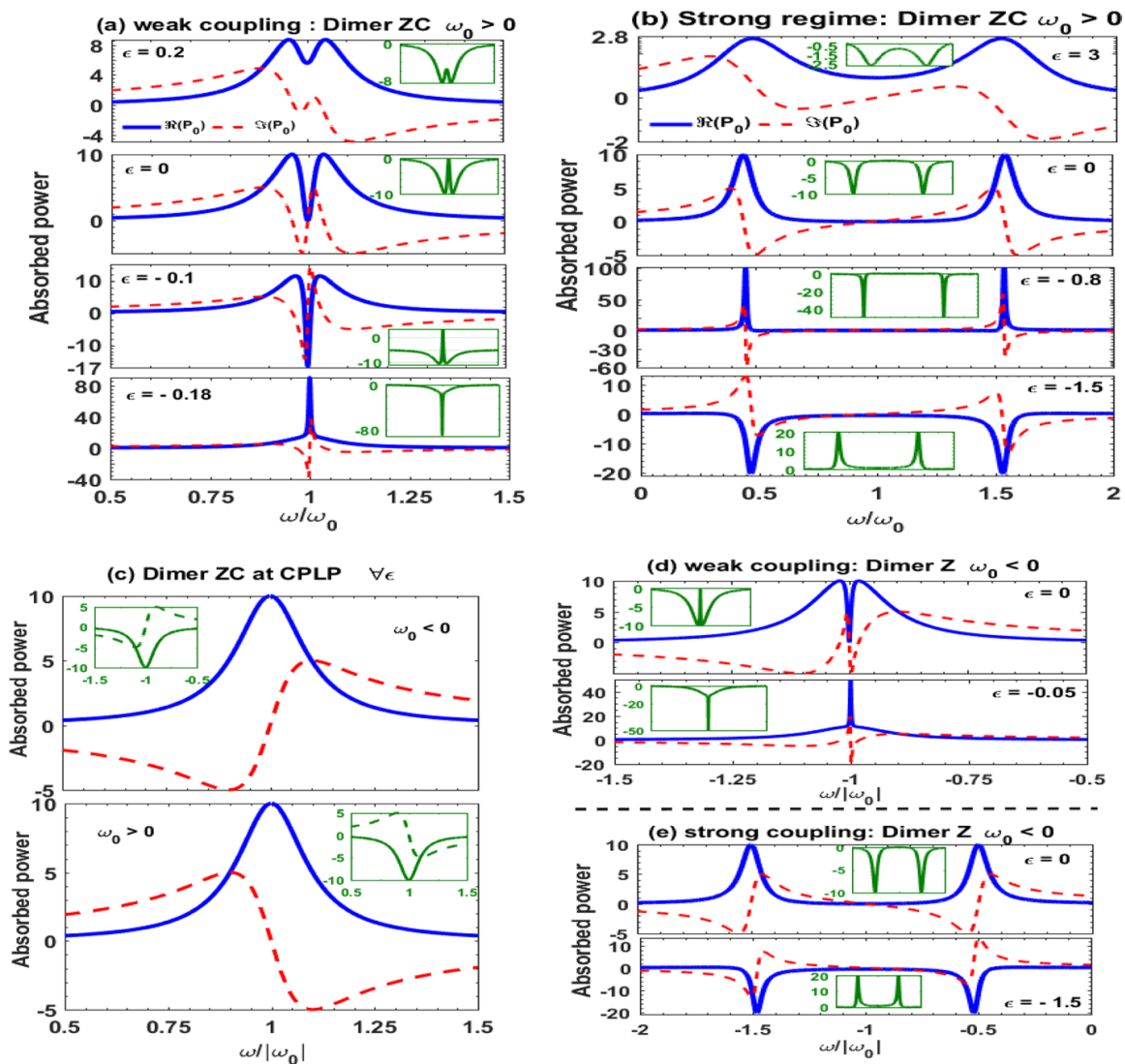


**Fig. 7** Absorbed power (dissipated) by the main loop of the dimer ZC [from (a) to (c)] when the natural frequencies of the loops are positive  $\omega_0 > 0$  and the one of the dimer Z (d) when natural frequencies are negative  $\omega_0 < 0$ . The solid blue and dashed red correspond to the real and imaginary parts of the absorbed power when the main loop is loss ( $\beta_0 = 0.1 > 0$ ). The insets in green show the real part of the power corresponding to the main loop gain ( $\beta_0 = -0.1 < 0$ ). The other plot parameters are identical to those used in Fig. 5

introduced into the pumping  $Z_1R_1C_1$  loop, a negative absorption occurs in the transparency zone. The negative absorption refers to the amplification (Hai-Chao and Guo-Qin 2014). The later behavior is referred as the Electromagnetically Induced Amplified Transparency (EIAT). For a further decrease of  $\varepsilon$  until the value  $\varepsilon = -0.18$ , an enhanced absorption peak occurs in the profile where the dip was expected to be. This mimics the absorption spectrum of atomic systems with three energy levels in lambda ( $\Lambda$ ) configuration, in the regime of Electromagnetically Induced Absorption (EIA) (Lezama et al. 1999). EIA has been interpreted for atomic systems, as a manifestation of constructive interferences between the normal modes of oscillations.

Figure 7b shows the absorption profile of the  $Z_0R_0C_0$  loop when a strong coupling ( $\kappa = 0.75$ ,  $\beta_C = 0.2$ ,  $\omega_0 > 0$ ) is established in the dimer system. If much losses are introduced into the pumping loop ( $\varepsilon = 3$ ), it is observed in the spectrum, two absorption peaks separated by a large transparency window. These peaks are clearly identified when the losses decrease to zero (i.e.  $\varepsilon = 0$ ). The phenomenon is similar to the well-known Autler–Townes Splitting (ATS) effect which is generally interpreted as a consequence of a gap between two atomic resonances peaks. The peaks are located on both sides of the central frequency  $\omega_0$ . For a further decreasing of the damping, such as to introduce a negative dissipation into a pumping oscillator ( $\varepsilon = -0.8$ ), a negative absorption occurs in the spectrum. This leads the enhancement of the absorption peaks. Such a behavior can be generalized to the values of  $\varepsilon$  in the domain between 0 and  $-1$ , where  $\varepsilon = -1$  corresponds to the Parity Time Symmetric (PTS) case. However, when  $\varepsilon$  is less than  $-1$ , the peaks become inverted so that, only a negative absorption (amplification) is observed in the profile. The behavior can be called Autler–Townes splitting with amplification (ATSA).

The question we can ask now is what happens at the CPLP where the effective coupling cancels?

To answer to this question, we substitute the couplingless condition given in Eq. (6) into the Eq. (18) and the expression of the absorbed power by the main loop is reduced to the power of a free  $Z_0R_0C_0$  loop as obtained in Eq. (14). As we could predict, the cancellation of the effective coupling has the effect to decouple parts of the system such that, no exchange of energy can be observed between them. Therefore, no interference could be obtained. The absorption spectrum is then reduced to that of a free oscillator, a lorentzian curve illustrated in Fig. 7c. Accordingly, all the other replicated atomic phenomena disappear. These results indicate that operating at the CPLP could be an efficient way to control applications of EIT with real atomic systems. Except for the CPLP, all the results discussed here with the ZC dimer when  $\omega_0 > 0$ , can also be obtained with a single coupled dimer. For example, Fig. 7d illustrates the absorption spectrum in the case of the dimer Z ( $\beta_C = 0.02$  and  $\beta_C = 0.5$ ) when  $\omega_0 < 0$ . The transparent window observed agrees well the observation made with the dimer ZC when  $\omega_0 > 0$ . This demonstrates that EIT and related phenomena can be observed with negative frequencies of the system, and show a wide range of frequency for investigations with ZRC circuits. Also mention that the green curves illustrated in the insets show the active power obtained in the same conditions, however with the main loop gain ( $\beta_0 = -0.1 < 0$ ).

Knowing now the dynamics of the dimer system, in the next paragraph, we will focus on the dynamics of the multidimer systems.

### 3.3 Dynamic of the ZRC multi dimer

Let us consider the multi dimer circuit. In the previous section, we have seen from the absorption spectrum of the ZRC dimer ( $N = 1$ ) that, the circuit allows to reproduce EIT,

EIAT, EIA or ATS. What happens in the spectrum when  $N > 1$ ? Is the multi dimer circuit could be used to replicate a multiple EIT, EIA or ATS windows? Indeed it has been demonstrated (Harden et al. 2011) that, to obtain multiple transparency windows, each part of the circuit must oscillates with its own natural frequency  $\omega_i (i = 0 \dots N)$ , which differs from one loop to another. Considering harmonic solutions for the charges, the dynamic of the multidimer can be described by the Eq. (8) when adding the voltage term  $u(t) = V_0 e^{j\omega t} + c.c$  in its right term. Solving such equation, the amplitudes  $A_i (i = 0 \dots N)$  can be obtained and accordingly, the charge solution  $Q_0(t)$  through the central loop. Thanks to Eq. (13), we have calculated the expression of the steady state frequency-dependence power  $P_0(\omega)$ , which is dissipated by the main loop as a function of the N number ( $N \geq 1$ ) of multipod loops. Under the approximation  $|\omega - \varpi| \ll \omega$ ,  $\beta_i \omega \approx \beta_i \varpi$ , where  $\varpi = \omega_0$  is the mean frequency of the system and, using steps of algebra, the steady state power  $P_0(\omega)$  is found to be:

$$P_0(\omega) = \frac{j}{D(\omega)} \left( \prod_{l=1}^N \chi_l - (N-1)c^N - \sum_{n=2}^N \sum_{m=1}^{N-n+2} \sum_{h=m+1}^{N-n+3} \dots \sum_{v=m+u}^{N-n+u} (N-n)c^{N-n+1} \chi_m \chi_h \dots \chi_v \right), \tag{19}$$

where  $(i = 0 \dots N)$ ,  $c_i = \beta_{c_i} - \kappa_i$ ,  $\beta_{c_i} = r_c / r_{ei}$ ,  $\kappa_i = \Omega_i / \omega_0$ ,  $\chi_i = \delta_i / \omega_0 + j\beta_i$ ,  $\delta_i = \omega_i - \omega$ ,  $\beta_i = R_i / r_{ei}$ ,  $\omega_i = 1 / r_{ei} C_{ei}$ ,  $r_{ei} = r_i + r_c$  and  $C_{ei} = C_i C_c / (C_i + C_c)$ . The denominator  $D(\omega)$  was expressed in Eq. (8):

$$D(\omega) = \prod_{i=0}^N \chi_i - Nc^{N+1} - \sum_{p=1}^N \sum_{i=0}^{N-p+1} \sum_{k=i+1}^{N-p+2} \dots \sum_{s=i+q}^{N-p+q} (N-p)c^{N-p+1} \chi_i \chi_k \dots \chi_s$$

$$1 \leq p \leq N, 2 \leq n \leq N, N \geq 1, q \geq 2, u \geq 3$$

In the following, we will focus the analysis on three cases of the multi dimer ZC circuits: the bi dimer, the tri dimer and the tetra dimer. The aim is to show that the interferences in the system can allow to reproduce the multiple EIT, EIA and ATS, with the number of windows consistent with the N number of the multipods. Assuming Eq. (10) for the multipod loops frequencies' and the central loop as a loss one ( $\beta_0 = 0.5 > 0$ ), the steady state power  $P_0(\omega)$  can be investigated when controlling the coupling parameter  $\beta_c$  and the non Hermitian parameter ratio  $\epsilon$ .

In Fig. 8, the real (solid blue) and the imaginary (dashed red) parts of the normalized dissipated power  $P_0(\omega)/p_0$  are reported as a function of the normalized frequency  $\omega/|\omega_0|$  for different values of the  $\epsilon$  parameter.

### 3.3.1 Case 1: the bi dimer ZC (N = 2)

As illustrated in Fig. 8a, in presence of the weak coupling ( $\kappa = 0.75$ ,  $\beta_c = 0.85$ ), it is noticed in the absorption spectrum when  $\epsilon = 0$ , the occurrence of two symmetric dips centered at  $\omega = 0.9\omega_0$  and  $\omega = 1.1\omega_0$  on both sides of the central peak. This gives rise to two EIT windows. The behavior is similar to the quantum phenomenon of a double Electromagnetically Induced Transparency (DEIT). Accordingly, two steep slopes are observed in the dispersion curve near the transparency domain. It is interesting to note that these results are consistent with DEIT demonstrated in ref. (Harden et al. 2011) where the LRC circuits have been used. However, notice that one difference between our results and the previous

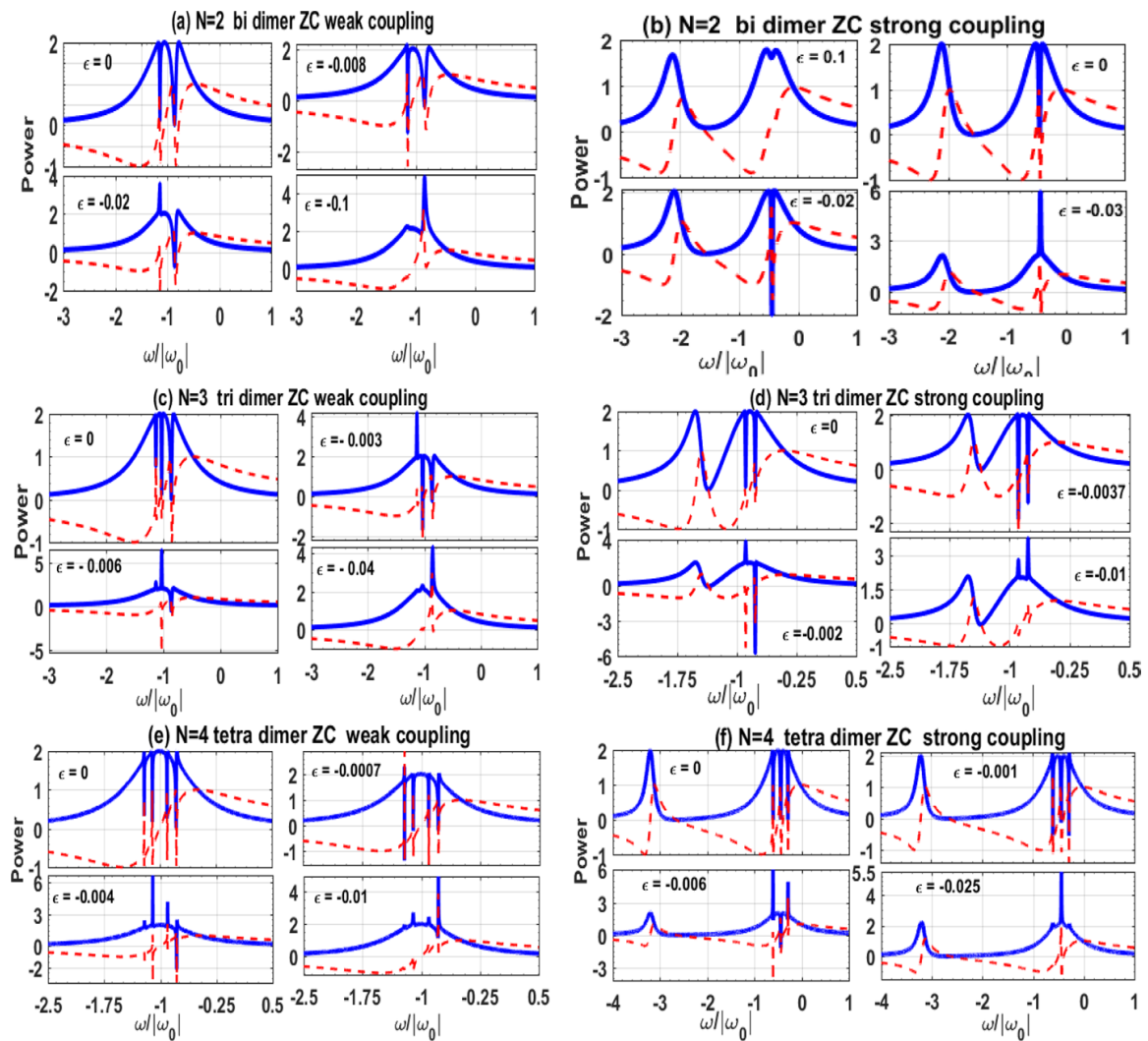


**Fig. 8** The real and imaginary parts of the steady state normalized dissipated power  $P_0/p_0$  as a function of the normalized frequency  $\omega/|\omega_0|$  for different cases of the multi dimer ZC according to the coupling regime: weak coupling (first column), strong coupling (second column). In all plots, we set  $\omega_0 < 0$ ,  $\beta_0 = 0.5$  and  $\kappa = 0.75$ . **(a)** and **(b)**: bi dimer ZC ( $N=2$ ) **(c)** and **(d)**: tri dimer ZC ( $N=3$ ) **(e)** and **(f)**: tetra dimer ZC ( $N=4$ ). The other plot parameters are inserted in text

ones is that for the previous ones, the frequencies of the system were positive, while for our system, the frequencies can be as well positive or negative, as described above.

By decreasing  $\epsilon$  to the value  $\epsilon = -0.008$ , a phenomenon similar to the EIAT appears in the absorption spectrum. However it is centered at two frequencies, where a negative power is observed. Accordingly, this new behavior is called double EIAT (DEIAT). For a further decreasing of  $\epsilon$  to  $-0.002$ , and then to the value  $-0.1$ , it is remarked in the spectrum the occurrence of one EIA peak where the first EIT dip was observed and then another one, where the second dip was expected to be. As a consequence, it results two enhanced absorption peaks. Then, the bi dimer ZC circuit allows to replicate double EIA (DEIA). So, the bi dimer allows the replication of two EIT, EIAT or EIA windows in the weak coupling regime.

Figure 8b shows in presence of the strong coupling ( $\kappa = 0.75$ ,  $\beta_C = 0.2$ ) that, when a dissipation is introduced into the coupling fields ( $\epsilon = 0.1$ ), it is observed two dips inside the absorption profile. One of the dips is more pronounced and centered at the frequency  $\omega_0$  while the other one is very narrow. Both dips are separated by a large transparency domain, similar



to the ATS effect described above. The location of the peaks is in perfect accordance with the eigenmodes behavior presented in Fig. 4, where the multipod modes frequencies are closed together while the central mode splits. A further decrease of  $\varepsilon$  to the value  $\varepsilon = 0$  reduces the dips to zero, leading to the phenomenology of EIT. The system then allows to reproduce simultaneously EIT and ATS windows instead of two ATS windows as we could expected in the strong coupling regime. As one would imagine, by lowering  $\varepsilon$  to negative values for example  $\varepsilon = -0.02$ , a negative power, typical to the EIAT effect observed in the weak coupling for  $\varepsilon = 0$ , occurs in the region of transparency between the two EIT peaks. For  $\varepsilon = -0.03$ , it is not surprising to note that the spectrum just pass from EIAT to the EIA behavior exhibited in the case of the dimer ZC. In all cases, the dispersion curve is modified according to the phenomenon reproduced. The bi dimer can then allow to replicate simultaneously ATS and EIT, EIAT or EIA windows in the strong coupling regime.

### 3.3.2 Case 2: the tri dimer ZC (N=3)

In the presence of the weak coupling ( $\kappa = 0.75$ ,  $\beta_C = 0.803$ ) as illustrated in Fig. 8c, if  $\varepsilon = 0$ , the absorption spectrum shows three narrow dips centered at the naturel loops frequencies  $0.9\omega_0$ ,  $1.02\omega_0$  and  $1.1\omega_0$  [see Eq. (10)], thus exhibiting three EIT windows. This behavior is similar to the Triple EIT (TEIT) effect observed in atomic context (Wang et al. 2019). TEIT was also studied in a superconducting quantum circuit with a four-level V-type energy spectrum (Tiaz et al. 2019). A further decreasing of  $\varepsilon$  to  $-0.003$ , then to  $-0.006$  and thereafter to  $-0.04$  allows to the spectrum to switch from the triple EIAT (TEIAT) to a double EIA (DEIA) and then to triple EIA (TEIA), respectively. So, a tri dimer can provides up to three EIT, EIAT or EIA windows in presence of the weak coupling.

In presence of a strong coupling ( $\kappa = 0.75$ ,  $\beta_C = 0.58$ ) as shown in Fig. 8d, when  $\varepsilon$  takes respectively the values  $\varepsilon = 0$ ,  $\varepsilon = -0.002$ , and  $\varepsilon = -0.01$ , the spectrum presents similar behaviors as those obtained in the strong coupling regime with the bi dimer ZC. However, the number of EIT, EIAT dips or EIA peaks is increased to two, whereas the number of ATS window remains constant to one.

### 3.3.3 Case 3: the tetra dimer ZC (N=4)

As illustrated in Fig. 8e, in the presence of the weak coupling ( $\kappa = 0.75$ ,  $\beta_C = 0.78$ ), it is observed in the profile when  $\varepsilon = 0$ , four EIT windows, called a quadruple EIT (QEIT). By playing on the value of  $\varepsilon$ , the tetra dimer allowed also to reproduce quadruple EIAT (QEIAT) windows when  $\varepsilon = -0.0007$ , then a TEIA when  $\varepsilon = -0.004$  and finally quadruple EIA (QEIA) if  $\varepsilon = -0.01$ .

In Fig. 8f where the tetra dimer is in presence of the strong coupling ( $\kappa = 0.75$ ,  $\beta_C = 0.2$ ), the system allows again to mimic TEIT ( $\varepsilon = 0$ ), TEIAT ( $\varepsilon = -0.001$ ), DEIA ( $\varepsilon = -0.006$ ) and TEIA ( $\varepsilon = -0.0025$ ) simultaneously accompanied in each case by just an ATS dynamic.

## 4 Conclusion

We have proposed a non-Hermitian electronic dimers, based on the imaginary resistor, which is analog to a  $(N+2)$  level atomic system in the multipod type configuration. The so-called ZRC multi dimer system is described by the equations of the first order. Under the resonance approximations, we have successfully investigated on the structural

characterization. Two main coupling regimes have emerged revealing a couplingless point (CPLP) associated to multiple couplings. In the weakly coupling regime, the eigenfrequencies cross. This demonstrates a non-reversible energy transfer between the coupled oscillators. On the other hand, in the strong coupling regime, the eigenfrequencies exhibit a splitting behavior. This indicates exchange between energy in the coupling oscillators in a periodical way. The proposed model is highly desired to develop quantum interference dynamic in dispersive media. When the central loop is coupled to  $N$  multipod loops, its absorption profile replicates the N-EIT, N-EIAT or N-EIA dynamic in the weakly coupling. When the strong coupling is established, the  $(N-1)$  EIT,  $(N-1)$  EIAT or  $(N-1)$  EIA with the ATS dynamic is simultaneously observed. It is remarkable that, at the CPLP all the quantum phenomena disappears. This reveals the efficiency of the imaginary resistive coupling in the cancellation of the capacitive coupling effect.

**Acknowledgements** Authors would like here to acknowledge TABEU Stéphane Boris of HITASTEC (High-tech and Slow Technology) for helpful discussions.

## References


- Autler, S.H., Townes, C.H.: Stark effect in rapidly varying fields. *Phys. Rev.* **100**, 703–722 (1955)
- Bai, Z., Hang, C., Huang, G.: Classical analogs of double electromagnetically induced transparency. *Opt. Commun.* **291**, 253–258 (2013)
- Bai, P., Ding, K., Wang, G., Luo, J., Zhang, Z.-Q., Chan, C.T., Wu, Y., Lai, Y.: Simultaneous realization of a coherent perfect absorber and laser by zero-index media with both gain and loss. *Phys. Rev. A* **94**, 6 (2016)
- Bermel, P., Rodriguez, A., Johnson, S.G., Joannopoulos, J.D., Soljačić, M.: Single-photon all-optical switching using waveguide-cavity quantum electrodynamics. *Phys. Rev. A* **74**, 043818 (2006)
- Bharti, V., Wasan, A.: Complete wavelength mismatching effect in a doppler broadened Y-type six-level EIT atomic medium. *Opt. Commun.* **324**, 238–244 (2014)
- Christodoulides, D., Yang, J.: Parity-time symmetry and its applications. Springer (2018)
- Cohen-Tannoudji, C.N.: The autler–townes effect revisited. In: Chiao, R.Y. (eds) *Amazing Light*. Springer, New York, NY, pp 109–123 (1996). [https://doi.org/10.1007/978-1-4612-2378-8\\_11](https://doi.org/10.1007/978-1-4612-2378-8_11)
- Conforti, M., Westerberg, N., Baronio, F., Trillo, S., Faccio, D.: Negative-frequency dispersive wave generation in quadratic media. *Phys. Rev. A* **88**, 013829 (2013)
- Dastidar, K.R., Dutta, S.: Broadening of EIT window by incoherent pumping in a three-level  $\Lambda$  system: effect of homogeneous and inhomogeneous broadening. *EPL* **82**, 54003 (2008)
- Dolfo, G., Vigué, J.: Damping of coupled harmonic oscillators. *Eur. J. Phys* **39**, 025005 (2018)
- Elwakil, A.S., Maundy, B.J.: Indirect realization of the imaginary resistor  $jR$ . *Analog Integr. Circuits Signal Process.* **35**, 2610–2615 (2015)
- Fleischhauer, M., Imamoglu, A., Marangos, J.P.: Electromagnetically induced transparency: optics in coherent media. *Rev. Mod. Phys.* **77**, 633–673 (2005)
- Fotsa-Ngaffo, F., Tabeu, S.B., Tagouegni, S., Kenfack-Jiotsa, A.: Thresholdless characterization in space and time reflection symmetry electronic dimers. *J. Opt. Soc. Am. B* **34**, 658 (2017)
- Frimmer, M., Novotny, L.: The classical bloch equations. *Am. J. Phys.* **82**, 947–954 (2014)
- Fujii, T., Shouno, K.: Realization of impedance-scaled complex filters using reciprocal elements. In: 2019 34th international technical conference on circuits/systems, computers and communications (ITC-CSCC), (2019)
- Garrido Alzar, C.L., Martinez, M.A.G., Nussenzeig, P.: Classical analog of electromagnetically induced transparency. *Am. J. Phys.* **70**, 37–41 (2002)
- Hai-Chao, L., Guo-Qin, G.: Switching from positive to negative absorption with electromagnetically induced transparency in circuit quantum electrodynamics. *Chin. Phys.* **23**, 054206 (2014)
- Harden, J., Joshi, A., Serna, J.D.: Demonstration of double EIT using coupled harmonic oscillators and RLC circuits. *Eur. J. Phys.* **32**, 541–558 (2011)
- Harris, S.E.: Electromagnetically induced transparency. *Phys. Today* **50**, 36–42 (1997)

- Harris, S.E., Field, J.E., Imamoğlu, A.: Nonlinear optical processes using electromagnetically induced transparency. *Phys. Rev. Lett.* **64**, 1107–1110 (1990)
- Hétet, G., Peng, A., Johnsson, M.T., Hope, J.J., Lam, P.K.: Characterization of electromagnetically-induced-transparency-based continuous-variable quantum memories. *Phys. Rev. A* **77**, 012323 (2008)
- Huy, B.N., Le Van, D., Xuan, K.D.: Controllable optical properties of multiple electromagnetically induced transparency in gaseous atomic media. *Commun. Phys.* **29**, 1 (2019)
- Lezama, A., Barreiro, S., Akulshin, A.M.: Electromagnetically induced absorption. *Phys. Rev. A* **59**, 4732–4735 (1999)
- Liu, C., Dutton, Z., Behroozi, C.H., Hau, L.V.: Observation of coherent optical information storage in an atomic medium using halted light pulses. *Nature* **409**, 490–493 (2001)
- Liu, N., Weiss, T., Mesch, M., Langguth, L., Eigenthaler, U., Hirscher, M., Sönnichsen, C., Giessen, H.: Planar metamaterial analogue of electromagnetically induced transparency for plasmonic sensing. *Nano Lett.* **10**, 1103–1107 (2010)
- Lourés, C.R., Faccio, D., Biancalana, F.: Nonlinear cavity and frequency comb radiations induced by negative frequency field effects. *Phys. Rev. Lett.* **115**, 193904 (2015)
- Matsko, A.B., Rostovtsev, Y.V., Fleischhauer, M., Scully, M.O.: Anomalous stimulated brillouin scattering via ultraslow light. *Phys. Rev. Lett.* **86**(10), 2006–2009 (2001)
- McGloin, D., Fulton, D.J., Dunn, M.H.: Electromagnetically induced transparency in N-level cascade schemes. *Opt. Commun.* **190**, 221–229 (2001)
- Mompart, J., Corbalán, R.: Lasing without inversion. *J. Opt. B Quantum Semiclass. Opt.* **2**, R7–R24 (2000)
- Nakagawa, T., Shouno, K., Kuniya, K.: Synthesis of a first-order passive complex filter with band-pass/band-elimination characteristics. *Analog Integr. Circuits Signal Process.* **78**, 33–42 (2013)
- Nezlin, M.V.: Negative-energy waves and the anomalous doppler effect. *Sov. Phys. Uspekhi* **19**, 946–954 (1976)
- Paspalakis, E., Knight, P.L.: Electromagnetically induced transparency and controlled group velocity in a multilevel system. *Phys. Rev. A* **66**, 015802 (2002)
- Pendharker, S., Guo, Y., Khosravi, F., Jacob, Z.: PT-symmetric spectral singularity and negative-frequency resonance. *Phys. Rev. A* **95**, 033817 (2017)
- Petrosyan, D., Malakyan, Y.P.: Magneto-optical rotation and cross-phase modulation via coherently driven four-level atoms in a tripod configuration. *Phys. Rev. A* **70**, 023822 (2004)
- Phillips, D.F., Fleischhauer, A., Mair, A., Walsworth, R.L.: Storage of light in atomic vapor. *Phys. Rev. Lett.* **86**, 783–786 (2001)
- Ramzan, R., Siddiqui, O.F., Arshad, M.W., Ramahi, O.M.: A complex permittivity extraction method based on anomalous dispersion. *IEEE Trans. Microw. Theory Tech.* **64**, 3787–3796 (2016)
- Ramzan, R., Omar, M., Siddiqui, O.F., Amin, M., Bastaki, N., Ksiksi, T.S.: Electromagnetically induced absorption in the near-field of microwave radiative elements with application to foliage moisture sensing. *IEEE Access* **6**, 77859–77868 (2018)
- Rodriguez, S.R.-K.: Classical and quantum distinctions between weak and strong coupling. *Eur. J. Phys.* **37**, 025802 (2016)
- Rubino, E., McLenaghan, J., Kehr, S.C., Belgiorno, F., Townsend, D., Rohr, S., Kuklewicz, C.E., Leonhardt, U., König, F., Faccio, D.: Negative-frequency resonant radiation. *Phys. Rev. Lett.* **108**, 253901 (2012)
- Schindler, J., Lin, Z., Lee, J.M., Ramezani, H., Ellis, F.M., Kottos, T.: PT-symmetric electronics. *J. Phys. A Math. Theor.* **45**, 444029 (2012)
- Scully, M.O.: From lasers and masers to phaseonium and phasers. *Phys. Rep.* **219**, 191 (1992)
- Shouno, K., Ishibashi, Y.: Synthesis and active realization of a three-phase complex coefficient filter using gyrators. In: 2008 51st midwest symposium on circuits and systems, (2008)
- Siddiqui, O., Ramzan, R., Amin, M., Ramahi, O.M.: A non-invasive phase sensor for permittivity and moisture estimation based on anomalous dispersion. *Sci. Rep.* **6**, 28626 (2016)
- Smith, D.D., Chang, H., Fuller, K.A., Rosenberger, A.T., Boyd, R.W.: Coupled-resonator-induced transparency. *Phys. Rev. A* **69**, 6 (2004)
- Tabeu, S.B., Fotsa-Ngaffo, F., Kenfack-Jiotsa, A.: Imaginary resistor based parity-time symmetry electronics dimers. *Opt. Quant. Electron.* **51**, 1–17 (2019)
- Tagouegni, S., Fotsa-Ngaffo, F., Tabeu, S.B., Kenfack-Jiotsa, A.: Energy transport and anderson-like localization in non-hermitian electrical transmission line. *Phys. Scr.* **95**(9), 095808 (2020)
- Tiaz, G., Shahaliyev, E., Ashiq, M.A., Ghafoor, F.: Multiple color electromagnetically induced switching using a five-level atomic medium. *J. Quantum Electron.* **55**, 1–10 (2019)

- Totsuka, K., Kobayashi, N., Tomita, M.: Slow light in coupled-resonator-induced transparency. *Phys. Rev. Lett.* **98**, 213904 (2007)
- Wang, H., Goorskey, D., Xiao, M.: Enhanced kerr nonlinearity via atomic coherence in a three-level atomic system. *Phys. Rev. Lett.* **87**, 0736601 (2001)
- Wang, Y., Xue, C., Zhang, Z., Zheng, H., Zhang, W., Yan, S.: Tunable optical analog to electromagnetically induced transparency in graphene-ring resonators system. *Sci. Rep.* **6**, 1 (2016)
- Wang, T., Hu, Y.-Q., Du, C.-G., Long, G.-L.: Multiple EIT and EIA in optical microresonators. *Opt. Express* **27**, 7344 (2019)

**Publisher's Note** Springer Nature remains neutral with regard to jurisdictional claims in published maps and institutional affiliations.

# Energy transport and Anderson-like localization in non-Hermitian electrical transmission line

Senghor Tagouegni<sup>1,2</sup> , Fernande Fotsa-Ngaffo<sup>2,3</sup>,  
Stéphane Boris Tabeu<sup>1,2,4</sup> and Aurélien Kenfack-Jiotsa<sup>2</sup>

<sup>1</sup>Laboratory of Mechanics, Materials and Structures, Department of Physics, Faculty of Science, University of Yaoundé I, P.O. Box 812, Yaounde, Cameroon

<sup>2</sup>Nonlinear Physics and Complex Systems Group, Department of Physics, The Higher Teachers' Training College, University of Yaoundé I, P.O. Box 47, Yaounde, Cameroon

<sup>3</sup>Institute of Wood Technologies, University of Yaounde I, P.O. Box 306, Mbalmayo, Cameroon

<sup>4</sup>Laboratory of Electronics and Signal Processing, Department of Electrical and Telecommunication Engineering, National Advanced School of Engineering, University of Yaoundé I—P.O. Box 8390, Yaoundé, Cameroon

E-mail: [stagouegni@yahoo.fr](mailto:stagouegni@yahoo.fr)

Received 7 June 2020, revised 24 July 2020

Accepted for publication 6 August 2020

Published 14 August 2020



CrossMark

## Abstract

We investigate on the right and left-handed (RH/LH) balanced gain and loss non-Hermitian electrical transmission lines (ETL) modeled using an imaginary resistor. The hamiltonian of each system is successfully derived in the framework of the tight-binding theory. We discuss the underlying symmetries and calculate the breaking thresholds of the Parity time (PT) and Anti PT (APT) symmetry phase transitions. Moreover, the modes dynamic characterization reveal the existence of critical points beyond which operation requires thresholdless transition and the eigen modes are either real or complex. We also present a self-consistent theory to investigate on their scattering properties. In particular, we demonstrate that the Anderson-like localized modes mostly emerge in the broken phase where eigen modes are complex with the localization length proportional to the cell numbers. Importantly, the mode localization is most likely to occur in structures consisting of a large cells number for RH ETL while LH ETL will confined modes even for infinitesimal small cell numbers. These results unveil embryonic applications in cryptography, switching and system control.

Keywords: Energy transport, Anderson-like localization, right/left handed, non-Hermitian, PT/APT symmetry, gain/loss

(Some figures may appear in colour only in the online journal)

## 1. Introduction

The notion of localization of a quantum particle was introduced by Anderson for about 50 years ago [1]. This phenomenon led insights on Metal Insulator Transition (MIT) [2, 3] and the transport properties of Hermitian systems [4, 5] in diverse fields of physics ranging from photonic lattices [4, 5] to transmission lines (TLs) [6–10]. Recently the study of localization has attracted significant interest in arbitrary dissipative media [11–13], including lattice

structures with spatially periodic modulated loss/gain [14–17]. Most canonical realizations has emerged in optoelectronics with highly applicability in switching behavior and stability [18] and nonreciprocal wave propagation [19]. Particularly, the PT-symmetric lattices exhibit breaking transition [20, 21] also known as Exceptional points (EPs) [22] separating the exact and the broken phase. These EPs have paved the way to the design of nano-integrated structures with novel functionalities such as unidirectional invisibility [23–25], single-mode PT lasers [26] and simultaneous coherent

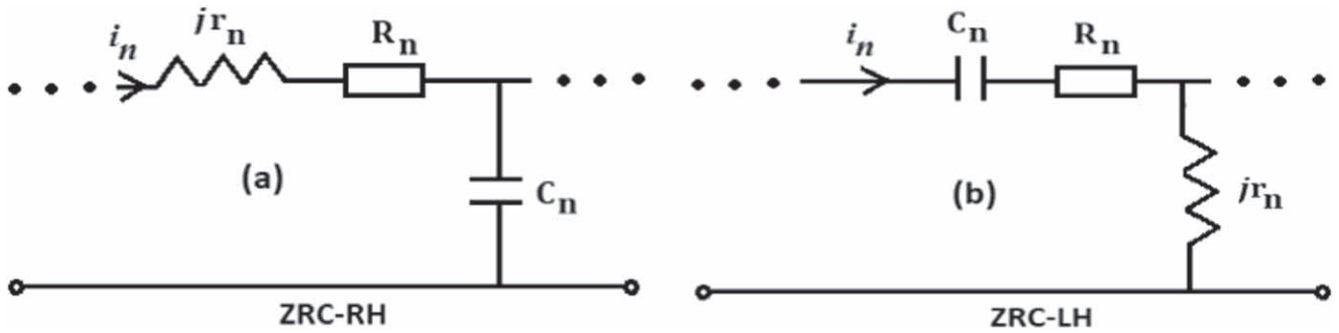


**Figure 1.** Unit cell of ZRC electrical transmission line. (a) Right handed (RH) model. (b) Left handed (LH) model. Each model exhibits under specific conditions (disclosed in tables 1 and 2) the PT and APT symmetries.

perfect-absorber lasing [27]. Another fundamental property of these non-Hermitian systems is the anti-parity time symmetry (APT) [28–33] where the spontaneous symmetry breaking results in a phase transition from the broken phase to the purely imaginary modal phase. These are the counter part of the PT-symmetry systems as their Hamiltonian is mapped to its opposite by the parity (P) and time reversal (T) operators,  $[H, PT]_{+} = 0$ . The APT symmetry systems have offered a variety of noteworthy effects where asymmetry mode transport is required such as energy difference-conserving dynamics [34], coherent asymmetry switch [35], bidirectional invisibility [36], a flat total transmission band [37] and a continuous lasing spectrum [28]. Moreover, they have demonstrated a high sensitivity of amplification and ultrafast all-optical control [29]. Periodic low-dimensional systems have shown sensitivity to periodicity-breaking disorder where the energy transport is limited to distances not exceeding the confinement length. On the other hands, due to the analogy of the TLs to quantum and classical systems, their dynamical equations can be mapped into the quantum tight-binding model such that studies of disordered electrical transmission lines (ETLs) have been proposed [6–10]. In complete accordance with the behavior of the quantum wave function of Fibonacci distribution, the ETL with long-range correlated disorder indicated the existence of extended states and mobility edges [38–40]. In a generalized Thue-Morse aperiodic sequence, ETLs demonstrate a transition from localized states to extended states [41, 42]. In addition for non-Hermitian ETL, the influence of the phase transitions on the localization properties of the electric current function have been demonstrated high sensitivity to the symmetry phase and broken region. However, the effect of the TL size as well as the additive electrical component such as imaginary resistor as a tool to fabricate non conservative gain/loss structures [43, 44] on the mode confinement remains unexplored. Much further the modes localization and the effect of the sharp transition occurring in APT symmetry system is still a matter of controversy. In this paper, we propose a one-dimensional (1D) ETL of finite size  $2N$  whose unit cell embedded an imaginary resistor. The impedance frequency independent of the imaginary resistor makes it a useful candidate for supplementing inductor whose frequency may induces instability in localizing mode. When the cells are limited to next neighbor interactions, we demonstrate that the dynamics

restricted sequential cell can be described by a 1D tight-binding Anderson model [1, 2]. The scattering properties are investigated in the self-consistent theory. Results demonstrate symmetry/asymmetry energy transport for even and odd modes for the corresponding PT/APT ETL. Remarkably, Anderson-like localized modes emerge in the broken PT/APT phase where eigen modes are complex with the localization length proportional to the cell numbers. Extended modes dominate the transport in the exact PT/APT phase. We also found that mode localization is most likely to occur in structures consisting of a large cells number for RH ETL while LH ETL will be confined modes even for infinitesimal small cell numbers. The results demonstrate potential applications in information encryption, optical switching and devices system control.

## 2. Models description

The systems considered here are the  $2N$  size discrete one dimensional (1D) ETLs, resulting in a cascade association of the ZRC unit cells for the Right handed (RH) and the Left handed (LH) configurations, as illustrated in figures 1(a) and (b), respectively. Each cell is made up of a linear capacitor  $C_n$ , a resistor  $R_n$  admitting only real values and an imaginary resistor  $Z$ , whose impedance is given by  $Z = jr_n$ ,  $n$  being the position of the cell. In the RH configuration, both the imaginary and the linear resistors are shunted by the capacitor. On contrary, in the LH configuration, the capacitor is in series with the real resistor shunted by the imaginary resistor. The singularity of the models is based on the use of an imaginary resistor which allow the cells to oscillate with a natural frequency  $\omega_n = 1/r_n c_n$ , where  $\omega_n$  can be positive or negative according to the signs of  $r_n$  and  $C_n$ . The practical implementation of the imaginary resistor has been recently proposed using gyrators [43, 45]. Another feature of our models is that the systems can support negative frequencies without altering its operating mode. In addition, the value of the linear resistance value  $R_n$  is associated to a dissipation (loss) if it is positive or to an amplification (gain) when it is negative. The negative resistance and capacitance can be implemented using the negative impedance converters built from simple linear amplifiers [46]. It is instructive to analyze the equations dynamic and symmetries of a pair of unit cells,  $n$  and  $(n + 1)$ ,

referred to as a dimer in other contexts [24, 43, 44] representing the smallest chain size. The equations can be derived using the Kirchhoff's laws from which, the electric currents,  $i_n(t)$  and  $i_{n+1}(t)$  of the  $n$ -th and  $(n+1)$ -th cells, respectively, can be described by the following first order differential equations:

**RH dimer:**

$$\begin{cases} (\beta_n + j) \frac{di_n}{dt} + a_1 \omega_n i_n - \omega_n i_{n+1} = 0, \\ (\beta_{n+1} + j) \frac{di_{n+1}}{dt} + a_2 \omega_{n+1} i_{n+1} - c_2 \omega_{n+1} i_n = 0, \end{cases} \quad (1)$$

**LH dimer:**

$$\begin{cases} j \frac{d}{dt} ((-b_1 + j\beta_n) i_n + i_{n+1}) = \omega_n i_n, \\ j \frac{d}{dt} ((-b_2 + j\beta_{n+1}) i_{n+1} + \alpha_2 i_n) = \omega_{n+1} i_{n+1}, \end{cases} \quad (2)$$

where  $j = \sqrt{-1}$ ,  $\beta_n = R_n/r_n$ ,  $\beta_{n+1} = R_{n+1}/r_{n+1}$ ,  $c_1 = C_n/C_{n-1}$ ,  $c_2 = C_{n+1}/C_n$ ,  $a_1 = 1 + c_1$ ,  $a_2 = 1 + c_2$ ,  $\alpha_1 = r_{n-1}/r_n$ ,  $\alpha_2 = r_n/r_{n+1}$ ,  $b_1 = 1 + \alpha_1$ ,  $b_2 = 1 + \alpha_2$ ,  $\omega_n = 1/r_n C_n$  and  $\omega_{n+1} = 1/r_{n+1} C_{n+1}$ .

Defining  $\psi = (i_n, i_{n+1})^T$ , and using few steps of algebra, equations (1) and (2) are successfully transformed into a Schrodinger-like equation, where we have introduced an effective Hamiltonian  $H_{eff}$  as follow:

$$j \frac{d\psi}{dt} = H_{eff}^{RH/LH} \psi, \quad (3)$$

where

$$H_{eff}^{RH} = \begin{pmatrix} \frac{-(j\beta_n + 1)a_1\omega_n}{\Delta_1} & \frac{(j\beta_n + 1)\omega_n}{\Delta_1} \\ \frac{(j\beta_{n+1} + 1)c_2\omega_{n+1}}{\Delta_2} & \frac{-(j\beta_{n+1} + 1)a_2\omega_{n+1}}{\Delta_2} \end{pmatrix}, \quad (4)$$

$$H_{eff}^{LH} = \frac{1}{\Delta_3} \begin{pmatrix} (-b_2 + j\beta_{n+1})\omega_n & -\omega_{n+1} \\ -\alpha_2\omega_n & (-b_1 + j\beta_n)\omega_{n+1} \end{pmatrix}, \quad (5)$$

with

$$\Delta_1 = 1 + \beta_n^2, \quad \Delta_2 = 1 + \beta_{n+1}^2, \quad \Delta_3 = (-b_1 + j\beta_n)(-b_2 + j\beta_{n+1}) - \alpha_2.$$

Applying the Parity-time symmetry operator,  $\mathbf{PT} = \sigma_x K$ , where  $\sigma_x$  is the first Pauli matrix and  $K$  is the complex conjugation operation, we can demonstrate that these hamiltonians commute with the join  $\mathbf{PT}$  operator i.e  $[H_{eff}^{RH/LH}, \mathbf{PT}] = 0$ , if the following conditions are fulfilled:

**RH dimer:**

$$c_1 = c_2 = 1, \quad \omega_n = \omega_{n+1}, \quad \beta_n = -\beta_{n+1}, \quad (6)$$

**LH dimer:**

$$\alpha_1 = \alpha_2 = 1, \quad \omega_n = \omega_{n+1}, \quad \beta_n = -\beta_{n+1}. \quad (7)$$

By the same token, it can be also demonstrated that these Hamiltonians anti-commute with the  $\mathbf{PT}$  operator i.e  $[H_{eff}^{RH/LH}, \mathbf{PT}]_+ = 0$ , when the conditions below are fulfilled:

**RH dimer:**

$$c_1 = c_2 = 1, \quad \omega_n = -\omega_{n+1}, \quad \beta_n = -\beta_{n+1}, \quad (8)$$

**LH dimer:**

$$\alpha_1 = \alpha_2 = 1, \quad \omega_n = -\omega_{n+1}, \quad \beta_n = -\beta_{n+1}. \quad (9)$$

Based on these findings, we can as well demonstrate the  $PT$  or

**Table 1.** RH ETL characteristics.

configuration	$PT^{RH}$	$APT^{RH}$
site $n$	odd   even	odd   even
$C_n$	$C   C$	$C   C$
$r_n$	$r   r$	$-r   r$
$R$	$-R   R$	$R   R$
$\beta_n$	$-\beta   \beta$	$-\beta   \beta$
$\omega_n$	$\omega_0   \omega_0$	$-\omega_0   \omega_0$

**Table 2.** LH ETL characteristics.

configuration	$PT^{LH}$	$APT^{LH}$
site $n$	odd   even	odd   even
$r_n$	$r   r$	$r   r$
$C_n$	$C   C$	$-C   C$
$R_n$	$-R   R$	$-R   R$
$\beta_n$	$-\beta   \beta$	$-\beta   \beta$
$\omega_n$	$\omega_0   \omega_0$	$-\omega_0   \omega_0$

$APT$  symmetry behaviors of a bigger chain. To do so, let's consider a chain of  $2N$  size. The electric currents in any three successive cells  $(n-1)$ ,  $n$  and  $(n+1)$  obey to:

$$(RH): (\beta_n + j) \frac{di_n}{dt} - \omega_n (c_1 i_{n-1} - a_1 i_n + i_{n+1}) = 0, \quad (10)$$

$$(LH): j \frac{d}{dt} (\alpha_1 i_{n-1} + (-b_1 + j\beta_n) i_n + i_{n+1}) - \omega_n i_n = 0, \quad (11)$$

where  $1 \leq n \leq 2N$ ,  $j = \sqrt{-1}$ ,  $\beta_n = R_n/r_n$ ,  $c_1 = C_n/C_{n-1}$ ,  $a_1 = 1 + c_1$ ,  $\alpha_1 = r_{n-1}/r_n$ ,  $b_1 = 1 + \alpha_1$  and  $\omega_n = 1/r_n C_n$ .

By applying the following transformation for the parity operator  $\mathbf{P}$ :  $n \leftrightarrow 2N - n + 1$  and for the time reversal operator  $\mathbf{T}$ :  $t \rightarrow -t$ ;  $j \rightarrow -j$ , in the equations (10) and (11) the systems become  $PT$  and  $APT$ - symmetric, respectively, under the conditions (6-7) and (8-9). The  $PT$  and  $APT$  necessary conditions are summarized in tables 1 and 2.

In what follow, we investigate on the electric current intensity dynamic and the vibration frequency on each site. The capacitances and resistances in each cell are considered constants and positive ( $C > 0$ ,  $r > 0$ ,  $R > 0$ ). In addition, the gain/loss parameter,  $\beta = R/r$  and the reference frequency,  $\omega_0 = 1/rC$  are also restricted to positive values.

Applying the zero boundary conditions in both ETLs on sites  $n = 0$  and  $n = 2N + 1$ , respectively, lead to:

$$i_{(n=0)} = i_{(n=2N+1)} = 0. \quad (12)$$

Looking for stationary modes  $i_n(t) = e^{j\omega t} I_n$ , where  $I_n$  is the complex amplitude of the electric current circulating in the cell  $n$  and  $\omega$  the vibration frequency of the  $n$  site, the complex amplitude dynamic is derived as:

$$(RH): \alpha_n I_n - c_1 I_{n-1} - I_{n+1} = 0, \quad (13)$$

$$(LH): \varepsilon_n I_n - \alpha_1 I_{n-1} - I_{n+1} = 0, \quad (14)$$

where

$$\alpha_n = a_1 + \omega(j\beta_n - 1)/\omega_n,$$

$$\varepsilon_n = b_1 - j\beta_n - (\omega/\omega_n)^{-1}, \quad a_1 = 1 + c_1, \quad b_1 = 1 + \alpha_1, \\ c_1 = C_n/C_{n-1} \text{ and } \alpha_1 = r_{n-1}/r_n.$$

The damping coefficient  $\beta_n = R_n/r_n$  refers to the loss (if  $\beta_n = \beta > 0$ ) or gain (if  $\beta_n = -\beta < 0$ ) and  $\omega_n = \pm\omega_0$  is the natural frequency of the  $n$  site.

The general solutions for  $I_n$  can be found in the form [47, 48]:

$$I_n = \begin{cases} \rho(ae^{ink} + be^{-ink}), & \text{for } n \text{ odd,} \\ ae^{ink} + be^{-ink}, & \text{for } n \text{ even,} \end{cases} \quad (15)$$

where  $a$ ,  $b$  and  $\rho$  are constants and  $k$  is the wave number.

Taking into account the boundary conditions, the above solutions allow to obtain the discrete values for the wave number  $k$  as:

$$k_p = \frac{p\pi}{2N+1}, \quad (16)$$

where  $p = 1 \dots N$ .

### 3. Modes dynamic

#### 3.1. PT-symmetric configuration

We assume both ETL models in PT configuration (see tables 1 and 2 for details). For conciseness, by replacing equation (15) into equations (13) and (14) it turns out that:

$$\text{(RH): } \begin{cases} 2 - (1 + j\beta)\Omega = \frac{2}{\rho} \cos(k), & \text{for } n \text{ odd,} \\ 2 - (1 - j\beta)\Omega = 2\rho \cos(k), & \text{for } n \text{ even,} \end{cases} \quad (17)$$

$$\text{(LH): } \begin{cases} 1 - (2 + j\beta)\Omega = -\frac{2}{\rho} \Omega \cos(k), & \text{for } n \text{ odd,} \\ 1 - (2 - j\beta)\Omega = -2\Omega\rho \cos(k), & \text{for } n \text{ even,} \end{cases} \quad (18)$$

where  $\Omega = \omega/\omega_0$ .

Combining equations (17) and (18) lead to the normalized eigenfrequencies  $\Omega_{\pm}^{RH}(\beta, k_p)$  and  $\Omega_{\pm}^{LH}(\beta, k_p)$  describing the normalized modes frequencies of the RH and LH ETLs, respectively.

$$\Omega_{\pm}^{RH}(\beta, k_p) = \frac{2}{\Delta} (1 \pm \sin(k_p) \sqrt{(\beta_{cr}^{RH})^2 - \beta^2}), \quad (19)$$

$$\Omega_{\pm}^{LH}(\beta, k_p) = \frac{2}{\Delta'} (1 \pm \sqrt{(\beta_{cr}^{LH})^2 - \beta^2}), \quad (20)$$

where  $\Delta = \beta^2 + 1$ ,  $\Delta' = \beta^2 + 4\sin^2(k_p)$ ,  $\beta_{cr}^{RH} = 1/\tan(k_p)$  and  $\beta_{cr}^{LH} = 2\cos(k_p)$ .

In the expression of  $\Omega_{\pm}^{RH}(\beta, k_p)$  (resp.  $\Omega_{\pm}^{LH}(\beta, k_p)$ ), one easily identifies the square root singularity  $\Omega \propto \sqrt{(\beta_{cr})^2 - \beta^2}$ , a characteristic of the PT-symmetric modes expansion [24].  $\beta_{cr}$  is the threshold value of  $\beta$  at which the PT symmetric breaking occurs. Consequently, for  $\beta < \beta_{cr}$ , the system is in the PT symmetry phase with real frequencies and for  $\beta > \beta_{cr}$ , the system is in the broken symmetry phase with complex frequencies. At the transition point also called exceptional point (EP) [22], there is a coalescence of the eigenfrequencies. For our system, the gain/loss parameter depends on the wave number  $k_p$ ,  $\beta_{cr} = \beta_{cr}(k_p)$ ,

and we can evaluate that:

$$\beta_{cr}^{RH} = 1/\tan(k_p) \text{ and } \beta_{cr}^{LH} = 2\cos(k_p) \quad (21)$$

The PT-symmetric phase exists for real frequencies, and this condition is fulfilled for the values of the wave numbers  $k_1 < k_p < k_N$ , corresponding to the critical transitions domain defined by  $\beta_{cr1} < \beta_{cr} < \beta_{cr2}$ . The two limiting values  $\beta_{cr1}$  and  $\beta_{cr2}$  for the RH and LH configurations are given by equation (21) for  $k_p = k_N$  and  $k_p = k_1$ , respectively. In other words, for  $\beta < \beta_{cr1}^{RH} = 1/\tan(k_N)$  (resp.  $\beta < \beta_{cr1}^{LH} = 2\cos(k_N)$ ), the eigenspectrum is entire real. When  $\beta > \beta_{cr2}^{RH} = 1/\tan(k_1)$  (resp.  $\beta > \beta_{cr2}^{LH} = 2\cos(k_1)$ ), the eigenspectrum is totally complex. For values of  $\beta_{cr}$  in the range  $\beta_{cr1}^{RH} < \beta_{cr} < \beta_{cr2}^{RH}$  (resp.  $\beta_{cr1}^{LH} < \beta_{cr} < \beta_{cr2}^{LH}$ ), the spectrum displays two domains, one of which the frequencies are totally real and the other where they are complex, both domains being separated by a critical wave number  $k_{cr}^{RH} = \tan^{-1}(1/\beta_{cr}^{RH})$  (resp.  $k_{cr}^{LH} = \cos^{-1}(\beta_{cr}^{LH}/2)$ ).

In figure 2, the real (first column) and the imaginary (second column) parts of normal modes frequencies  $\Omega_{\pm}^{RH(LH)}(\beta, k_p)$  and the threshold values  $\beta_{cr}^{RH(LH)}$  (white curves) are reported as a function of the wave number  $k_p$  for both ETLs in the  $PT^{RH}$  and  $PT^{LH}$  configurations respectively. The ETLs size is set to  $N = 25$  throughout this paper, unless otherwise specified. When the system is in the  $PT^{RH}$  configuration (subplots (a) and (b)),  $\beta_{cr1}^{RH} = 0.03$  and  $\beta_{cr2}^{RH} = 16.2$ . For  $\beta < \beta_{cr1}^{RH}$ , as illustrated by the insets (i) and (ii), the spectrum is entirely real since the imaginary part  $Im(\Omega_{\pm}^{RH}) = 0$ . The value  $\beta = 0.01$  used in figure 3(a) agrees well this observation. On the contrary, for the values of  $\beta$  taken between 0.03 and 16.2, the plot in figure 3(b),  $\beta = 1$ , displays two domains: the first region where  $\Omega_{\pm}^{RH}$  is real and the second region where it is complex. The separation between the two regions occurs at  $k_{cr}^{RH} = \pi/4$ . The case  $\beta = 20$ , corresponds to the broken phase (see figure 3(c)). For the system in  $PT^{LH}$  configuration, the boundary threshold values are found to be  $\beta_{cr1}^{LH} = 0.06$  and  $\beta_{cr2}^{LH} = 2$ . As shown in figures 3(d) for  $\beta = 0.01$ , the frequencies are real, when it is increased to 1, figure 3(e) exhibits adomain where the frequencies are totally real and another one where they are complex. For the case  $\beta = 3$  in figure 3(f), all frequencies are totally complex.

#### 3.2. APT-symmetric configuration

Applying now the APT criteria to equations (13) and (14) the wave number can be analyzed from the following systems:

$$\text{(RH): } \begin{cases} 2 + (1 + j\beta)\Omega = \frac{2}{\rho} \cos(k), & \text{for } n \text{ odd,} \\ 2 - (1 - j\beta)\Omega = 2\rho \cos(k), & \text{for } n \text{ even,} \end{cases} \quad (22)$$

$$\text{(LH): } \begin{cases} 1 + \Omega(2 + j\beta) = \frac{2}{\rho} \Omega \cos(k), & \text{for } n \text{ odd,} \\ 2 - (2 - j\beta)\Omega = -2\Omega\rho \cos(k), & \text{for } n \text{ even.} \end{cases} \quad (23)$$

Combining these equations and taking into account the discrete relation (16), the normal modes frequencies  $\Omega_{\pm}^{RH}(\beta, k_p)$  and  $\Omega_{\pm}^{LH}(\beta, k_p)$  are obtained as:



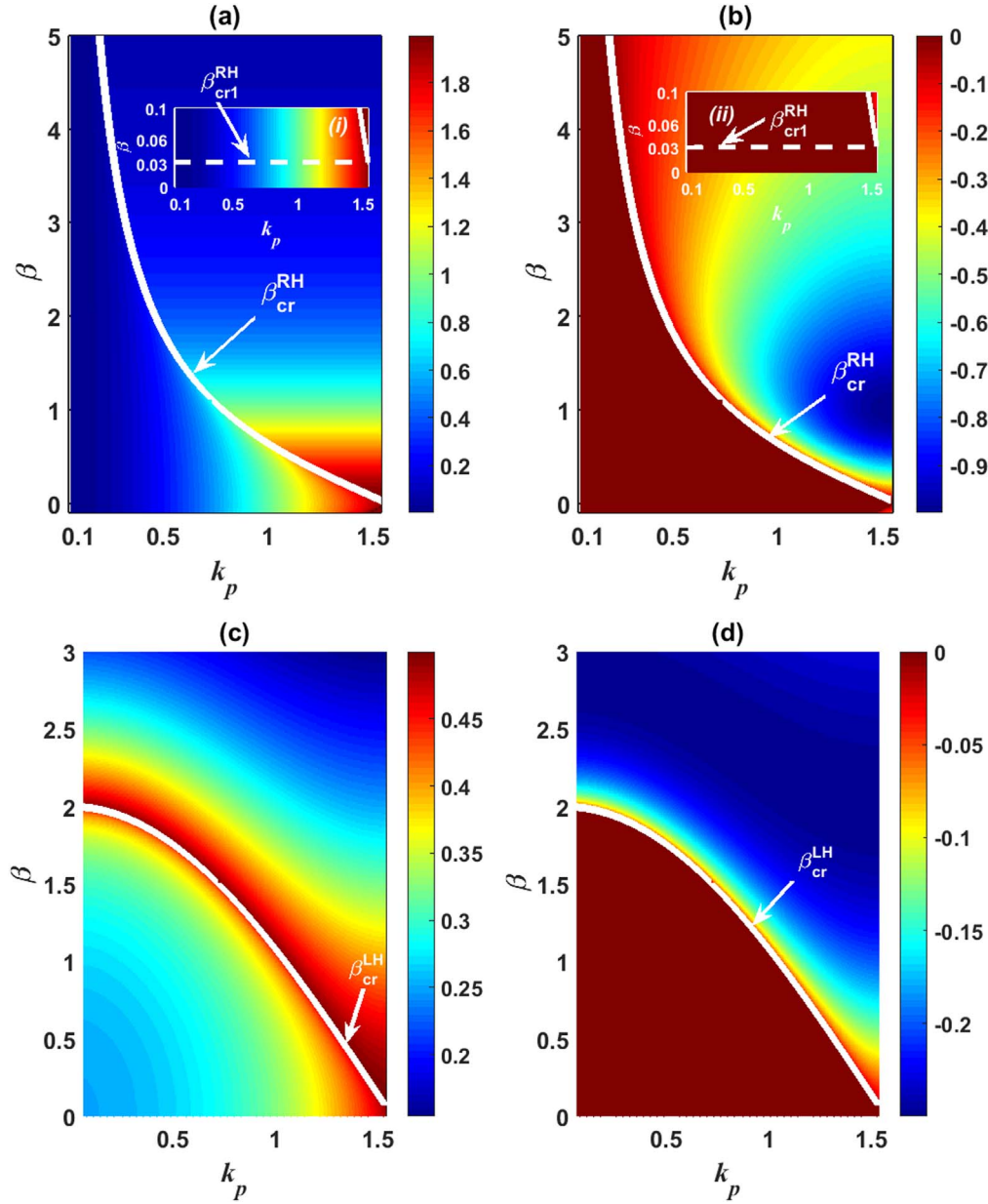


**Figure 2.** 3D top view ETLs normalized frequencies spectra  $\Omega_{\pm}$  as function of  $k_p$  and  $\beta$ . The 1st column for the real parts and the 2nd column for the imaginary parts, of (a), (b): the  $PT^{RH}$  and (c), (d): the  $PT^{LH}$ .  $\beta_{cr1} < \beta_{cr} < \beta_{cr2}$  is the transition range values separating the real and the complex modes. Beyond this range the modes are thresholdless. The insets (i) and (ii) highlight the domain situated before  $\beta_{cr1}$ .

$$\Omega_{\pm}^{RH}(\beta, k_p) = \frac{2}{\Delta}(j\beta \pm \cos(k_p)\sqrt{(\beta_{cr}^{RH})^2 - \beta^2}), \quad (24)$$

$$\Omega_{\pm}^{LH}(\beta, k_p) = \frac{1}{\Delta'}(j\beta \pm \cos(k_p)), \quad (25)$$

with  $\beta_{cr}^{RH} = \tan(k_p)$ ,  $\Delta = \beta^2 + 1$  and  $\Delta' = \beta^2 + 4 \sin^2(k_p)$ .

The analysis of the  $APT^{RH}$  eigenmodes (equation (24)) also reveals a square-root singularity  $\Omega \propto \sqrt{(\beta_{cr}^{RH})^2 - \beta^2}$ , a fingerprint of non hermitian APT-symmetric systems. The atypical APT symmetric breaking occurs at  $\beta = \beta_{cr}^{RH} = \tan(k_p)$  for any value of  $p$ . Since this expression depends on the wave number, two critical points  $\beta_{cr1}^{RH} = \tan(k_1)$  and  $\beta_{cr2}^{RH} = \tan(k_N)$  are evinced to bind the region of the gain/loss parameter where the frequencies of the system result in a thresholdless operation regime. Thus, when

$\beta < \beta_{cr1}^{RH}$ , the eigenspectrum is characterized by complex frequencies (see the inset (i) and (ii)), while for  $\beta > \beta_{cr2}^{RH}$ , the entire eigen spectrum become purely imaginary. As  $\beta$  moves in the range  $[\beta_{cr1}^{RH}, \beta_{cr2}^{RH}]$ , we can distinguish a region below  $k_{cr} = \tan^{-1}(\beta_{cr}^{RH})$  where the frequencies are purely imaginary and a region above where system is complex.

Unlike the case of the  $APT^{RH}$ , a quick analysis of equation (25) reveals that the  $APT^{LH}$  is unbreakable. We have plotted in figure 4, the real (first column) and the imaginary (second column) parts of the normalized eigenfrequencies of both ETLs in the APT configuration. We obtained the threshold values  $\beta_{cr1}^{RH} = 0.061$  and  $\beta_{cr2}^{RH} = 32.5$ . The plots are consistent with the analysis made above. Furthermore, for  $\beta = 0.01$  (figure 5(a)), the system is in the broken phase even

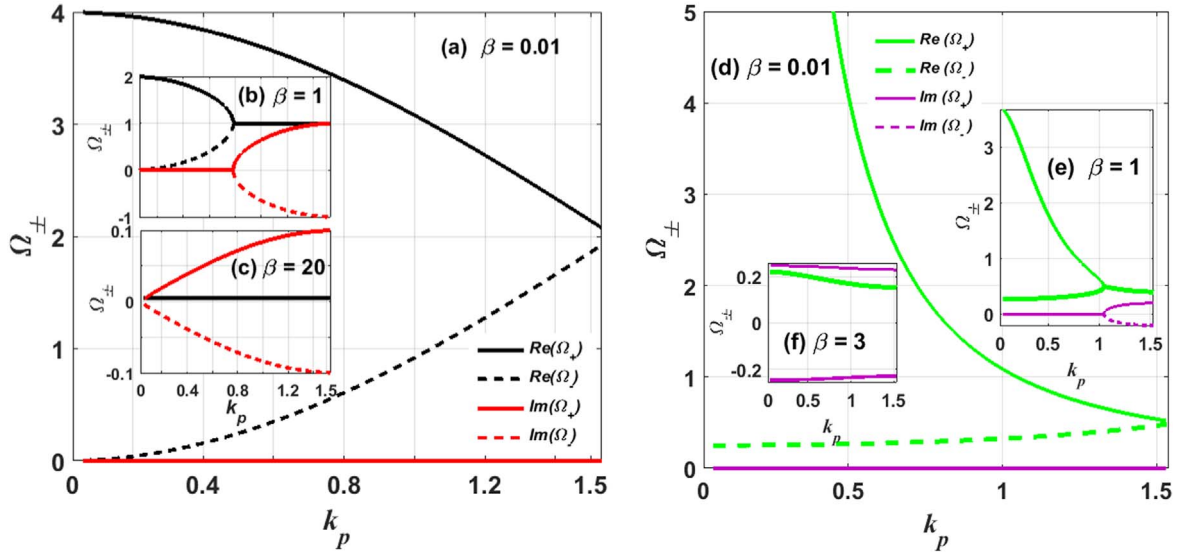


**Figure 3.** The real and the imaginary parts of the eigenvalues  $\Omega_{\pm}$  as function of the wave number  $k_p$  for several values of the gain/loss  $\beta$  in different PT-symmetric configurations. (a)–(c): in  $PT^{RH}$ , and (d)–(f): in  $PT^{LH}$ . The values of  $\beta$  used correspond to the domains illustrated in figure 2. (a), (d):  $\beta = 0.01 < \beta_{cr1}^{RH(LH)}$ ; (b), (e):  $\beta_{cr1}^{RH(LH)} < \beta = 1 < \beta_{cr2}^{RH(LH)}$ ; (c):  $\beta = 20 > \beta_{cr2}^{RH}$ ; (f):  $\beta = 3 > \beta_{cr2}^{LH}$ .

when the imaginary part of the frequencies is closed to, but remains non zero. The value  $\beta = 1$  chosen in the range  $\beta_{cr1}^{RH} < \beta < \beta_{cr2}^{RH}$  (figure 5(b)) allows to obtain  $k_{cr}^{RH} = \pi/4$ , below which all the frequencies are imaginary and complex above. Here, as  $\beta$  grows toward  $\beta_{cr2}^{RH}$ ,  $k_{cr}^{RH} \approx k_N$  and the imaginary phase dominates. However, when  $\beta$  tends to  $\beta_{cr1}^{RH}$ ,  $k_{cr}^{RH} \approx k_1$ , the broken phase becomes larger. Finally, when  $\beta = 35$  (see figure 5(c)), all frequencies are purely imaginary. We have also illustrated in figure 5(d) the normal mode frequencies for the  $APT^{LH}$  when taking  $\beta = 1$ . It emerges from the plot that the system remains in the broken phase whatever the value of the wave number considered. There, the real part of the frequencies are symmetrical to zero whereas imaginary parts are degenerated for any  $k_p$ .

#### 4. Transport properties

In this section, we investigate on the exact solutions of the electric current flowing on the  $n$  site through each ETL. For this purpose, we recall equation (15), and using the boundary conditions (see equation (12)), the electric current  $I_n(k_p)$  can be rewritten for the two ETLs as:

$$I_n(k_p) = \begin{cases} 2a\rho \sin(nk_p), & \text{for } n \text{ odd,} \\ 2a \sin(nk_p), & \text{for } n \text{ even,} \end{cases} \quad (26)$$

where the constant  $a$  is obtained from the normalized condition, namely  $\sum_{n=1}^{2N} |I_n|^2 = 1$  as  $|a| = 1/(2\sqrt{S_n})$ , with  $S_n$  expressed as:

$$S_n = \sum_{n=1}^N (\sin^2(2nk_p) + |\rho|^2 \sin^2((2n-1)k_p)). \quad (27)$$

#### 4.1. PT-symmetric configuration

It is interesting to introduce in equations (17) and (18) a new variable  $\vartheta$  to determine the parameter  $\rho$  as  $\rho = e^{j\vartheta}$ , where

$$(RH): \vartheta = \tan^{-1}(\beta\Omega_{\pm}^{RH}(\beta, k_p)/(2 - \Omega_{\pm}^{RH}(\beta, k_p))), \quad (28)$$

$$(LH): \vartheta = \tan^{-1}(\beta\Omega_{\pm}^{LH}(\beta, k_p)/(1 - 2\Omega_{\pm}^{LH}(\beta, k_p))). \quad (29)$$

We have illustrated in two ways the modulus square  $|I_n(\beta, \Omega)|^2$  of the electric current which is proportional to the light power and then to the energy in the ETL, as a function of  $n$  for different values of  $p$ . First, we have considered  $\Omega_{\pm}$  as a function of  $\beta$  and we have shown the 3D top view (see figures 6(a) and (b)),  $|I_n(\beta, \Omega)|^2$  as function of  $n$  and  $\beta$  for different values of  $p$ . In the second case, the value of  $\Omega_{\pm}$  is calculated for a fixed value of  $\beta$  and is used to plot  $|I_n|^2$  as a function of  $n$  as illustrated in figures 6(c), (d) and (e). In the 3D top view, the plot of  $|I_n|^2$  clearly highlights two distinct behavioral regimes which are separated by the critical PT breaking point  $\beta_{cr}^{LH}$ . The values of  $p$  used and the corresponding thresholds are indicated in the plots. We note that, in the regime below the breaking point (PT-symmetric phase) where the frequencies  $\Omega = \Omega_{\pm}^{LH}$  are real, the distribution of  $|I_n|^2$  is symmetrical for the frequencies  $\Omega = \Omega_{+}^{LH}$  (column (a)) and  $\Omega = \Omega_{-}^{LH}$  (column (b)) while it is asymmetric in the regime above the transition point where the frequencies are complex. The plots of figures 6(c) to (e) agree well with the analysis made on the previous figures 6(a) and (b). Indeed, for the value  $\beta = 0.01 < \beta_{cr1}^{LH}$ , and whether for  $p = 5; 20; 25$ , the current modulus square  $|I_n|^2$  is symmetric. However, when  $\beta$  is increased to  $\beta = 2.5 > \beta_{cr2}^{LH}$ ,  $|I_n|^2$  becomes asymmetric. The results obtained with frequencies  $\Omega = \Omega_{\pm}^{LH}$  are represented in solid and dashed, respectively. The observations made here are qualitatively valid for the case of  $PT^{RH}$ .

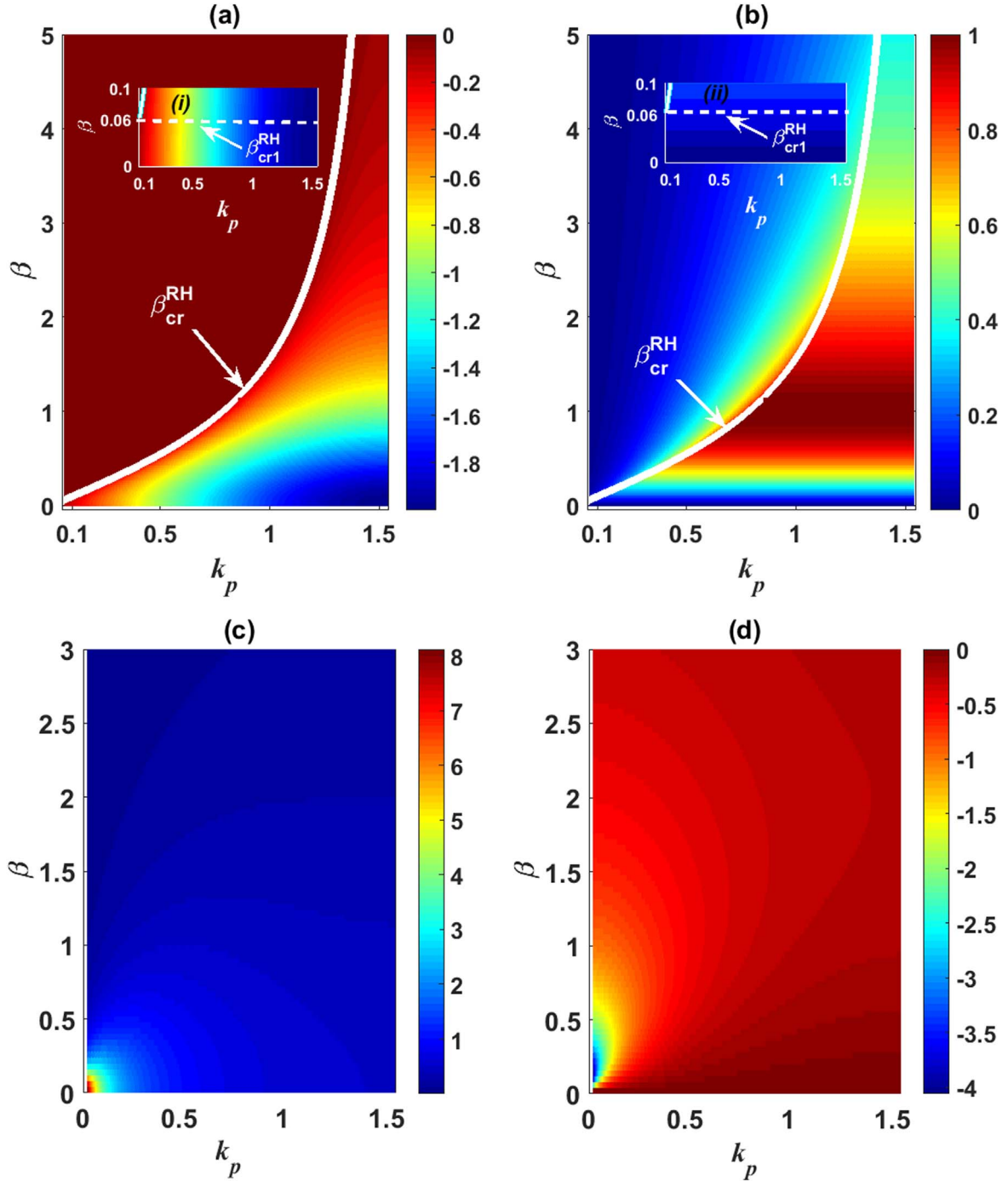


**Figure 4.** 3D top view ETLs normalized frequencies spectra  $\Omega_{\pm}$  as function of  $k_p$  and  $\beta$ . The 1st column for the real parts and the 2nd column for the imaginary parts, of (a), (b): the  $APT^{RH}$ . The threshold  $\beta_{cr}$  separates the complex and the purely imaginary mode regions. (c), (d): the  $APT^{LH}$ , where the system is unbreakable.

#### 4.2. APT-symmetric Configuration

Combining equations (22) and (23) the constant  $\rho$  can be determined for each model as:

$$(RH): \rho^2 = (2 + \Omega(j\beta - 1)) / (2 + \Omega(j\beta + 1)), \quad (30)$$

$$(LH): \rho^2 = (-1 + (2 - j\beta)\Omega) / (1 + (2 + j\beta)\Omega). \quad (31)$$

These expressions are used in the calculation of the complex amplitude of the current. In figure 7, we have plotted the 3D (top view) of the  $|I_n(\beta, \Omega)|^2$  in the  $APT^{RH}$  configuration, in (a)

for  $\Omega_+^{RH}$  and in (b) for  $\Omega_-^{RH}$ . This figure exhibits two domains for the energy transport: the APT broken phase where the energy is asymmetric, and the exact phase where the energy distribution is symmetric. This energy distribution is sensitive to the chain size. In figures 7(c), (d) and (e), the 2D plots of the energy are illustrated for  $\beta = 0.01 < \beta_{cr1}^{RH}$  (first row) and for  $\beta = 35 > \beta_{cr2}^{RH}$  (second row), for different cell sizes as indicated. In the  $APT^{RH}$  broken phase, the energy is asymmetric and in the  $APT^{RH}$  exact phase, the energy distribution is symmetric.

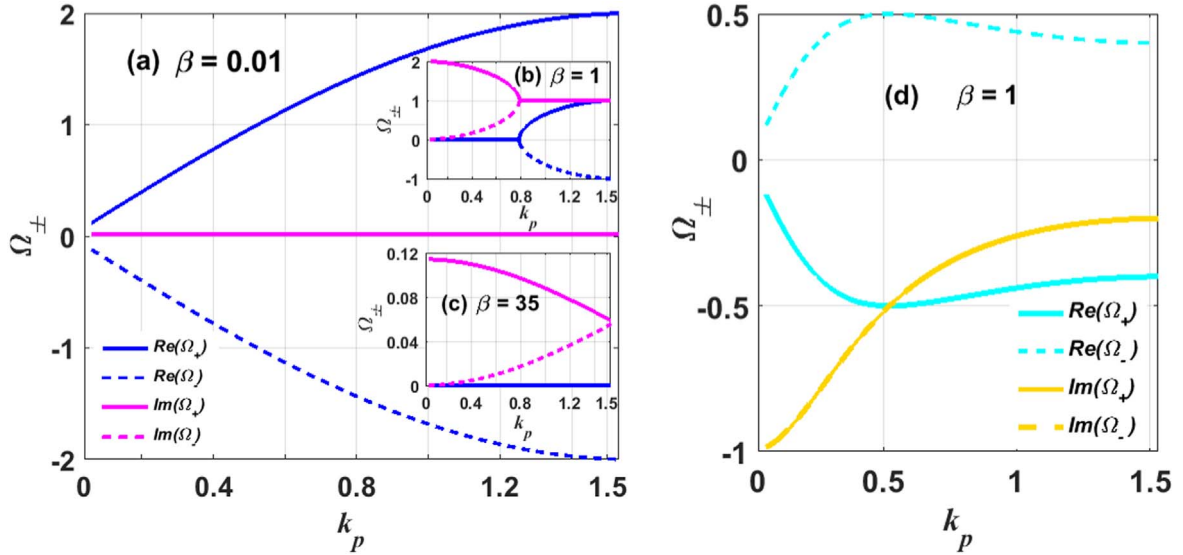


**Figure 5.** The real and the imaginary parts of the eigenvalues  $\Omega_{\pm}$  as function of the wave number  $k_p$  for different values of the gain/loss  $\beta$  in APT configuration (a)–(c): in  $PT^{RH}$  and (d): in  $PT^{LH}$ . The values of  $\beta$  used corresponds to the domains evoked in figure 4: (a)  $\beta = 0.01 < \beta_{cr1}^{RH}$ , (b)  $\beta_{cr1}^{RH} < \beta = 1 < \beta_{cr2}^{RH}$ , (c)  $\beta = 35 > \beta_{cr2}^{RH}$ , (d)  $\beta = 1$ .

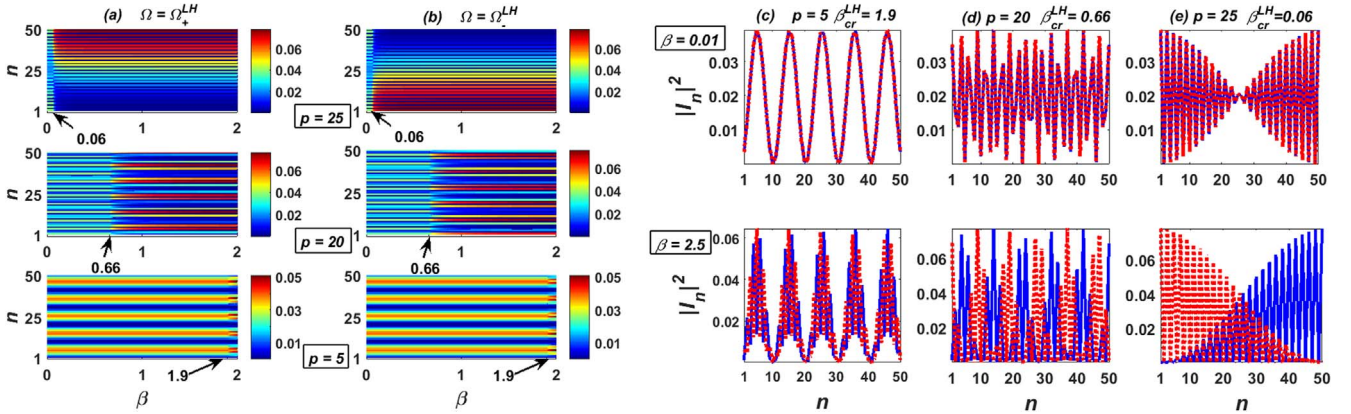


**Figure 6.** The modulus square  $|I_n(\beta, \Omega)|^2$  of the electric current in the  $PT^{LH}$  configuration. Columns (a) and (b): 3D top view for several values of  $p$  as a function of  $\beta$  and  $n$ . Columns (c)–(e): 2D plot as function of  $n$  for different values of  $p$ ,  $\beta = 0.01$  in the 1st row and  $\beta = 2.5$  in the 2nd row. We note a symmetric energy transport of the  $PT^{LH}$  exact phase whereas energy transport is asymmetrical in the  $PT^{LH}$  broken phase.

Remarkably, for the  $APT^{LH}$  configuration, the energy distribution becomes symmetric at higher values of  $\beta$  despite be in the complex regime (see figure 8).

## 5. Anderson-like localization

The systems discuss here can be used to describe a 1D tight-binding Anderson model such as:

$$(E - \varepsilon_j)\phi_j - \phi_{j-1} - \phi_{j+1} = 0, \quad (32)$$

where  $E$  is the eigenenergy and  $\varepsilon_j$  is the on-site energy. This correspondence between the tight-binding equation (32), and equations (13) and (14) for electrical circuit can be used to test the quantum effects of the Anderson localization. There are several tools used to study the localization behavior of quantum systems, namely, the normalized localization length  $\Lambda(\omega)$ , the participation number  $D(\omega)$ , the inverse participation

ratio  $IPR(\omega)$ , the global density of states  $DOS(\omega)$ , the Rényi entropies  $R_q(\omega)$ , just to name but a few, [6–10, 14, 38–41]. In the electrical circuit's scheme, these tools are defined as a function of the normalized electric current amplitude. Singularly, for fixed value of the frequency  $\omega$  and a system size  $M = 2N$ , the localization property is expressed using the normalized localization length  $\Lambda(\beta, \omega)$  defined as:

$$\Lambda(\beta, \omega) = (M\lambda(\beta, \omega))^{-1}, \quad (33)$$

where  $\lambda(\beta, \omega)$  is the Lyapunov exponent expressed as:

$$\lambda(\beta, \omega) = \lim_{M \rightarrow \infty} \frac{1}{M} \sum_{n=1}^M \ln \left| \frac{I_{n+1}}{I_n} \right|. \quad (34)$$

$I_n$  and  $I_{n+1}$  represent the current circulating in the cells at position  $n$  and  $(n + 1)$  respectively. Thus, the following criteria are used to differentiate between the localized and the extended modes transport of the electric current through the

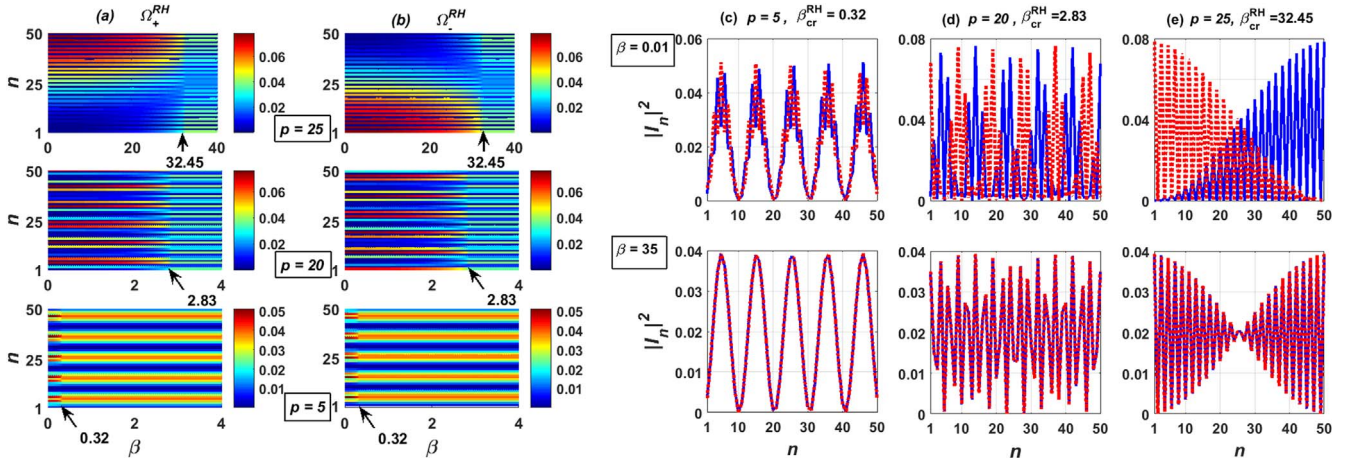


**Figure 7.** The modulus square  $|I_n(\beta, \Omega)|^2$  of the electric current in the  $APT^{RH}$  configuration. Columns (a) and (b): 3D top view for several values of  $p$  as a function of  $\beta$  and  $n$ . Columns (c)–(e): 2D plot as function of  $n$  for different values of  $p$ ,  $\beta = 0.01$  in the 1st row and  $\beta = 35$  in the 2nd row. We note an asymmetric energy transport of the  $APT^{RH}$  broken phase whereas energy transport is symmetric in the  $APT^{RH}$  exact phase.

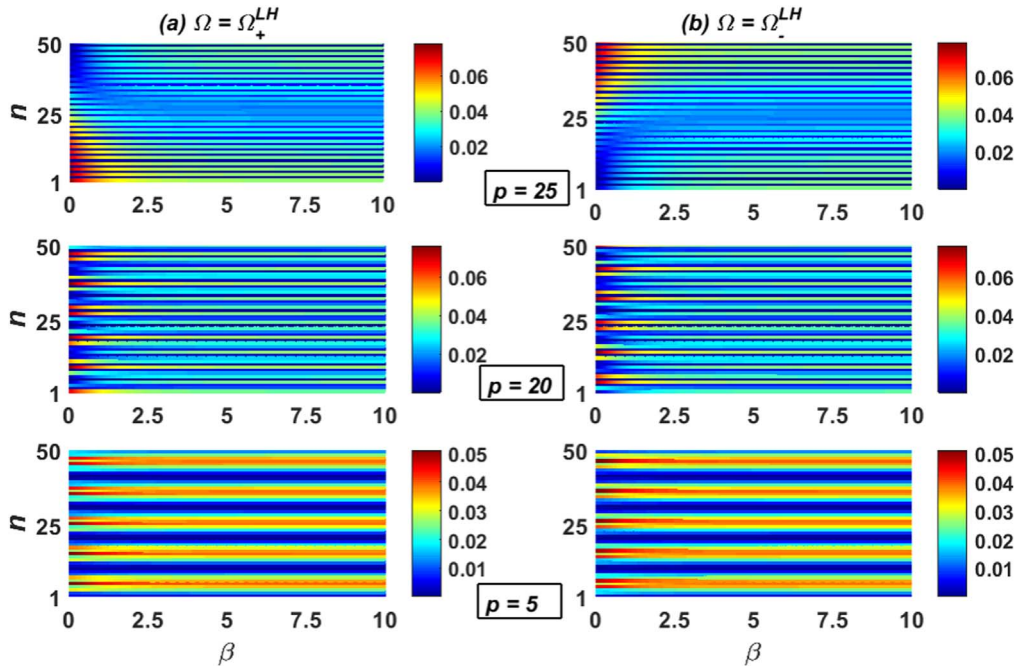


**Figure 8.** 3D (top view) representation of  $|I_n(\beta, \Omega)|^2$  for different values of  $p$  as function of  $\beta$  and  $n$  when  $\Omega_{\pm}^{LH}$  is a function of  $\beta$  for the ETL in  $APT^{LH}$ . In column (a):  $\Omega = \Omega_{+}^{LH}$  and in column (b):  $\Omega = \Omega_{-}^{LH}$ . In all plots, we are situated in the broken phase since the system is unbreakable and we note an asymmetry transport of energy for small values  $\beta$ , even if it becomes almost symmetry for higher values of  $\beta$ .

lines: if  $\lambda(\beta, \omega) \leq 1/M$  (i.e  $\Lambda(\beta, \omega) \geq 1$ ), the electric current  $I_n$  is an extended function, and if  $\lambda(\beta, \omega) > 1/M$  (i.e  $\Lambda(\beta, \omega) < 1$ ),  $I_n$  is the localized function. So, we introduce the recurrence relation:

$$\gamma_n = \frac{I_{n+1}}{I_n}. \quad (35)$$

Such that, equation (34) becomes:

$$\lambda(\beta, \omega) = \lim_{M \rightarrow \infty} \frac{1}{M} \sum_{n=1}^M \ln |\gamma_n|. \quad (36)$$

The above equation (35) can be obtained for each model as:

$$(RH): \gamma_n = \alpha_n - (\gamma_{n-1})^{-1}, \quad (37)$$

$$(LH): \gamma_n = \varepsilon_n - (\gamma_{n-1})^{-1}, \quad (38)$$

where  $\alpha_n = 2 + \omega(j\beta_n - 1)/\omega_n$  and  $\varepsilon_n = 2 - j\beta_n - (\omega/\omega_n)^{-1}$ .

Subsequently, we numerically calculated the normalized localization length  $\Lambda(\beta, \Omega)$  as a function of both normalized frequencies  $\Omega_{\pm}(\beta, k_p)$  and the gain/loss  $\beta$  parameter.

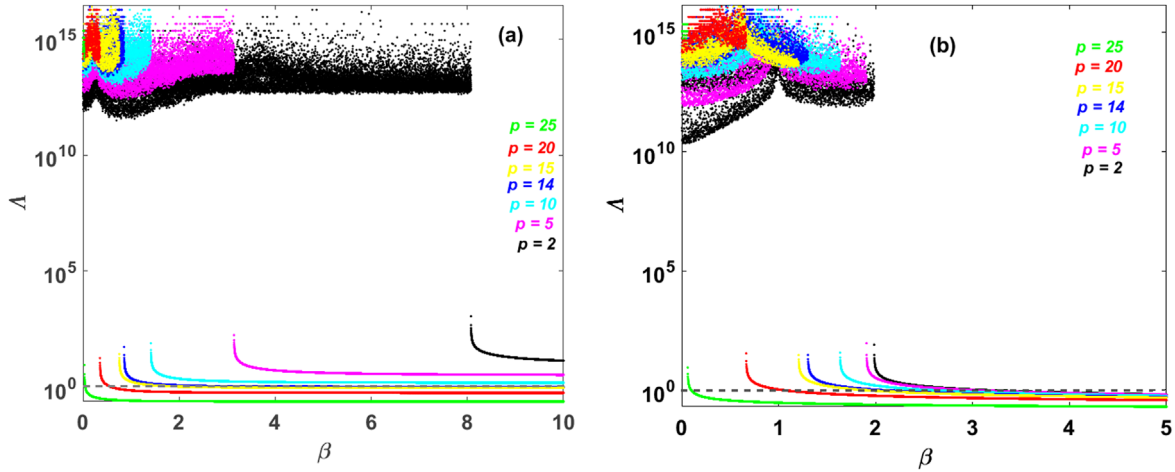


**Figure 9.** Normalized localization length  $\Lambda(\beta, \Omega_{\pm})$  in semi-log scale for the system in  $PT$  symmetry configuration as function of  $\beta$  for different values of  $p$  when  $N = 25$ . (a):  $PT^{RH}$ , and (b):  $PT^{LH}$ . For the values of  $p$  indicated in the plots, we observed extended modes (i.e  $\Lambda(\beta, \Omega_{\pm}) > 1$ ) in the  $PT$  exact phase, while the localized modes (i.e  $\Lambda(\beta, \Omega_{\pm}) < 1$ ) occur in the  $PT$  broken phase. Both localization behavior are separated by the gray curves which marks  $\Lambda(\beta, \Omega_{\pm}^{RH,LH}) = 1$ . In  $PT^{RH}$ , the appearance of the localized modes in the broken phase required a minimum of cells ( $p = 15$ ) since below that value, all modes remain extended (i.e  $\Lambda(\beta, \Omega_{\pm}^{RH}) > 1$ ). While,  $PT^{LH}$  configuration, confined modes even for the smallest value  $p = 1$  (not shown).

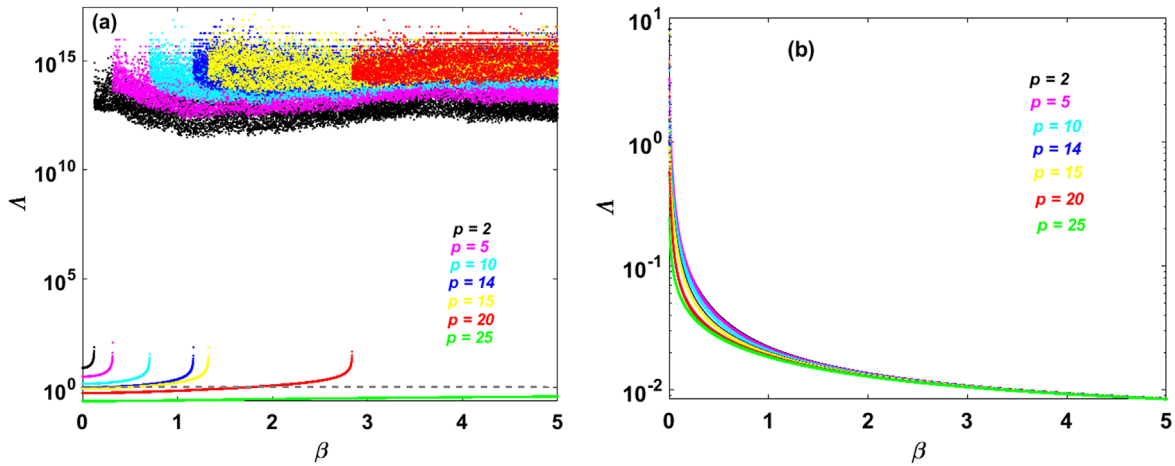


**Figure 10.** Normalized localization length  $\Lambda(\beta, \Omega_{\pm})$  in semi-log scale for the system in  $APT$ -symmetry configuration as function of  $\beta$  for different values of  $p$  when  $N = 25$ . (a):  $APT^{RH}$ , and (b):  $APT^{LH}$ . For the values of  $p$  indicated in the plots, we observe in  $APT^{RH}$  extended modes (i.e  $\Lambda(\beta, \Omega_{\pm}^{RH}) > 1$ ) in the exact phase (pure imaginary frequencies), while the localized modes (i.e  $\Lambda(\beta, \Omega_{\pm}^{RH}) < 1$ ) occur in the  $APT$  broken phase (complex frequencies). Both localization behaviors are separated by the gray curve corresponding to  $\Lambda(\beta, \Omega_{\pm}^{RH,LH}) = 1$ . Also remark that for the  $APT^{RH}$ , the appearance of the localized modes in the broken phase required a minimum of cells ( $p = 15$ ) since below that value, all modes become extended (i.e  $\Lambda(\beta, \Omega_{\pm}^{RH}) > 1$ ) however in  $APT^{LH}$  configuration, the modes are localized even for infinitesimal value  $p = 1$  (not shown).

**5.1. Numerical results in  $PT$ -symmetric configuration**

In the  $PT$ -symmetric configuration a general overview of the normalized localization length  $\Lambda(\beta, \Omega)$  plotted in figure 9 allows to identify two zones: the first zone, where  $\Lambda(\beta, \Omega)$  describes an extended function ( $\Lambda(\beta, \Omega_{\pm}^{RH,LH}) > 1$ ) corresponding to the  $PT$  unbroken phase and the localized function zone where  $\Lambda(\beta, \Omega_{\pm}^{RH,LH}) < 1$  corresponding to the broken region. Interestingly, two striking differences appear between the ETL models. Thanks to the horizontal gray dashed curves corresponding to  $\Lambda(\beta, \Omega_{\pm}) = 1$ , it can be noticed that for the system in  $PT^{RH}$  configuration (figure 9(a)), the Anderson-like localized mode required a minimum of 15 cells to occur in the broken regime. In fact, when the value of  $\beta$  becomes greater

than the transition point, there is a sharp decreased of the function  $\Lambda(\beta, \Omega_{\pm})$  whereas, in the  $PT^{LH}$  configuration (figure 9(b)), the large cells number is not required for the mode localization. In this LH configuration, even for the smallest value  $p = 1$  (not shown in the plots), the localized mode can be identified. Such results have been obtained for the RLC based ETLs and have demonstrated revealed applications in the field of information security [6]. Another important difference which emerges from the localization behavior of the two ETLs is the conduction range. This range gets larger in extended state for  $PT^{RH}$  at compared to  $PT^{LH}$ . Moreover, this range can be widen upon tunneling the system parameters such as the real and imaginary resistances.

## 5.2. Numerical results in APT-symmetric configuration

We have also numerically calculated  $\Lambda(\beta, \Omega_{\pm}^{RH})$  (resp.  $\Lambda(\beta, \Omega_{\pm}^{LH})$ ) in the APT-symmetric configurations. The results are shown in figure 10(a) for the  $APT^{RH}$  and in figure 10(b) for the  $APT^{LH}$  configuration. Interestingly, figure 10(a) shows that for the structure in  $APT^{RH}$ , there are two behavioral domains whatever the value of  $p$  used: the first  $APT^{RH}$  domain (broken phase) characterized by the Anderson-like localized modes, and the second domain ( $APT^{RH}$  exact phase) which is dominated by the extended state. The  $APT^{RH}$  configuration exhibits a wider range of extended states in the purely imaginary phase. Finally, in  $APT^{LH}$  configuration, we have seen in section 3 that the system is unbreakable and behaves in complex frequencies domain. The figure 10(b) shows that, the Anderson-like localized mode dominates the system whatever the values of  $p$  and  $\beta$  considered.

## 6. Conclusion

In summary, we have proposed 1D ETLs of ZRC right/left handed (RH/LH) model of  $2N$  size. This unit cell made it possible to simplify a description of the conventional direct and dual ETL with a simple first order differential equation. In our systems, components were distributed such as to have two ETL non-Hermitian models  $PT^{RH}$  (resp.  $PT^{LH}$ ) and  $APT^{RH}$  (resp.  $APT^{LH}$ ). We demonstrated that both ETL models are PT breakable and allow a phase transition of the eigenfrequencies from real to complex domain. However, only the RH ETL is APT breakable and allows frequencies from the complex to the exact phase where modes become totally imaginary. In the APT configuration, the LH ETL remains in the broken phase and no phase transition is possible. On the other hand, the Anderson-like localized modes appears in the broken PT/APT phase while others regions evince extended modes with the localization length proportional to the cell numbers. Furthermore, the results indicate that the mode localization is most likely to occur in structures consisting of a large cells number for RH ETL while LH ETL will confine modes even for infinitesimal small cell numbers. Giving the ability of our system to exist in both PT or APT configurations, this may offer interesting application in information encryption, optical switching and devices system control.

## ORCID iDs

Senghor Tagouegni  <https://orcid.org/0000-0003-0862-5681>

## References

- [1] Anderson P W 1958 *Phys. Rev.* **109** 1492
- [2] Mott N F and Twose W D 1961 *Adv. Phys.* **10** 107

- [3] Shin S, Suga S, Taniguchi M, Fujisawa M, Kanzaki H, Fujimori A, Daimon H, Ueda Y, Kosuge K and Kachi S 1990 *Phys. Rev. B* **41** 4993
- [4] Vatik I D, Tikan A, Onishchukov G, Churkin D V and Sukhorukov A A 2017 *Sci Rep.* **7** 4301
- [5] Lahini Y, Avidan A, Pozzi F, Sorel M, Morandotti R, Christodoulides D N and Silberberg Y 2008 *Phys. Rev. Lett.* **100** 1
- [6] Lazo E and Diez E 2010 *Phys. Lett. A* **374** 3538
- [7] Lazo E and Diez E 2011 *Phys. Lett. A* **375** 2122
- [8] Lazo E and Diez E 2013 *Physica B* **419** 19
- [9] Lazo E, Mellado F and Saavedra E 2012 *Phys. Lett. A* **376** 3423
- [10] Lazo E and Cortés-Cortés F 2019 *Eur. J. Phys. Plus* **134** 1
- [11] He Y, Malomed B A and Mihalache D 2014 *Philos. Trans. R. Soc. A* **372** 20140017
- [12] Lam C K, Malomed B A, Chow K W and Wai P K A 2009 *Eur. Phys. J. Spec. Top.* **173** 233
- [13] Zezyulin D A, Kartashov Y V and Konotop V V 2011 *Opt. Lett.* **36** 1200
- [14] Humire F R and Lazo E 2019 *Phys. Rev. E* **100** 2
- [15] He Y, Zhu X, Mihalache D, Liu J and Chen Z 2012 *Phys. Rev. A* **85** 1
- [16] Makris K G, El-Ganainy R, Christodoulides D N, Musslimani Z H and Makris K G 2008 *Phys. Rev. Lett.* **100** 10
- [17] Nixon S, Ge L and Yang J 2012 *Phys. Rev. A* **85** 2
- [18] Lupu A, Benisty H and Degiron A 2014 *Photonics Nanostructures Fundam. Appl.* **12** 305
- [19] Shramkova O V and Tsironis G P 2015 *17th International Conference on Transparent Optical Networks IEEE, XVII ICTON* (<https://doi.org/10.1109/icton.2015.7193378>)
- [20] Makris K G, El-Ganainy R, Christodoulides D N and Musslimani Z H 2010 *Phys. Rev. A* **81** 6
- [21] Bender C M and Boettcher S 1998 *Phys. Rev. Lett.* **80** 5243
- [22] Suchkov S V, Fotsa-Ngaffo F, Kenfack-Jiotsa A, Tikeng A D, Kofane T C, Kivshar Y S and Sukhorukov A A 2016 *New J. Phys.* **18** 065005
- [23] Zhu X, Feng L, Zhang P, Yin X and Zhang X 2013 *Opt. Lett.* **38** 2821
- [24] Fotsa-Ngaffo F, Tabeu S B, Tagouegni S and Kenfack-Jiotsa A 2017 *J. Opt. Soc. Am. B* **34** 658
- [25] Lin Z, Ramezani H, Eichelkraut T, Kottos T, Cao H and Christodoulides D N 2011 *Phys. Rev. Lett.* **106**
- [26] Feng L, Wong Z J, Ma R-M, Wang Y and Zhang X 2014 *Science* **346** 972
- [27] Longhi S 2010 *Phys. Rev. A* **82** 3
- [28] Ge L and Türeci H E 2010 *Phys. Rev. A* **88** 5
- [29] Antonosyan D A, Solntsev A S and Sukhorukov A A 2015 *J. Nonlinear Opt. (https://doi.org/10.1364/nlo.2015.nw4a.14)*
- [30] Peng P, Cao W, Shen C, Qu W, Wen J, Jiang L and Xiao Y 2016 *Nat. Phys.* **12** 1139
- [31] Wang X and Wu J-H 2016 *Opt. Expr.* **24** 4289
- [32] Wu J-H, Artomi M and La Rocca G C 2015 *Phys. Rev. A* **91** 3
- [33] Yang F, Liu Y-C and You L 2017 *Phys. Rev. A* **96** 5
- [34] Choi Y, Hahn C, Yoon J W and Song S H 2018 *Nat. Commun.* **9** 1
- [35] Konotop V V and Zezyulin D A 2018 *Phys. Rev. Lett.* **120** 12
- [36] Koutserimpas T T, Alù A and Fleury R 2018 *Phys. Rev. A* **97** 1
- [37] Xia S, Hu Y, Song D, Zong Y, Tang L and Chen Z 2016 *Opt. Lett.* **41** 1435
- [38] Lazo E 2014 *Physica B* **432** 121
- [39] Lazo E, Humire F R and Saavedra E 2014 *Physica B* **452** 74
- [40] Diez E, Izrailev F, Krokhin A and Rodriguez A 2008 *Phys. Rev. B* **78** 3
- [41] Lazo E, Saavedra E, Humire F R, Castro C and Cortés-Cortés F 2015 *Eur. Phys. J. B* **88** 9

- [42] Kolář M, Ali M K and Nori F 1991 *Phys. Rev. B* **43** 1034
- [43] Tabeu S B, Fotsa-Ngaffo F and Kenfack-Jiotsa A 2019 *Opt. Quant. Electron.* **51** 10
- [44] Tabeu S B, Fotsa-Ngaffo F and Kenfack-Jiotsa A 2019 *EPL* **125** 24002
- [45] Shouno K and Ishibashi Y 2008 *LI Midwest Symposium on Circuits and Systems* (<https://doi.org/10.1109/mwscas.2008.4616858>)
- [46] Schindler J, Lin Z, Lee J M, Ramezani H, Ellis F M and Kottos T 2012 *J. Phys. A: Math and Theor.* **45** 444029
- [47] Shramkova O V and Tsironis G P 2016 *Phys. Rev. B* **94** 3
- [48] Lupu A, Benisty H and Degiron A 2014 *Photonics Nanostructures: Fundam. Appl.* **12** 305



# Thresholdless characterization in space and time reflection symmetry electronic dimers

FERNANDE FOTSA-NGAFFO,<sup>1,2,3,\*</sup> STEPHANE BORIS TABEU,<sup>3,4</sup> SENGHOR TAGOUEGNI,<sup>3,4</sup> AND AURÉLIEN KENFACK-JIOTSA<sup>3</sup>

<sup>1</sup>Department of Physics, Faculty of Science, University of Buea, P.O. Box 63, Buea, Cameroon

<sup>2</sup>Institute of Wood Technologies, University of Yaoundé I, P.O. Box 306, Mbalmayo, Cameroon

<sup>3</sup>Nonlinear Physics and Complex Systems Group, Department of Physics, The Higher Teachers' Training College, University of Yaoundé I, P.O. Box 47, Yaoundé, Cameroon

<sup>4</sup>Laboratory of Mechanics, Materials and Structures, Department of Physics, Faculty of Science, University of Yaoundé I, P.O. Box 812, Yaoundé, Cameroon

\*Corresponding author: ngafotsa@yahoo.com

Received 17 October 2016; revised 4 February 2017; accepted 4 February 2017; posted 7 February 2017 (Doc. ID 278836); published 24 February 2017

We develop a general mutual inductive M, inductive L, and capacitive C couplings parity time symmetry (MLC PTS) electronic dimer model. We successfully show that the dimers separately coupled with M, L, or ML can be made thresholdless by adding a capacitance C in parallel. Thus, sufficient conditions for thresholdless transitions were determined. The scattering properties of our model reveal the suppression of unidirectional invisibility from the gain input when the Hermitian line coupling exceeds a critical point. Likewise, the scattering system becomes unidirectional PTS. Remarkably, under the thresholdless conditions, lasing modes appear for imaginary values of wavenumbers corresponding to either real or purely imaginary values of the gain/loss modulation. This latter demonstrates the ability to control prohibited waves in the linear regime. © 2017 Optical Society of America

**OCIS codes:** (250.4480) Optical amplifiers; (260.5740) Resonance; (290.5839) Scattering, invisibility.

<https://doi.org/10.1364/JOSAB.34.000658>

## 1. INTRODUCTION

Quantum field theory generalization in optical physics has elicited a substantial equivalence between the Schrödinger and the paraxial wave equations. In particular, it has been demonstrated that non-Hermitian Hamiltonians featuring invariance under the combined operation of space and time reflection symmetry (PTS) can produce entirely real spectra and phase transition from real to broken spectra [1,2]. In general, such Hamiltonians can be non-Hermitian with some gain/loss modulation that controls the non-Hermiticity [3,4]. As the balanced gain/loss modulation increases, there is a spontaneous phase transition from net energy conservation (real solutions) to net nonconservation energy (complex solutions). Interestingly, this spontaneous symmetry breaking of the PT symmetric systems is related to an exceptional point (EP) [5–7] and was demonstrated to be a hallmark of a general class of pseudo-Hermitian systems with not necessarily PT symmetries [8,9].

PT synthetic materials have demonstrated several intriguing features, such as power oscillations, unidirectional invisibility [6,10–14], nonreciprocal Bloch oscillations [15], absorption-enhanced transmission [8], simultaneous coherent-perfect-absorber lasing [16], and localized termination modes [17],

in numerous experimental and theoretical developments, including acoustics [18–20], optics-photonics [5,11,21–29], and electronic systems [30–34]. Remarkably, PTS in electronics is emerging as a fertile ground due to its relative theoretical and experimental simplicity [34]. The nonzero spontaneous PTS breaking is the ordinary fundamental properties of PT dimer systems where the system has eigenvalues that correspond, not to a degeneracy of the relevant operator, but to a point at which it becomes defective [35]. In PTS systems, however, another extraordinary property is emerging to be a thresholdless (THL) transition for which the spectrum becomes complex in the absence of gain/loss modulation (i.e., a real spectrum cannot exist even at infinitesimal strength of gain and loss). Such transition in PTS optics results as degeneracy of the PTS operator [29,36–38]. THL PTS systems offer intriguing properties such as all-angle supercollimation and superprism effect. The THL transition was also proven to achieve single-mode laser emission in microrings [24].

To the best of our knowledge, the THL behavior of any PTS electronic dimer has never been addressed. In this paper, we develop a general model of a mutual inductive M, inductive L, and capacitive C couplings electronic dimer (MLC PTS). This model offers different advantages, as it helps to understand

the behavior of both single and combined active couplings of distinct circuitry elements.

The main objective of our paper is twofold. First, we demonstrate that when the gain and loss electronic cells are coupled with a combination of the capacitance  $C$  in parallel with other electronic components, there is a set of circuit parameters for which the real spectrum disappears completely. Such a point in the eigenvalues spectrum is called the THL point (THLP). For reference in our paper, we call threshold (TH) dimers the ones that feature ordinary transition, and THL (THL) dimers the ones that can admit a zero-value breaking point. Second, we demonstrate that for any set of PTS dimers, there is a critical transmission line (TL) coupling point above which the unidirectional invisibility is suppressed from the gain input signal. This indicates that the scattering system is PTS only in the loss side. Throughout this work and taking into account the good agreement between PTS experimental, numerical, and theoretical investigations, we are confident in being solely concerned with theoretical and numerical analysis. We begin our investigation by describing in Section 2 the general PTS dimer model MLC, and we derive the mode equations that display the characteristic behavior of the square-root singularity  $|\omega| \propto \pm \sqrt{\gamma^2 - \gamma_{PT}^2}$ , a generic feature of the PTS breaking. In Section 3, we investigate the eigenmodes characteristics of the TH and THL dimers. We also analyze the phase dynamic behavior of these modes, which relates the THLP to a second-order phase transition of the corresponding mode dynamics. Then, we consider the different dimers in a chain of conservative TL and show that the scattering systems modes propagation strongly depends on the type of dimer inserted into it. Finally, we conclude and offer some remarks.

## 2. MODEL DESCRIPTION

The experimental setup consists of two oscillators made of inductor  $L$ , resistor  $R$ , and capacitor  $C$  (LRC oscillators), the gain cell with an amplification generated by a negative resistance  $-R$ , and the loss cell with an attenuation introduced by a positive  $R$ . The “active” dimer is made of linear electronic components; hence, the dimer is nonconservative, but the balanced gain and loss of each cell can result in net energy conservation of the solutions to the system. The schematic model of the general PTS dimer is demonstrated in Fig. 1.

The different PTS dimers are modeled so that only the active coupling is used to refer to the dimer. For example, in dimer  $L$ , only the inductance coupling  $L_0$  is active, while in the dimer  $LC$  both the inductance  $L_0$  and the capacitance  $C_0$  couplings are active. The characteristics of all the PTS dimer

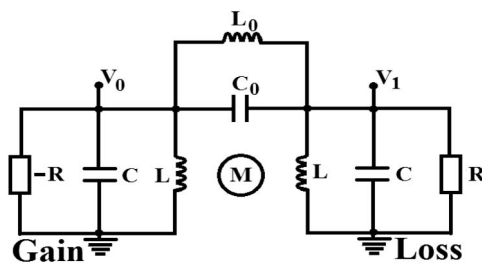


**Fig. 1.** Electronic model of a general PTS dimer MLC. The model takes into account all types of coupling: mutual inductive coupling ( $M$ ), inductor coupling ( $L_0$ ), and capacitive coupling ( $C_0$ ).

configurations are presented in Table 1. The modes of the PT dimer are found using standard current and voltage circuits’ laws [32–34], and thus we can derive a set of coupled second-order differential equations the dimensionless equations for the charge capacitors  $Q_n^C = CV_n$ :

$$\begin{aligned} (1+c)\frac{d^2Q_0}{d\tau^2} - c\frac{d^2Q_1}{d\tau^2} &= -(\alpha+\nu)Q_0 + (\alpha\mu+\nu)Q_1 + \gamma\frac{dQ_0}{dt} \\ -c\frac{d^2Q_0}{d\tau^2} + (1+c)\frac{d^2Q_1}{d\tau^2} &= (\alpha\mu+\nu)Q_0 - (\alpha+\nu)Q_1 - \gamma\frac{dQ_1}{dt}. \end{aligned} \tag{1}$$

Each cell has a natural frequency  $\omega_0^2 = \frac{1}{LC}$  and a natural phase  $\tau = \omega_0 t$ ,  $\gamma = \frac{1}{R}\sqrt{\frac{L}{C}}$  is the dimensionless gain/loss parameter,  $\mu = \frac{M}{L}$ ,  $\alpha = \frac{1}{1-\mu^2}$  with  $\mu < 1$ ,  $\nu = \frac{L}{L_0}$ ,  $c = \frac{C_0}{C}$ ,  $Q_j = \frac{q_j}{Q}$ , and  $q_j$  is the charge at node  $j$ .

The sign of  $\gamma$  is the sign of  $R$ . System (1) reflects the PTS as it remains invariant under simultaneous permutation of the indices 0, 1 and reversal of the dimensionless time parameter  $\tau$ . The charge of a capacitor of the system oscillates according to  $Q_j = A_j e^{i\omega\tau}$ . The eigenfrequencies  $\omega_i$  can be found by solving the secular equation resulting from Eq. (1), which admits four normal mode frequencies expressed in Eq. (2) with the square-root singularity  $|\omega| \propto \pm \sqrt{\gamma^2 - \gamma_{PT}^2}$ , a generic feature of the PTS breaking.  $\gamma_{PT}$  is the value of  $\gamma$  at which PT symmetric breaking occurs [21]. The oscillation amplitude decays with time if  $\gamma > 0$ , and grows if  $\gamma < 0$ :

$$\omega_{1,2,3,4} = \pm \frac{1}{2(1+2c)} \sqrt{\frac{2(1+2c)(2\alpha+2\nu+2\alpha c-2\alpha\nu}{-\gamma^2 \pm \sqrt{\gamma_{PT}^2 - \gamma^2}}}. \tag{2}$$

The two breaking values of  $\gamma_{PT}$ ,  $\gamma_1$  and  $\gamma_2$ , are expressed in Eq. (3). We note that  $\gamma_1 = 0$  and  $\gamma_2 = 2$  are associated with a pair of double degenerated frequencies,  $\omega_1 = \pm 1$  and  $\omega_2 = \pm i$ , respectively, when considered a single isolated circuit ( $\mu = \nu = c = 0$ ):

$$\gamma_{1,2} = \sqrt{2[\alpha c(1-\mu) + \alpha + \nu \mp \sqrt{\alpha(1-\mu)(1+2c)(\alpha\mu + \alpha + 2\nu)}}. \tag{3}$$

The general active PTS dimer MLC allows for a direct observation for a transition from exact phase to the broken phase controlled by a gain and loss parameter  $\gamma_1$ . A quick analysis

**Table 1.** Characteristics of THs and THL PTS Dimers

PT-Dimers		Coupling Parameters			Requirements
		M	$L_0$	$C_0$	
$\gamma_1 \neq 0$	M	$\mu \neq 0$	$\nu = 0$	$c = 0$	$0 < \mu < 1$ , $\mu, \nu$ , $c > 0$
	L	$\mu = 0$	$\nu \neq 0$	$c = 0$	
	ML	$\mu \neq 0$	$\nu \neq 0$	$c = 0$	
	C	$\mu = 0$	$\nu = 0$	$c \neq 0$	
THL ( $\gamma_1 = 0$ )	MC	$\mu \neq 0$	$\nu = 0$	$c \neq 0$	$c = \mu/1 - \mu$
	LC	$\mu = 0$	$\nu \neq 0$	$c \neq 0$	$c = \nu$
	MLC	$\mu \neq 0$	$\nu \neq 0$	$c \neq 0$	$c > \nu$ $c = \frac{\nu + \alpha\mu}{\alpha(1-\mu)}$

of  $\gamma_1$  and  $\gamma_2$  shows that  $\gamma_2 \neq 0$  but always increases with the coupling between the gain and loss cell, whatever the other circuit parameters combinations. However, if the capacitance obeys Eq. (4),  $\gamma_1 = 0$  and the PTS dimer is said to be THL:

$$c = \frac{\nu + \alpha\mu}{\alpha(1 - \mu)}. \quad (4)$$

In what follows, we distinguish between two groups of dimers, the TH dimers ( $\gamma_1 \neq 0$ ) and the THL dimer ( $\gamma_1 = 0$ ), and we study their mode dynamics.

### 3. EIGENMODE CHARACTERISTICS

#### A. TH Dimers

In Fig. 2, we report the normal modes frequencies and TH parametric variation for the dimers, C (a) and (b), and ML (c)–(f) with respect to the coupling nature and strength. In all cases, we show only the positive eigenfrequencies. The PTS TH dimers feature an ordinary nonzero transition. For a given value of the active coupling strength, the four normal mode frequencies are completely real in the exact phase  $0 < \gamma < \gamma_1$ . The motion is plain oscillatory due to the unfolding of nonorthogonal

eigenmodes [14] and the eigenvector solutions  $Q_0$  and  $Q_1$  are PT symmetric [33]. At  $\gamma = \gamma_1$ , the PTS dimer displays a spontaneous symmetry breaking. The solutions undergo a sudden transition from net conservation to net nonconservation. The normal modes coalesce, and their imaginary parts are degenerated; thus the motion grows quadratically due to the biorthogonal nature of the eigenstates [3,4]. For  $\gamma_1 < \gamma < \gamma_2$  corresponding to the broken phase, the normal modes frequencies are complex conjugate pairs with nonzero real and imaginary parts. This induces an exponential growth of one mode and decay of the other, both of which oscillate at the same frequency; the corresponding solutions are no longer PT symmetric. Finally, when  $\gamma_1 > \gamma_2$ , all the eigenvalues are imaginary, and the modes have no oscillatory part.

In TH dimers,  $\gamma = 0$  would be satisfied only for the zero values of the different couplings corresponding to single isolated gain or loss cells. As the active coupling increases, so does  $\gamma_1$ , implying that the exact phase enlarges with the coupling; however, the broken phase band remains constant, as indicated by the straight dark line on the graphs. It is instructive that these observations are true for all TH dimers except when

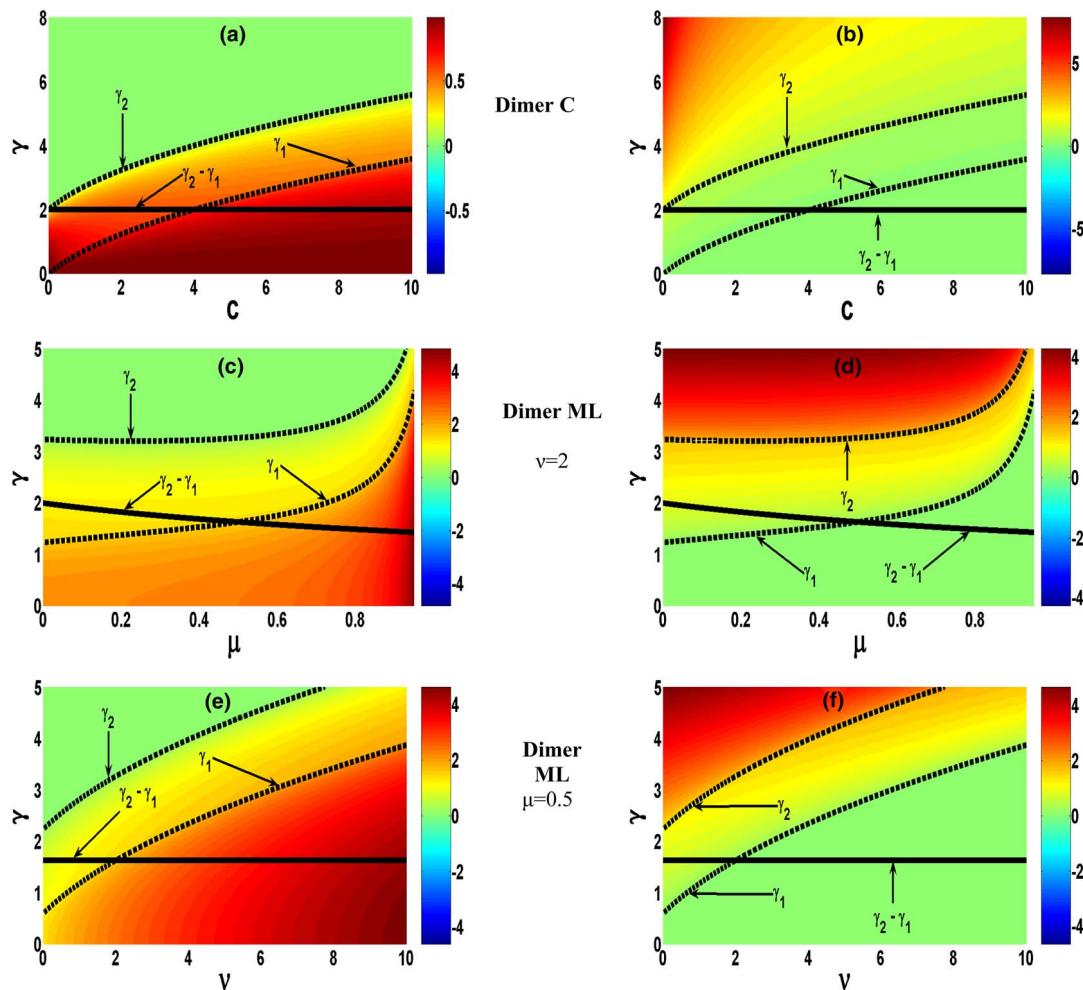


**Fig. 2.** Normal modes and thresholds evolution of PTS dimers: C in (a) and (b), and ML in (c)–(f). The first and second columns represent the real and the imaginary parts, respectively. The values of the fixed parameters are specified in the graphs. The transitions values curves are indicated as  $\gamma_1$  and  $\gamma_2$  in dotted dark lines, while their relative difference is plotted in a plain dark line. The color bar indicates the magnitude of the eigenfrequencies.

the controlling coupling is the mutual inductance, where the broken phase rather reduces with the increased coupling. In the case of combined  $M$  and  $L$  couplings, the transition values are upshifted according to the passive coupling, but its dynamics is dictated by the active varying coupling. Otherwise, for single coupling  $M$  or  $L$ , the first transition will start at  $\gamma_1 = 0$ . Remarkably, the TH variation for  $\gamma_1$  and  $\gamma_2$  in dimer  $L$  (dimer  $ML$  when  $\mu = 0$ ) and dimer  $C$  follows the same parametric evolution, giving the impression that the two dimers may be identical. However, the magnitude of the eigenvalues in dimer  $C$  has a homogeneous variation for the real part of the eigenvalues spectrum with a maximum value of 1 (for the parameter set of our plot) throughout the spectrum, while the imaginary eigenvalues increase with increasing  $\gamma$  and decrease with  $C$ .

In dimer  $L$ , there is a strong variation of the real part of the eigenvalues spectrum with a maximum value of five throughout the spectrum, while the imaginary eigenvalues increase with increasing  $\gamma$  and does not change much with  $L$ .

**B. THL Dimers**

A crossover point, where the normal modes coalesce along the controlling coupling constant of the dimer, characterizes the THL dimers. This happens when the relation between the combined coupling parameters are imposed by the equation  $\gamma_1 = 0$ . At this point of the corresponding combination set of THL coupling parameters, there is needless gain/loss modulation strength to enter the broken phase. Such behavior is dictated by Eq. (4), with the restriction that  $c > \nu$ . This THL transition arises only when the capacitance coupling  $C$  is added to the previous coupling  $M$ ,  $L$ , and  $ML$ . In the particular cases of  $LC$  and  $MC$  dimers, the active couplings obey the simplified relations  $\nu = c$  and  $c = \mu/(1 - \mu)$ , respectively. Table 1 describes the seven PTS dimers configurations that can result by considering a general  $MLC$  dimer. The relationship between

the different combinations to be considered as either a TH or a THL dimer are explicitly given for each dimer. As an example, the positive normal modes of dimers  $MC$  ( $\mu = 0.75$ ) and  $C$  ( $\mu = 0$ ) are plotted in Figs. 3(a) and 3(b), respectively. We can clearly distinguish three regimes of mode dynamics. In the first regime,  $c < c_{THL}$ , (i.e., before the THLP). PT electronic dimer has a nonzero PT transition.

The real part of the normal modes converges in two pairs of positive and negative values but the first TH transition value  $\gamma_1$  decreases, while the second TH  $\gamma_2$  increases with the capacitance coupling constant  $c$ . This explains why the real phase reduces progressively and ultimately disappears. This dynamic finds its origin from the phase dynamics analytically expressed in Eq. (5):

$$\Delta\phi(\omega_{\pm}) = \tan^{-1} \left[ \frac{1}{\gamma} \left( (1 + c)\omega_{\pm} - \frac{(\nu + \alpha)}{\omega_{\pm}} \right) \right]. \quad (5)$$

This phase dynamic is plotted in Figs. 4(a) and 4(b) for THL dimer  $MC$  and TH dimer  $C$ , respectively. As can be clearly observed in Fig. 4(a), when the gain/loss parameter increases, the THL dimer phase dynamic undergoes a second-order phase transition around  $\gamma_1$  and  $\gamma_2$ , which is only seen around  $\gamma_1$  for values of the controlling coupling constant  $c$  greater than  $c_{THL}$ . In the second regime,  $\gamma_1 = 0$  and  $c = c_{THL}$ ; this is the THL transition. The system prohibits real propagation frequencies. The phase dynamic indicates a crossover point of the normal mode pairs solely in the real part of the spectrum.

Figure 4(a) exhibits an abrupt phase transition in the broken phase that ultimately dominates the normal mode phase dynamic around  $\gamma_2$  along the growing coupling constant. In the case of TH dimer  $C$  plotted in Fig. 4(b), the second-order transition is observed only from the complex to imaginary phase. However, the real and complex phase analyses indicate a smooth variation and, consequently, identical phase dynamics throughout the variation of the active coupling  $C$ . In the last

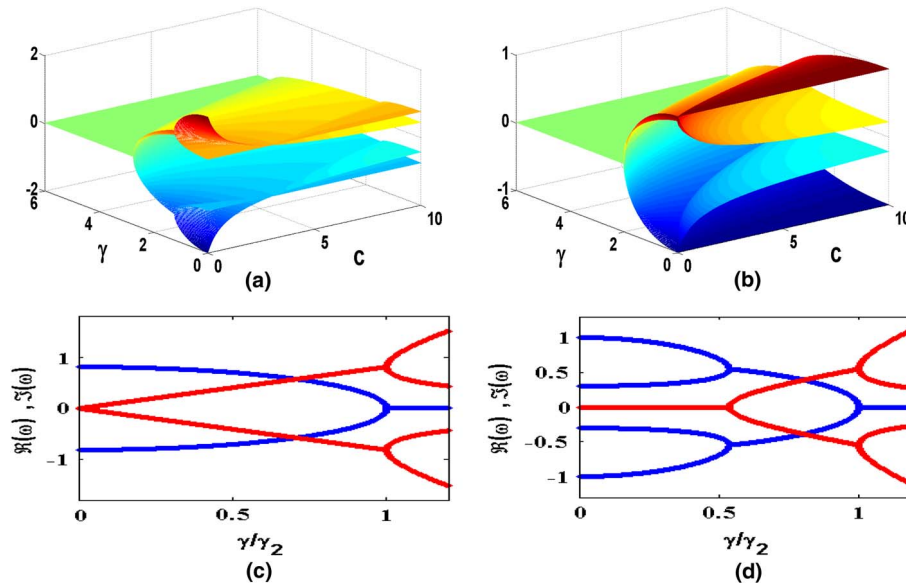


**Fig. 3.** Normal modes dynamics of (a) THL dimer. The modes converge toward each other and cross over at  $\gamma_1 = 0$  ( $c = 5$ ) where they degenerate. (b) Case of TH dimer indicating that the crossing would happen at  $c = 0$ . In (c) and (d) cross section of (a) done at the THLP and (b), respectively.

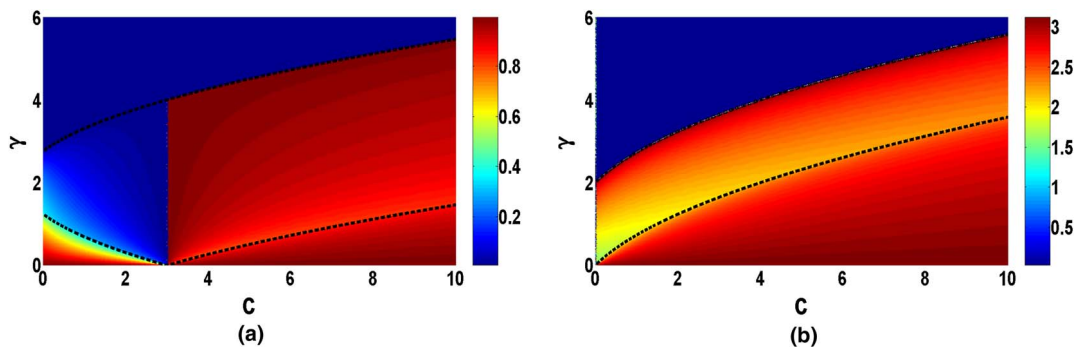


**Fig. 4.** Phase dynamic of THL MC ( $\mu = 0.75$ ) dimer normal modes in (a) and TH dimer C ( $\mu = 0$ ) in (b). The THL transition induces a phase bump up that dictates the dynamic of the normal modes. The dark dotted lines are the first and second PT transition variations with the coupling constant.

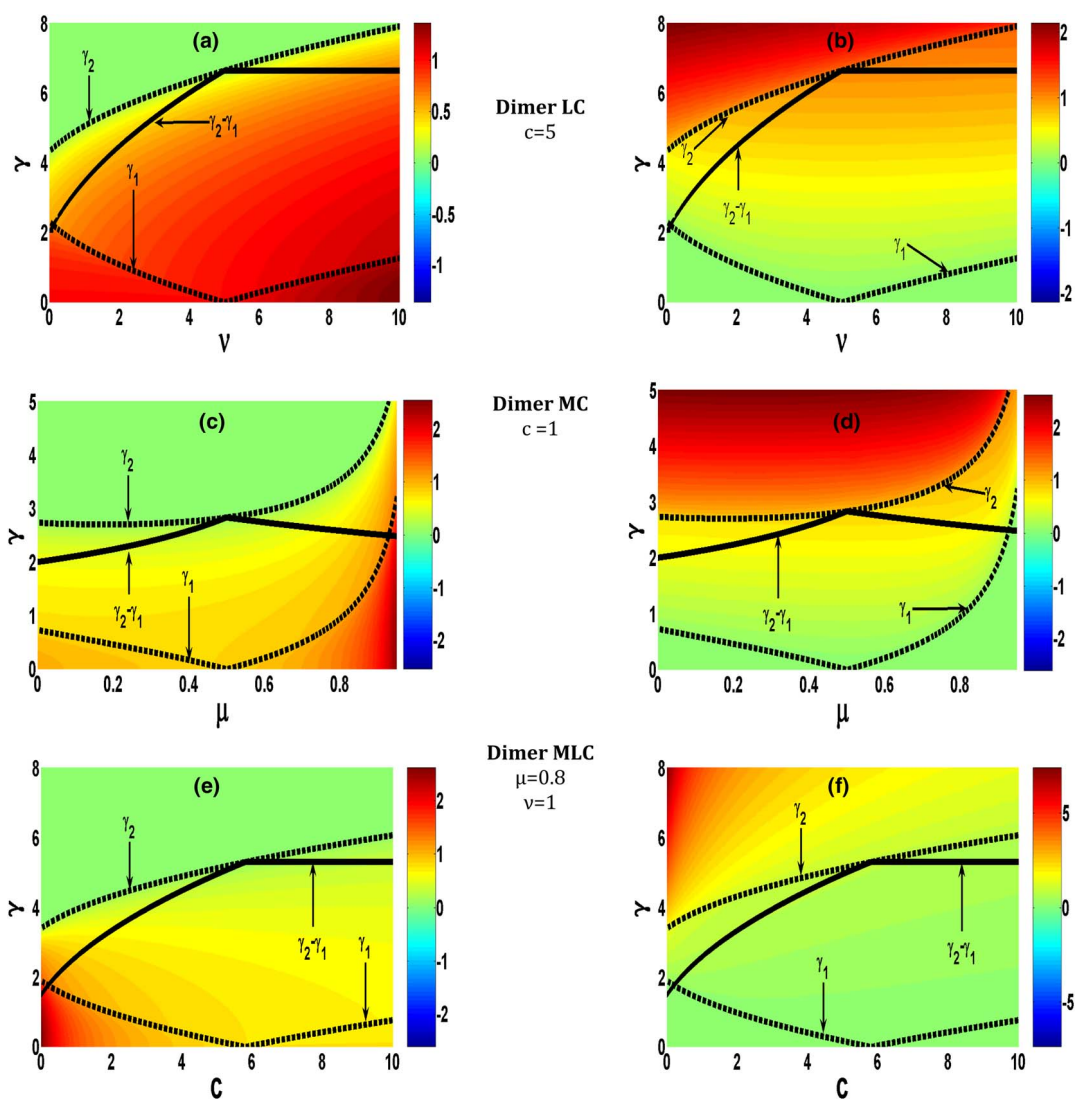


**Fig. 5.** Normal modes and thresholds parametric evolution of PTS THL dimers: LC in (a) and (b), MC in (c) and (d), and MLC in (e) and (f). The first column represents the real parts, and the imaginary parts are depicted in the second column. The values of the fixed parameters are specified in the graphs. The transition value curves are indicated as  $\gamma_1$  and  $\gamma_2$  in dotted dark lines, while their relative difference is plotted in a plain dark line. The color bar indicates the magnitude of the modes.

regime, the normal modes depart from  $c > c_{\text{THL}}$ , and the system enters into an ordinary transition with a similar phase dynamic behavior as that of the TH dimers.

For a finite coupling strength, the modal phases progress gradually along the gain/loss modulation and coalesce at the transition. The dark dotted lines represent the evolution of the first and second PT transition variation with the coupling constant. The normal mode frequencies dynamic for different THL dimers are plotted in Fig. 5. Precisely, when the dimer is coupled with a combination of two or more coupling parameters, the mode dynamics is better observed by controlling only one coupling parameter, while maintaining the other ones constant. For example, in the case of dimers LC, as seen in Figs. 5(a) and 5(b), and MC [see Figs. 5(c) and 5(d)], the coupling parameters are  $c = 5$  and  $c = 1$ , respectively. This makes the couplings  $\mu$  and  $\nu$  be the controlling parameters, respectively. For the THL dimer MLC [Figs. 5(e) and 5(f)], the controlling parameter is  $c$ , and other couplings are fixed to  $\mu = 0.8$  and  $\nu = 1$ . In all cases, the broken phase enlarges with the controlling coupling and reaches its maximum depth at the THLP where  $\gamma_1 = 0$ . This variation of the broken domain before the THLP is also evidenced by the sharp increase of the parameter  $\gamma_2 - \gamma_1$ . After the THL transition, the broken phase reduces with the increasing coupling  $\mu$ . However, this broken phase remains constant for other coupling parameters, as already indicated in Fig. 2. In the case of combined dimers, the transition values of  $\gamma$  are shifted compared to a single coupling dimer, due to the combination with another coupling (the passive or fixed one, depending on the cases), but its dynamics is dictated by the active varying coupling constant.

#### 4. SCATTERING PROPERTIES

The scattering is achieved by linearly coupling the left and the right sides of the PTS dimer to an inductively coupled parallel LC cell TL. Then the dimensionless charges of the capacitors at any point along a TL are written in the form

$$\begin{aligned} (1+c) \frac{d^2 Q_0}{d\tau^2} - c \frac{d^2 Q_1}{d\tau^2} &= -\vartheta Q_{-1} - (\alpha + \nu + \vartheta) Q_0 + (\alpha\mu + \nu) Q_1 + \gamma \frac{dQ_0}{dt} \\ -c \frac{d^2 Q_0}{d\tau^2} + (1+c) \frac{d^2 Q_1}{d\tau^2} &= (\alpha\mu + \nu) Q_0 - (\alpha + \nu + \vartheta) Q_1 + \vartheta Q_2 - \gamma \frac{dQ_1}{dt} \\ \frac{d^2 Q_j}{d\tau^2} &= \vartheta Q_{j-1} + \vartheta Q_{j+1} - (1+2\vartheta) Q_j, \quad \text{for } j \neq 0, 1, \end{aligned} \quad (6)$$

where  $\vartheta = \frac{1}{L}$ .

We are interested in investigating the transmission, reflection, and amplification properties of the different PT electronic dimers and in comparing the scattering properties of PT TH dimers to the ones of the PT THL dimers. For this purpose, we put the solutions into the form

$$\begin{cases} Q_j = I e^{i(kj - \omega\tau)} + R_g e^{i(-kj - \vartheta\tau)} & j \leq 0 \\ Q_j = T_g e^{i(kj - \omega\tau)} & j \geq 1 \end{cases} \quad (7)$$

where  $I$ ,  $R_g$ , and  $T_g$  are, respectively, the incident, reflected, and transmitted coefficients from the gain side;

$k$  is wavenumber of the incident wave. The dispersion frequency of the wave in a TL far away from the PT dimer defect is defined in Eq. (8). Such dispersion indicates that the TL is a bandpass with a lower cutoff frequency of  $f_1 = 1/2\pi$  and an upper cutoff frequency of  $f_2 = (1 + 4\vartheta)^{1/2}/2\pi$ , which occur at wavenumbers  $k = 0$  and  $k = \pi$ , respectively:

$$\omega^2 = 1 + 4\vartheta \sin^2\left(\frac{k}{2}\right). \quad (8)$$

After substitution of Eq. (7) into Eq. (6), the scattering coefficients for an incidence from the gain/loss side are derived to be

$$T_g = i \frac{2\vartheta B \sin(k) e^{ik}}{(A - \vartheta e^{ik})(A^* - \vartheta e^{ik}) - B^2} I, \quad (9)$$

$$R_g = \frac{B^2 - (A - \vartheta e^{ik})(A^* - \vartheta e^{-ik})}{(A - \vartheta e^{ik})(A^* - \vartheta e^{ik}) - B^2} I, \quad (10)$$

$$R_l = \frac{(B^2 - (A - \vartheta e^{-ik})(A^* - \vartheta e^{ik})) e^{-2ik}}{(A - \vartheta e^{ik})(A^* - \vartheta e^{ik}) - B^2} I, \quad (11)$$

where  $A = b - a\omega^2 - i\gamma\omega$ ,  $B = c\omega^2 - d$ ,  $a = 1 + c$ ,  $b = \alpha + \nu + \vartheta$ ,  $d = \alpha\mu + \nu$ , and the subscripts  $g$  and  $l$  refer to the incident wave arriving on the PTS dimer from the gain or lossy cell sides, respectively.

A simple analysis reveals that the scattering coefficients share a common denominator,  $D = (A - \vartheta e^{ik})(A^* - \vartheta e^{ik}) - B^2$ . Due to the reciprocity of transmission for any linear stationary and nonmagnetic medium [9,36], the transmission coefficients coincide for the left and right propagations ( $T_g = T_l$ ). The reflection coefficients are nonreciprocal ( $R_g \neq R_l$ ), and the corresponding scattering signals satisfy the generalized unitary conservation relation  $||T^2| - 1| = |R_L \cdot R_g^*|$ , which reveals the underlying symmetries of the scattering PTS dimer defect. As mentioned earlier in this paper, the TH or THL characteristic of the dimer plays an interesting role in the scattering features, such as lasing modes, unidirectional transparency, mirror-like behavior, etc. In order to study the lasing modes properties of the dimer systems, we analytically investigate the lasing gain/loss parameter  $\gamma_r$  when the denominator  $D$  turns to zero at some critical wavenumber  $k_r$ . This means at  $\gamma_r$ , the dimer operates at a lasing mode  $k_r$ . These lasing modes are mathematically expressed as

$$\cos k = \frac{b - a(1 + 2\vartheta)}{(1 - 2a)\vartheta}, \quad (12a)$$

$$\gamma_r = \frac{1}{\omega} \sqrt{B^2 + \vartheta^2 \sin^2 k}. \quad (12b)$$

We have plotted the lasing mode spectra for the dimer TH ML in Figs. 6(a) and 6(b), while the ones of dimer THL MLC are represented in Figs. 6(c) and 6(d). The first column is the real part of  $\gamma_r$ , and the second column represents its imaginary part. We derive the boundaries of the values of  $k$ , F1, and F2 from Eq. (12a) as

$$\vartheta = (1 - \mu^2)(\nu - c - 1) + 1/[2(1 + 2c)(1 - \mu^2)] \quad \text{for F1}, \quad (13a)$$

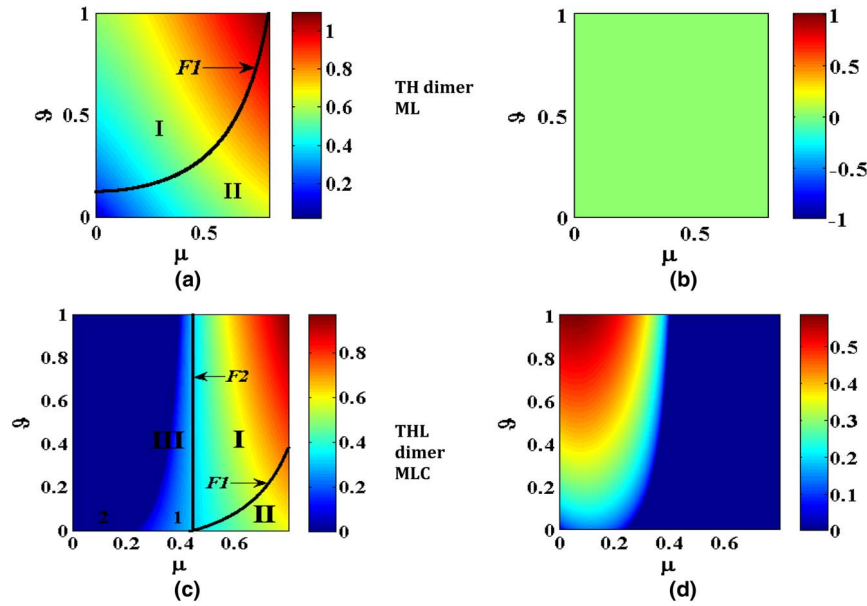


**Fig. 6.** Spectra of  $\gamma_r$  for which  $D = 0$ . The case TH dimer ML is depicted in (a) and (b), and the case THL dimer MLC is plotted in (c) and (d). The first column is the real part representation, while the imaginary part is depicted in the second column. F1 and F2 define the frontiers of regions I (real  $k$ ), II (complex  $k$ ), and III (purely imaginary  $k$ ). The TH dimer does not allow imaginary wave propagation;  $\gamma_r$  is either real or complex. The THL dimer allows control of real, complex, and imaginary propagation wavenumbers. The existence of region III-2 implies that lasing modes occur for imaginary  $\gamma_r$  and  $k_r$ .

$$1/(1 - \mu^2) + \nu = 1 + c \quad \text{for F2.} \quad (13b)$$

As indicated by the graphs, F1 and F2 delimit three regions: I, II, and III. F2 is independent of  $\vartheta$ . Region I corresponds to purely real and positive values of the wavenumbers  $k$  and frequencies  $\omega$  (i.e.,  $-1 < \cos(k) < 1$  and  $1 < \omega < (1 + 2\vartheta)^{1/2}$ ). These are the allowed frequencies from our TL dispersion relation [Eq. (8)]; we can then see that the values of  $\gamma_r$  for which lasing modes occurs are real. Region II is the upper forbidden gap where  $\cos(k) < -1$  and  $\omega > (1 + 2\vartheta)^{1/2}$ . The wavenumbers are complex, with a constant real part (equal to  $\pi$ ) and a varying negative imaginary part,  $k = \pi - i\kappa$ . The frequencies are also complex in this region, but the lasing modes exist for real values of  $\gamma_r$  [Eq. (12b)]. Region III is the lower forbidden bandgap for which  $\cos(k) > 1$  and the wavenumbers  $k$  are purely imaginary (i.e.,  $k = +i\kappa$ ). Therefore, the frequency propagation ( $\omega < 1$ ) is real for  $2\vartheta (\cosh k - 1) > 1$  and purely imaginary for  $2\vartheta (\cosh k - 1) < 1$ . From Figs. 6(c) and 6(d), it can be clearly seen that the lasing parameter  $\gamma_r$  can be either real region III-1 or purely imaginary region III-2.

These analyses indicate three regions of wavenumber propagation and subsequently lasing modes operation in THL dimers, the third region being the region of purely imaginary  $k$ , while TH dimer can only operate in two regions in which  $k$  is either real or complex. It is interesting that there are two exceptions for these rules: The TH dimer C does not have real or complex operating modes. Regions II and I are not observed. F2 frontier occurs at  $C = 0$ . Therefore,  $\gamma_r$  is purely imaginary, so the lasing modes could only be observed for purely imaginary values of the wavenumbers [Fig. 7(a)]. The second exception is that in the THL dimer LC, the frontier F2

[Figs. 7(b) and 7(c)] coincides with the THL transition of the isolated LC dimer; consequently, region III-1 does not exist. We also notice that when the active coupling controlling parameter is  $\mu$  or  $\nu$ , the real values of  $\gamma_r$  are observed at the right-hand side of the limiting curve  $\gamma_r = 0$ . When the active coupling is  $c$ , the real values of  $\gamma_r$  are rather observed at the left-hand side of the limiting line  $\gamma_r = 0$  [Figs. 7(b) and 7(c)].

In what follows, we analyze the scattering coefficients' dependence on the different regions detailed above. Whenever a region is observed in the  $k$  spectrum of a dimer, the behavior is dictated by the related scattering coefficients. Specifically, for the dimer MLC, which includes all regions in the spectrum [Figs. 6(c) and 6(d)], the value of  $\mu$  can be taken as the region-selective parameter and thus be tuned from one region to another while the other parameters  $\vartheta = 0.1$ ,  $c = 0.5$ , and  $\nu = 0.25$  remain unchanged unless otherwise specified. As predicted from the above analysis, we identify in Figs. 8 and 9 spectral singularities of zero-width resonances ( $D = 0$ ) [39] corresponding to intense scattering coefficients amplifications (i.e.,  $T_{g,l} = R_{l,g} = \infty$ ) in all the propagation regions except at the frontiers, where the waves are perfectly reflected (i.e.,  $T_{g,l} = 0$  and  $R_{l,g} = 1$ ). These spectral singularities give rise to lasing modes  $k_r$  at  $\gamma_r$ . Notwithstanding this analysis, the scattering coefficients have specific features in each region depending on the nature of  $k$ .

In region I [Fig. 8(a)], for example, at  $\mu = 0.5$ , the wavenumbers are all real and positive (allowed frequencies), two close EPs emerge ( $\gamma_g = 0.282$ ,  $\gamma_l = 0.438$ ) as gain/loss values at which the gain/loss reflected wave vanishes, i.e.,  $R_g = 0$  ( $R_l \neq 0$ ) and  $R_l = 0$  ( $R_g \neq 0$ ), respectively. The parameters  $\gamma_{g,l}$  are the gain/loss reflectionless points. Due to the unitary transmission ( $T_{g,l} = 1$ ), moreover, at these points,

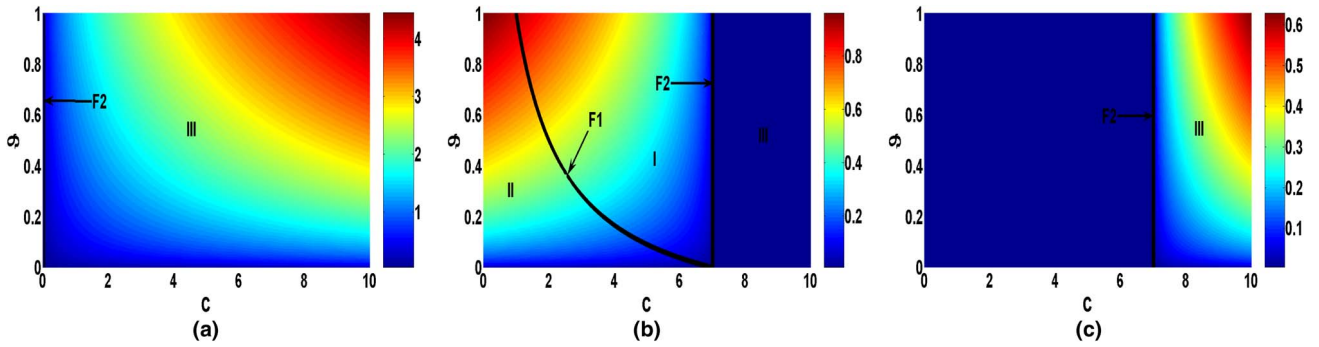


**Fig. 7.** Spectrum of imaginary  $\gamma_r$  for TH dimer C in (a). F2 occurs at  $c = 0$ , indicating no propagation for real or complex values of  $k$ ;  $\gamma_r$  is purely imaginary (the real part of  $\gamma_r$  being zero), and so is the wavenumber  $k$ . The case of THL dimer LC ( $\nu = 7$ ) LC in (b) real part of  $\gamma_r$  and (c) its imaginary part. F2 coincides both with the THL conditions and with the limit curve  $\gamma_r = 0$ , as it separates totally the regions for real and purely imaginary  $\gamma_r$ . The active coupling is the capacitance  $c$  and the real values of  $\gamma_r$  are observed at the left-hand side of the limiting zone  $\gamma_r = 0$ . There is no real value of  $\gamma_r$  in region III.

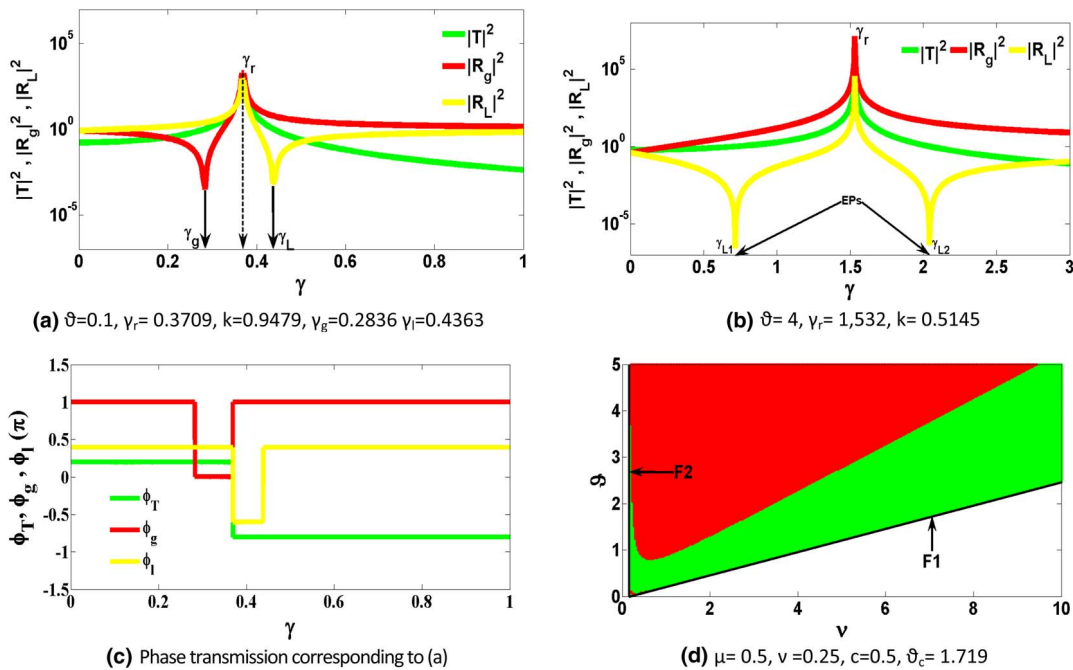


**Fig. 8.** Scattering normalized coefficient  $T$  and  $R$  of THL dimer MLC versus the gain/loss parameter in region I.  $\nu = 0.25$ ,  $c = 0.5$ , and  $\vartheta = 0.1$  and  $\mu = 0.5$ . (a)  $k$  and  $\gamma$  are real; EPs occur for the gain/loss incidence while in (b)  $\vartheta = 4$ , and the EP occurs only for the loss incidence at two different points.  $T > 1$  in between the EP in both cases. Lasing modes are observed inside the EPs, where the transmission is superunitary. (c) At  $\gamma_g$  and  $\gamma_l$ , the phase transmission corresponding to (a) does not change. In (d), the spectrum of  $\vartheta$  is plotted for  $c = 0.5$  and  $\mu = 0.5$ ; the green color indicates the region where the dimer is PTS in two opposite directions (at  $\gamma_{g/l}$ ), while in the red region, the dimer is PTS in one direction (two distinct values of  $\gamma_l$ ).

the transmission phase is not affected, as indicated in Fig. 8(c). These points refer to regions of unidirectional invisibility [24,40] from left and right, respectively. In the range between unidirectional invisibility from the left ( $R_g = 0$ ,  $T = 1$ ) and unidirectional invisibility from the right ( $R_l = 0$ ,  $T = 1$ ) (i.e.,  $\gamma_g < \gamma < \gamma_l$ ) the transmission is superunitary ( $T > 1$ ); otherwise, the transmission is subunitary ( $T < 1$ ). These unidirectional reflectionlessness and invisibility are the characteristics of any PTS scattering system. They are of technological interest, as they offer the means of one-way designing of linear optical devices [24,40,41]. It was demonstrated [39,42–43] that in PTS systems, the transition from the PTS phase to the PTS

broken phase is dictated by the unitary related transmission. In particular, it was shown that  $T < 1$  corresponds to the PTS phase, while  $T > 1$  induces a PTS broken phase; thus our scattering system is phase-broken PT symmetric between  $\gamma_g$  and  $\gamma_l$ .

Importantly, we find a critical value of the TL coupling parameter  $\vartheta_c$  above which the reflection scattering coefficient from the right does not vanish any longer, but the left reflection vanishes at two different points. This critical value is obtained by solving the equation  $R_{g/l} = 0$ . For the set of parameters we have considered, the calculated critical value is  $\vartheta_c = 1.719$ . In Fig. 8(b), we have taken  $\vartheta = 4 > \vartheta_c$ , the scattering plots exhibit two far-apart EPs at  $\gamma_{L1} = 0.7156$  and  $\gamma_{L2} = 2.042$  for which  $R_l = 0$  ( $T = 1$ ).



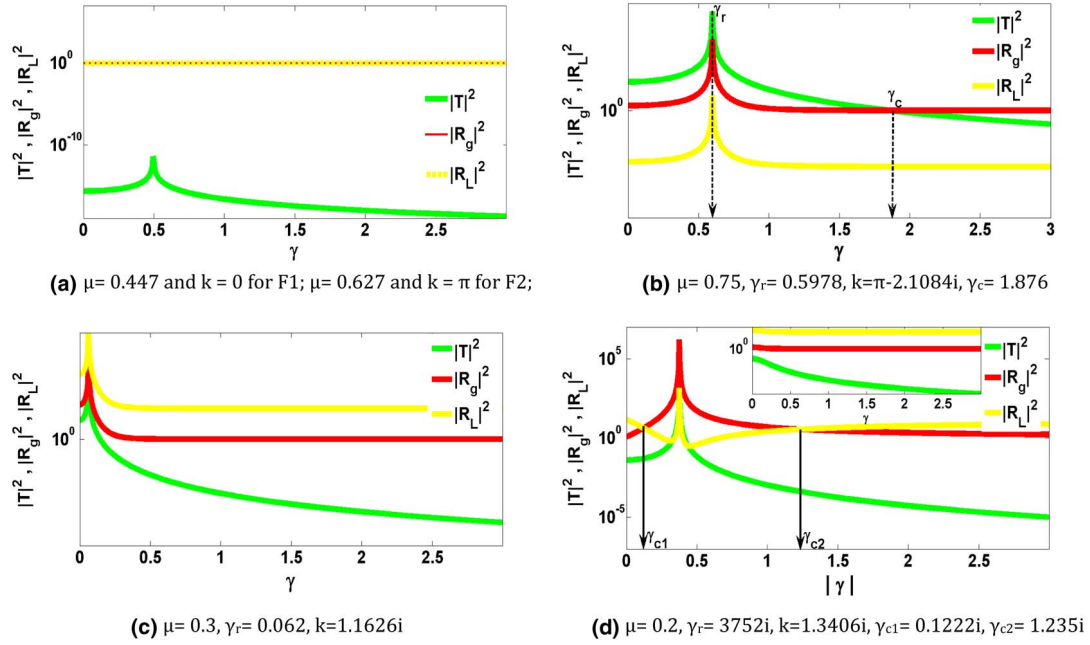


**Fig. 9.** Scattering normalized coefficient  $T$  and  $R$  of THL dimer MLC versus the gain/loss parameter  $\nu = 0.25$ ,  $c = 0.5$  and  $\vartheta = 0.1$ . (a) At the frontiers F1 ( $\mu = 0.447$ ,  $k = 0$ ) and F2 ( $\mu = 0.627$ ,  $k = \pi$ ), the transmission vanishes completely:  $T = 0$ ,  $R_g = R_l = 1$ . (b) In region II,  $\mu = 0.75$ ,  $k$  is complex and  $\gamma$  is real,  $\gamma_c$  occurs at  $R_g = T = 1$  below which  $T > 1$  and  $T < 1$  above. Lasing modes occur in the region of superunitary transmission. Far from  $\gamma_r$ ,  $R_l = 0$ . (c) Region III-1,  $k$  is imaginary but  $\gamma$  is real. Lasing mode occurs around  $\gamma_r = 0.062$ . The transmission vanishes completely, i.e.,  $T = 0$  and  $R_g = 1 (< R_l)$ . (d) Region III-2,  $\mu = 0.75$ ;  $k$  and  $\gamma$  are both imaginary.  $|\gamma|$  is the magnitude of the imaginary gain/loss parameter  $\gamma$ . Lasing mode is observed inside the region defined by  $\gamma_{c1}$  and  $\gamma_{c2}$  where  $R_g = R_l$ . Far from  $\gamma_c$ ,  $T = 0$  and  $R_l > R_g$ . The inset indicates that all real  $\gamma$  incidences are totally attenuated in transmission and perfectly reflected in the gain side ( $R_g = 1$ ), while the loss reflected wave is amplified ( $R_l > R_g$ ).

In Fig. 8(d), the spectrum of  $\vartheta$  is numerically plotted for the parameters  $c = 0.5$ ,  $\mu = 0.5$ . The green color identifies the region where  $R_{g/l} = 0$  admits one solution each. Consequently, there are two EPs, one in each direction, giving rise to the PTS behavior in the gain/loss direction. In the red region, there are two solutions for  $R_l = 0$  and no solution for  $R_g = 0$ . Likewise, there are two EPs but only in the loss direction and no EP in the right direction. Moreover, the right reflection is greater than the transmission and the EPs are very far apart. This behavior has drastic consequence on the scattering system, as this latter becomes non-PTS and mainly mirrors in the gain direction. The PTS behavior is observed only in the allowed values of real frequency as defined by the frontiers F1 and F2. It is useful to reveal that this transmission tends to vanish as both reflections (from gain and loss sides) tend to unity far away from the inner region of unidirectionality  $R_{l,g} \rightarrow 1$  when  $T \rightarrow 0$ .

At the two frontiers, the transmission vanishes completely and the dimer behaves like a perfect mirror throughout the  $\gamma$  range (i.e.,  $R_{l,g} = 1$  and  $T = 0$ ) as predicted by the combined Eq. (13) in Eqs. (9)–(11). For example, in Fig. 9(a), the scattering parameters are plotted at F1 for  $\mu = 0.447$ ,  $k = 0$ , and at F2 for  $\mu = 0.627$ ,  $k = \pi$ . In region II, the upper forbidden gap with complex wavenumbers ( $k = \pi - ik$ ), the scattering coefficients are plotted for  $\mu = 0.75$  in Fig. 9(b). As indicated in the graph,  $\gamma_r$  exists and is real and  $T > R_g > R_l$ . It is, however, instructive that far from this lasing zone, the left reflection is totally attenuated while the gain reflection is unity; likewise there is a critical value of  $\gamma = \gamma_c$  where  $R_g = T = 1$ , below which the  $(T + R)$  is superunitary and subunitary above. In

region III, the lower forbidden gap having purely imaginary wavenumbers, we distinguish the plot in region III-1 where  $\gamma_r$  is real [Fig. 9(c)] and in region III-2 where  $\gamma_r$  is purely imaginary [Fig. 9(d)]. For real  $\gamma_r$  (for example,  $\mu = 0.3$ ), there is a resonant mode indicated by  $\gamma_r$  and  $R_l > R_g > T$  and outside the resonant mode, the transmission is completely attenuated while the reflection scatterings are constants,  $R_g = 1$  and  $R_l > R_g$ . For imaginary values of  $\gamma_r$  (for example,  $\mu = 0.2$ ), the scattering coefficients are plotted in the imaginary plane. There are two critical points at which  $R_g = R_l$  ( $T = 0$ ), inside which the gain reflection is amplified and the loss reflection is attenuated;  $R_g > R_l$  with  $R_l < 1$  except at the resonance. Indeed, a lasing mode does exist where all the scattering coefficients are intensely amplified simultaneously with the reflections are more amplified than the transmission. Outside the region of simultaneously left and right unitary reflection, the loss reflection is slightly amplified, while the gain reflection is slightly attenuated, and thus  $R_l > R_g$ . As indicated at the inset of the curve, all real  $\gamma$  incidences are totally attenuated in transmission and perfectly reflected in the gain side ( $R_g = 1$ ), while the loss reflected wave is amplified ( $R_l > R_g$ ). This indicates the absence of lasing states for real values of  $\gamma_r$ .

## 5. CONCLUSION

We have investigated the mode dynamics of a general PTS dimer MLC. We have shown that PTS dimers can be grouped into TH dimers, for which  $\gamma_1 \neq 0$ , and THL dimers that can have a vanishing breaking point  $\gamma_1$  under some specified

conditions. This THLP is marked by the degeneracy of the modes along the controlling coupling constant inside the PTS dimer cells. The THL transition is related to the phase dynamic modes and is characterized by an abrupt phase transition in the broken phase along the increasing coupling parameter, which however arises only when the coupling  $M$ ,  $L$ , and  $ML$  are associated in parallel with  $C$ . When the TH dimers are inserted into a TL, the scattering systems admit real waves in the allowed band and complex waves in the upper forbidden gap. A THL scattering system will additionally control purely imaginary waves in the lower gap corresponding to a real or an imaginary gain/loss parameter. We have also demonstrated that when the PTS dimers scattering systems propagate real wavenumbers, they undergo a spontaneous breaking symmetry at the EP, inside which the transmission is superunitary and subunitary outside. Interestingly, the PTS scattering system exhibits qualitative new behavior, such as the canceling of the PTS property in one direction, which arises when  $\vartheta$ , the TL coupling parameter, exceeds a TH limit  $\vartheta_c$ . The results demonstrate promising applications in wave manipulations for artificial structures, which exhibit novel properties and control mechanisms. We anticipate that our work can also stimulate many experimental studies to uncover the full potential of PTS TH and THL dimers, especially in the nonlinear interactions for electro-optical applications.

## REFERENCES

- C. M. Bender and S. Boettcher, "Real spectra in non-Hermitian Hamiltonians having PT symmetry," *Phys. Rev. Lett.* **80**, 5243–5246 (1998).
- C. M. Bender, S. Boettcher, and P. N. Meisinger, "PT-symmetric quantum mechanics," *J. Math. Phys.* **40**, 2201–2229 (1999).
- A. Mostafazadeh, "Invisibility and PT symmetry," *Phys. Rev. A* **87**, 012103 (2013).
- A. Mostafazadeh, "Pseudo-Hermiticity versus PT symmetry: the necessary condition for the reality of the spectrum of a non-Hermitian Hamiltonian," *J. Math. Phys.* **43**, 205–214 (2002).
- A. Regensburger, C. Bersch, M.-A. Miri, G. Onishchukov, D. N. Christodoulides, and U. Peschel, "Parity-time synthetic photonic lattices," *Nature* **488**, 167–171 (2012).
- K. G. Makris, R. El-Ganainy, D. N. Christodoulides, and Z. H. Musslimani, "Beam dynamics in PT symmetric optical lattices," *Phys. Rev. Lett.* **100**, 103904 (2008).
- T. Kato, *Perturbation Theory for Linear Operators*, 2nd ed. (Springer, 1995).
- A. Mostafazadeh, "Self-dual spectral singularities and coherent perfect absorbing lasers without PT-symmetry," *J. Phys. A* **45**, 444024 (2012).
- S. V. Suchkov, F. Fotsa-Ngaffo, A. Kenfack-Jiotsa, A. D. Tikeng, T. C. Kofane, Y. S. Kivshar, and A. A. Sukhorukov, "Non-Hermitian trimers: PT-symmetry versus pseudo-Hermiticity," *New J. Phys.* **18**, 065005 (2016).
- Z. H. Musslimani, R. El-Ganainy, K. G. Makris, and D. N. Christodoulides, "Optical solitons in PT periodic potentials," *Phys. Rev. Lett.* **100**, 030402 (2008).
- C. E. Rüter, K. G. Makris, R. El-Ganainy, D. N. Christodoulides, M. Segev, and D. Kip, "Observation of parity-time symmetry in optics," *Nat. Phys.* **6**, 192–195 (2010).
- S. V. Suchkov, D. I. Borisov, A. A. Sukhorukov, and Y. S. Kivshar, "Signal manipulation with a PT-symmetric coupler embedded into an array of optical waveguides," *Lett. Mater.* **4**, 222–225 (2014).
- A. A. Sukhorukov, S. V. Dmitriev, S. V. Suchkov, and S. Yuri, "Nonlocality in PT-symmetric waveguide arrays with gain and loss," *Opt. Lett.* **37**, 2148–2150 (2012).
- M. C. Zheng, D. N. Christodoulides, R. Fleischmann, and T. Kottos, "PT optical lattices and universality in beam dynamics," *Phys. Rev. A* **82**, 010103(R) (2010).
- S. Longhi, "Bloch oscillations in complex crystals with PT symmetry," *Phys. Rev. Lett.* **103**, 123601 (2009).
- S. Longhi, "PT-symmetric laser absorber," *Phys. Rev. A* **82**, 031801 (2010).
- Y. D. Chong, L. Ge, and A. D. Stone, "PT-symmetry breaking and laser-absorber modes in optical scattering systems," *Phys. Rev. Lett.* **106**, 093902 (2011).
- X. Zhu, H. Ramezani, C. Shi, J. Zhu, and X. Zhang, "PT-symmetric acoustics," *Phys. Rev. X* **4**, 031042 (2014).
- R. Fleury, D. Sounas, and A. Alu, "An invisible acoustic sensor based on parity-time symmetry," *Nat. Commun.* **6**, 5905 (2015).
- C. Shi, M. Dubois, Y. Chen, L. Cheng, H. Ramezani, Y. Wang, and X. Zhang, "Accessing the exceptional points of parity-time symmetric acoustics," *Nat. Commun.* **7**, 11110 (2016).
- T. Kottos, "Optical physics: broken symmetry makes light work," *Nat. Phys.* **6**, 166–167 (2010).
- L. Chang, X. Jiang, S. Hua, C. Yang, J. Wen, L. Jiang, G. Li, G. Wang, and M. Xiao, "Parity-time symmetry and variable optical isolation in active-passive-coupled microresonators," *Nat. Photonics* **8**, 524–529 (2014).
- A. A. Sukhorukov, Z. Xu, and Y. S. Kivshar, "Nonlinear suppression of time reversals in PT-symmetric optical couplers," *Phys. Rev. A* **82**, 043818 (2010).
- Z. Lin, H. Ramezani, T. Eichelkraut, T. Kottos, H. Cao, and D. N. Christodoulides, "Unidirectional invisibility induced by PT-symmetric periodic structures," *Phys. Rev. Lett.* **106**, 213901 (2011).
- A. Mostafazadeh, "Semiclassical analysis of spectral singularities and their applications in optics," *Phys. Rev. A* **84**, 023809 (2011).
- R. El-Ganainy, K. G. Makris, D. N. Christodoulides, and Z. H. Musslimani, "Theory of coupled optical PT-symmetric structures," *Opt. Lett.* **32**, 2632–2634 (2007).
- S. Longhi and L. Feng, "PT-symmetric microring laser-absorber," *Opt. Lett.* **39**, 5026–5029 (2014).
- H. Alaeian and J. A. Dionne, "Parity-time-symmetric plasmonic metamaterials," *Phys. Rev. A* **89**, 033829 (2014).
- L. Feng, Z. J. Wong, R.-M. Ma, Y. Wang, and X. Zhang, "Single-mode laser by parity-time symmetry breaking," *Science* **346**, 972–975 (2014).
- J. Schindler, A. Li, M. C. Zheng, F. M. Ellis, and T. Kottos, "Experimental study of active LRC circuits with PT symmetries," *Phys. Rev. A* **84**, 040101 (2011).
- Z. Lin, J. Schindler, F. M. Ellis, and T. Kottos, "Experimental observation of the dual behavior of PT-symmetric scattering," *Phys. Rev. A* **85**, 050101 (2012).
- H. Ramezani, J. Schindler, F. M. Ellis, U. Gunther, and T. Kottos, "Bypassing the bandwidth theorem with PT symmetry," *Phys. Rev. A* **85**, 062122 (2012).
- J. Schindler, Z. Lin, J. M. Lee, H. Ramezani, F. M. Ellis, and T. Kottos, "PT-symmetric electronics," *J. Phys. A* **45**, 444029 (2012).
- L. J. Matthew, "Wave transport phenomena in systems with generalized parity-time symmetry," Honors theses—All (Wesleyan University, 2014), 1285.
- L. Ge and A. D. Stone, "Parity-time symmetry breaking beyond one dimension: the role of degeneracy," *Phys. Rev. X* **4**, 031011 (2014).
- A. Cerjan, A. Raman, and S. Fan, "Exceptional contours and band structure design in parity-time symmetric photonic crystals," *Phys. Rev. Lett.* **116**, 203902 (2016).
- H. Alaeian, B. Baum, V. Jankovic, M. Lawrence, and J. A. Dionne, "Towards nanoscale multiplexing with parity-time symmetric plasmonic coaxial waveguides," *Phys. Rev. B* **93**, 205439 (2016).
- A. Mock, "Characterization of parity-time symmetry in photonic lattices using Heesh-Shubnikov group theory," *Opt. Express* **24**, 22693 (2016).
- A. Mostafazadeh, "Spectral singularities of complex scattering potentials and infinite reflection and transmission coefficients at real energies," *Phys. Rev. Lett.* **102**, 220402 (2009).
- A. Mostafazadeh, "Unidirectionally invisible potentials as local building blocks of all scattering potentials," *Phys. Rev. A* **90**, 023833 (2014).
- L. Feng, Y.-L. Xu, W. S. Fegasolli, M.-H. Lu, J. E. B. Oliveira, V. R. Almeida, Y.-F. Chen, and A. Scherer, "Single-mode laser by parity-time symmetry breaking," *Nat. Mater.* **12**, 108–113 (2012).
- L. Ge, Y. D. Chong, and A. D. Stone, "Conservation relations and anisotropic transmission resonances in one-dimensional PT-symmetric photonic heterostructures," *Phys. Rev. A* **85**, 023802 (2012).
- Y. Fu, Y. Xu, and H. Chen, "Zero index metamaterials with PT symmetry in a waveguide system," *Opt. Express* **24**, 1648–1657 (2016).